Engineering Journal

First Quarter 2026 | Volume 63, No. 1

Smarter. Stronger. Steel.

Engineering Journal

American Institute of Steel Construction

Dedicated to the development and improvement of steel construction, through the interchange of ideas, experiences, and data.

 Engineering Journal (ISSN 0013-8029) is published quarterly. Published by the American Institute of Steel Construction at 130 E Randolph Street, Suite 2000, Chicago, IL 60601.

Torsion of Rectangular HSS and Box Section Members: A Critical Review

BO DOWSWELL

ABSTRACT

The purposes of this paper are to summarize the research on the torsional performance of square and rectangular hollow section members and compare the available experimental results to the applicable provisions in the AISC *Specification* (2022). A review of the research on the torsional strength of square and rectangular hollow section members revealed 49 experimental tests from 11 projects. A first-order reliability analysis was used to calculate appropriate resistance factors for the current design equations, revealing inconsistent reliability indices that are dependent on the predicted failure mode. Revisions are proposed for the provisions in AISC *Specification* Section H3.1 that result in a simpler design method with increased accuracy. Also, the accuracy of serviceability rotation calculations is evaluated using the available experimental data.

Keywords: torsion, rectangular HSS, box section, serviceability rotation.

INTRODUCTION

Square and rectangular hollow sections are often used to resist twisting because they are more efficient at resisting torsional loads than open sections. These hollow sections are defined as HSS or box sections based on the manufacturing and fabrication methods. The AISC *Specification* (2022) Glossary defines two types of hollow sections:

- Box section: Square or rectangular doubly symmetric members made with four plates welded together at the corners such that it behaves as a single member.
- HSS (hollow structural section): Square, rectangular or round hollow structural steel section produced in accordance with one of the product specifications in Section A3.1a(b).

The torsional strength of square and rectangular HSS shapes is evaluated according to AISC *Specification* Section H3.1. Both the yielding and wall buckling limit states are addressed only for HSS shapes. The design method is based on the classical plate buckling equation and research related primarily to I-shaped member webs subjected to shear. Although the load transfer mechanism is similar to that of I-shaped beam webs, the accuracy of these equations has not been established for HSS members subjected to torsion.

Bo Dowswell, PhD, PE, Principal, ARC International, LLC, Birmingham, Ala.
Email: bo@arcstructural.com

Paper No. 2024–09R

The purposes of this paper are to summarize the research on the torsional performance of square and rectangular hollow section members and compare the available experimental results to the applicable provisions in the AISC *Specification*. A first-order reliability analysis is used to calculate appropriate resistance factors for the current design equations and revisions to the AISC *Specification* are proposed. Also, the accuracy of serviceability rotation calculations is evaluated using the available experimental data.

AISC *SPECIFICATION* SECTION H3

The nominal torsional strength of an HSS member is calculated with Equation H3-1 in AISC *Specification* Section H3.1.

$$T_n = F_{cr}C \qquad \text{(AISC } Spec. \text{ H3-1)}$$

For rectangular HSS members, the critical shear stress is determined as follows.

When $\frac{h}{t} \le 2.45\sqrt{\frac{E}{F_y}}$

$$F_{cr} = 0.6F_y \qquad \text{(AISC } Spec. \text{ H3-3)}$$

When $2.45\sqrt{\frac{E}{F_y}} < \frac{h}{t} \le 3.07\sqrt{\frac{E}{F_y}}$

$$F_{cr} = 0.6F_y \frac{2.45\sqrt{\frac{E}{F_y}}}{\left(\frac{h}{t}\right)} \qquad \text{(AISC } Spec. \text{ H3-4)}$$

When $3.07\sqrt{\frac{E}{F_y}} < \frac{h}{t} \le 260$

$$F_{cr} = \frac{0.458\pi^2 E}{\left(\frac{h}{t}\right)^2} \quad \text{(AISC } \textit{Spec.}\text{ H3-5)}$$

where

C = torsional modulus constant, in.^{3}
E = modulus of elasticity, ksi
F_y = specified minimum yield stress, ksi
h = flat width of longer side, in.
t = design wall thickness, in.
ϕ_T = 0.90 (LRFD)
Ω_T = 1.67 (ASD)

The cross-sectional dimensions of a rectangular HSS are shown in Figure 1.

AISC *SPECIFICATION* SECTION G2

For rectangular HSS members, torques are resisted primarily by shear in the walls. Because the behavior of HSS walls is similar to that of I-shaped member webs subjected to shear loads, AISC *Specification* Section G2.1 is reviewed in this section of the paper. The nominal shear strength of I-shaped members is calculated with Equation G2-1 in AISC *Specification* Section G2.1.

$$V_n = 0.6F_y A_w C_{v1} \quad \text{(AISC } \textit{Spec.}\text{ G2-1)}$$

where A_w is the web area. Built-up members are addressed in Section G2.1(b), where the web strength coefficient, C_{v1}, is defined as follows.

When $\frac{h}{t} \le 1.10\sqrt{\frac{k_v E}{F_y}}$

$$C_{v1} = 1.0 \quad \text{(AISC } \textit{Spec.}\text{ G2-3)}$$

When $\frac{h}{t} > 1.10\sqrt{\frac{k_v E}{F_y}}$

$$C_{v1} = \frac{1.10\sqrt{\frac{k_v E}{F_y}}}{\left(\frac{h}{t}\right)} \quad \text{(AISC } \textit{Spec.}\text{ G2-4)}$$

According to Section G2.1(b)(2)(i), $k_v = 5.34$ for webs without transverse stiffeners.

EUROCODE 3, PART 1-1

Eurocode 3, Part 1-1 (CEN, 2005) Section 6.2.7(7) states, "As a simplification, in the case of a member with a closed hollow cross-section, such as a structural hollow section, it may be assumed that the effects of torsional warping can be neglected." The design philosophy for closed hollow sections in Part 1-1 Section 6.2.7(8) is similar to that of AISC *Specification* Section H3.1, with the shear strength calculated using the provisions for plated structural elements in Eurocode 3, Part 1-5 (CEN, 2006).

Part 1-5 Section 5 specifies the design method for the shear resistance of plate elements. The factor η is used to estimate the ultimate shear buckling strength. Here, $\eta = 1.2$ is recommended for calculating the shear strength of steel grades up to and including S460 (F_y = 460 MPa = 67 ksi), and $\eta = 1.0$ is recommended for higher strength steels. For values of η greater than 1.0, the increased strength is attributed to strain hardening (Beg et al., 2010). Because large inelastic rotations may be required to obtain the torsional strengths calculated with $\eta > 1.0$, $\eta = 1.0$ is used in the equations below. This limits the critical stress to the shear yield stress. Where applicable, the variable name symbols defined in the AISC *Specification* were used in lieu of the Eurocode symbols. This is intended to make direct comparisons between the two design requirements easier.

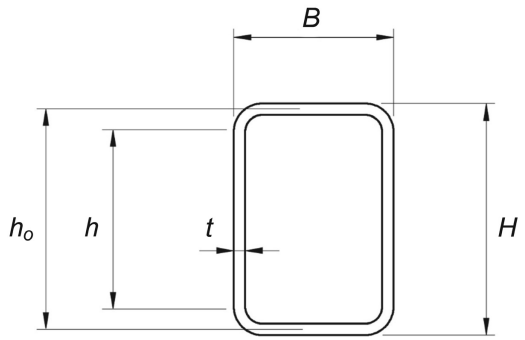

Fig. 1. Cross-sectional dimensions of a rectangular HSS.

The critical shear stress is

$$F_{cr} = \frac{F_y C_v}{\sqrt{3}} \tag{1}$$

When $\lambda_T < 0.83$

$$C_v = 1.00 \tag{2}$$

When $\lambda_T \geq 0.83$

$$C_v = \frac{0.83}{\lambda_T} \tag{3}$$

The slenderness is

$$\lambda_T = \sqrt{\frac{\tau_y}{\tau_e}} = 0.76\sqrt{\frac{F_y}{\tau_e}} \tag{4}$$

where the shear yield stress, τ_y, is $F_y/\sqrt{3}$. The elastic critical shear stress, τ_e, of an infinitely long plate with simply supported edges subjected to shear is (Ziemian, 2010)

$$\tau_e = k_v \frac{\pi^2 E}{12(1-\nu^2)\left(\frac{h}{t}\right)^2} \tag{5}$$

where

k_v = buckling coefficient
= 5.34 for plates with simply supported edges
= 8.98 for plates with clamped edges
ν = Poisson's ratio

When the elements are assumed to be simply supported, the slenderness can be determined by substituting Equation 5 into Equation 4 with $k_v = 5.34$.

$$\lambda_T = 0.35\frac{h}{t}\sqrt{\frac{F_y}{E}} \tag{6}$$

For comparison, the Eurocode provisions can be written in the same format as the AISC *Specification*. To make the comparisons easier, the shear yield stress, $\tau_y = 0.6F_y$, is used in lieu of $\tau_y = F_y/\sqrt{3}$.

When $\frac{h}{t} < 2.4\sqrt{\frac{E}{F_y}}$

$$F_{cr} = 0.6F_y \tag{7}$$

When $\frac{h}{t} \geq 2.4\sqrt{\frac{E}{F_y}}$

$$F_{cr} = 0.6F_y \frac{2.4\sqrt{\frac{E}{F_y}}}{\left(\frac{h}{t}\right)} \tag{8}$$

SECTION PROPERTIES

The torsional modulus constant, C, is used in strength calculations, and the torsional inertia constant, J, is used in rotational stiffness calculations. As discussed in AISC *Specification* Section H3.1 Commentary, the torsional modulus constant can be defined using a membrane analogy. The area enclosed by the sectional mid-thickness is

$$A_o = (B-t)(H-t) - r_m^2(4-\pi) \tag{9}$$

The torsional modulus constant is

$$C = 2tA_o = 2t\left[(B-t)(H-t) - r_m^2(4-\pi)\right] \tag{10}$$

where

B = overall width, in.
H = overall height, in.
r_m = mid-thickness corner radius, in.

Assuming $r_m = 1.5t$, which is based on an outside corner radius, r_o, of $2t$, results in the HSS torsional constant in the User Note in AISC *Specification* Section H3.1:

$$C = 2t(B-t)(H-t) - 4.50t^3(4-\pi) = 2t(B-t)(H-t) - 3.86t^3 \tag{11}$$

For the rectangular HSS materials listed in *Specification* Section A3.1a.(b) [ASTM A500 (2021), A501 (2014), A1085 (2015a), and A618 (2015b)], the maximum permissible outside corner radius is $3t$. Equation 12, which is based on $r_m = 2.5t$, can be used for this condition.

$$C = 2t(B-t)(H-t) - 12.5t^3(4-\pi) = 2t(B-t)(H-t) - 10.7t^3 \tag{12}$$

The torsional inertia constant is

$$J = \frac{4tA_o^2}{p_m} \tag{13}$$

The mid-thickness perimeter is

$$p_m = 2(B+H-4r_o) + 2\pi r_m = 2\left[B+H-2t+r_m(\pi-4)\right] \tag{14}$$

where

r_o = outside corner radius, in.

Equations 10 through 13 were derived using thin-wall theory, which is based on the assumption that the shear stress is constant across the wall thickness. Thin-wall theory is generally deemed valid when $H/t \geq 10$ (Seaburg and Carter, 1997). Thick-wall theory, which considers the shear stress gradient across the wall thickness, was used to derive the torsional inertia and modulus constants in Equations 15 and 16, respectively.

$$J_t = \frac{4tA_o^2}{p_m} + \frac{p_m t^3}{3} \tag{15}$$
$$= J + \frac{p_m t^3}{3}$$

$$C_t = \frac{J_t}{t + 2\dfrac{A_o}{p_m}} \tag{16}$$

The second term in Equation 15 is negligible, and the torsional inertia constant can be calculated with Equation 13 for all practical conditions. For box sections, the sectional properties can be calculated with $r_o = r_m = 0$.

RESIDUAL STRESSES

Although residual stresses do not affect the torsional strength, the buckling strength is dependent on both the magnitude and the pattern of residual stresses. Also, serviceability rotations can be significantly higher than calculated if the residual stresses cause inelasticity prior to reaching the calculated yield moment.

Cold-Formed HSS

Due to the cold-bending process, cold-formed square and rectangular HSS members have high through-thickness residual stresses at the corners. Liu et al. (2017) summarized the research on these residual stresses and determined that a mean value for the bending residual surface stress is 70% of the yield stress. This agrees well with the recommendations of Key et al. (1988) and Davison and Birkemoe (1983).

Longitudinal membrane residual stresses are compressive at the corners (Sherman, 1992). Measurements showed that these stresses are dependent to the HSS geometry, with values at the corners, flats, and weld approximately equal to 35%, 60%, and 70% of the yield strength, respectively (Zhang et al., 2016). Sherman (1971) developed a simplified pattern for cold-formed rectangular HSS members, where the longitudinal residual stresses varied linearly from 40% of the yield stress in compression at the corners to 40% of the yield stress in tension at the wall mid-width.

Box Sections

For box sections, the longitudinal residual stresses at the corners are approximately equal to the plate yield stress. Depending on the plate width, compression residual stresses are between 10% and 30% of the yield stress. Compression residual stresses are nearly constant and cover most of the wall width. These characteristics have been verified for both fillet-welded sections (Uy, 1998; Ingvarsson, 1977; ECCS, 1976) and groove-welded sections (Chen and Chang, 1993).

Hot-Formed HSS

Because the final cooling pattern is relatively uniform for hot-formed HSS members, residual stresses are usually considered negligible in buckling analysis (Sherman, 1992; ECCS, 1976). However, for the assumed pattern in ECCS, the residual stress varied linearly from 50% of the yield stress in compression at the corners to 20% of the yield stress in tension. For this pattern, the tension residual stress was constant over most of the wall width.

BEHAVIOR

Rectangular HSS torsion members can fail by shear yielding, shear buckling, or cross-sectional collapse. The limit states that are applicable to common building members, shear yielding, and shear buckling will be discussed further in the remaining parts of this paper.

Cross-Sectional Collapse

Cross-sectional collapse can occur when second-order effects cause the walls to deform inward at large torsional rotations as shown in Figure 2 (Chen, 2000). This cross-sectional flattening reduces the torsional strength, which causes an unstable post-buckling curve, resulting in collapse under large plastic deformations (Zaifuddin et al., 2017). Often identified as a distortional mode, the buckled shape is characterized by inward deformation at the wall mid-width (Chen, 2000; Chen and Wierzbicki, 2000; Zaifuddin et al., 2017), sometimes accompanied by inward deformation of the corners (Omidvari and Hematiyan, 2015). The length of diagonal half-waves along the member longitudinal axis are several times the half-wavelengths for

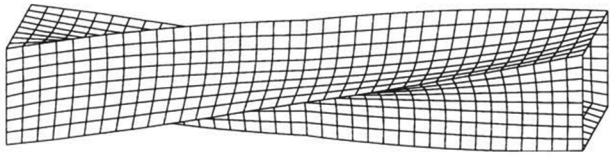

Fig. 2. Cross-sectional collapse (Chen, 2000).

the shear buckling mode, and they often extend over the full member length.

Because this limit state is applicable only when torsional rotations are significantly higher than the yield rotation, it is usually a consideration only for extreme loadings (such as for vehicle impact studies) and will not be addressed further in this paper. However, the unstable collapse behavior is a consideration for a reliability analysis that considers the consequences of failure. Also, the second-order effects in earlier loading stages can potentially affect the behavior by lowering the proportional limit torque.

Shear Yielding

The shear yielding limit state is shown in Figure 3 (Chen, 2000). The behavior of rectangular HSS torsion members is similar to that of flexural members, where the moment-rotation curve is nonlinear. For a perfect flexural member with linear elastic–perfectly plastic material behavior, the moment-rotation curve is linear up to the yield moment, M_y. At higher moments, the curve is nonlinear up to the maximum value, which is the plastic moment, M_p. Figure 4 shows the torque versus twist plots for the specimens tested by Ridley-Ellis et al. (2003).

Because thick-wall theory considers the shear stress gradient across the wall thickness, the yield torsion can be calculated with Equation 17.

$$T_y = \tau_y C_t \tag{17}$$

Equation 18, which is based on thin-wall theory, is used to calculate the plastic torsion.

$$T_p = \tau_y C \tag{18}$$

For HSS sizes typically used in buildings, Ridley-Ellis (2000) determined that T_p/T_y ranged between 1.05 and 1.25. Using the experimental data in Appendix A, the 20 specimens with an experimental failure mode of yielding had a mean torsional shape factor, C/C_t, of 1.12.

Figure 5 shows the data points for the experimental specimens that are documented in Appendix A, where T_p/T_y is plotted versus the maximum overall wall width-to thickness ratio, H/t, with $H \geq B$. The plot shows a significant difference between the elastic and plastic properties when $H/t < 40$.

With flexural members, the moment-rotation curve becomes nonlinear at moments lower than M_y due to stress concentrations, residual stresses, and geometric

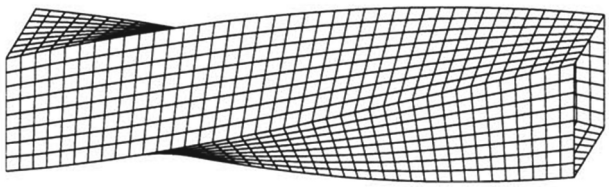

Fig. 3. Shear yielding (Chen, 2000).

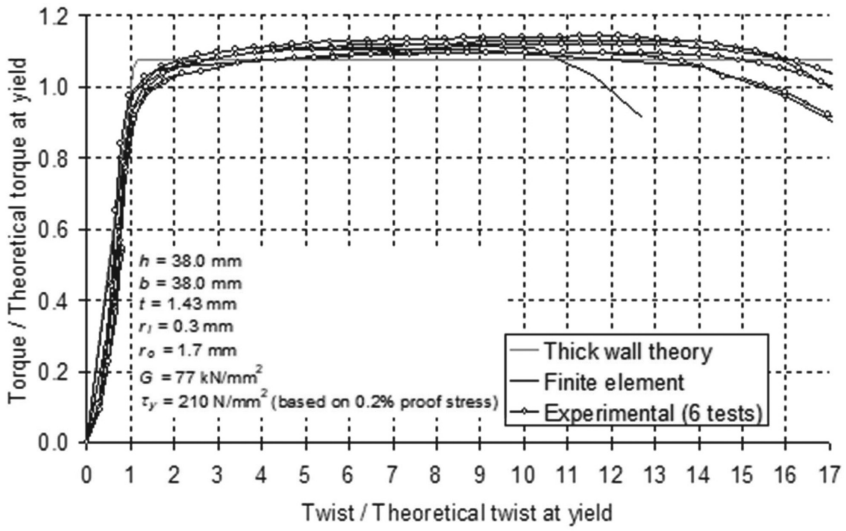

Fig. 4. Torque versus twist for the specimens tested by Ridley-Ellis et al. (2003).

imperfections. Rectangular HSS torsion members behave similarly, with residual stresses, geometric imperfections, and corner stress concentrations causing yielding at torques lower than T_y. Additionally, the proportional limit torque can be affected by cross-sectional collapse due to second-order flexural stresses in the walls.

Shear Buckling

The shear buckling limit state is shown in Figure 6 (Zaifuddin et al., 2017). The critical stresses in AISC *Specification* Section H3.1 are identical to those calculated with the equations in AISC *Specification* Section G4. Section G4 defines the web shear buckling strength coefficient, C_{v2}, using the equations in Section G2.2, with a buckling coefficient, $k_v = 5.0$. Although the provisions of Chapter G were developed for beams that are subjected to direct shear, the Commentary to Section H3.1 discusses the similarities between direct shear and torsional shear: "The shear distribution due to torsion is uniform in the longest sides of a rectangular HSS, and this is the same distribution that is assumed to exist in the web of an I-shape beam. Therefore, it is reasonable that the provisions for buckling are the same in both cases." The design philosophy in Eurocode 3, Part 1-1 (CEN, 2005) Section 6.2.7 is similar to that of AISC *Specification* Section H3.1, with the critical shear stress calculated with the direct shear provisions in Eurocode 3, Part 1-5 (CEN, 2006).

Warping

Theoretically, warping is not present in square HSS members or square box section members with constant wall thickness (Zyczkowski, 1991). Although corner details and geometric imperfections may affect the warping stresses, finite element models by Ridley-Ellis (2000) and experimental strain measurements by Konate (2015) showed that the warping stresses are negligible for these members.

Ridley-Ellis (2000) verified the presence of warping in rectangular HSS members and noted that the warping strains vary linearly across the width of the four walls. Warping strains are maximum at the corners and zero where a wall intersects a transverse axis of symmetry. Although warping is present in these members, it is common practice to neglect warping when designing rectangular HSS members for torsional loads. Ahlfors (2015) showed that this is conservative for the yielding limit state. For all practical aspect ratios, H/B, Derler and Unterweger (2021) showed that this practice is also conservative when the controlling limit state is buckling of the cross-sectional elements.

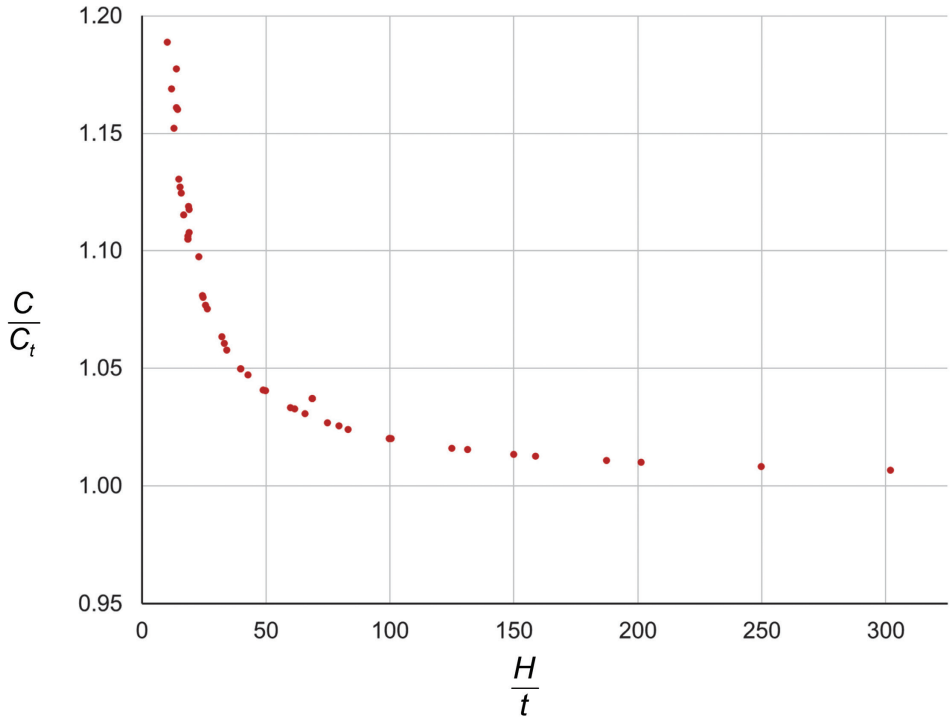

Fig. 5. Graph of the torsional shape factor versus the overall wall slenderness for the experimental specimens.

In some cases, it may be appropriate to consider the increased torsional resistance caused by warping for rectangular box sections with short lengths relative to the cross-sectional dimensions. Smith et al. (1970) provides information on analyzing the effects of warping in rectangular box sections. Also, including the warping stresses should be considered for a fatigue analyses (Ahlfors, 2015).

Nonlinear Behavior

Nonlinear strength can result from stress redistribution, strain hardening, and post-buckling. Although significant nonlinear strength is available for the full range of wall slenderness values, utilization of the nonlinear range, whether characterized by gross inelastic yielding with strain hardening or post-buckling, can result in unacceptably large rotations of several times the yield rotation.

Serviceability

When designing flexural members, properly designing for strength ensures that the serviceability design is accurate by limiting the moments to the linear portion of the moment-rotation curve. Beams are designed for deflection limits using serviceability loads and elastic sectional properties. For braced compact beams that are designed according to LRFD, $\phi_b M_p \le M_u$, where $\phi_b = 0.90$ and M_u is the required flexural strength. As discussed in the Commentary to AISC *Specification* Section B3.1, LRFD is calibrated to ASD at a live-to-dead load ratio of 3.0. This results in an average LRFD load factor of 1.5 for live and dead load combinations. In this case, M_p must be equal to or greater than $1.5/\phi_b = \Omega_b = 1.67$ times the maximum service moment for both ASD and LRFD. To ensure that the serviceability moments are limited to the linear portion of the moment-rotation curve, the combined effect of residual stresses and geometric imperfections must reduce M_y by no more than 1/1.67 times the shape factor, Z_x/S_x. This is the case for rolled W-shapes that are bent about the major axis. Although the typically minor detrimental effects of shear deformation and secondary load interaction are usually neglected in beam deflection calculations, potentially beneficial effects are also neglected. These include the partial end rotational restraint provided by typical shear connections, the stiffness of nonstructural building elements, and the higher expected yield stress relative to the specified minimum value.

Although serviceability rotations for torsion members are calculated in a manner that is analogous to the calculation of beam deflections, it is unclear if the serviceability torques are on the linear portion of the torque-rotation curve. Rectangular HSS sections typically have high residual stresses at the weld seam and cold-bending residual stresses at the corners. This, combined with the stress concentrations at the corners and second-order effects can cause yielding at torques significantly lower than T_y.

HISTORICAL REVIEW

This part of the paper provides a review of the existing research on square and rectangular hollow section members that are subjected to torsion. Experimental tests that were included in the reliability analysis are discussed as well as the relevant research on shear buckling and residual stresses.

Hovgaard (1937)

Hovgaard (1937) documented the torsional tests of three rectangular tubes of drawn and annealed mild steel. The shear strains were measured at several locations on the cross section. The measured torsional rotations "showed fair agreement with theory" in the elastic range. However, the torque-rotation curves became nonlinear at torques less than the calculated yield torques, $T_c = 0.6\sigma_y C$, where σ_y is the measured uniaxial tension yield stress.

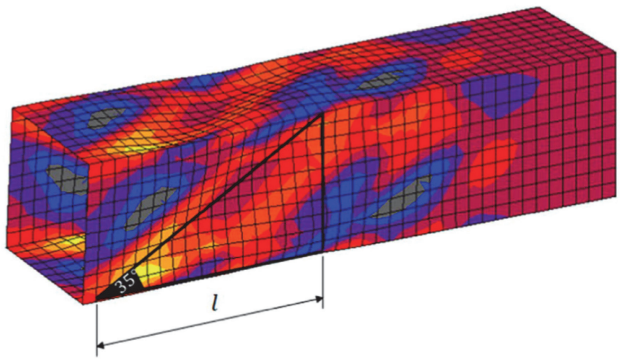

Fig. 6. Shear buckling (Zaifuddin et al., 2017).

Specimen C was $3 \times 3 \times 0.070$ in. $\times$ 52 in. long, with σ_y = 24.0 ksi. Nonlinear behavior initiated at a torque of only 75% of the theoretical yield torque.

Specimen D was $6 \times 3 \times 0.313$ in. $\times$ 51 in. long, with σ_y = 35.5 ksi. Nonlinear behavior initiated at a torque of only 49% of the theoretical yield torque.

Specimen E was $4 \times 4 \times 0.192$ in. $\times$ 51 in. long, with σ_y = 26.0 ksi. Because this test was used primarily to accurately determine the stress distribution, it was loaded only in the linear range. The measured torsional rotation was 87% of the calculated value. The measured shear stresses were higher than average near the corners.

Peters (1954)

Peters (1954) recognized that the HSS wall shear stresses caused by torsional loading are similar to the stresses caused by direct shear. He compared the theories for buckling of long flat plates with the results of elastic and plastic buckling tests on long square tubes loaded in compression, torsion, and combined compression and torsion. It was determined that the torsional loading direction has little to no effect on the shape of the interaction curve. Peters recommended a design procedure based on the classical shear buckling equation, where the elastic critical stress is multiplied by a plasticity reduction factor. The elastic critical stress, $\tau_{e,}$ of an infinitely long plate with simply supported edges subjected to shear is calculated with Equation 5.

Basler (1963)

An empirical transition curve between shear yielding and elastic buckling was proposed by Basler (1963). He observed a proportional limit at 80% of the shear yield stress: $\tau_p = 0.8\tau_y$. For stresses greater than the proportional limit, the inelastic buckling stress is

$$\tau_{cr} = \sqrt{\tau_p \tau_e} = \sqrt{0.8\tau_y \tau_e} \tag{19}$$

Equation 19 can be used to derive AISC *Specification* Equation G2-4.

$$C_{v1} = \frac{\tau_{cr}}{\tau_y} = \sqrt{\frac{0.8\tau_e}{\tau_y}} = \sqrt{\frac{0.8}{\tau_y}\frac{\pi^2 k_v E}{12(1-\nu^2)(h/t)^2}} = \frac{1.10\sqrt{k_v E/F_y}}{h/t} \tag{20}$$

Substituting k_v = 4.96 into Equation 20 results in Equation 21, where the web shear strength coefficient produces the same shear strength as AISC *Specification* Equation H3-4.

$$C_{v1} = \frac{2.45\sqrt{\frac{E}{F_y}}}{\left(\frac{h}{t}\right)} \tag{21}$$

Wittrick and Curzon (1968)

Wittrick and Curzon (1968) developed stability functions for the buckling strength of square HSS members subjected to torsion and solved the equations iteratively to determine appropriate buckling coefficients. Although the corners remained straight, buckling caused corner rotations, inducing interaction between adjacent walls. The buckling mode was characterized by continuous two-start spirals advancing by one complete wavelength for each revolution of the member. The buckling half-wavelength is 1.24*H*. The buckling coefficient is 5.3395, which is almost identical to the value that was derived by the authors for an infinitely long simply supported plate: 5.336.

Marshall (1970, 1971, 1972)

Marshall (1970) derived approximate equations for thick-walled rectangular hollow sections without corner radii. He noted that thin-wall theory predicts stresses with 12% nonconservative error for sections with B/t = 20, and the error "gets rapidly worse for thicker sections."

Marshall (1971) expanded the solution of Marshall (1970) to include corner radii. The equations were solved numerically, using the finite difference method.

Nine square and rectangular HSS torsion specimens were tested by Marshall (1971, 1972). All specimens were 4.5 ft long. The outside dimensions were 1.5, 2.0, 2.5, 3.0, 4.0, and 5.0 in. The wall thicknesses were 0.128, 0.160, 0.192, and 0.250 in. The measured uniaxial tension yield stresses, σ_y, were 44.57 and 62.71 ksi. All specimens were loaded until the strain hardening region was reached.

Comparisons with the experimental results showed that thin-wall theory underpredicts the shear stresses by an average of 14.2%. The measured torsional rotations were in reasonable agreement with the calculated rotations in the elastic range. Both the experimental results and the numerical models showed significant stress concentration at the corners; however, the areas of elevated stress covered less than 1% of the cross-sectional area.

Kitada et al. (1989)

Kitada et al. (1989) tested seven box sections with various combinations of axial compression, flexure, and torsion. Only one specimen was subjected solely to torsion. The specimens were 450 mm (17.7 in.) long. The outer dimensions were 133 mm (5.24 in.) × 163 mm (6.42 in.), and the plates were 4.5 mm (0.177 in.) thick. The initial out-of-flatness of the walls was approximately equal to 1/150 of the plate width. The measured uniaxial tension yield stresses, σ_y, was 289 N/mm^2 (41.9 ksi). The experimental-to-calculated strength ratio was 1.04, where the calculated yield torque is $T_c = 0.6\sigma_y C$.

Mahendran and Murray (1990)

Mahendran and Murray (1990) tested 54 built-up hollow square sections in various combinations of axial compression and torsion. Sixteen of the specimens were subjected solely to torsion. The section was formed of two elements that were cold bent at the corners. The two elements were connected by spot welding at the corners to form a hollow square section. The outer dimension was 151 mm (5.94 in.), and the thickness ranged from 0.500 mm (0.0197 in.) to 2.45 mm (0.0965 in.). This resulted in h/t ratios between 60 and 300. The measured uniaxial tension yield stresses, σ_y, were 220 MPa (31.9 ksi) and 285 MPa (41.3 ksi).

The buckled specimens had waves that were inclined at approximately 30° to the longitudinal member axis. The authors noted that the presence of initial geometric imperfections "did not seem to have a significant effect" on the strength.

White et al. (1993)

White et al. (1993) tested built-up hollow square sections in various combinations of axial compression and torsion. Five of the specimens were subjected solely to torsion. The "closed-hat" section was formed of two elements, with a cold-bent U-shaped element and a flat plate element. The two elements were connected by spot welding at 20 mm (0.79 in.) intervals to form a hollow square section. The outer dimension was 50 mm (2.0 in.), and the thickness ranged from 0.38 mm (0.015 in.) to 1.5 mm (0.059 in.). This resulted in h/t ratios between 31 and 130. The material was "cold-rolled automotive grade steel sheet," with measured uniaxial tension yield stresses, σ_y, between 269 MPa (39.0 ksi) and 590 MPa (85.6 ksi).

For the specimens with low h/t ratios, the experimental strengths were slightly overpredicted when the calculated strength was based on thin-wall theory. In this case, the calculated strength is $T_c = 0.6\sigma_y C$. For the specimens with high h/t ratios, the experimental strength was predicted with reasonable accuracy using Equation 5 to calculate the elastic critical shear stress with $k_v = 5.35$.

Ridley-Ellis et al. (2003)

Ridley-Ellis et al. (2003) tested five square and rectangular HSS members subjected to torsion. All specimens were 2,000 mm (78.7 in.) long. The specified outside dimensions were 100, 150, and 200 mm (3.9, 5.9, and 7.9 in.). The wall thicknesses were 6.3 and 8 mm (0.25 and 0.32 in.). The shapes were manufactured and "hot-finished" by either British Steel Tubes/Corus or Vallourec and Mannwsmann Tubes. Because the specimens were normalized after forming, the residual stresses were expected to be significantly lower than for a typical cold-formed HSS section. The materials were either S275 or S355, with measured uniaxial tension yield stresses, σ_y, between 329 MPa (47.7 ksi) and 405 MPa (58.7 ksi).

All specimens were loaded into the plastic range without buckling. For S275 and S355 HSS, the maximum experimental torques were approximately 20% and 12% lower than the strengths calculated with thin-wall theory, respectively. In this case, the calculated strength is $T_c = 0.6\sigma_y C$. They determined that "the experimentally measured torque-twist relationships differ significantly from the theoretical predictions," when thin-wall theory was used. The authors recommended thick-wall theory for design because it results in calculated strengths and stiffnesses that are more consistent with the experimental results and finite element models.

Kim and Yoo (2008)

Kim and Yoo (2008) studied box sections using finite element models that were subjected to various combinations of flexure and torsion. Width-to-thickness ratios of 20, 40, and 80 were used to simulate elastic, inelastic, and plastic behavior. Welding residual stresses were modeled using a simplified pattern made up of rectangular stress blocks. At the corners, tensile residual stresses were equal to the yield stress. The remaining wall width had compressive residual stresses equal to 20% of the yield stress.

By curve fitting the results of 64 models that were subjected to torsional loads, the authors developed Equation 22 to calculate the torsional strength ratio based on the wall slenderness. The range of validity for Equation 22 is $0.7 < \lambda_T < 2$.

$$\alpha = \frac{T_n}{T_p} = \frac{F_{cr}}{\tau_y} = 0.78 + 0.71\lambda_T - 0.85\lambda_T^2 + 0.22\lambda_T^3 \quad (22)$$

Belingardi et al. (2008)

Belingardi et al. (2008) tested 10 built-up hollow square sections in torsion. The section was formed of two hat or C-shaped elements that were cold bent at the corners. The two elements were connected by either spot welding or adhesive bonding of the lap joints on opposite walls to form a hollow square section. The outer dimension was 40 mm

(1.57 in.), and the thickness was 1.00 mm (0.0394 in.). This resulted in $h/t = 36$. The low carbon sheet steel had a measured uniaxial tension yield stress, σ_y, of 210 MPa (30.5 ksi).

After the specimens reached the elastic limit torques, approximately 15% to 30% more strength was available; however, this post-yield strength was accompanied by large rotations. At large rotations, cross-sectional collapse occurred, where the walls deformed inward.

Chahkand et al. (2013)

In addition to carbon fiber reinforced polymer (CFRP)-reinforced specimens, Chahkand et al. (2013) tested two non-reinforced square HSS specimens that were subjected to torsion. The specified outside dimension for all specimens was 50 mm (2.0 in.), and the specified wall thickness was 3 mm (0.12 in.). This resulted in an h/t ratio of 15.5. The hot-formed shapes had a measured uniaxial tension yield stress, σ_y, of 382 MPa (55.4 ksi). Due to the low h/t ratio, the specimens exhibited a stable post-yield curve, with increased strength caused by strain hardening.

Goncalves and Camotim (2013)

Using finite element models of square HSS members, Goncalves and Camotim (2013) showed that the buckling strength increases with decreasing member length; however, significant increases are applicable only for $L/H < 3$. For $L/H = 10$, the results were within 2% of those for infinitely long members. The authors developed buckling coefficients of 5.444 and 5.390 for $L/H = 10$ using different modeling techniques; however, they noted that $k_v = 5.34$ is an appropriate lower-bound design value.

Omidvari and Hematiyan (2015)

Using a parametric finite element study, Omidvari and Hematiyan (2015) showed that two buckling modes exist for rectangular HSS torsion members. For members with very high h/t ratios, the first mode is similar to plate shear buckling, where the deformation of the HSS corners is negligible.

Members with lower h/t ratios, which more closely represent the HSS members used in building structures, have a distortional first buckling mode. The distortional mode is characterized by considerable inward deformation of the corners and diagonal waves along the member length that are several times the half-waves for the shear buckling mode. This mode is applicable in the inelastic range, which is generally accepted to be the range between 80% and 100% of the yield strength due to material and geometric imperfections (Basler, 1963).

Curve fit equations were developed from the finite element models to predict the distortional buckling stress. Equation 23 is a simplified version of the equations with an applicability range of $h_o/t \geq 50$.

$$\tau_e = 24.1G\frac{t^2}{h_o(h_o + b_o)} \tag{23}$$

where $h_o = H - t$, $b_o = B - t$, and $h_o \geq b_o$.

Konate (2015)

Konate (2015) tested 60 HSS1.5×1.5×⅛ in. members in various combinations of flexure, axial compression, and torsion. Only two of the specimens were subjected solely to torsion. All specimens were 34 in. long. The measured uniaxial tension yield stress, σ_y, was 59.0 ksi.

Strain gages were used to measure the longitudinal strains that were induced by warping. Because the measured strains were between 1.35% and 5.52% of the yield strains, the authors concluded that the warping stresses are negligible.

The analysis used a yield torque based on the limiting shear stress calculated with Equation 24, where σ_r is the maximum longitudinal residual stress. For the simplified residual stress pattern that was used in the analysis, $\sigma_r = 0.5\sigma_y$, resulting in $\tau_{yr} = 0.5\sigma_y = 0.87\tau_y$.

$$\tau_{yr} = \sqrt{\frac{\sigma_y^2 - \sigma_r^2}{3}} \tag{24}$$

Sharrock et al. (2015)

In addition to aluminum and CFRP-reinforced specimens, Sharrock et al. (2015) tested six non-reinforced steel square HSS specimens that were subjected to torsion. The specified outside dimension for all specimens was 100 mm (3.9 in.). The specified wall thicknesses were 2, 3, and 6 mm (0.079, 0.12, and 0.24 in.). This resulted in h/t ratios of 11.9, 30.3, and 44.9, respectively. The cold-formed shapes were manufactured by One Steel Tube Mills. The material was C450PLUS, with measured uniaxial tension yield stresses, σ_y, between 383 MPa (55.5 ksi) and 444 MPa (64.4 ksi).

Shear buckling in the specimens with 2 and 3 mm wall thickness caused a "dramatic drop in the torsional capacity" at torsional rotations of approximately 5° and 10°, respectively. Buckling did not occur in the specimens with 6 mm wall thickness. These specimens reached at least 20° rotations prior to significant reductions in the strength.

Chen (2016)

A finite element study by Chen (2016) showed buckling waves inclined at approximately 30° to the longitudinal member axis. Based on this, a plate buckling coefficient of $k_v = 5.35 + [2\tan(30°)]^2 = 6.68$ was recommended.

Zaifuddin et al. (2017)

For square HSS, finite element models developed by Zaifuddin et al. (2017) showed buckling waves inclined at approximately 35° to the longitudinal member axis. This angle was essentially constant for all models regardless of the width-to-thickness ratio. Based on this, a plate buckling coefficient of $k_v = 5.35 + [2\tan(35°)]^2 = 7.31$ was recommended.

Rendall et al. (2018)

A study of square HSS members using the finite strip method by Rendall et al. (2018) resulted in a buckling half-wavelength of $1.24H$ and a buckling coefficient of 5.3396, which is almost identical to the values determined by Wittrick and Curzon (1968).

Devi et al. (2019)

In addition to tests of HSS members with circular openings in the walls, Devi et al. (2019) tested two square HSS torsion specimens without openings. Additionally, finite element models were used to determine the behavior of members with various wall slenderness ratios. The specified outside dimension for the experimental specimens was 60 mm (2.4 in.), and the specified wall thickness was 3.2 mm (0.13 in.). For the finite element models, the specified outside dimension was 150 mm (5.9 in.), and the specified wall thicknesses varied from 0.6 to 10 mm (0.024 to 0.39 in.). This resulted in h/t ratios that varied from 11 to 250. The specimens were cold formed, with a measured uniaxial tension yield stress, σ_y, of 412 MPa (59.8 ksi).

The authors developed a method to calculate the rotation capacity based on the wall slenderness. Empirical equations were then developed to calculate the strength based on the rotation capacity ratio. Both their proposed deformation-based method and the AISC *Specification* equations provided accurate predictions for the torsional strength.

RELIABILITY ANALYSIS

In this part of the paper, a first-order reliability analysis will be used to calculate appropriate resistance factors for use with AISC *Specification* Equation H3-1. The resistance factor required to obtain a specific reliability level is (Galambos and Ravinda, 1978).

$$\phi = C_R \rho_R e^{-\beta \alpha_R V_R} \tag{25}$$

where

C_R = correction factor
V_R = coefficient of variation
α_R = separation factor
β = reliability index
ρ_R = bias coefficient

Galambos and Ravinda (1973) proposed a separation factor, α_R, of 0.55. For $L/D = 3.0$, Li et al. (2007) developed Equation 26 for calculating the correction factor.

$$C_R = 1.40 - 0.156\beta + 0.0078\beta^2 \tag{26}$$

Based on the Commentary to *Specification* Section B3.1, the target reliability index, β_T, is 2.6, which results in $C_R = 1.05$. The reliability analysis also includes calculations using $\beta_T = 3.0$, which results in $C_R = 1.00$. The coefficient of variation and bias coefficient are calculated using the statistical parameters of the specific joint. The bias coefficient is

$$\rho_R = \rho_M \rho_G \rho_P \tag{27}$$

where

ρ_G = bias coefficient for the geometric properties
ρ_M = bias coefficient for the material properties
ρ_P = bias coefficient for the test-to-predicted strength ratios; mean value of the professional factor calculated with the measured geometric and material properties

The coefficient of variation is

$$V_R = \sqrt{V_M^2 + V_G^2 + V_P^2} \tag{28}$$

where

V_G = coefficient of variation for the geometric properties
V_M = coefficient of variation for the material properties
V_P = coefficient of variation for the test-to-predicted strength ratios

Material and Geometric Parameters

Osterhof and Driver (2011) used $\rho_t = 1.00$ and $V_t = 0.050$ for the thickness characteristics of HSS shapes. For ASTM A500 Grade C HSS shapes, Dowswell (2021) calculated $\rho_t = 0.994$ and $V_t = 0.00710$. For plates, Hess et al. (2002) recommended $\rho_t = 1.05$ and $V_t = 0.044$, and Schmidt and Bartlett (2002) recommended $\rho_t = 1.04$ and $V_t = 0.025$.

The author was unable to locate statistical data regarding deviations from the specified overall height and width of HSS shapes. However, for members meeting ASTM A500 and A1085 tolerances, any variation of the overall dimensions results in only a 2% worst-case strength reduction. Additionally, extensive statistical data related to HSS corner radii are unavailable. Packer and Frater (2005) and Gong (2008) measured corner radii of HSS flare bevel weld specimens, resulting in r_o/t ratios between 1.78 and 2.43. Comparison of the torsional modulus constants for HSS

shapes with various r_o/t ratios calculated with Equation 10 indicate that the variability of the corner radii is negligible. When both the overall dimensions and corner radii are considered deterministic quantities, ρ_G and V_G are dependent only on the wall thickness, t.

Depth variations for welded structural members are in AWS D1.1 (2020) Subclause 7.22.9. The maximum underrun is ⅛ in. for depths up to and including 36 in. and 3⁄16 in. for depths over 36 in. Schmidt and Bartlett (2002) compiled actual-to-specified ratios for welded built-up I-shaped members, with mean flange width and overall depth ratios of 0.998 and 0.999, respectively. Because the torsional strength reduction is insignificant for these values, the overall dimensions are considered a deterministic quantity. For these conditions, ρ_G and V_G are dependent only on the wall thickness, t.

The material characteristics for modulus of elasticity are $\rho_E = 1.04$ and $V_E = 0.045$ for HSS shapes and $\rho_E = 1.04$ and $V_E = 0.026$ for plates (Schmidt and Bartlett, 2002). For plates, Hess et al. (2002) recommended $\rho_E = 0.987$ and $V_E = 0.076$.

Dowswell (2021) summarized the tensile strengths parameters from five HSS research projects (Zhao et al., 2008; Han et al., 2007; Yang and Mahin, 2005; Zhao et al., 1999; Zhao and Hancock, 1995). For these tests, coupons were extracted from the flat portions of the walls of ASTM A500 Grade B, A500 Grade C, and similar international grades. Using 20 data points from these papers, the yield strength parameters were calculated, resulting in $\rho_M = 1.20$ and $V_M = 0.0686$.

Liu et al. (2007) reported the material characteristics for the yield stress of rectangular HSS shapes manufactured according to ASTM A500 Grade B to be $\rho_y = 1.31$ and $V_y = 0.08$. However, these values are based on only one of the eight approved material grades listed in AISC *Specification* Section A3.1 for rectangular HSS shapes. Also, AISC *Manual* (2023) Table 2-4 designates ASTM A500 Grade C as the preferred HSS material specification. Therefore. the more conservative values from Schmidt and Bartlett (2002) may be more appropriate: $\rho_y = 1.18$ and $V_y = 0.063$.

Brockenbrough (2001) reported the material characteristics for ASTM A36, A514, A572 Grade 50, A572 Grade 60, A572 Grade 65, A588, and A852 plates. The mean values were $\rho_y = 1.18$ and $V_y = 0.063$. The lowest bias coefficient was $\rho_y = 1.11$ with $V_y = 0.06$ for A588 plates with 2 in. $< t \leq$ 4 in. When the A36 plates are excluded from the data set, the mean values were $\rho_y = 1.16$ and $V_y = 0.064$.

Schmidt and Bartlett (2002) reported the material characteristics for the yield stress of plates based on the thickness. The mean values were $\rho_y = 1.11$ and $V_y = 0.056$. The lowest bias coefficient was $\rho_y = 1.07$ with $V_y = 0.054$ for plates less than 30 mm (1.2 in.) thick. ρ_y increased with thickness up to a maximum value of 1.16 for plates between 40 and 50 mm.

For "high-strength" steels, which had a mean measured yield stress of 49.6 ksi, Hess et al. (2002) recommended $\rho_y = 1.19$ and $V_y = 0.083$. For ASTM A572 and A588 Grade 50 plates, Suwan et al. (2003) reported $\rho_y = 1.16$ and $V_y = 0.0637$.

Liu et al. (2007) reported the material characteristics for ASTM A36, A529 Grade 50, A529 Grade 55, A572 Grade 50, and A572 Grade 55 plates. The mean values were $\rho_y = 1.20$ and $V_y = 0.06$. The lowest bias coefficient was $\rho_y = 1.10$ with $V_y = 0.05$ for A529 Grade 55 plates. For the four groups with only A529 and A572 plates, $\rho_y = 1.15$ with $V_y = 0.06$.

The reliability analysis must be based on the three equations for yielding (H3-3), inelastic buckling (H3-4), and elastic buckling (H3-5). For a first-order multivariate analysis, the mean and variance of T_c can be approximated with Equations 29 and 30, respectively (Benjamin and Cornell, 1970).

$$T_{cm} \approx f(X_{1m}, X_{2m}, ..., X_{nm}) \tag{29}$$

$$\sigma_{T_c}^2 \approx \sum_{i=1}^{n} \left(\left[\frac{\partial T_c}{\partial X_i} \right]_m \right)^2 \sigma_{X_i}^2 \tag{30}$$

where

T_c = critical torsional strength, kip-in.

T_{cm} = mean value of the critical torsional strength, kip-in.

X_i = uncorrelated variables affecting T_c

Substituting Equations H3-3 and 10 into Equation H3-1, the critical torsional strength for the limit state of yielding is

$$T_c = 1.2 F_y t A_o \tag{31}$$

Because Equation 31 is linear with respect to both F_y and t, the statistical parameters for the material and geometric properties are used without manipulation as listed in the third column of Table 1.

Substituting Equations H3-4 and 10 into Equation H3-1, the critical torsional strength for the limit state of inelastic buckling is

$$T_c = 2.94 \sqrt{E F_y} \frac{A_o t^2}{h} \tag{32}$$

The derivative of T_c with respect to E is

$$\frac{\partial T_c}{\partial E} = \left(\frac{1}{2} \right) 2.94 \sqrt{\frac{F_y}{E}} \frac{A_o t^2}{h} \tag{33}$$

The derivative of T_c with respect to F_y is

$$\frac{\partial T_c}{\partial F_y} = \left(\frac{1}{2} \right) 2.94 \sqrt{\frac{E}{F_y}} \frac{A_o t^2}{h} \tag{34}$$

Table 1. Reliability Functions				
			Buckling	
		Yielding	Inelastic	Elastic
Material	ρ_M	$\rho_y = 1.15$	$(\rho_E\rho_y)^{½} = 1.09$	$\rho_E = 1.04$
	V_M	$V_y = 0.06$	$V_E/2 + V_y/2 = 0.053$	$V_E = 0.045$
Geometric	ρ_G	$\rho_t = 0.994$	$(\rho_t)^2 = 0.988$	$(\rho_t)^3 = 0.982$
	V_G	$V_t = 0.04$	$(2)(V_t) = 0.08$	$(3)(V_t) = 0.12$

Table 2. Statistical Parameters for Test-to-Predicted Strength Ratios Using the AISC *Specification* Section H3 Equations					
			Buckling		
	All	Yielding	All	Inelastic	Elastic
N	48	30	18	2	16
ρ_P	1.23	0.922	1.74	0.831	1.85
V_P	0.621	0.118	0.607	0.145	0.575
N = number of specimens					

The derivative of T_c with respect to t is

$$\frac{\partial T_c}{\partial t} = (2)2.94\sqrt{EF_y}\frac{A_o t}{h} \tag{35}$$

The statistical parameters for the geometric and material properties for inelastic buckling are listed in the fourth column of Table 1. Substituting Equations H3-5 and 10 into Equation H3-1, the critical torsional strength for the limit state of elastic buckling is

$$T_c = 9.04E\frac{A_o t^3}{h^2} \tag{36}$$

Equation 36 is linear with respect to E. The derivative of T_c with respect to t is

$$\frac{\partial T_c}{\partial t} = (3)9.04E\frac{A_o t^2}{h^2} \tag{37}$$

The statistical parameters for the geometric and material properties for elastic buckling are listed in the fifth column of Table 1.

Professional Factors

The statistical parameters for the test-to-predicted strength ratios were calculated using 48 experimental tests from 11 research projects described previously in this paper. Of the research discussed in the historical review, only the experiments with adequate data were included in the analysis. This included tests by Marshall (1972), Kitada et al. (1989), Mahendran and Murray (1990), Al-Ayish (2004), White et al. (1993), Ridley-Ellis et al. (2003), Belingardi et al. (2008), Chahkand et al. (2013), Sharrock et al. (2015), Konate (2015), and Devi et al. (2019). The specimen details and experimental results are listed in Appendix A, Tables A1 and A2, respectively. Mahendran and Murray (1990) Specimen 6 was omitted from the data set because $h/t = 300$, which exceeds the AISC *Specification* limit of 260.

Because the reliability functions are separated into three groups (yielding, inelastic buckling, elastic buckling), each group was analyzed separately. Statistical parameters for test-to-predicted strength ratios, ρ_P and V_P, as well as the number of specimens, N, within each group are listed in Table 2.

Analysis

From Table 2, $\rho_P = 1.23$ when the AISC *Specification* equations are used with all specimens. Without further consideration, this appears reasonable. However, when the yielding and buckling limit states are considered separately, inconsistencies are revealed. For yielding, $V_P = 0.118$ is reasonable; however, $\rho_P = 0.922$ is significantly less than 1.00. For buckling, $\rho_P = 1.74$ is significantly greater than 1.00, and $V_P = 0.607$ indicates that the design model is inaccurate.

With $\phi = 0.90$, the *Specification* equations result in $\beta = 2.63$ for the 30 specimens with a predicted failure mode of yielding. With $\beta_T = 2.6$, $\phi = 0.906$. With $\beta_T = 3.0$, $\phi = 0.841$.

With $\phi = 0.90$, the *Specification* equations result in $\beta = 2.47$ for the 16 specimens with a predicted failure mode of elastic buckling. With $\beta_T = 2.6$, $\phi = 0.853$. With $\beta_T = 3.0$, $\phi = 0.716$.

Discussion

Figure 7 shows a graph of T_e/T_y versus λ for the experimental data. T_e is the maximum experimental torsional moment. T_y is the torsional yield moment calculated with the measured specimen geometry and the measured uniaxial yield stress: $T_y = 0.6\sigma_y C$. The slenderness parameter, λ, is calculated with Equation 38. For the calculation of λ for the experimental data points, the measured dimensions and material properties were used in lieu of the nominal values.

$$\lambda = \frac{h}{t}\sqrt{\frac{\sigma_y}{E}} \tag{38}$$

The AISC *Specification* curve is inaccurate over most of the buckling range, with excessive conservatism when $\lambda > 4$ and a nonconservative range when $1.5 < \lambda < 3$. The accuracy and transition (anchor) points of AISC *Specification* Equations H3-4 and H3-5 can be improved by addressing the sources of error in the design model.

In AISC *Specification* Section H3.1, the definition of h is inaccurate. Because the buckled shape is usually characterized by buckling of all four walls, the interaction between walls should be considered. This can be accomplished by defining the buckling width as the larger of the two midwall-to-midwall distances for pairs of opposite walls (i.e., $h_o = H - t$ in Figure 1).

Equation 11 was derived using thin-wall theory, which is based on the assumption that the shear stress is constant across the wall thickness. However, the experimental results indicate that thin-wall theory results in overestimates of the torsional strength. Equation 16, which was derived using thick-wall theory, is more accurate that Equation 11.

DISCUSSION AND RECOMMENDATIONS

This part of the paper discusses potential improvements to the AISC *Specification* design method. Revised design equations are proposed, and the reliability of the new design method is analyzed. Serviceability considerations are also discussed.

Section Properties

As discussed previously in this paper, the yield and plastic torsion properties can be calculated with thick- and thin-wall theory, respectively. The differences in the elastic and plastic section properties are on the same order as for the flexural design of common I-shaped members (Ridley-Ellis, 2000). Therefore, for a highly refined torsional design method, a linear transition between the plastic and elastic strengths could be implemented. However, a review of the experimental data points on the yield plateau of Figure 2 indicate that a more refined method may

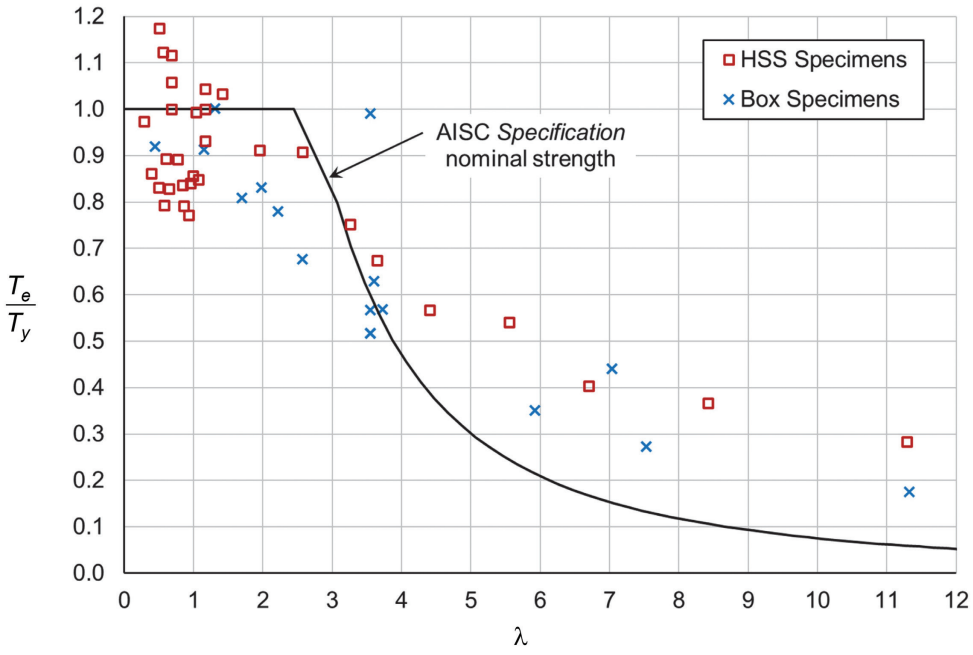

Fig. 7. Graph of AISC equations with experimental data.

not be justified. This is because, for the 20 specimens with an experimental failure mode of yielding, the data trend is relatively constant in the range $0 \le \lambda \le 1.5$. For $\lambda > 1.5$, the AISC *Specification* equations should be revised to include the effect of buckling.

The reliability analysis shows that the yield strength bias coefficient offsets the slightly nonconservative nature of using section properties calculated with thin-wall theory over the entire yielding plateau. Therefore, it is recommended that Equation 11 is used to calculate the torsional modulus constant, C, for HSS members. For box sections, the sectional properties can be calculated using Equation 10 with $r_m = 0$.

Equation 12, which was derived using the maximum permissible outside corner radius, results in slightly lower values for C. However, the difference between Equations 11 and 12 is negligible for most HSS shapes. Also, measurements by Packer and Frater (2005) and Gong (2008) showed that the outside corner radius is closer to 2 times the wall thickness, which was assumed in the derivation of Equation 11.

Wall Buckling

The experimental data clearly showed that the wall buckling model should be based on a buckling width, h_o, defined as the largest distance between the mid-thickness of adjacent walls. The research of Wittrick and Curzon (1968), Goncalves and Camotim (2013), Chen (2016), Zaifuddin et al. (2017), and Rendall et al. (2018) indicated that a buckling coefficient of $k_v = 5.34$ is appropriate for use in Equation 5. Equation 42 was derived by substituting Equation 5 into Equation 4 with $k_v = 5.34$ and h_o replacing h.

Figure 7 clearly shows that the yield plateau in the current AISC *Specification* design model should be shortened. Theoretically, this can be accomplished by revising the assumed residual stresses and geometric imperfections. Although research data are available to quantify the residual stresses, their magnitudes and patterns vary significantly between the various sections due to the different manufacturing and fabrication processes. Because the experimental specimens in the database included all common manufacturing and fabrication processes, the best-fit curve can be established first, and then the implied effect of imperfections can be calculated based on the intersection of the yield and buckling curves.

After the yielding-buckling anchor point is established, the shape of the curve can be adjusted to improve the accuracy of the design model. The inelastic and elastic buckling curves can be replaced by a single nonlinear curve that simplifies the design process. Equation 41 is of the form that was proposed by Devi et al. (2019); however, the constants were adjusted to result in similar reliabilities for the yielding and buckling limit states.

Proposed Design Method

AISC *Specification* Section H3 is limited to HSS shapes. The proposed design method is applicable to both HSS and box section members. The proposed method uses *Specification* Equation H3-1 and replaces Equations H3-3, H3-4, and H3-5 with Equations 39, 40, and 41.

The nominal torsional strength of an HSS or box section member is calculated with Equation H3-1 in AISC *Specification* Section H3.1.

$$T_n = F_{cr}C \qquad \text{(AISC } Spec. \text{ H3-1)}$$

For rectangular HSS and box section members, the critical shear stress is

$$F_{cr} = 0.6F_yC_v \tag{39}$$

When $\lambda_T \le 0.530$

$$C_v = 1.00 \tag{40}$$

When $\lambda_T > 0.530$

$$C_v = \frac{1}{0.471 + \lambda_T} \tag{41}$$

The slenderness is

$$\lambda_T = 0.353\frac{h_o}{t}\sqrt{\frac{F_y}{E}} \tag{42}$$

where

h_o = largest distance between the mid-thickness of adjacent walls, in.

Reliability of the Proposed Method

Because the reliability functions are separated into two groups (yielding, buckling), each group was analyzed separately. Statistical parameters for test-to-predicted strength ratios, ρ_P and V_P, as well as the number of specimens, N, within each group are listed in Table 3.

From Table 3, $\rho_P = 1.01$ when the proposed equations are used with all specimens. For the 25 specimens controlled by yielding, $\rho_P = 0.932$. When C_t according to Equation 16 is used in lieu of C, $\rho_P = 1.03$. However, using C_t is unnecessary because the yield strength bias coefficient offsets the slightly nonconservative nature of using section properties calculated with thin-wall theory.

The anchor point and shape of the buckling curve was adjusted to result in approximately equal reliability for the yielding and buckling limit states. The difference in ρ_P values for yielding and buckling are offset by the differences in V_P. Compared to yielding, the buckling limit state has a higher V_P; therefore, ρ_P must also be higher to produce similar reliabilities. By comparing the values of V_P for the buckling limit state, it is clear that the proposed design

Table 3. Statistical Parameters for Test-to-Predicted Strength Ratios Using the Proposed Equations			
	All	**Yielding**	**Buckling**
N	49	25	24
ρ_P	1.01	0.932	1.10
V_P	0.183	0.118	0.189
N = number of specimens			

method is significantly more accurate than the AISC *Specification* equations.

With $\phi = 0.90$, the proposed equations result in $\beta = 2.69$ for the 25 specimens with a predicted failure mode of yielding. With $\beta_T = 2.6$, $\phi = 0.916$. With $\beta_T = 3.0$, $\phi = 0.850$.

With $\phi = 0.90$, the proposed equations result in $\beta = 2.68$ for the 24 specimens with a predicted failure mode of buckling. With $\beta_T = 2.6$, $\phi = 0.917$. With $\beta_T = 3.0$, $\phi = 0.837$.

Figure 8 shows a graph of T_e/T_y versus λ_o for the experimental data. The slenderness parameter, λ_o, is calculated with Equation 43. For the calculation of λ_o for the experimental data points, the measured dimensions and material properties were used in lieu of the nominal values. The solid lines plot the proposed design equations, and the AISC *Specification* equations are plotted with dashed lines.

$$\lambda_o = \frac{h_o}{t}\sqrt{\frac{\sigma_y}{E}} \tag{43}$$

Experimental Failure Modes

The failure mode for each experimental specimen is listed in Table A2 of Appendix A. Compared to the AISC *Specification* equations, the proposed design method results in more accurate predictions of the experimental failure mode. The *Specification* equations provided successful predictions for 38 of 48 specimens for a 79% success rate. The proposed equations provided successful predictions for 44 of 49 specimens for a 90% success rate.

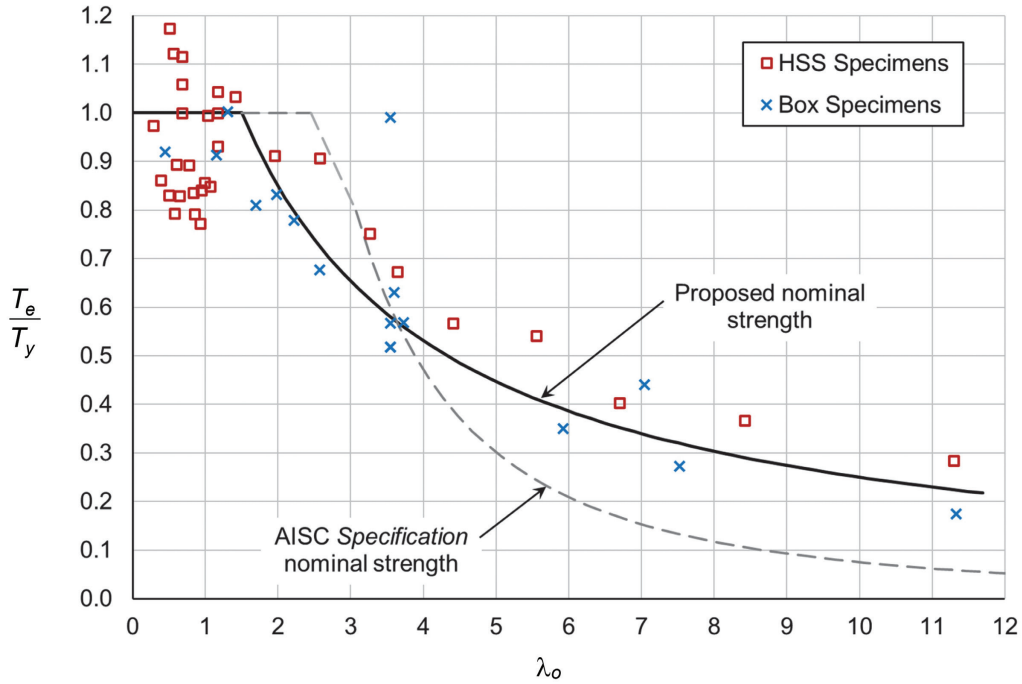

Fig. 8. Graph of proposed equations with experimental data.

Serviceability

For a member subjected to uniform torsion over the length, the twist angle is calculated with Equation 44.

$$\theta = \frac{T_u L}{GJ} \tag{44}$$

where

G = shear modulus of elasticity, 11,200 ksi

L = member length, in.

T_u = uniform torsional moment, kip-in.

θ = angle of torsional rotation

The twist angle of 20 experimental specimens was reported in the referenced research. These data are shown in Figure 9, where θ_{ep}/θ_c is plotted versus T_{el}/T_p. T_{el} is the experimental proportional limit torque. T_p is the plastic torsion calculated using Equation 18 with the measured specimen geometry and the measured uniaxial yield stress. θ_{ep} is the experimental proportional limit rotation. θ_c is the rotation at torque $T_u = T_{el}$, calculated using Equation 44 with the measured specimen geometry and the measured modulus of elasticity.

As discussed previously in this paper, residual stresses, geometric imperfections, corner stress concentrations, and second-order effects cause yielding at torques lower than T_y. This can potentially cause inaccurate serviceability calculations if the serviceability torques are on the nonlinear portion of the torque-rotation curve. To ensure that the serviceability torques are on the linear portion of the torque-rotation curve, the combined effect of residual stresses and geometric imperfections must reduce T_p by no more than 1/1.67 = 0.60. Because the minimum value for T_{el}/T_p is 0.665, this condition is satisfied for all 20 specimens. The mean value of T_{el}/T_p is 0.803.

Figure 9 shows that the experimental rotations generally exceed the rotations calculated with Equation 44. The mean value of θ_{ep}/θ_c is 1.22. Because the theoretical equations can significantly underestimate the rotation, this should be considered in the design of critical members where serviceability rotation is the controlling limit state.

CONCLUSIONS

A review of the available research on the torsional strength of square and rectangular hollow section members revealed 49 experimental tests from 11 projects. Theoretical, experimental, and numerical research identified two strength limit states for members commonly used in buildings: yielding and wall buckling.

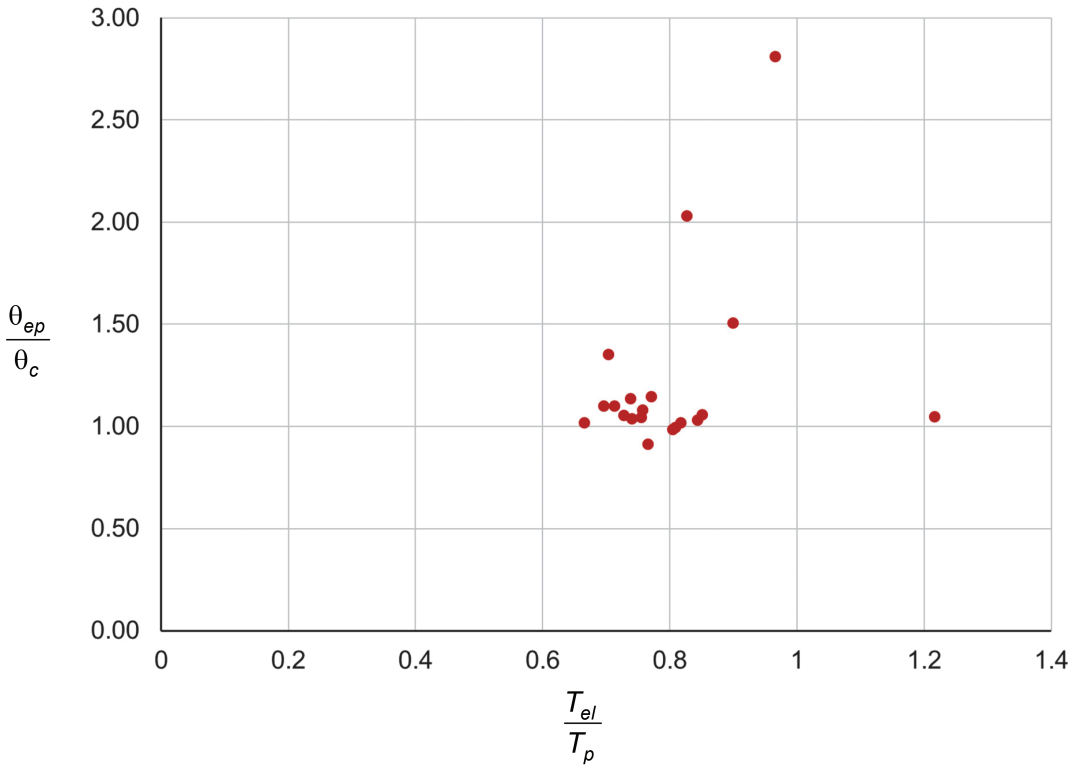

Fig. 9. Graph of the normalized twist angle versus the normalized yield torsion.

An evaluation of the AISC *Specification* provisions revealed inconsistent reliability indices that are dependent on the predicted failure mode. The reliability level for the yielding limit state is appropriate. However, for the wall buckling limit state, the reliability index is less than the target reliability index.

Revisions are proposed for the provisions in AISC *Specification* Section H3.1. The improved accuracy of the proposed design method is illustrated in Figure 8, which shows a graph of the normalized strength versus wall slenderness for the AISC *Specification* equations, the proposed equations and the experimental data. In addition to providing a simpler design method and increasing the accuracy, the proposed design equations

- Include provisions for both HSS shapes and box sections.
- Are verified by experimental results.
- Are more successful in predicting the actual failure mode.
- Result in more consistent reliability between the yielding and wall buckling limit states.
- Ensure that the reliability index is greater than the target reliability index for the wall buckling limit state.

The experimental data related to torsional rotation indicated that serviceability torques are low enough to be on the linear portion of the torque-rotation curve. However, the torsional rotations were underpredicted for most of the specimens, with a mean experimental-to-calculated ratio of 1.22. Because the theoretical equations can significantly underestimate the rotation, this should be considered in the design of critical members where serviceability rotation is the controlling limit state.

SYMBOLS

A_o Area enclosed by the sectional mid-thickness, in.^{2}

A_w Web area, in.^{2}

B Overall width, in.

C Torsional modulus constant, in.^{3}

C_R Correction factor

C_t Torsional modulus constant based on thick-wall theory, in.^{3}

C_v Web shear strength coefficient (Eurocode 3, Part 1-1)

C_{v1} Web shear strength coefficient (AISC *Specification* Section G2.1)

E Modulus of elasticity, ksi

F_{cr} Critical shear stress, ksi

F_y Specified minimum yield stress, ksi

H Overall height, in.

J Torsional inertia constant, in.^{4}

J_t Torsional inertia constant based on thick-wall theory, in.^{4}

L Length, in.

T_c Critical torsional strength

T_{cm} Mean value of the critical torsional strength

T_p Plastic torsion, kip-in.

T_y Yield torsion, kip-in.

V_E Coefficient of variation for modulus of elasticity

V_G Coefficient of variation for the geometric properties

V_M Coefficient of variation for the material properties

V_P Coefficient of variation for the test-to-predicted strength ratios

V_R Coefficient of variation

V_t Coefficient of variation for wall thickness

V_y Coefficient of variation for yield stress

X_i Uncorrelated variables affecting T_c

b_o $B - t$

h Flat width of longer side, in.

h_o $H - t$

k_v Buckling coefficient

p_m Mid-thickness perimeter, in.

r_m Mid-thickness corner radius, in.

r_o Outside corner radius, in.

t Design wall thickness, in.

Ω_T Safety factor for torsion

α_R Separation factor

β Reliability index

η Shear buckling strength factor

λ Slenderness parameter calculated with Equation 38, which uses a buckling width equal to the flat width of longer side, h

λ_o Slenderness parameter calculated with Equation 43, which uses a buckling width equal to the larger of the two midwall-to-midwall distances for pairs of opposite walls, h_o

λ_T Slenderness

ρ_E Bias coefficient for modulus of elasticity

ρ_G Bias coefficient for the geometric properties

ρ_M Bias coefficient for the material properties

ρ_P Bias coefficient for the test-to-predicted strength ratios

ρ_R Bias coefficient

ρ_t Bias coefficient for wall thickness

ρ_y Bias coefficient for yield stress

σ_r Maximum longitudinal residual stress

σ_y Measured uniaxial tension yield stress, ksi

τ_{cr} Inelastic shear buckling stress, ksi

τ_e Elastic critical shear stress, ksi

τ_p Proportional limit shear stress, ksi

τ_y Shear yield stress, ksi

τ_{yr} Shear residual stress, ksi

ν Poisson's ratio

ϕ_T Resistance factor for torsion

REFERENCES

AISC (2023), *Steel Construction Manual*, 16th Ed., American Institute of Steel Construction, Chicago, Ill.

AISC (2022), *Specification for Structural Steel Buildings*, ANSI/AISC 360-22, American Institute of Steel Construction, Chicago, Ill.

Ahlfors, M. (2015), *Distortion and Internal Warping Torsion of a Double Symmetric Hollow Section*, Master's Thesis, Lappeenranta University of Technology, Lappeenranta, Finland.

Al-Ayish, N.A. (2004), "Steel Box Girders under Pure Torsion: A Comparison between Plate and Lattice Box Girders," Master's Thesis, University of Technology, Baghdad.

ASTM (2014), *Standard Specification for Hot-Formed Welded and Seamless Carbon Steel Structural Tubing*, ASTM A501/501M, ASTM International, West Conshohocken, Pa.

ASTM (2015a), *Standard Specification for Cold-Formed Welded Carbon Steel Hollow Structural Sections (HSS)*, ASTM A1085/1085M, ASTM International, West Conshohocken, Pa.

ASTM (2015b), *Standard Specification for Hot-Formed Welded and Seamless High Strength Low Alloy Structural Tubing*, ASTM A618/618M, ASTM International, West Conshohocken, Pa.

ASTM (2021), *Standard Specification for Cold-Formed Welded and Seamless Carbon Steel Structural Tubing in Rounds and Shapes*, ASTM A500/500M, ASTM International, West Conshohocken, Pa.

AWS (2020), *Structural Welding Code—Steel*, AWS D1.1, American Welding Society, Miami, Fla.

Basler, K. (1963), "Strength of Plate Girders in Shear," *Journal of the Structural Division*, American Society of Civil Engineers, October.

Beg, D., Kuhlmann, U., Davaine, L., and Braun, B. (2010), *Design of Plated Structures*, European Convention for Structural Steelwork.

Belingardi, G., Peroni, L., and Scattina, A. (2008), "Experimental Evaluation of the Torsional Behavior of Thin Walled Beams: Elastic and Buckling Situations," *High Performance Structures and Materials IV,* WIT Transactions on the Built Environment, Vol. 97.

Benjamin, J.R. and Cornell, C.A. (1970), *Probability, Statistics and Decision for Civil Engineers*, McGraw-Hill.

Brockenbrough, R.L. (2001), *MTR Survey of Plate Material Used in Structural Fabrication—Part A, Yield-Tensile Properties*, Final Report Submitted to American Institute of Steel Construction, March 1.

CEN (2005), *Eurocode 3—Design of Steel Structures—Part 1-1: General Rules and Rules for Buildings*, European Committee for Standardization, Brussels, Belgium.

CEN (2006), *Eurocode 3—Design of Steel Structures—Part 1-5: Plated Structural Elements*, European Committee for Standardization, Brussels, Belgium.

Chahkand, N.A., Jumat, M.Z., Sulong, N.H.R., Zhao, X.L., and Mohammadizadeh, M.R. (2013), "Experimental and Theoretical Investigation on Torsional Behavior of CFRP Strengthened Square Hollow Steel Section," *Thin-Walled Structures*, Vol. 68.

Chen, D.H. (2016), *Crush Mechanics of Thin-Walled Tubes*, CRC Press.

Chen, S.J. and Chang, S.C. (1993), "Residual Stresses in Welded Jumbo Box Columns," *Journal of Constructional Steel Research*, Vol. 25, pp. 201–209.

Chen, W. (2000), *Plastic Resistance of Thin-Walled Prismatic Tubes under Large Twisting Rotations*, Master's Thesis, Massachusetts Institute of Technology, Boston, Mass.

Chen, W. and Wierzbicki, T. (2000), "Torsional Collapse of Thin-Walled Prismatic Columns," *Thin-Walled Structures*, Vol. 36.

Davison, T.A., and Birkemoe, P. (1983), "Column Behavior of Cold-Formed Hollow Structural Steel Shapes," *Canadian Journal of Civil Engineering*, Vol. 10, No. 1, pp. 125–141.

Derler, C. and Unterweger, H. (2021), "Effects of Warping Torsion on the Buckling Behavior of Slender Box Sections," *CE Papers*, Nos. 2–4.

Devi, S.V., Singh, T.G., and Singh, K.D. (2019), "Cold-Formed Steel Square Hollow Members with Circular Perforations Subjected to Torsion," *Journal of Constructional Steel Research*, Vol. 162.

Dowswell, B. (2021), "Analysis of the Shear Lag Factor for Slotted Rectangular HSS Members," *Engineering Journal*, AISC, Vol. 58, No. 3. pp. 155–164.

ECCS (1976), *Manual on Stability of Steel Structures*, 2nd Ed., European Convention for Constructional Steelwork.

Galambos, T.V. and Ravinda, M.K. (1973), *Tentative Load and Resistance Factor Design Criteria for Steel Buildings*, Research Report No. 18, Department of Civil and Environmental Engineering, Washington University, St. Louis, Mo.

Galambos, T.V. and Ravinda, M.K. (1978), "Properties of Steel for Use in LRFD," *Journal of the Structural Division*, ASCE, Vol. 104, No. ST9, pp. 1459–1468.

Goncalves, R. and Camotim, D. (2013), "Buckling Behavior of Thin-Walled Regular Polygonal Tubes Subjected to Bending or Torsion," *Thin-Walled Structures*, Vol. 73.

Gong, Y. (2008), "Double-Angle Shear Connections with Small Hollow Structural Section Columns," *Journal of Constructional Steel Research*, Vol. 64, No. 5, pp. 539–549.

Han, S.W., Kim, W.T., and Foutch, D.A. (2007), "Tensile Strength Equation for HSS Bracing Members Having Slotted End Connections," *Earthquake Engineering and Structural Dynamics*, Vol. 36, pp. 995–1008.

Hess, P.E., Bruchman, D., Assakkaf, I.A., and Ayyub, B.M. (2002), "Uncertainties in Material Strength, Geometric and Load Variables," *Naval Engineers Journal*, Vol. 114, No. 2, pp. 139–166.

Hovgaard, W. (1937), "Torsion of Rectangular Tubes," *Journal of Applied Mechanics*, ASME, pp. A-131–A-135.

Ingvarsson, L. (1977), *Welding and Cold-Forming Residual Stresses and Their Effect on Buckling of Box Columns of High Strength Steel*, Bulletin No. 130, The Royal Institute of Technology, Stockholm, Sweden.

Key, P.W., Hasan, S.W., and Hancock, G.J. (1988), "Column Behavior of Cold-Formed Hollow Sections," *Journal of Structural Engineering,* ASCE, Vol. 114, No. 2.

Kim, K. and Yoo, C.H. (2008), "Ultimate Strengths of Steel Rectangular Box Beams Subjected to Combined Action of Bending and Torsion," *Engineering Structures*, Vol. 30.

Kitada, T, Nakai, H., and Kunihiro, M. (1989), "Ultimate Strength of Box Stub Columns under Combined Actions of Compression, Bending and Torsion," *Journal of Constructional Steel Research*, Vol. 13.

Konate, M. (2015), *Inelastic Behavior and Strength of Steel Beam-Columns with Applied Torsion*, PhD Dissertation, Old Dominion University, Norfolk, Va.

Li, C., Grondin, G.Y., and Driver, R.G. (2007), *Reliability Analysis of Concentrically Loaded Fillet Welded Joints*, Structural Engineering Report No. 271, University of Alberta, Alberta, Canada.

Liu, J., Sabelli, R., Brockenbrough, R.L., and Fraser, T.P. (2007), "Expected Yield Stress and Tensile Strength Ratios for Determination of Expected Member Capacity in the AISC Seismic Provisions," *Engineering Journal*, AISC, Vol. 44, No. 1, pp. 15–25.

Liu, W., Rasmussen, K.J.R., and Zhang, H. (2017), "Modeling and Probabilistic Study of the Residual Stress of Cold-Formed Hollow Steel Sections," *Engineering Structures*, Vol. 150, pp. 986–995.

Mahendran, M. and Murray, N.W. (1990), "Ultimate Load Behavior of Box-Columns under Combined Loading of Axial Compression and Torsion," *Thin-Walled Structures*, Vol. 9.

Marshall, J. (1970), "Derivation of Torsional Formulas for Multiply Connected Thick-Walled Rectangular Sections," *Journal of Applied Mechanics*, ASME, June.

Marshall, J. (1971), "Torsional Behavior of Structural Rectangular Hollow Sections," *The Structural Engineer*, Vol. 49, No. 8.

Marshall, J. (1972), *Aspects of Torsion of Structural Rectangular Hollow Sections*, PhD Dissertation, University of Strathclyde, Glasgow, Scotland.

Omidvari, A. and Hematiyan, M.R. (2015), "Approximate Closed-Form Formulae for Buckling Analysis of Rectangular Tubes under Torsion," *International Journal of Engineering*, Vol. 28, No. 8.

Osterhof, S.A. and Driver, R.G. (2011), "Performance of the Unified Block Shear Equation for Common Types of Welded Steel Connections," *Engineering Journal*, AISC, Vol. 48, No. 2, pp. 77–92.

Packer, J.A. and Frater, G.S. (2005), "Recommended Effective Throat Sizes for Flare Groove Welds to HSS," *Engineering Journal*, AISC, Vol. 42, No. 1, pp. 31–44.

Peters, R.W. (1954), "Buckling of Long Square Tubes in Combined Compression and Torsion and Comparison with Flat-Plate Buckling Theories," *NACA Technical Note 3184*, National Advisory Committee for Aeronautics.

Rendall, M.A., Hancock, G.J., and Rasmussen, K.J.R. (2018), "Modal Buckling Behavior of Long Polygonal Tubes in Uniform Torsion Using the Generalized cFSM," *Thin-Walled Structures*, Vol. 128, pp. 141–151.

Ridley-Ellis, D.J. (2000), *Rectangular Hollow Sections with Circular Web Openings*, PhD Dissertation, University of Nottingham, Nottingham. England.

Ridley-Ellis, D.J., Owen, J.S., and Davies, G. (2003), "Torsional Behavior of Rectangular Hollow Sections," *Journal of Constructional Steel Research, Vol. 59.*

Schmidt, B.J. and Bartlett, F.M. (2002), "Review of Resistance Factor for Steel: Data Collection," *Canadian Journal of Civil Engineering*, Vol. 29, pp. 98–108.

Seaburg, P.A. and Carter, C.J. (1997), *Torsional Analysis of Structural Steel Members*, Design Guide 9, AISC, Chicago, Ill.

Sharrock, J., Wu, C., and Zhao, X.L. (2015), "CFRP Strengthened Square Hollow Section Subjected to Pure Torsion," *Tubular Structures XV, CRC Press.*

Sherman, D. (1971), "Residual Stresses and Tubular Compression Members," *Journal of the Structural Division*, ASCE, Vol. 97, No. ST3.

Sherman, D.R. (1992), "Tubular Members," Chapter 2.4 in *Constructional Steel Design—An International Guide*, Elsevier.

Smith, F.A., Thomas, F.M., and Smith, J.O. (1970), "Torsion Analysis of Heavy Box Beams in Structures," *Journal of the Structural Division*, American Society of Civil Engineers, March.

Suwan, S., Manuel, L., and Frank, K.H. (2003), *Statistical Analysis of Structural Plate Mechanical Properties*, Final Report Submitted to American Iron and Steel Institute.

Uy, B. (1998), "Local and Post-Local Buckling of Concrete Filled Steel Welded Box Columns," *Journal of Constructional Steel Research*, Vol. 47, pp. 47–72.

White, G.J., Grzebieta, R.H., and Murray, N.W. (1993), "Maximum Strength of Square Thin-Walled Sections Subjected to Combined Loading of Torsion and Bending," *International Journal of Impact Engineering*, Vol. 13, No. 2.

Wittrick, W.H. and Curzon, P.L.V. (1968), "Local Buckling of Long Polygonal Tubes in Combined Compression and Torsion," *International Journal of Mechanical Sciences*, Vol. 10.

Yang, F. and Mahin, S. (2005), "Limiting Net Section Fracture in Slotted Tube Braces," *Steel Tips*, Structural Steel Education Council, April.

Zaifuddin, S.A.M., Chen, D.H., and Ushijima, K. (2017), "Estimation of Maximum Torsional Moment for Multicorner Tubes," *Thin-Walled Structures*, Vol. 112, No. 66–67.

Zhang, X.Z., Liu, S., Zhao, M.S., and Chiew, S.P. (2016), "Comparative Experimental Study of Hot-Formed, Hot-Finished and Cold-Formed Rectangular Hollow Sections," *Case Studies in Structural Engineering*, Vol. 6, pp. 115–129.

Zhao, R.G., Huang, R.F., Khoo, H.A., and Cheng, J.J.R. (2008), "Experimental Study on Rectangular and Square Hollow Structural Section (HSS) Tension Connections," *Canadian Journal of Civil Engineering*, Vol. 35, pp. 1318–1330.

Zhao, X.L., Al-Mahaidi, R., and Kiew, K.P. (1999), "Longitudinal Fillet Welds in Thin-Walled C450 RHS Members," *Journal of Structural Engineering*, ASCE, Vol. 25, No. 8, pp. 821–828.

Zhao, X.L. and Hancock, G.J. (1995), "Longitudinal Fillet Welds in Thin Cold-Formed RHS Members," *Journal of Structural Engineering*, ASCE, Vol. 121, No. 11, pp. 1683–1690.

Ziemian, R.D. (2010), *Guide to Stability Design Criteria for Metal Structures*, 6th Ed., John Wiley & Sons.

Zyczkowski, M. (1991), *Strength of Structural Elements*, Elsevier.

APPENDIX A

Table A1. Specimen Details					
Specimen	***B* (in.)**	***H* (in.)**	***t* (in.)**	***E* (ksi)**	**σ_y (ksi)**
Marshall (1972)					
A	2.00	2.00	0.193	30690	44.6
B	2.50	2.50	0.193	30690	44.6
C	3.00	3.00	0.193	30690	62.7
D	4.00	4.00	0.252	30690	44.6
E	4.00	4.00	0.161	30690	44.6
F	2.00	5.00	0.252	30690	44.6
G	1.50	3.00	0.161	30690	44.6
H	2.00	3.00	0.130	30690	44.6
I	2.00	4.00	0.130	30690	44.6
Kitada et al. (1989)					
T-3	4.83	6.41	0.173	30023	41.9
Mahendran and Murray (1990)					
1	5.94	5.94	0.0965	29000[a]	31.9
2	5.94	5.94	0.0748	29000[a]	31.9
3	5.94	5.94	0.0591	29000[a]	41.3
4	5.94	5.94	0.0374	29000[a]	41.3
5	5.94	5.94	0.0295	29000[a]	41.3
6	5.94	5.94	0.0197	29000[a]	41.3
White et al. (1993)					
1	1.97	1.97	0.0591	29000[a]	39.0
2	1.97	1.97	0.0394	29000[a]	36.3
3	1.97	1.97	0.0299	29000[a]	35.1
4	1.97	1.97	0.0197	29000[a]	39.2
5	1.97	1.97	0.0150	29000[a]	85.6
Ridley-Ellis et al. (2003)					
1	3.92	7.78	0.307	28311	50.0
2	5.87	5.87	0.240	28311	47.8
3, 4	3.94	7.83	0.312	29457	55.2
5	5.89	5.89	0.228	28993	58.7
I	1.50	1.50	0.0563	29000[a]	52.8

Table A-1 continues on the next page

Table A1. Specimen Details (continued)					
Specimen	***B* (in.)**	***H* (in.)**	***t* (in.)**	***E* (ksi)**	**σ_y (ksi)**
Al-Ayish (2004)					
1	5.91	15.75	0.157	29000[a]	38.0
2	5.91	15.75	0.157	29000[a]	38.0
3	5.91	15.75	0.157	29000[a]	38.0
4	5.91	15.75	0.157	29000[a]	38.0
Belingardi et al. (2008)					
1	1.57	1.57	0.0394	29000[a]	30.5[b]
2	1.57	1.57	0.0394	29000[a]	30.5[b]
3	1.57	1.57	0.0394	29000[a]	30.5[b]
Chahkand et al. (2013)					
1, 2	1.98	1.98	0.106	29008	55.4
Sharrock et al. (2015)					
SC-2	3.93	3.93	0.0803	29298	55.5
SC-3	3.96	3.96	0.115	29153	62.9
SC-6	3.96	3.96	0.234	29153	64.4
Konate (2015)					
TR1, TR44	1.50	1.50	0.125	29599	59.0
Devi et al. (2019)					
P1, P2	2.36	2.36	0.126	28355	59.8
1	5.91	5.91	0.0236	28355	59.8
2	5.91	5.91	0.0315	28355	59.8
3	5.91	5.91	0.0394	28355	59.8
4	5.91	5.91	0.0472	28355	59.8
5	5.91	5.91	0.0591	28355	59.8
6	5.91	5.91	0.0709	28355	59.8
7	5.91	5.91	0.0787	28355	59.8
8	5.91	5.91	0.0984	28355	59.8
9	5.91	5.91	0.315	28355	59.8
10	5.91	5.91	0.394	28355	59.8

[a] The modulus of elasticity was not measured for these specimens.
[b] The yield stress was not measured for these specimens.

Table A2. Experimental Results								
	Experimental		AISC Specification			Proposed		
Specimen	T_e (kip-in.)	FM	T_c (kip-in.)	FM	T_e/T_c	T_c (kip-in.)	FM	T_e/T_c
Marshall (1972)								
A	32.5	Y	33.3	Y	0.974	33.3	Y	0.974
B	47.0	Y	54.6	Y	0.861	54.6	Y	0.861
C	90.3	Y	114	Y	0.793	114	Y	0.793
D	157	Y	189	Y	0.831	189	Y	0.831
E	106	Y	127	Y	0.836	127	Y	0.836
F	92.0	Y	111	Y	0.829	111	Y	0.829
G	29.1	Y	32.6	Y	0.893	32.6	Y	0.893
H	33.2	Y	37.2	Y	0.893	37.2	Y	0.893
I	42.6	Y	50.2	Y	0.848	50.2	Y	0.848
Kitada et al. (1989)								
T-3	254	Y	253	Y	1.00	253	Y	1.00
Mahendran and Murray (1990)								
1	105	B	126	Y	0.831	107	B	0.981
2	66.9	B	94.1	B	0.711	71.1	B	0.941
3	57.7	B	55.1	B	1.05	56.4	B	1.02
4	22.7	B	13.9	B	1.63	25.2	B	0.902
5	14.0	B	6.82	B	2.05	16.3	B	0.858
6	6.00	B	–[a]	–[a]	–[a]	7.65	B	0.785
White et al. (1993)								
1	9.20	B	10.1	Y	0.913	10.1	Y	0.913
2	5.16	B	6.38	Y	0.809	5.89	B	0.876
3	3.69	B	4.74	Y	0.779	3.74	B	0.986
4	2.21	B	2.04	B	1.08	2.00	B	1.10
5	2.58	B	0.891	B	2.90	1.97	B	1.31
Ridley-Ellis et al. (2003)								
1	381	Y	494	Y	0.772	494	Y	0.772
2	343	Y	434	Y	0.792	434	Y	0.792
3, 4	473	Y	562	Y	0.841	562	Y	0.841
5	439	Y	513	Y	0.856	513	Y	0.856
I	7.35	B	7.39	Y	0.994	7.39	Y	0.994

Table A-2 continues on the next page

Table A2. Experimental Results (continued)								
	Experimental		AISC Specification			Proposed		
Specimen	T_e (kip-in.)	FM	T_c (kip-in.)	FM	T_e/T_c	T_c (kip-in.)	FM	T_e/T_c
Al-Ayish (2004)								
1	333	B	385	B	0.865	371	B	0.898
2	333	B	385	B	0.865	371	B	0.898
3	365	B	385	B	0.947	371	B	0.984
4	638	B	385	B	1.66	371	B	1.72
Belingardi et al. (2008)								
1	3.39	B	3.39	Y	1.00	3.39	Y	1.00
2	3.53	B	3.39	Y	1.04	3.39	Y	1.04
3	3.16	B	3.39	Y	0.931	3.39	Y	0.931
Chahkand et al. (2013)								
1, 2	24.6	Y	24.6	Y	1.00	24.6	Y	1.00
Sharrock et al. (2015)								
SC-2	72.3	B	79.3	Y	0.912	65.7	B	1.10
SC-3	133	B	129	Y	1.03	126	B	1.05
SC-6	278	Y	248	Y	1.12	248	Y	1.12
Konate (2015)								
TR1, TR44	15.4	Y	16.7	Y	0.919	16.7	Y	0.919
Devi et al. (2019)								
1, 2	47.5	Y	44.9	Y	1.06	44.9	Y	1.06
1	16.6	B	3.46	B	4.81	13.0	B	1.28
2	28.6	B	8.27	B	3.45	22.3	B	1.28
3	39.2	B	16.3	B	2.40	33.7	B	1.16
4	62.9	B	28.4	B	2.21	46.9	B	1.34
5	82.2	B	56.1	B	1.46	69.8	B	1.18
6	116	B	98.2	B	1.19	95.9	B	1.22
7	144	B	136	B	1.06	115	B	1.25
8	216	B	227	B	0.952	167	B	1.29
9	783	Y	702	Y	1.12	702	Y	1.12
10	997	Y	849	Y	1.17	849	Y	1.17

T_c = calculated torsional moment, kip-in.
T_e = experimental torsional moment, kip-in.

FM: Failure mode
B: Buckling
Y: Yielding

[a] $h/t = 300$, which exceeds the AISC *Specification* limit of 260.

Design of Noncontact Lap Splice Connections for C-PSW/CF (SpeedCore)

SHIVAM SHARMA, SOHEIL SHAFAEI, AMIT VARMA, and RON KLEMENCIC

ABSTRACT

Concrete-filled composite plate shear walls (C-PSW/CF) are an emerging structural system in building construction. The composite wall-to-base connection is a critical component influencing system behavior and design. Different types of composite wall-to-base connections are possible, but the noncontact lap splice connection between the dowel bars of the reinforced concrete (RC) base and the steel faceplates of the composite walls is of interest due to its constructability and potential structural efficiency. This type of wall-to-base connection can govern the lateral resistance of the overall wall system, which may be acceptable for wind loading situations and, depending on ductility, may also be acceptable for seismic loading conditions. This study presents the design and detailing of noncontact dowel bar lap splice connections for composite walls-to-RC foundations or walls. Design parameters include embedment length and arrangement of dowel bars within the composite wall cross section and the interfacial shear strength provided using ties or a combination of ties and stud anchors (shear studs) to transfer forces from the dowel bar to the steel faceplates. Previous recommendations for these parameters, provided in the literature, are used and verified experimentally. Three large-scale specimens with different connection details are designed, constructed, and tested to failure. The experimental results are evaluated, and design recommendations are proposed along with methods to calculate the flexural stiffness and flexural strength of the composite wall-to-base connections.

Keywords: composite plate shear walls/concrete-filled, SpeedCore system, experimental study, seismic and wind design, lap splice, connections, composite walls, wall-to-foundation connection.

INTRODUCTION

Concrete-filled composite plate shear walls (C-PSW/CF) effectively combine the advantages of steel construction with concrete materials to result in a composite wall system that has excellent structural performance and efficient constructability. These composite plate shear walls have been used in the construction of nuclear power plants (e.g., AP 1000®) and energy related structures, where they are referred as steel-plate composite (SC) structures and designed in accordance with the ANSI/AISC N690, *Specification for Safety-Related Steel Structures for Nuclear Facilities* (AISC, 2024), hereafter referred to as AISC N690–24, and AISC Design Guide 32, *Modular Steel-Plate Composite Walls for Safety-Related Nuclear Facilities* (Bhardwaj and Varma, 2017).

The use of composite plate shear walls has gained more acceptance in the commercial building construction industry over the past few years due to the advantages of modularization and resulting improvements in construction schedule. For example, the construction of Rainier Square Tower (Traut-Todaro, 2019) using C-PSW/CF core walls reduced the construction time by approximately 40% viz-a-viz traditional reinforced concrete (RC) core walls and demonstrated these benefits. The construction of 200 Park Avenue using C-PSW/CF core walls saved 3 months on the overall construction schedule and reduced costs (Klemencic et al., 2023). The system was conferred the name "SpeedCore" by the American Institute of Steel Construction (AISC) in recognition of these advantages.

For example, a planar C-PSW/CF comprised of web and flange steel plates, forming a box section enclosing the concrete infill, is shown in Figure 1. Complete-joint-penetration (CJP) groove welds are typically used to connect the flange plates to the web plates. Regularly spaced tie bars are used to connect the web plates. They ensure stability of the empty steel modules during the transportation and erection phases. These tie bars can either be welded to the web plates, or threaded rods can also be used. Steel headed stud anchors (also referred to as shear studs) can be used to supplement or partially replace tie bars, offering similar composite action between steel and concrete. These shear studs can be welded to the inner surface of web plates

Shivam Sharma, PhD Candidate, Lyles School of Civil and Construction Engineering, Purdue University, West Lafayette, Ind. Email: sharm368@purdue.edu (corresponding author)

Soheil Shafaei, PhD, M.ASCE, Assistant Professor, Department of Civil and Environmental Engineering, Utah State University, Logan, Utah. Email: soheil.shafaei@usu.edu

Amit Varma, PhD, M.ASCE, Karl H. Kettelhut Professor, Lyles School of Civil and Construction Engineering, Purdue University, West Lafayette, Ind. Email: ahvarma@purdue.edu

Ron Klemencic, PE, SE, Dist.M.ASCE, President and CEO, Magnusson Klemencic Associates (MKA), Seattle, Wash. Email: rklemencic@mka.com

Paper No. 2024-15

(Bhardwaj et al., 2017). In C-PSW/CF, steel plates provide the primary resistance to tensile and shear stresses, whereas the concrete infill contributed to resisting compressive and shear stresses while acting composite with the steel. Acting together through composite action, both steel and concrete enhance the flexural and shear stiffness of the system.

A C-PSW/CF system could either be coupled or uncoupled. ASCE 7-16 (2016) included uncoupled C-PSW/CF as a seismic force-resisting system, and the corresponding design provisions were first laid out in the 2016 ANSI/AISC *Seismic Provisions for Structural Steel Buildings* (AISC, 2016) and further enhanced in the 2022 version of the AISC *Seismic Provisions for Structural Steel Buildings* (AISC, 2022a), hereafter referred to as the AISC *Seismic Provisions*, and in the 2022 version of the AISC *Specification for Structural Steel Buildings* (AISC, 2022b), hereafter referred to as the AISC *Specification*, based on recent research (Agrawal et al., 2020; Broberg et al., 2023).

In design situations with high base shear and overturning moments (e.g., taller buildings), it is beneficial to connect the individual (or uncoupled) C-PSW/CF to each other using coupling beams, resulting in coupled C-PSW/CF system. ASCE 7–22 (2022) incorporated seismic modification factors for coupled C-PSW/CF, and the design and detailing requirements were included in the 2022 AISC *Seismic Provisions* and in the 2022 AISC *Specification* based on recent research (Broberg et al., 2022; Kizilarslan et al., 2021; Ahmad et al., 2024).

PRIOR INVESTIGATIONS

The response of C-PSW/CF under wind and seismic loading has been studied extensively. Design recommendations based on experimental and numerical studies (Shafaei et al., 2022, 2023) have been outlined and incorporated into AISC Design Guide 38, *SpeedCore Systems for Steel Structures* (Varma et al., 2023).

The lateral forces resisted by these walls and the corresponding base shear and overturning moment need to be transferred to the base, making this connection a critical aspect in their commercial applications. C-PSW/CF may be connected directly to the RC foundation or through an RC wall. The C-PSW/CF–RC wall connection may be favored for certain projects due to lower costs of construction and other design preferences. In both cases, the embedded dowel bar technique, commonly referred as a noncontact lap splice connection, can be effective in establishing the connection between the C-PSW/CF and the RC base, with or without an RC wall. In this type of connection, the forces from the C-PSW/CF steel plates are transferred to the dowels through the formation of compression struts in the concrete infill. For example, Figure 2 illustrates the force transfer from C-PSW/CF flange plate to an adjacent dowel bar. The tensile stresses in the dowels are transferred to the surrounding concrete through the concrete-dowel rebar bond.

Seo and Varma (2017) conducted experimental and numerical investigations on the behavior of SC-to-RC

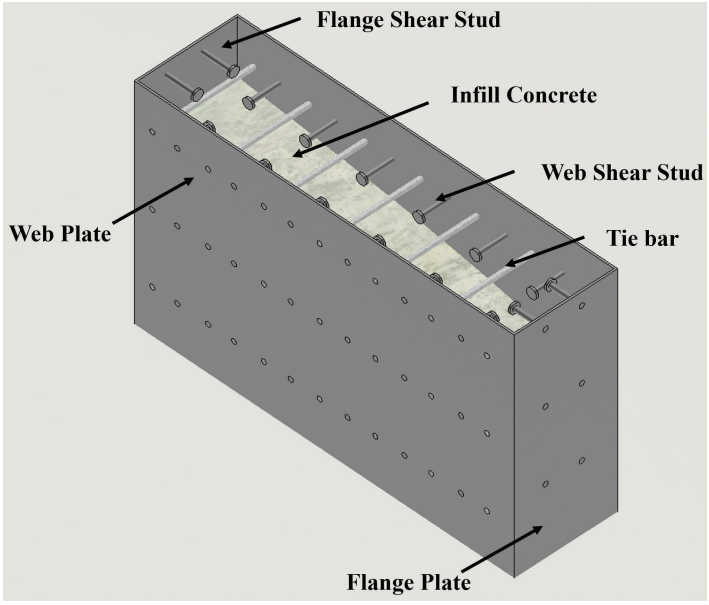

Fig. 1. Typical details of planar (uncoupled) C-PSW/CF.

noncontact lap splice connections and developed recommendations for their design and detailing. These included (1) using continuous tie bars in the SC walls to prevent splitting failure, (2) providing adequate embedment/development length for the dowel bars in both the C-PSW/CF and RC base, (3) providing sufficient shear studs/tie bars for interfacial shear transfer, and (4) placing the dowel at a minimum distance from the steel faceplates for complete formation of compression struts. Seo et al. (2021) corroborated and expanded these recommendations by conducting further experiments. They suggested using a maximum distance between steel faceplates and dowel rebar for ductile failure.

Cyclic tests on SC wall-to-RC foundation lap splice connections were conducted by Wang et al. (2020) to evaluate their seismic performance. The connections exhibited highly ductile behavior and failed in a flexure-dominated mode, marked by tensile yielding of the dowels. Kurt et al. (2022) investigated the behavior of lap splice connections under cyclic lateral load. The development length of dowels in the connection was in accordance with ACI 318-19 (2019), and they were expected to reach their yield strength. The connections exhibited highly ductile behavior with failure occurring due to crushing of concrete in compression followed by tensile rupture of the dowels. Both these studies demonstrate that the noncontact lap splice technique is an effective way of connecting C-PSW/CF to the RC foundation. Moreover, unlike these studies where infill concrete spalling led to lower connection capacity, the presence of flange plates required in C-PSW/CF as per the AISC *Specification* will constrain the concrete from spalling, thus providing additional confinement of the dowels. Consequently, the dowels are expected to achieve their ultimate tensile strength, thus enhancing the overall ductility of the connection. Additionally, evaluating the performance of these connections for wind loading histories can provide valuable insights while designing for wind-governed designs.

This paper presents the design and detailing of noncontact lap splice connections for C-PSW/CF for wind and seismic applications. Three full-scale specimens—including two specimens connecting C-PSW/CF to the RC foundation and one connecting C-PSW/CF to the RC wall with different connection details—are designed and experimentally evaluated. Design recommendations for prescriptive design of noncontact lap splice connections for C-PSW/CF are provided for engineers. In addition, methods to calculate the flexural stiffness and flexural capacities of the connections are proposed.

DESIGN OF NONCONTACT LAP SPLICE CONNECTIONS

Wind and seismic events impose large force demands on noncontact splice connections. The tensile stresses from steel plates of C-PSW/CF must be transferred to the dowels continuing into the RC base. To ensure adequate strength, ductility, and energy dissipation during such events, the design of these connections should favor limit states like yielding of the dowel bar or C-PSW/CF steel plates while avoiding premature failure in the stud anchors, dowel bar pullout, or concrete infill splitting.

The overall system consists of (1) the C-PSW/CF wall; (2) the RC base—that is, wall and/or foundation; and (3) the noncontact lap splice connection region between the wall and the base. This section discusses the design and detailing recommendations available in literature for developing ductile failure modes that consist of yielding in the dowel

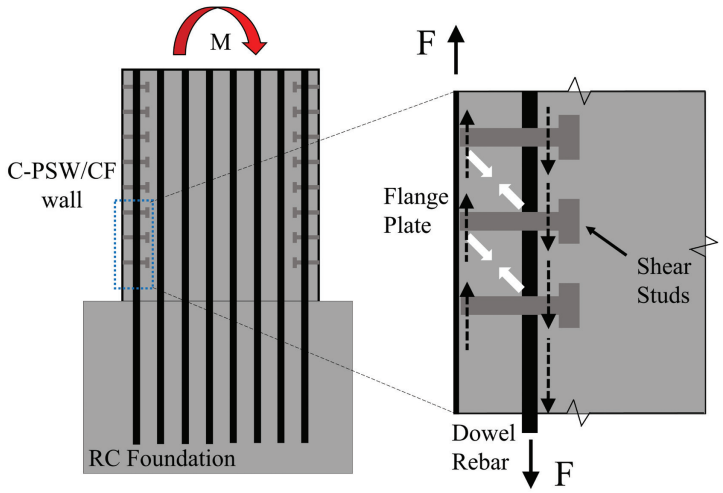

Fig. 2. Load transfer mechanism in the noncontact lap splice connection.

bars of the connection region. For further clarity, the RC section in the connection region, which is confined by the steel modules of C-PSW/CF, is referred to as the "confined RC section."

Confined RC Section

AISC *Seismic Provisions* Section H7.7c specifies that the C-PSW/CF-to-foundation connection should be detailed such that the connection is able to transfer the base shear force, axial force, and overturning moment corresponding to 1.1 times the plastic flexural strength of the composite wall. This is comparable to the full-strength design philosophy specified in AISC N690-24, which requires the connection to develop at least 125% of the nominal strength of the weaker of the two connected components.

The noncontact lap splice connection can be designed to develop the full strength of the composite wall. However, it is typically designed and detailed to develop the full strength of the confined RC section in the connection region, which will be the weaker of the two connected components. This is done to improve constructability by reducing rebar congestion. This is also practical for wind-governed designs where the connection must be designed only for the calculated demands. This may also be practical for situations where the steel plates of the C-PSW/CF are overdesigned (in terms of plate thickness) to facilitate fabrication, handling, etc., and/or to meet drift requirements if they govern over strength requirements.

The contributions of the C-PSW/CF steel plates are not considered while calculating the strength (e.g., axial, flexural, etc.) of the confined RC section. Analytical methods have been developed by the authors to calculate the flexural and shear capacities of the confined RC section. These methods have been adapted from existing design codes and are presented later in this paper.

Design Recommendations

The recommendations provided by Seo and Varma (2017) and Seo et al. (2021) were used to design and detail the connection region. While the presence of steel flange plates and tie bars in C-PSW/CF helps in inhibiting splitting failure, requirements concerning interfacial shear, dowel bar development length, and appropriate placement of dowel bars still need to be met.

Interfacial Shear Strength

The connection must be designed to have interfacial shear strength greater than or equal to 1.25 times the nominal yield strength of the dowel bars in the confined RC section. The connection interfacial strength is the sum of the nominal shear strength provided by tie bars and shear studs inside the dowel embedment region. Direct shear strength equations provided in AISC *Specification* Section I8.3a, are used for the shear studs, and those developed by Seo et al. (2019) are adapted for the threaded tie rods. These equations are presented later in the paper.

Embedment/Development Length

Wall Portion

Adequate embedment length needs to be provided for the dowels to develop their full tensile strength. Development lengths for deformed bars can be calculated using ACI 318-19, Section 25.4.2.3 or 25.4.2.4. The shorter development lengths calculated using ACI 318-19, Section 25.4.2.4, account for the effects of confinement. For tension splice lengths, ACI 318-19, Section 25.5.2, recommends using a multiplication factor of 1.3. However, multiplying the development lengths calculated using ACI 318-19, Section 25.4.2.3 (which does not account for effects of confinement), by 1.3 can lead to extremely conservative designs. Therefore, the development lengths calculated using ACI 318-19, Section 25.4.2.4 (which includes the effects of confinement), multiplied by the factor of 1.3 are recommended as the minimum embedment length for design and detailing.

RC Base Portion

The development length for hooked dowel bars in the RC base can be calculated using ACI 318-19, Section 25.4.3.1. These hooked dowel bars need to be provided with the minimum inside bend diameter and straight extension length in accordance with ACI 318-19, Table 25.3.1. However, in most practical cases, these bars are just extended to the bottom of the RC base for convenience.

Dowel Location

To facilitate the development of concrete compression struts between C-PSW/CF steel plates and the dowel bars, the spacing between the dowels and the interior surface of C-PSW/CF steel plates must be greater than the diameter of the dowel. At the same time, the dowel in the exterior layers must also be placed within the length of shear stud anchors and those in the middle layers must be placed within the length of the tie bars, as shown in Figure 3. These recommendations follow those by Seo and Varma (2017) and Seo et al. (2021).

EXPERIMENTAL PROGRAM AND RESULTS

Three specimens with noncontact lap splice connections were tested under wind and seismic loading and their behavior was evaluated. Two of these specimens (SP-1 and SP-2)

consisted of C-PSW/CF wall connected to RC foundation directly, while one (SP-3) included an RC wall in-between. Figure 3 shows these two types of connections evaluated in this study.

As shown in Figure 3, the dowel bars form a noncontact lap splice with the steel plates of C-PSW/CF and facilitate the transfer of tensile forces from C-PSW/CF to the RC foundation. The connection region consists of an RC section with rebar dowels embedded in the C-PSW/CF, previously defined as the confined RC section. Adequate C-PSW/CF wall and foundation embedment lengths, denoted as l_{d_wall} and l_{d_fnd}, respectively, are provided for the dowels to develop the full strength of the confined RC section. Shear studs and tie bars are provided to ensure adequate interfacial strength in the connection. The tie bars also help in preventing splitting failure in the connection. For the connection having an RC wall, transverse shear reinforcement is provided to prevent failure in the RC wall.

Test Matrix

All specimens had an identical C-PSW/CF wall with details provided in Table 1. The C-PSW/CF had length, l_w, and thickness, t_{sc}, of 37.5 in. and 10 in., respectively. ASTM A572/A572M Gr. 50 steel faceplates (ASTM, 2021), having thickness, t_p, of 3⁄16 in., were used in the web whereas the C-shape section, MC 10×8.4, was used as the flange section. ASTM A193 B7 steel threaded tie bars and shear studs (ASTM, 2023) having a diameter of 0.5 in. and spacing of 5 in. on center were provided in the web and flange plates. Figure 4 provides the geometric details of the C-PSW/CF.

For SP-3, the RC wall had a length and thickness of 39.5 in. and 12 in., respectively. The height of the wall was 24 in., extending from the top of the RC foundation to the C-PSW/CF base. It was transversely reinforced using #3 Gr. 60 ties. Several layers of transverse reinforcement were provided to ensure sufficient shear strength, as shown in Figure 4(f). Perimeter hoops with supplemental 135° cross ties were also provided for further reinforcement. The various sublayers of the horizontal reinforcement are shown later in Figure 6.

The connection consisted of dowel bars of different diameters, d_{bar}, and nominal yield strengths, F_{y_bar}. Their details are presented in Table 2. SP-1 and SP-3 consisted of #6 Gr. 60 dowel bars, whereas SP-2 had #8 Gr. 80 dowel bars. These dowels had different embedment lengths in the wall, $l_{d\_wall\_provided}$, as shown in Table 2. For adequate interfacial strength, the dowel embedment region was reinforced with additional shear studs welded to the C-PSW/CF web plate.

The RC foundation block for the specimen was designed to resist all loads originating during the test. SP-1 and SP-2 had identical foundation design, while SP-3 had a different foundation design. Figure 5 shows the geometric details and rebar layout for the foundations for all three specimens.

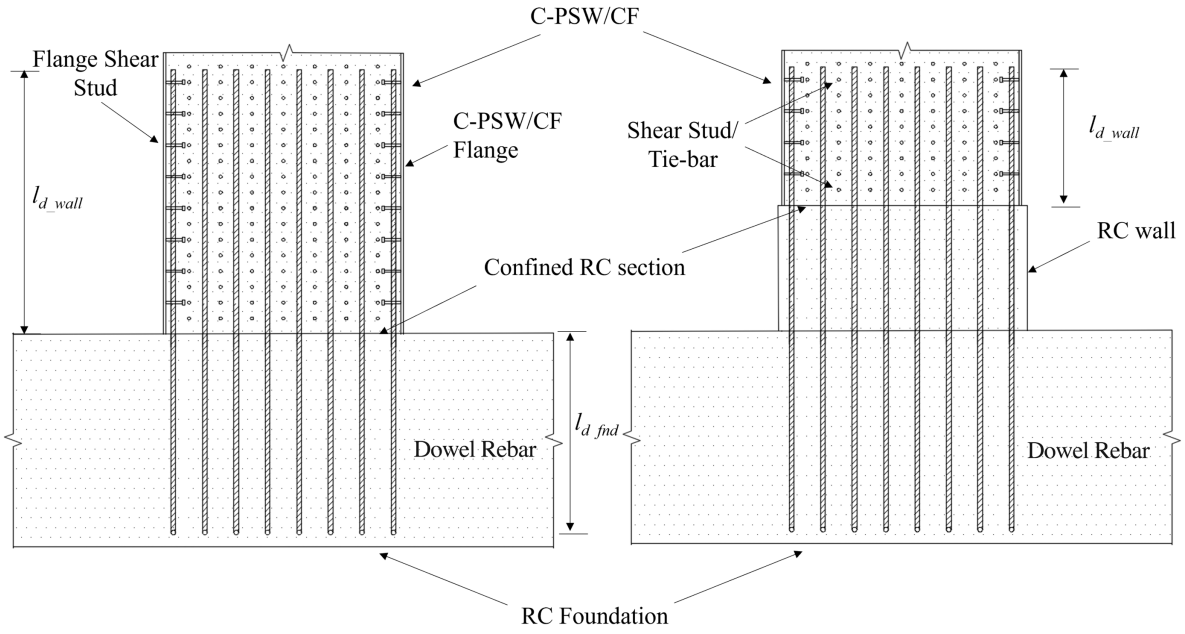

(a) Without RC wall *(b) With RC wall*

Fig. 3. Schematics of the noncontact lap splice connections.

Table 1. Details of Planar C-PSW/CF														
General			Web											Flange
h_w (in.)	l_w (in.)	t_{sc} (in.)	t_p (in.)	ρ %	s_{stud} (in.)	d_{stud} (in.)	F_{u_stud} (ksi)	$\frac{s_{stud}}{t_p}$	s_{tie} (in.)	d_{tie} (in.)	F_{y_tie} (ksi)	$\frac{s_{tie}}{t_p}$	ρ_{tie} %	MC 10×8.4
120	37.5	10	3/16	3.75	5	0.5	65	26.7	5	0.5	60	26.7	0.78	

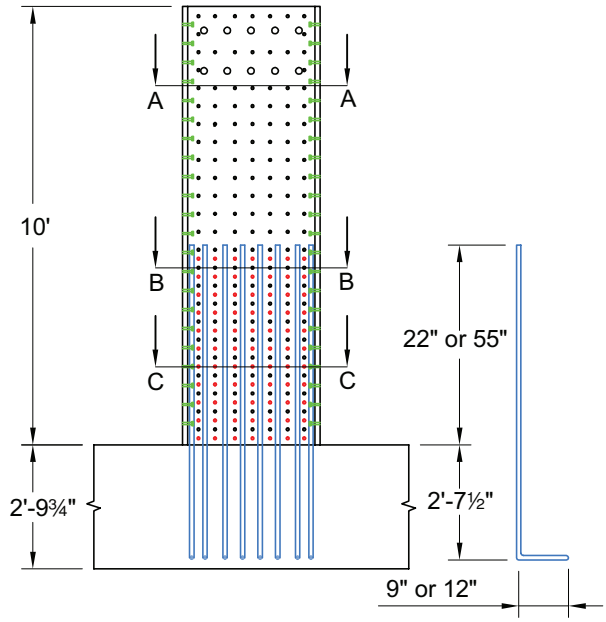

(a) SP-1 and SP-2

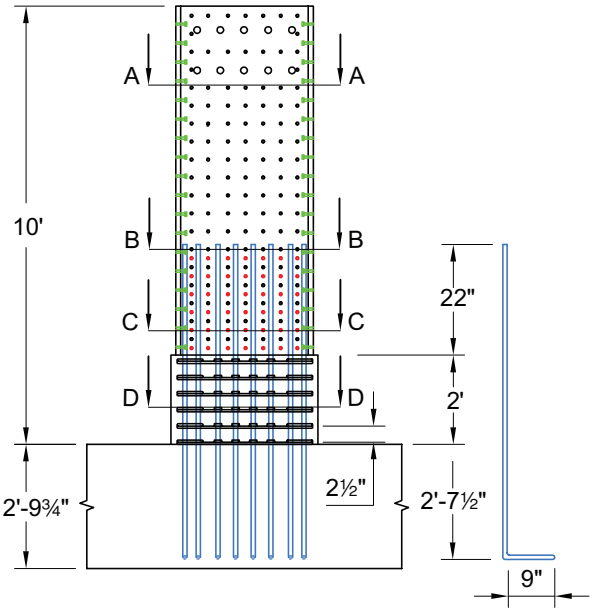

(b) SP-3

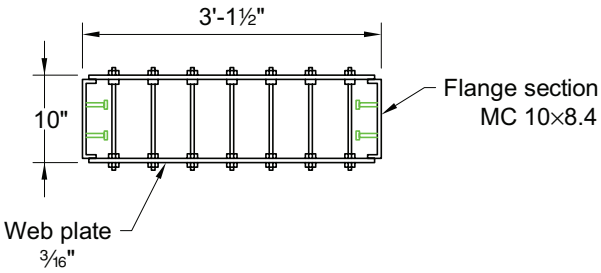

(c) Section A-A

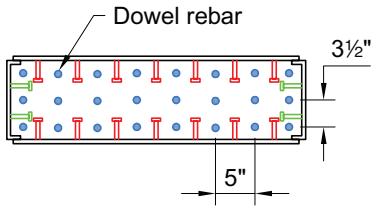

(d) Section C-C

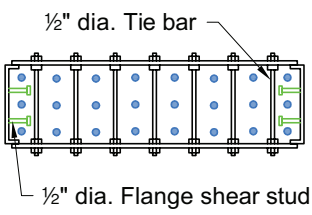

(e) Section B-B

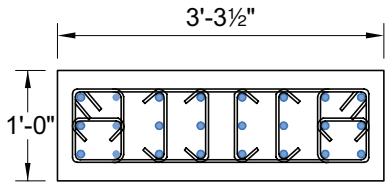

(f) Section D-D

Fig. 4. Specimen geometric details.

Table 2. Details of Dowels in Lap Splice Connections			
	Dowels		
Specimen	F_{y_bar} (ksi)	$l_{d\_wall\_provided}$ (in.)	d_{bar} (in.)
SP-1	60	22	¾
SP-2	80	55	1
SP-3	60	22	¾

Design of Test Specimens

This section presents the design details of the test specimens.

C-PSW/CF Wall Portion

Several archetype structures, using coupled and uncoupled C-PSW/CF systems for the primary lateral-force-resisting system, were designed for wind and seismic loading governed designs (Shafaei et al., 2022). The planar C-PSW/CF wall portions used in the cyclic experiments represented the individual walls of these uncoupled or coupled C-PSW/CF systems subjected to axial forces and lateral loading. The specimens were not precisely scaled down models of the individual planar C-PSW/CF walls of the archetype building structures. Instead, relevant structural characteristics were retained, such as (1) the steel reinforcement ratio ($\rho = 2t_p/t_{sc}$), (2) the steel plate slenderness ratio (s/t_p), (3) the tie bars reinforcement ratio ($\rho_{tie} = 2A_{tie}/s_{tie}$), and (4) the tie

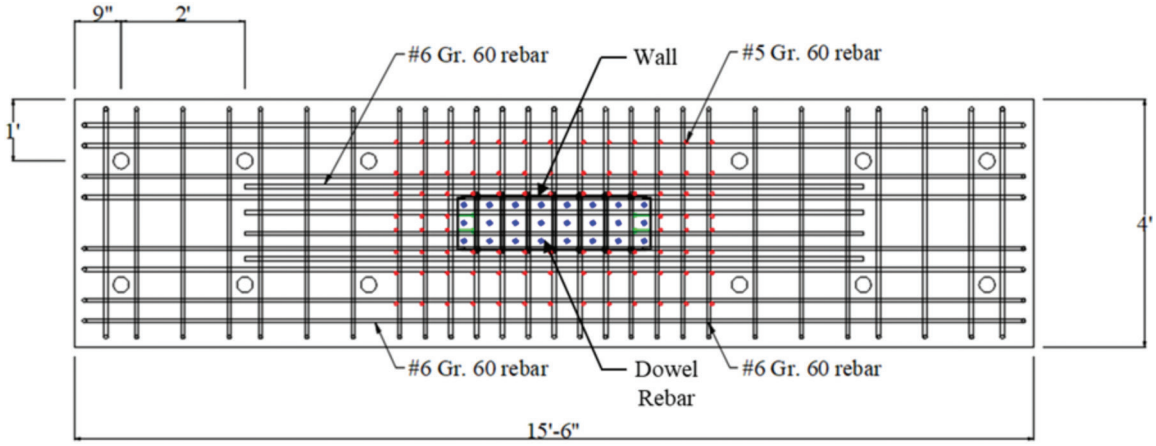

(a) SP-1 and 2

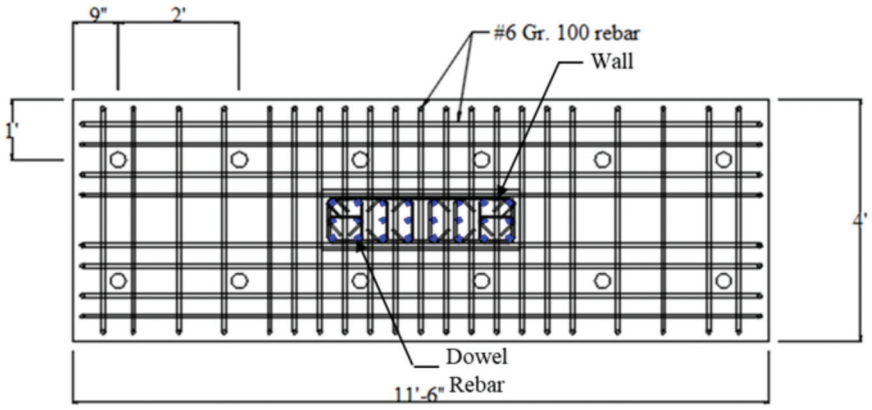

(b) SP-3

Fig. 5. Foundation details.

bar spacing to wall thickness ratio (s_{tie}/t_p). All ratios met the applicable requirements of AISC *Specification* Section I-1.5 and the AISC *Seismic Provisions*. The height-to-length ratio of the wall specimens was close to 3.0 to ensure flexure-dominant behavior. The authors have tested similar C-PSW/CF wall specimens with other types of wall-to-base connections that were designed to develop the full strength (plastic flexural capacity) of the C-PSW/CF walls under wind and seismic loading conditions (Shafaei et al., 2021, 2023).

RC Wall Portion (SP-3 Only)

The RC wall portion was designed using ACI 318-19, Chapter 18, to resist seismic loads while providing ductile inelastic response. For design, the height of the wall, h_w, was taken as 9 ft, which was the distance between the base of the RC and the load application point during the cyclic tests. The wall section was 39.5 in. long and 12 in. wide. Consequently, the coefficient of concrete contribution to wall shear strength, α_c, was taken as 2.0, per ACI 318-19, Section 18.10.4.1.

Dowel bars served as the longitudinal reinforcement for the RC wall. In addition, transverse reinforcement was provided for adequate shear strength. Figure 6 presents the various layers of transverse reinforcements provided in the RC wall. The reinforcement was provided in two orthogonal directions as per ACI 318-19, Section 18.10.4.3. In addition to horizontal web reinforcement, perimeter hoops with supplemental 135° cross ties and through web cross ties were also provided. Here, #3 Gr. 60 steel was used for the transverse reinforcement. The longitudinal and transverse wall reinforcement ratios (ρ_l and ρ_t) were 0.022 and 0.007, respectively, greater than the required value of 0.0025 as per ACI 318-19, Section 18.10.2.1.

The nominal shear strength of the RC wall, V_n, was calculated using the expression provided in ACI 318-19, Section 18.10.4.1, subject to an upper limit (shear strength of $10\sqrt{f'_c}A_{cv}$, where f'_c is expressed in psi and A_{cv} is the area of the concrete cross section). The nominal shear strength of the RC wall was calculated as 289 kips, which is approximately 73% of the upper limit. While designing, it was ensured that the RC wall had adequate shear strength, V_n, to transfer the lateral force, H_n, corresponding to the flexural strength of the confined RC section in the connection region, which was calculated as 142 kips (explained later).

Table 3 summarizes the geometric properties and design strengths for the RC wall.

Noncontact Lap Splice Connection Region

The full-strength connection design philosophy and the design recommendations discussed earlier were used to design and detail the noncontact lap splice connections. The applied loading subjects the connection region to axial force, *P,* bending moment, *M*, and shear force, *V*. The *P-M* combination results in tensile stresses (and forces) in the dowel bars on the tension side of the neutral axis. Under reversed cyclic loading, the dowel bars at both ends of the section are subjected to large tensile stresses and strains. The shear force, *V*, is resisted by either a direct shear mechanism or shear friction mechanism afforded by the dowel bars closer to the center (neutral axis) of the cross section. Thus, all the dowel bars in the connection region are subjected to large tensile stresses. Consequently, the design and detailing of dowel bars in the connection region focuses on developing their tensile strength.

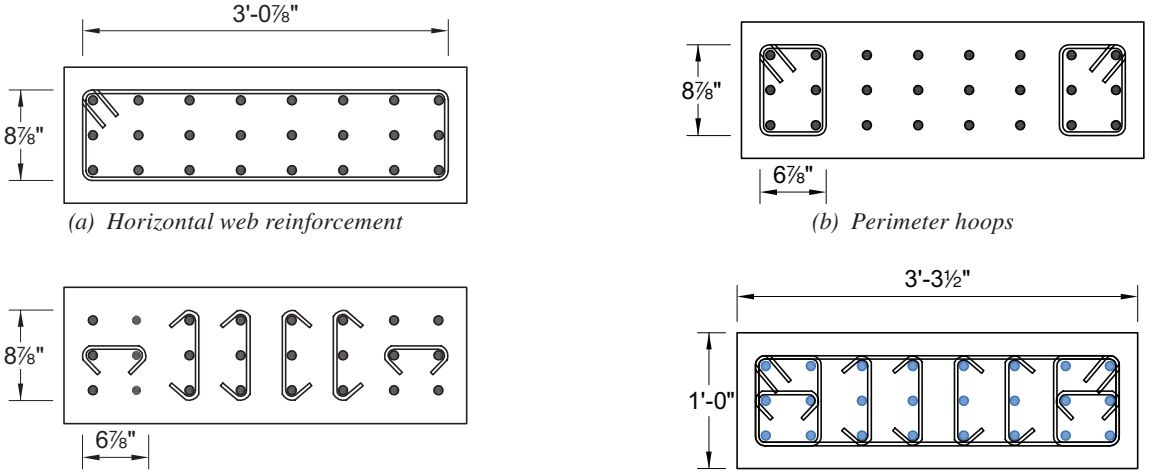

(a) Horizontal web reinforcement

(b) Perimeter hoops

(c) Cross ties

(d) All shear reinforcement (Section D-D in Figure 4)

Fig. 6. RC wall cross section.

Table 3. Section Details and Calculations for the RC Wall	
RC Wall Dimensions	
h_w, ft	9.0
l_w, in.	39.5
t_w, in.	12.0
Design Parameters	
h_w/l_w	2.83
α_c	2.00
Wall Reinforcement	
ρ_l	0.022
ρ_t	0.007
ρ_{min_req}	0.0025
Shear Strength	
V_n, kips (ACI 318, Section 18.10.4.1)	289
$\frac{V_n}{10\sqrt{f'_c}A_{cv}}$	0.727
H_n, kips	142

The connections were designed to develop the full tensile strength, N_r, of the weaker of the connected parts—that is, 1.25 times the nominal yield strength of the dowels $A_{bar}F_{y\_bar}$ in the connection. The tensile forces in the dowels are transferred to the steel plates of the C-PSW/CF by interfacial shear stresses produced by direct shear of the stud anchors and tie bars (see Figure 2). The connections were detailed such that the net interfacial strength, $\sum_n Q_n$, calculated as the sum of the direct shear strengths of the stud anchors (ψR_{stud}) and tie bars (ψR_{tie}) in the dowel embedment region, exceeded the required tensile strength (N_r) to be transferred through them. In the specimens, the direct shear strengths of individual headed stud anchors and threaded rods were calculated using Equation 1 from AISC *Specification* Section I8.3a, and Equation 2 adapted from Seo et al. (2019), respectively. In Equation 1, A_{stud} and F_{u_stud} denote the gross cross-sectional area and nominal tensile strength of the stud anchors, respectively. In Equation 2, A_{tie} and F_{y_tie} denote the gross cross-sectional area and nominal yield strength of the threaded rods, respectively. The 0.75 factor accounts for the effects of threads on the cross-sectional area, and 0.577 relates the tensile yield to shear yield stress.

$$\phi R_{stud} = (0.65)(1.0)A_{stud}F_{u\_stud} \quad (1)$$

$$\phi R_{tie} = (0.577)(0.75)A_{tie}F_{y\_tie} \quad (2)$$

Minimum spacing limits of the dowels were checked in accordance with ACI 318-19, Section 25.2. The minimum spacing of the dowels was taken as the greater of (1) 1 in., (2) the dowel bar diameter, or (3) 4/3 times the maximum size of aggregate. For effective development of concrete compression struts, the exterior layers of dowel bars were included within the length of the stud anchors, and the middle layer was included within the length of the tie bars.

The development length for dowel bars in the wall was calculated using ACI 318-19, Section 25.4.2.4, and then multiplied with 1.3 in accordance with Section 25.5.2 to calculate the required embedment length, l_{d_wall}. Hooked dowel bars were used in the foundation with development lengths also calculated using ACI 318-19. The calculated and provided values for the development lengths are listed in Table 4.

Test Setup and Loading Protocol

The test setup used for cyclic testing was similar to that used by Shafaei et al. (2021, 2023). Lateral and axial loads were applied to the top of the specimen after fixing them to the strong floor using 1¾-in.-diameter post-tensioning rods. Axial force, corresponding to 10% of the axial compression strength of the confined RC section, was applied at the top of the specimen. The axial loading was applied using a 500 ton Enerpac ram, while three MTS-100-kip actuators with a stroke length of 15 in. were used for lateral loading. Lateral loading beams were bolted to the specimens to apply the load. The axial loading was maintained constant while the cyclic lateral loading was applied. The test setup is shown in Figure 7.

Table 4. Design Calculations for Noncontact Lap Splice Connections			
Specimen	**SP-1**	**SP-2**	**SP-3**
Required Connection Strength			
$1.25A_{bar}F_{y\_bar}$, kips	33	79	33
N_r, kips	795	1885	795
Interfacial Shear Strength			
ϕR_{tie} (using Eq. 1), kips	286	714	286
ϕR_{stud} (using Eq. 2), kips	597	1493	597
$\sum_n Q_n$, kips	883	2207	883
Development Length (Wall)			
l_{d_wall} (using ACI 318-19, 25.4.2.4)*, in.	20.9	53.6	20.9
$l_{d\_wall\_provided}$, in.	22.0	55.0	22.0
Development Length (Base)			
l_{d_fnd} (using ACI 318-19, 25.4.3.1), in.	8.50	17.4	8.50
$l_{d\_fnd\_provided}$, in.	31.5	31.5	31.5
* Already multiplied by a factor of 1.3			

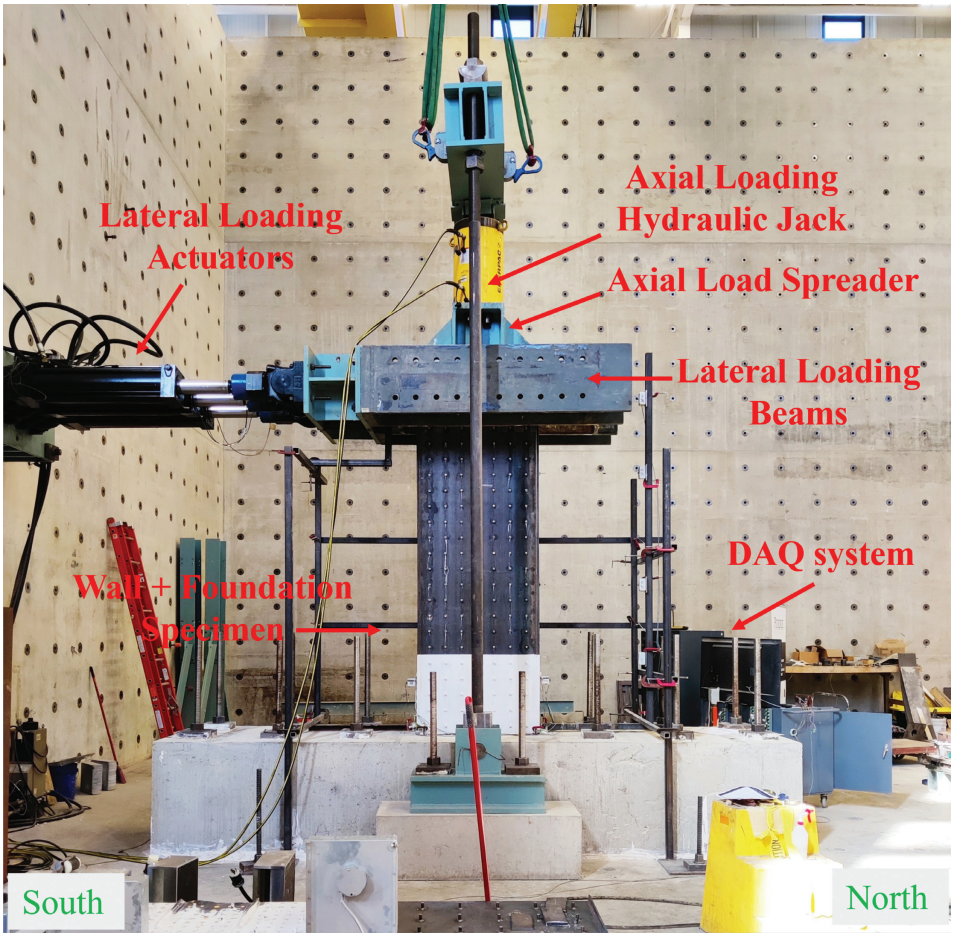

Fig. 7. View of the test setup.

Figure 8 presents the loading protocol for wind and seismic loading previously developed and used by the authors (Shafaei et al., 2021, 2023). The nominal flexural strength, M_n, used in the protocol was calculated as the nominal flexural strength of the confined RC section using the AISC *Specification* Section I-1.2a plastic stress distribution method. Nominal steel and concrete material properties were used, and the effect of axial forces was considered.

The wind loading protocol is shown in Figure 8(a). The wind loading cycles consisted of 500 force-controlled elastic cycles each at 0.25 and 0.50M_n, followed by 75 force-controlled elastic cycles at 0.75M_n. Inelastic wind cycles were applied thereafter. The yield rotation ($\theta_y = \Delta_y/h$) used for these cycles was computed based on the lateral stiffness reported in the first 0.75M_n elastic cycle. After the inelastic wind cycles, the elastic cycles were repeated to reevaluate the lateral stiffness of the specimen.

Seismic cycles in the inelastic range of behavior were performed after the wind cycles. Three cycles were applied at $2\theta_y$ and $3\theta_y$, followed by two cycles at $4\theta_y$, $5\theta_y$, $6\theta_y$, and so on. The cycles continued until (1) a significant drop in the peak lateral loads, and base moments, was observed or (2) fracture in the specimen occurred. Figure 8(b) shows the seismic loading protocol used in experimental investigations.

Summary of Experimental Results

The experimental behavior all three specimens is summarized in this section. Despite differences in connection detailing, variations in dowel size and layout, and the inclusion of an RC wall between C-PSW/CF and RC foundation, significant similarities were observed in the overall cyclic response of SP-1, SP-2, and SP-3. Eventually, after significant inelastic cycles and ductility, tensile rupture of the dowels occurred in the confined RC section of SP-1 and SP-2, and at the RC wall-RC base interface for SP-3. This failure mode was expected as per the full-strength design approach.

Figure 9(a)–(c) present the response of the three specimens to wind and seismic loading. The applied moment at the base of the connection and the corresponding lateral

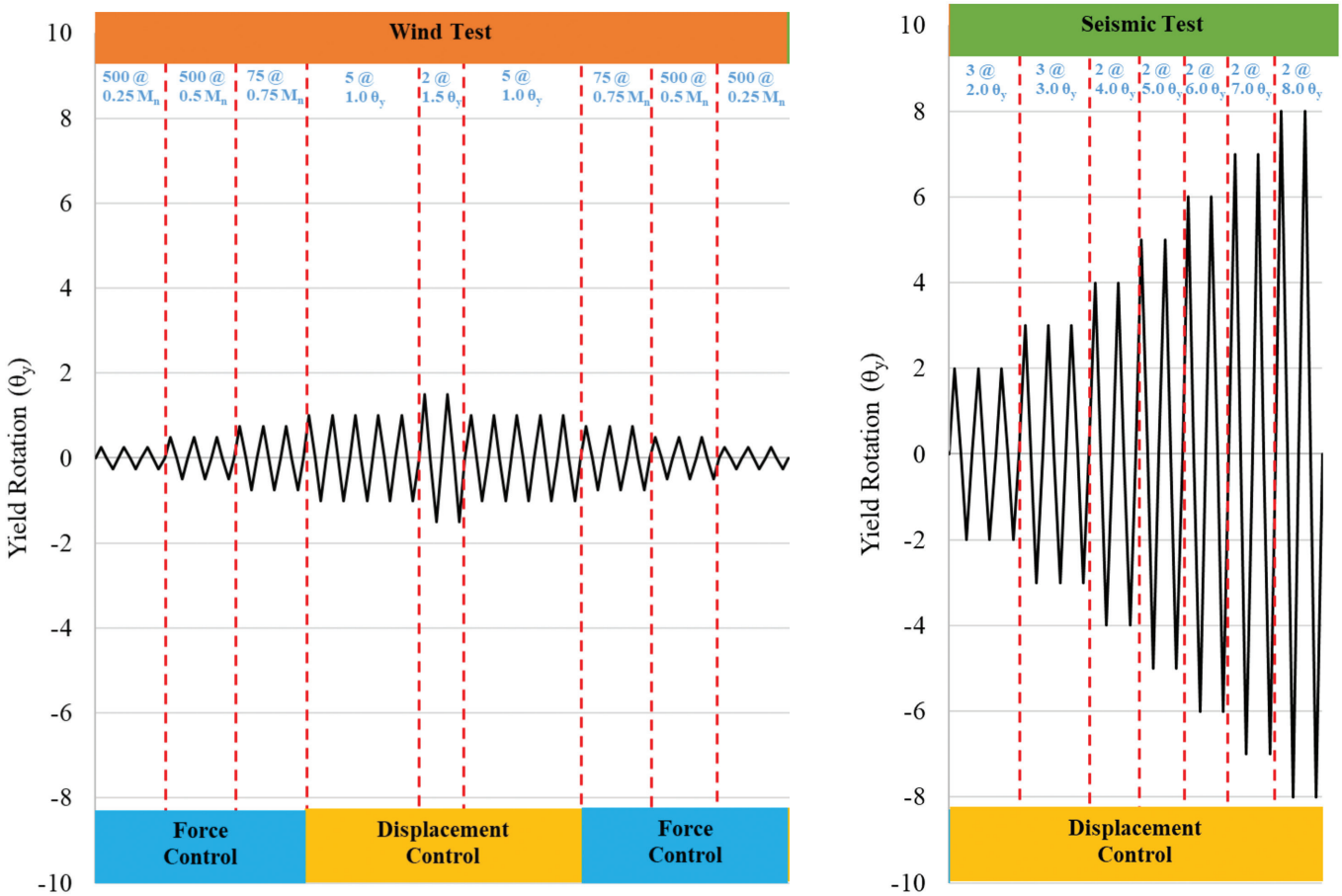

(a) Wind test *(b) Seismic test*

Fig. 8. Cyclic lateral loading protocol.

drift are shown. The lateral drift (Δ/h) is calculated by dividing the lateral displacement, Δ, at the lateral load application point by h, the distance between the load application point and the connection base. Results for all 2,162 wind cycles and seismic cycles are shown. The figure also includes horizontal dashed lines corresponding to 80% of the experimentally observed maximum capacity.

All three specimens exhibited linear behavior during the elastic wind cycles, and no major stiffness degradation was observed. Yielding of the dowels in the outermost layer was observed during the $0.75M_n$ elastic cycles across all specimens, as corroborated by the strain gauge data. Minor cracks in the RC wall were observed in SP-3 during the same cycles. Inelastic cycles at $1.0\theta_y$ and $1.5\theta_y$ led to yielding in additional dowels closer to the C-PSW/CF flanges. However, the specimens' overall behavior remained predominantly linear. During these inelastic cycles, the C-PSW/CF steel plates in SP-1 and SP-2 showed no signs of yielding, and the RC wall concrete in SP-3 remained intact. A loss in flexural stiffness was observed in the second set of elastic wind cycles, as expected.

The seismic cycles were based on the yield rotation of the specimen, θ_y, computed using the lateral stiffness reported during the first of $0.75M_n$ elastic cycle. All specimens behaved linearly during the three seismic cycles at $2\theta_y$. However, during the cycles at $3\theta_y$, minor excursions into the nonlinear range were observed. Specifically, the C-PSW/CF flanges of SP-2 exhibited yielding. In the $4\theta_y$ cycles, the C-PSW/CF flanges of SP-1 experienced yielding, while SP-2 had a loss in stiffness due to local deformations in the north C-PSW/CF flange, located between the C-PSW/CF base and the first row of flange shear studs. For SP-3, the behavior was marginally inelastic, and some cracking in the RC wall was observed. The second cycle at $5\theta_y$ resulted in a decrease in base moment and flexural stiffness for SP-2 accompanied by local deformations in the

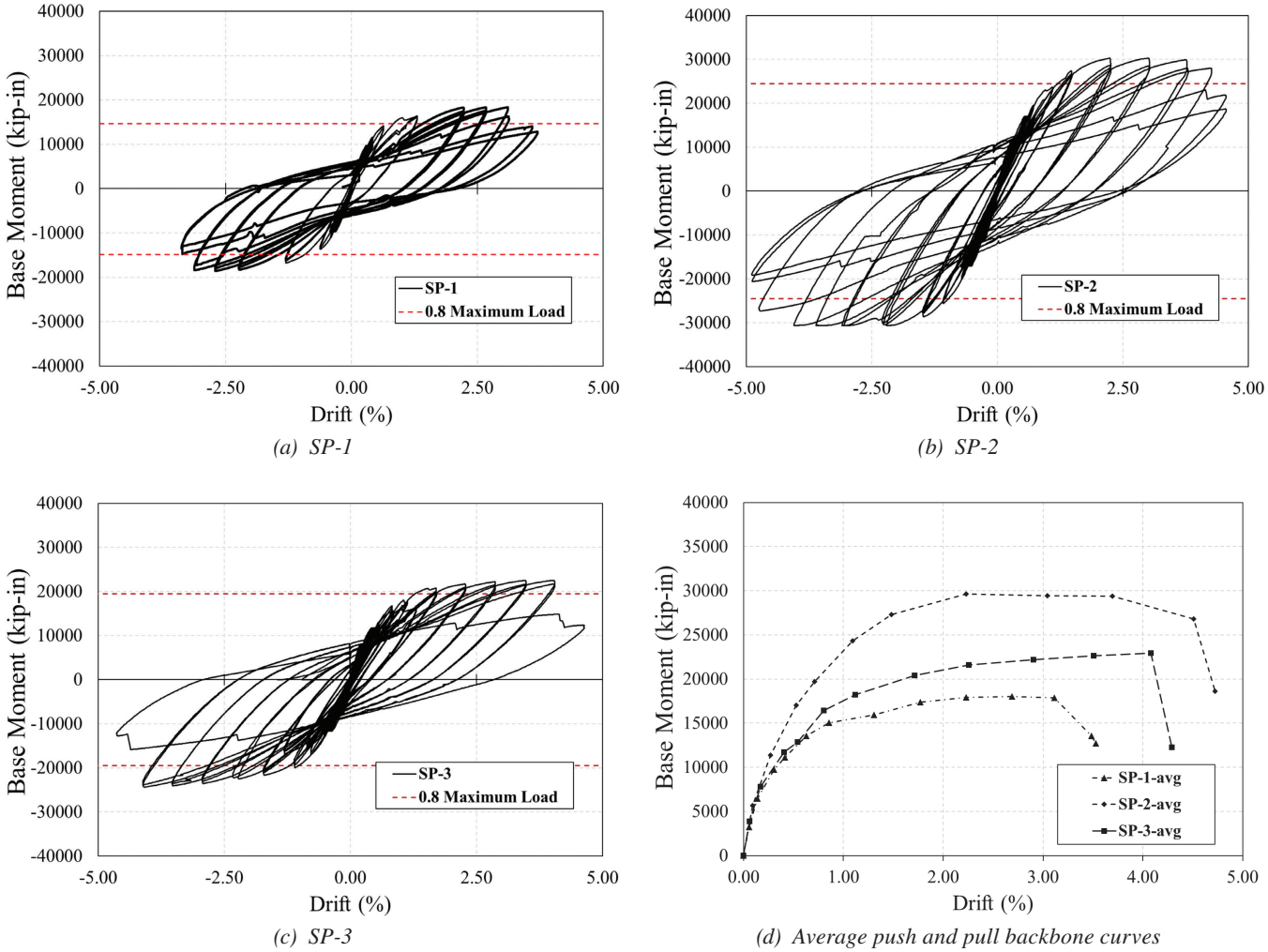

(a) SP-1 *(b) SP-2*

(c) SP-3 *(d) Average push and pull backbone curves*

Fig. 9. Base moment-drift responses.

Table 5. Measured Material Properties			
	Dowel Rebar		Concrete
Specimen	F_y (ksi)	F_u (ksi)	f'_{cm} (psi)
SP-1	66	108	7564
SP-2	91	118	7441
SP-3	69	108	8926

south C-PSW/CF flange. The south and north directions of the specimens are indicated in Figure 7. SP-1 and SP-3 also showed nonlinear behavior; however, no reduction in base moment was observed.

In $6\theta_y$ cycles, five out of six outermost dowels of SP-2 underwent tensile rupture, causing an abrupt reduction in stiffness. In addition, the maximum base moment decreased by more than 20%. An additional cycle at the same amplitude led to tensile rupture of the remaining dowel and a 40% reduction in the maximum base moment. The test was stopped as a result. SP-1 and SP-3 remained inelastic in these cycles and were subjected to two seismic cycles at $7\theta_y$. Excessive deformations in C-PSW/CF flanges of SP-1 were observed in the first cycle, while tensile rupture in one outermost dowel was observed during the second cycle. Moreover, there was a notable decrease in the maximum base moment during the second cycle. SP-3 also exhibited a highly nonlinear base moment-drift response with unchanged maximum base moments and loss in RC wall concrete cover due to cracking. However, no rupture in dowels occurred.

Both SP-1 and SP-3 were subjected to seismic cycles at $8\theta_y$. In SP-1, a decrease in the maximum base moments was seen along with tensile rupture in five outermost dowels throughout the two cycles. SP-3 was only subjected to a single cycle at $8\theta_y$, during which tensile rupture in six outermost dowels occurred. The maximum base moments in both push and pull directions reduced by more than 40%, and the test was concluded.

Figure 9(d) shows the backbone of the base moment-drift curves for the specimens. These backbone curves represent the average of the push and pull responses for the specimens. The initial behavior prior to concrete cracking is consistent for all three specimens, and no significant difference in secant stiffness is observed. However, after concrete cracking, the response of SP-2 is stiffer compared to SP-1 and SP-3 due to the presence of higher strength dowel bars. Significant changes in the base moment-drift response are observed during the seismic cycles, with losses in lateral stiffnesses because of dowel yielding. The peak base moment is highest for SP-2, due to higher strength rebar, followed by SP-3, having a larger confined RC section, and lowest for SP-1. All three specimens exhibited significant ductility prior to failure, which occurred during the $8\theta_y$ cycles for SP-1 and SP-3 and the $6\theta_y$ cycles for SP-2.

Failure in all three specimens occurred due to tensile rupture in the dowel bars. These dowels were in the peripheral (end) layers of the confined RC section. The failure occurred at the base of the C-PSW/CF for SP-1 and SP-2 and at the base of RC wall for SP-3. Following the cyclic test, concrete surrounding the ruptured dowels was removed from the specimens. Figure 10 shows the ruptured dowels on the north and south side of the specimens, with tensile failure clearly visible. The remaining dowels show no signs of failure.

FIBER-BASED MODEL OF CONFINED RC SECTION

A fiber-based model of the confined RC section in the noncontact lap splice connection region was developed and used to compute the moment curvature, M-ϕ, response. This fiber-based approach extended the Euler-Bernoulli beam bending theory, which assumes that plane sections remain plane and perpendicular to the neutral axis before and after bending. Additional assumptions included linear distribution of longitudinal strains through the cross section, full strain compatibility between the steel dowels and the surrounding concrete, and negligible tensile stress contribution from the concrete infill.

Axial loads acting on the section were considered while obtaining the M-ϕ relationship. The steel stress-strain behavior was modeled with linear elastic behavior up to the measured yield stress, F_y, followed by yield plateau, and then power-law strain hardening up to the measured ultimate stress, F_u. The concrete was modeled with stress-strain behavior based on Tao et al. (2013) up to the measured concrete strength, f'_{cm}, and plastic (no degradation in strength) behavior thereafter to account for the confinement from C-PSW/CF steel plates. The calculated M-ϕ relationship was used to evaluate the flexural stiffness and strength of the connection region, as discussed later. Table 5 includes the measured material properties used in the fiber analysis.

(a) SP-1 north side

(b) SP-1 south side

(c) SP-2 north side

(d) SP-2 south side

(e) SP-3 north side

(f) SP-3 south side

Fig. 10. Ruptured dowel bars on the north and south sides of the wall specimens.

These included the yield and tensile strengths of the dowel bars and the concrete compressive strengths.

FLEXURAL STIFFNESS

The flexural stiffness of the noncontact lap splice connection region can influence serviceability design (e.g., drift requirements). In this section, the flexural stiffness of the wall specimen, including the connection region, is estimated using experimental results and used to evaluate assumptions regarding the stiffness of the connection region. The experimental flexural stiffness, EI_{exp}, is calculated using the secant stiffness from the lateral force-displacement, H-Δ, response of the wall specimen during the $0.50M_n$ wind cycles because they are most representative of serviceability (story drift during wind cycles) performance. The specimen is assumed to be a fixed-base cantilever, and the entire specimen height is assumed to have the same effective stiffness, EI_{exp}, that can then be calculated using Equation 3. In this equation, h is the height of the wall between the fix base and lateral load location, and $(H/\Delta)_{0.50Mn}$ is the secant stiffness. Table 5 reports the experimental flexural stiffness values, EI_{exp}, for Specimens SP-1, SP-2, and SP-3.

$$EI_{exp} = \frac{h^3}{3}\left(\frac{H}{\Delta}\right)_{0.50M_n} \quad (3)$$

$$EI_{C\text{-}PSW/CF} = E_S I_S + 0.35E_c I_c \quad (4)$$

$$EI_{RC\_wall} = 0.35E_c I_g \quad (5)$$

Assumptions regarding the flexural stiffness of the connection region, EI_{con}, were then evaluated using elastic models of the specimens shown schematically in Figure 11. The composite wall portions were modeled using the flexural stiffness recommendation from AISC *Specification* Section I1.5(e) as shown in Equation 4. In this equation, $EI_{C\text{-}PSW/CF}$ is the flexural stiffness of the composite wall portion; E_s and E_c are the elastic modulus of steel and concrete, respectively; and I_s and I_c are the moments of inertia of the steel module and concrete infill of the composite cross section, respectively. The RC wall portion of Specimen SP-3 was modeled using flexural stiffness recommendations from ACI 318-19, Table 6.6.3.1.1(a), as shown in Equation 5. In this equation, EI_{RC_wall} is the flexural stiffness of the reinforced concrete wall portion of SP-3, E_c is the elastic modulus of concrete, and I_g is the moment of inertia of the gross concrete section.

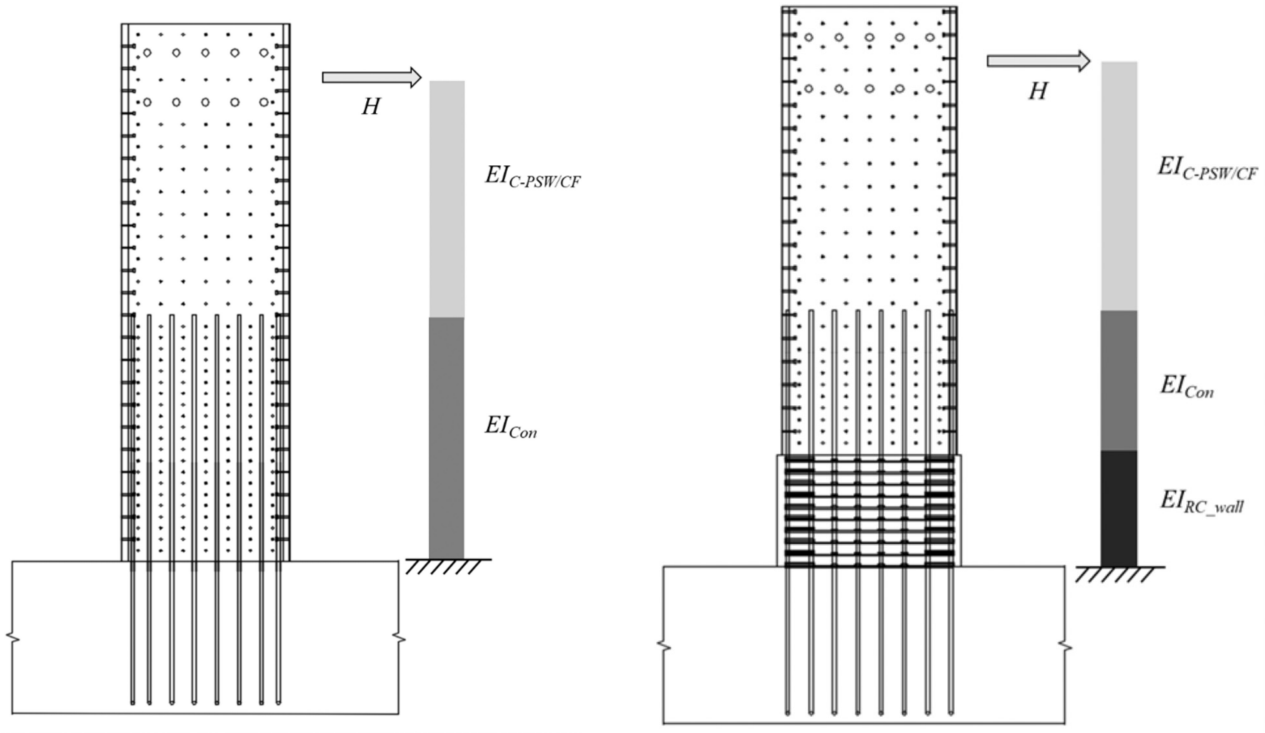

(a) SP-1 and SP-2 *(b) SP-3*

Fig. 11. Spring model system schematic.

Table 6. Flexural Stiffness Comparison (Experimental-to-Calculated)				
Specimen	**Flexural Stiffness**	**Stiffness Ratios (Experimental-to-Calculated)**		
	EI_{exp} $\times 10_6$ (kip-in.^{2})	$EI_{con} = 0.35E_cI_g$	$EI_{con} = E_sI_s + 0.35E_cI_c$	EI_{con} using M-ϕ
		$EI_{exp}/EI_{eff\text{-}i}$	$EI_{exp}/EI_{eff\text{-}ii}$	$EI_{exp}/EI_{eff\text{-}iii}$
SP-1	142	1.48	0.95	1.00
SP-2	128	1.73	1.16	0.91
SP-3	162	1.33	1.22	1.18

The connection region of the wall specimen was modeled considering three options for EI_{con}: (i) assuming that the connection region can be modeled with the same flexural stiffness as an RC wall ($EI_{con} = 0.35E_cI_g$), (ii) assuming that the connection region can be modeled with the same flexural stiffness as the composite wall ($EI_{con} = E_sI_s + 0.35E_cI_{c)}$, and (iii) assuming that the connection region flexural stiffness can be represented with the M-ϕ relationship obtained from fiber analysis of the confined RC section.

An elastic model of the specimen length with a fixed base was developed using different stiffnesses for different portions as explained above and shown schematically in Figure 11. This model was analyzed for the applied lateral loading, H, corresponding to the $0.50M_n$ cycles, and the lateral deflection, Δ, was calculated by integrating curvatures corresponding to the moments and section flexural stiffness along the height as per Lai et al. (2016). The calculated lateral deflection was used to estimate the effective (or smeared) wall stiffness using the right side of Equation 3. The estimated wall stiffnesses are referred to as $EI_{eff\text{-}i}$, $EI_{eff\text{-}ii}$, and $EI_{eff\text{-}iii}$, respectively, corresponding to the use of assumptions (i), (ii), and (iii) for the connection region stiffness.

Table 6 includes comparisons of the experimental stiffness, EI_{exp}, with the stiffness calculated using assumptions (i), (ii), and (iii) for the connection region. As shown by the ratios in the table, using assumption (i) significantly underestimates (ratios ranging from 1.33–1.73) the flexural stiffness of the walls with connection regions. Using assumption (ii) reasonably estimates the flexural stiffness (ratios ranging from 0.95–1.22) of walls with connection regions. Using assumption (iii) also reasonably estimates (ratios ranging from 0.91–1.18) the flexural stiffness of walls SP-1, SP-2, and SP-3. Due to its simplicity, assumption (ii), which models the noncontact lap splice connection region with the same flexural stiffness ($EI_{con} = E_sI_s + 0.35E_cI_c$) as the composite wall is recommended.

FLEXURAL STRENGTH

The flexural strength of the confined RC section in the connection region was calculated using analytical approaches based on ACI 318-19 code recommendations, the 2022 AISC *Specification*, and the fiber-based analysis of the cross section as mentioned earlier. These approaches inherently assume that the connection is designed and detailed appropriately with (1) sufficient interfacial shear strength, (2) adequate embedment (development) length for the dowels, and (3) appropriate placement of the dowels for a ductile failure mode. All the approaches accounted for the effects of axial force on the flexural strength and used the measured material properties for steel and concrete (reported in Table 5) in the calculations.

The ACI 318-19 approach used recommendations from Section 22.2 to compute the flexural strength. These included an extreme concrete compression fiber strain of 0.003, rectangular concrete stress distribution in compression, zero concrete stress contribution in tension, and elastic-perfectly plastic behavior for the dowels. Figure 12(a) illustrates a characteristic stress distribution in the confined RC section per ACI 318-19. In this figure, x_i is the distance from the rebar to the extreme compression fiber, and a is the depth of the rectangular (Whitney) stress block. The rebar stresses, F_i, increase linearly (in compression and tension) from the neutral axis but are limited to the maximum yield stress of F_y.

The AISC *Specification* approach used the plastic stress distribution method from *Specification* Section I1.2a to compute the flexural strength. Figure 12(b) illustrates the assumed plastic stress distribution. In this figure, a is the depth of the plastic neutral axis. The concrete in compression was assumed to reach $0.85f'_{cm}$, and its stress contribution in tension was neglected. All dowels were assumed to reach their yield strength of F_y in tension and in compression. Because the experiments eventually failed with tensile rupture of the dowels, the AISC *Specification* Section I1.2a approach was modified to assume that all dowels reach their ultimate tensile strength, F_u, and the flexural strength was calculated again.

Table 7 includes the experimental flexural strength, M_{exp}, from the tests. It also includes ratios of the experimental-to-calculated flexural strength using the approaches mentioned previously. As shown, using the ACI 318-19 method results in experimental-to-calculated strength ratios that are very

Table 7. Flexural Strength Comparisons (Experimental-to-Calculated)					
	Experimental Flexural Strength	Connection Flexural Strength Ratios (Experimental-to-Calculated)			
Specimen	M_{exp} (kip-ft)	ACI 318-19	AISC *Specification* (using F_y)	AISC *Specification* (using F_u)	M-ϕ
SP-1	1539	1.52	1.35	1.00	1.04
SP-2	2538	1.49	1.23	1.01	1.01
SP-3	1949	1.54	1.33	1.03	1.09

conservative (ratios ranging from 1.49–1.54). Using the AISC *Specification* method with yield stress, F_y, for the dowels also results in conservative experimental-to-calculated strength ratios (ranging from 1.23–1.35). However, using the AISC *Specification* method with ultimate stress, F_u, for the dowels results in accurate experimental-to-calculated strength ratios (ranging from 1.00–1.03). Similarly, using the fiber-based method also results in experimental-to-calculated strength ratios that are quite reasonable (ranging from 1.01–1.09).

Thus, the ACI 318-19 and AISC *Specification* (with F_y) approaches can be used to conservatively estimate the flexural strength of the confined RC section, and thus the connection region. Both these methods provide a lower-bound estimate of the flexural strength, but the ACI method is more conservative because it does not assume full plastification of the cross section. We recommend using the AISC *Specification* (with F_y) approach to estimate the flexural strength for design. The AISC *Specification* modified approach (using F_u instead of F_y) can be used to estimate the expected flexural strength of the confined RC section and thus the connection region. Similarly, the fiber-based analysis of the confined RC section can also be used to estimate the expected flexural strength.

SHEAR STRENGTH

The connection region is also designed with adequate shear strength to resist the corresponding (shear) demands associated with lateral loading on the C-PSW/CF wall. These shear demands are also resisted by the dowels located closer to the center (or neutral axis) of the confined RC section. The dowels resist the shear demands in direct shear, which is indicated by their deformed shapes at the end of testing and observed after removal of concrete (Varma et al., 2024).

For a lap splice connection with dowels having a gross cross-sectional area of A_{bar} and nominal yield strength of F_{y_bar}, the shear strength can be calculated as the direct shear strength ($0.6A_{bar}F_{y\_bar}$) of approximately 80% of the rebar in the connection, resulting in an estimated shear strength of $0.5A_{bar}F_{y\_bar}$. The ratio of the maximum lateral load (or base shear) from the experiment, H_{exp}, and the

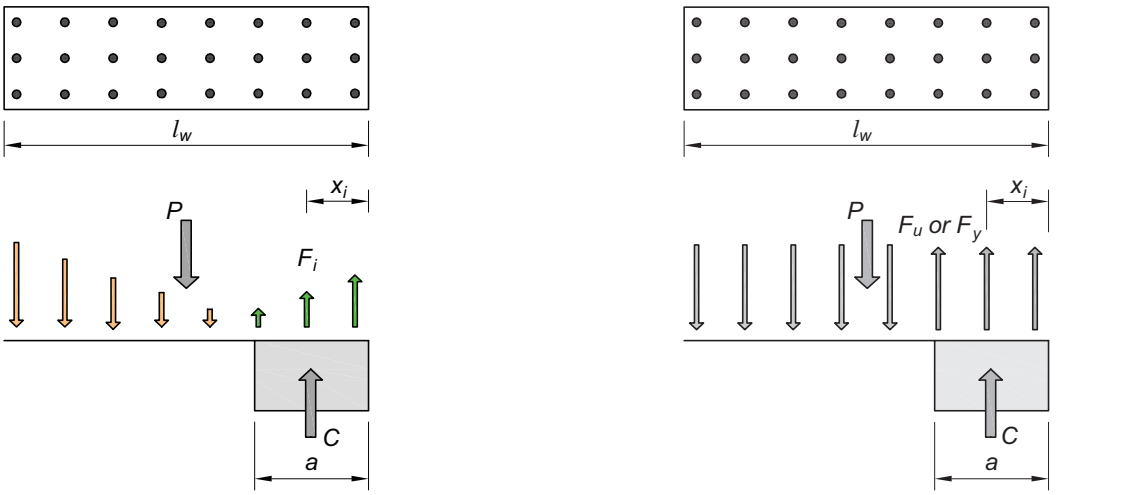

(a) ACI 318 approach *(b) AISC* Specification *plastic distribution approach*

Fig. 12. Analytical approaches for flexural strength calculation.

Table 8. Shear Demand to Estimated Strength Ratios		
	Maximum Lateral Load (kips)	Shear Strength Ratios (Experimental-to-Calculated)
Specimen	H_{exp}	$H_{exp}/0.5A_{bar}F_y$
SP-1	171	0.49
SP-2	282	0.33
SP-3	217	0.60

calculated expected shear strength, $0.5A_{bar}F_y$, for the tested specimens is provided in Table 8. As shown, the shear demand was just a fraction of the calculated shear strength with experimental-to-calculated strength ratios ranging from 0.33 to 0.60. This agrees with experimental results where no shear failure or cracking was observed.

The ratios of H_{exp} with respect to the upper limit of shear strength for reinforced concrete walls from ACI 318-19, Section 18.10.4.1 (mentioned earlier), were equal to 0.53, 0.87, and 0.49 for Specimens SP-1, SP-2, and SP-3, respectively. These ratios were calculated using measured material strengths and are provided for informational purposes and do not have any direct implication on the design of the confined RC section in the connection region.

CONCLUSIONS

This paper provides information on the design and detailing of noncontact lap splice connections for C-PSW/CF to RC base. These connections may be used to directly connect the C-PSW/CF to the RC foundation, or to an intermediate RC wall. They were designed to develop the full strength of the weaker of the connected parts, which is typically associated with 1.25 times the nominal yield strength of the dowels in the connection. Accordingly, previous design considerations proposed for noncontact lap splice connections for SC walls were applied here for C-PSW/CF-RC base connections. These primarily included (1) dowel development length, (2) interfacial shear strength, and (3) dowel layout.

Experimental investigations were conducted on large-scale C-PSW/CF-to-RC base specimens, and their response under wind and seismic loading was evaluated. Experimental results indicated that appropriately designed and detailed connections have excellent performance (stiffness, strength, and ductility), which are primarily governed by the behavior of the "confined RC section" in the connection region. Methods to estimate the flexural stiffness and flexural strength of the confined RC were evaluated. The following conclusions are drawn from the investigations:

1. The design recommendations offered by Seo and Varma (2017) and Seo et al. (2021) are effective and could be applied to detail C-PSW/CF-to-RC base connections. Specimens that were designed and detailed using these recommendations developed the full strength of confined RC section in the connection region as intended for ductile failure modes.
2. The specimens were able to resist wind cycles without any significant loss in lateral stiffness or yielding in the C-PSW/CF steel plates. However, minor yielding in the dowels was observed during the $0.75M_n$ cycles. In the seismic cycles, a reduction in the lateral stiffness of the specimens was apparent after excursions into the inelastic range of the behavior.
3. The seismic response of the specimens was very ductile, with SP-1, SP-2, and SP-3 failing during $8\theta_y$, $6\theta_y$, and $8\theta_y$ cycles, respectively, due to tensile rupture of multiple dowel bars. This can be attributed to the confinement provided by the steel plates of the C-PSW/CF to the concrete infill, inhibiting concrete spalling and delaying the buckling of the dowel.
4. Modeling the connection region with the same flexural stiffness as an RC wall ($EI_{con} = 0.35E_cI_g$) significantly underestimates the stiffness of walls with connection regions. Modeling the connection region with the same flexural stiffness as the composite wall ($EI_{con} = 0.35E_cI_c + E_sI_s$) adequately represents the stiffness of walls with connection regions.
5. Modeling the connection region using the moment-curvature relationship (M-ϕ) obtained from fiber analysis of the confined RC section also adequately represents the stiffness of walls with connection regions. However, due to its simplicity, modeling the connection regions with the same flexural stiffness as the composite wall is recommended.
6. The design flexural strength of the confined RC section in the connection region can be calculated conservatively using the AISC *Specification* Section I1.2a plastic stress distribution method. Calculating this flexural strength using ACI 318-19 code recommendations can be too conservative.
7. The expected flexural strength of the confined RC section in the connection region can be calculated accurately by

modifying the AISC *Specification* Section I1.2a plastic stress distribution method to use the ultimate or tensile stress, F_u, for the dowels instead of the yield stress, F_y. This expected flexural strength can also be estimated with reasonable accuracy using the fiber-based section moment-curvature (M-ϕ) analysis method.

8. Overall, noncontact lap splice connections are an effective method to connect C-PSW/CF walls to RC bases. They can be detailed and designed appropriately to achieve the full strength of the confined RC section in the connection region resulting in excellent stiffness, strength, and ductility of the composite wall system.

ACKNOWLEDGMENTS

The project was supported by Charles Pankow Foundation (CPF Research Grant 06–16) and the American Institute of Steel Construction (AISC). However, any opinions, findings, conclusions, and recommendations presented in this paper are those of the authors and do not necessarily reflect the view of the sponsors.

SYMBOLS

The following symbols are used in this paper:

A_{bar}	Gross cross-sectional area of dowel bars in the connection
A_{cv}	Cross-sectional area of concrete in confined RC section
A_{tie}	Area of tie bar
A_{stud}	Area of tie bar
E_c	Modulus of elasticity of concrete
EI_{exp}	Experimental flexural stiffness
EI_{con}	Flexural stiffness of the connection region
$EI_{C\text{-}PSW/CF}$	Flexural stiffness of the C-PSW/CF portion
EI_{RC_wall}	Flexural stiffness of the RC wall portion
E_s	Modulus of elasticity of steel
F_y	Measured dowel bar yield strength
F_{y_bar}	Dowel bar nominal yield strength
F_{y_tie}	Tie bar/threaded rod nominal yield strength
F_u	Measured dowel bar ultimate strength
F_{u_stud}	Stud anchor (shear stud) nominal ultimate strength
H	Lateral load applied at level of loading actuators
H_n	Lateral force corresponding to the nominal flexural strength of the confined RC section
H_{exp}	Maximum experimental lateral load
I_c	Moment of inertia of C-PSW/CF infill concrete core
I_g	Moment of inertia of RC wall section
I_s	Moment of inertia of C-PSW/CF steel section
M_{exp}	Maximum experimental moment strength
M_n	Nominal flexural strength of the confined RC section
N_r	Required tensile strength
Q_n	Shear resistance of individual anchor/tie bar
R_{stud}	Direct shear strength of the stud anchor
R_{tie}	Direct shear strength of the tie bar/threaded rods
S	Smallest distance between rows of tie bars or shear studs
d_{bar}	Diameter of dowel bar
d_{stud}	Diameter of shear stud
d_{tie}	Diameter of tie bar
f'_c	Nominal concrete compression strength
f'_{cm}	Measured concrete compression strength
h	Distance between the load application point and the connection base
h_w	Wall height
l_{d_fnd}	Dowel bar foundation development length
$l_{d\_fnd\_provided}$	Provided dowel bar foundation development length
l_{d_wall}	Dowel bar wall development length
$l_{d\_wall\_provided}$	Provided dowel bar wall development length
l_w	C-PSW/CF wall length
s_{stud}	Shear stud spacing
s_{tie}	Tie bar spacing
t_p	C-PSW/CF steel plate thickness
t_{sc}	C-PSW/CF wall thickness
t_w	RC wall thickness
α_c	Coefficient of concrete contribution to wall shear strength

Δ	Lateral displacement
Δ_y	Yield displacement
ρ	Steel reinforcement ratio
ρ_l	Longitudinal wall reinforcement ratio
ρ_t	Transverse wall reinforcement ratio
ρ_{tie}	Tie bar reinforcement ratio
θ_y	Yield rotation

REFERENCES

ACI (2019), *Building Code Requirements for Structural Concrete and Commentary*, ACI 318-19, American Concrete Institute, Farmington Hills, Mich.

Agrawal, S., Broberg, M., and Varma, A.H. (2020), "Seismic Design Coefficients for SpeedCore or Composite Plate Shear Walls-Concrete Filled (C-PSW/CF)," Bowen Laboratory Research Report, Purdue University, West Lafayette, Ind.

Ahmad, M,. Shafaei, S., Varma, A.H., and Klemencic, R. (2024), "Experimental Investigation of Composite Coupling Beam-to-Wall Connections in Coupled C-PSW/CF Systems." *Journal of Structural Engineering*, ASCE Vol. 150, No. 9, 04024114. https://doi.org/10.1061/JSENDH.STENG-13453

AISC (2016), *Seismic Provisions for Structural Steel Buildings*, ANSI/AISC 341-16, American Institute of Steel Construction, Chicago, Ill.

AISC (2022a), *Seismic Provisions for Structural Steel Buildings,* ANSI/AISC 341-22, American Institute of Steel Construction, Chicago, Ill.

AISC (2022b), *Specification for Structural Steel Buildings*, ANSI/AISC 360-22, American Institute of Steel Construction, Chicago, Ill.

AISC (2024), "*Specification for Safety-Related Steel Structures for Nuclear Facilities*, ANSI/AISC N690-24, American Institute of Steel Construction, Chicago, Ill.

ASCE (2016), *Minimum Design Loads for Buildings and Other Structures*, ASCE 7-16, American Society of Civil Engineers, Reston, Va.

ASCE (2022), *Minimum Design Loads for Buildings and Other Structures*, ASCE 7-22, American Society of Civil Engineers, Reston, Va.

ASTM (2021), *Standard Specification for High-Strength Low-Alloy Columbium-Vanadium Structural Steel,* ASTM A572/A572M, American Society for Testing and Materials, West Conshohocken, Pa.

ASTM (2023), *Standard Specification for Alloy-Steel and Stainless Steel Bolting for High Temperature or High Pressure Service and Other Special Purpose Applications,* ASTM A193/A193M, American Society for Testing and Materials, West Conshohocken, Pa.

Bhardwaj, S.R. and Varma, A.H. (2017*), Design of Modular Steel Plate Composite (SC) Walls for Safety-Related Nuclear Facilitie*s, Design Guide 32, AISC, Chicago, Ill.

Bhardwaj, S., Varma, A.H., and Malushte, S. (2017), "Minimum Requirements and Section Detailing Provisions for Steel-Plate Composite (SC) Walls in Safety-Related Nuclear Facilities," *Engineering Journal*, AISC, Vol. 54, No. 2, pp. 89–107.

Broberg, M., Agrawal, S., Varma, A., and Klemencic, R. (2023), "Seismic Design Parameters (R, Wo, and Cd) for Uncoupled Composite Plate Shear Walls–Concrete Filled," *Earthquake Engineering and Structural Dynamics*, Vol. 52, No. 10, pp. 3,149–3,170. https://doi.org/10.1002/eqe.3917

Broberg, M., Shafaei, S., Kizilarslan, E., Seo, J., Varma, A.H., Bruneau, M., and Klemencic, R. (2022), "Capacity Design of Coupled Composite Plate Shear Walls/Concrete Filled (CC-PSW/CF)," *Journal of Structural Engineering*, ASCE, Vol. 148, No. 4. https://dx.doi.org/10.1061/(ASCE)ST.1943–541X.0003296

Kizilarslan, E., Broberg, M., Shafaei, S., Varma, A.H., and Bruenau, M. (2021), "Seismic Design Coefficients and Factors for Coupled Composite Plate Shear Walls/Concrete Filled (CC-PSW/CF)," *Engineering Structures*, Elsevier, Vol. 244, 112766. https://doi.org/10.1016/j.engstruct.2021.112766

Klemencic, R., Kraning, C., Wend, C., Englund, K., Grimmer, C., and Mills, M. (2023), "200 Park Avenue—SpeedCore 2.0 from Three Perspectives," *Structures Magazine*, ASCE.

Kurt, E.G., Seo, J., and Varma, A.H. (2022), "SC Wall-to-RC Basemat Over-Strength Connection: Behavior and Design*," Civil Engineering*, Vol. 3, No. 2, pp. 503–524. https://doi.org/10.3390/civileng3020030

Lai, Z., Varma, A.H., and Connor, R.J. (2016), "Retrofit of Built-Up Steel Columns: Modeling and Fundamental Behavior," *Journal of Bridge Engineering,* ASCE, Vol. 21, No. 3. http://dx.doi.org/10.1061/(ASCE)BE.1943–5592.0000808

Seo, J. and Varma, A.H., (2017). "Experimental Behavior and Design of Steel Plate Composite-to-Reinforced Concrete (SC-to-RC) Lap Splice Connections," *Journal of Structural Engineering*, ASCE Vol. 143, No. 5. http://dx.doi.org/10.1061/(ASCE)ST.1943–541X.0001711

Seo, J., Varma, A.H., and Zhang, K. (2019), "Pushout Behavior of SC Wall Shear Connector," *Transactions,* SMiRT-25, Charlotte, N.C., August 4–19, 10 pp., IASMIRT. https://www.lib.ncsu.edu/resolver/1840.20/37769

Seo, J., Varma, A.H., and Zhang, K. (2021), "Non-Contact Lap Splice Connections of Steel-Plate Composite Wall-to-Reinforced Concrete Structures," *Engineering Structures*, Elsevier, Vol. 246, 112954. https://doi.org/10.1016/j.engstruct.2021.112954

Shafaei, S., Varma, A., Huber, D., and Klemencic, R., (2023), "Lateral Load Behavior of C-PSW/CFs Using Steel Members as Boundary Elements," *Journal of Structural Engineering*, ASCE, Vol. 149, No. 9, 04023112. https://doi.org/10.1061/JSENDH.STENG-12085

Shafaei, S., Varma, A.H., and Klemencic, R. (2021), "Cyclic Lateral Loading Behavior of Composite Plate Shear Walls/Concrete Filled (C-PSW/CF)," *Journal of Structural Engineering*, ASCE, Vol. 147, No. 10. https://doi.org/10.1061/(ASCE)ST.1943–541X.0003091

Shafaei, S., Varma, A.H., Seo, J., Huber, D., and Klemencic, R. (2022), "Wind Design of Composite Plate Shear Walls/Concrete Filled (SpeedCore) Systems," *Engineering Journal*, AISC, Vol. 59, No. 3, pp. 183–208.

Tao, Z., Wang, Z., and Yu, Q. (2013), "Finite Element Modelling of Concrete-Filled Steel Stub Columns under Axial Compression," *Journal of Construction Steel Research,* Elsevier, Vol. 89, pp. 121–131. https://doi:10.1016/j.jcsr.2013.07.001

Traut-Todaro, J. (2019), "SpeedCore, Lateral System Innovation for Today's Construction Challenges," *Modern Steel Construction,* AISC, November.

Varma, A.H., Broberg, M., Shafaei, S., and Anvari, A. (2023), *SpeedCore Systems for Steel Structures,* Design Guide 38, AISC, Chicago, Ill.

Varma, A.H., Shafaei, S., and Sharma, S. (2024), "Wind and Seismic Behavior and Design of C-PSW/CF-to-RC Foundation or Wall Connections," Final Report (CPF Research Grant 06–16), Charles Pankow Foundation, Haymarket, Va.

Wang, N., Zhou, F., Xu, H., and Xu, Z. (2020), "Experimental Study on Steel-Plate Composite Wall-to-Foundation Connections Subjected to Combined Axial Compression and Cyclic Lateral-Force," *Engineering Structures,* Elsevier, Vol. 207, 110205. https://doi.org/10.1016/j.engstruct.2020.110205

Seismic Design and Performance of Buckling Restrained Braced Frames with Eccentric Brace Configurations Part 1: Design Procedure and Case Studies

CHAO-HSIEN LI, PAUL W. RICHARDS, BRANDT W. SAXEY, and HEIDI L. RICHARDS

ABSTRACT

Buckling-restrained braced frames (BRBFs) are a widely used lateral system comprised of beams, columns, and diagonal buckling restrained braces (BRBs). The BRBs within these frames are typically oriented concentrically. Current U.S. design provisions limit the eccentricities in BRBFs to less than the beam depth, which results in less architectural flexibility as compared to eccentrically braced frames (EBFs). The purpose of the present study is to investigate the design and performance of BRBFs with larger beam eccentricities. BRBFs were designed with beam eccentricities ranging from 0 (control case) to 2 times the beam depth in the chevron (inverted-V) and single-diagonal configurations. In each case, the beams were designed to remain elastic under the maximum forces that could be delivered by the braces, including the effects of the brace eccentricity on the beam. Nonlinear response history analysis and pushover analysis were used to quantify the performance of the various frames under design earthquake shaking and to investigate the relationship between BRBF beam eccentricity and seismic performance for the cases considered. The results of this study are presented in a two-part paper. This paper, constituting Part 1, describes the design procedures for BRBFs with eccentricity in chevron and single-diagonal configurations. Analysis methods for determining force demands in braces, beams, and columns are presented. The analysis methods are illustrated through the design of nine case study buildings. The designs show the impact that eccentricities have on member sizing and overall frame weight. For chevron BRBFs, eccentricities of 1 to 2 times the beam depth resulted in overall frame weight increase of 1.07 to 1.32 times, due to heavier beams. For single-diagonal BRBFs, eccentricities of 2 times the beam depth resulted in a slight reduction of overall weight, due to moment frame action associated with the eccentric beam stub. The accompanying paper, Part 2 (Li et al., 2026), presents the nonlinear analysis studies, including response history analyses and pushover analysis, for evaluating the seismic performance of these nine case study designs.

Keywords: buckling restrained braced frames, eccentric bracing, eccentric braced frames.

INTRODUCTION

In the late 1970s and through the 1980s, there was a focused research effort to develop a ductile braced frame for U.S. practice. Eccentrically braced frames (EBFs) were viewed as a way to combine the desirable stiffness of braced frames, with the desirable ductility and architectural flexibility of moment frames. Experimental and analytical studies at Berkeley investigated isolated EBF yielding links, subassemblies, and systems (Engelhardt and Popov, 1992; Hjelmstad and Popov, 1983; Kasai and Popov, 1986; Malley and Popov, 1984; Roeder and Popov, 1978). Provisions for EBF design were included in the original AISC *Seismic Provisions for Structural Steel Buildings* (1990) and were updated in subsequent provisions. Since 1993, SEI/ASCE 7, *Minimum Design Loads and Associated Criteria for Buildings and Other Structures*, has recognized the ductility of EBFs with a response modification factor, R, of 8 (ASCE, 1993; Hines and Jacob, 2010).

While EBFs have been in the AISC *Seismic Provisions* for three decades, they are rarely used in U.S. practice, partly because buckling restrained braced frames (BRBFs) have filled the need for highly ductile braced frames. BRBFs provide high stiffness and ductility (R = 8), solving the main problem that EBFs were developed to address, with less complicated design and detailing and lower overall cost.

However, BRBFs do not have the architectural flexibility of EBFs. AISC *Seismic Provisions* currently restrict the eccentricities that are permitted in BRBFs to be less than a beam depth (AISC, 2022a), so BRBFs can only be used in essentially concentric configurations. When

Chao-Hsien Li, Senior Research Engineer, CoreBrace, LLC, West Jordan, Utah. Email: chaohsien.li@corebrace.com

Paul W. Richards, Associate Professor, Brigham Young University, Provo, Utah. Email: paul.richards@byu.edu (corresponding)

Brandt W. Saxey, Technical Director, CoreBrace, LLC, West Jordan, Utah. Email: brandt.saxey@corebrace.com

Heidi L. Richards, Student Research Assistant, Brigham Young University, Provo, Utah. Email: lynnhi@student.byu.edu

Paper No. 2024–18R

project architecture requires eccentricity greater than a beam depth, additional columns can be added to the BRBFs to make the design compliant with current AISC *Seismic Provisions* [see Figure 1(a) for a project example], but these added columns affect the cost and architecture, making it desirable to have a better alternative.

While the current AISC *Seismic Provisions* (2022a) permit eccentricities up to a beam depth in BRBFs, they do not explicitly define the "eccentricity." Different engineers may use different measures to determine the amount of eccentricity. As illustrated in Figure 1(b), some engineers use the vertical offset—denoted as e_v—measured from the beam centerline to the brace-to-brace or brace-to-column intersection. On the other hand, some designers prefer the horizontal offset e_h measured from a brace-to-beam intersection to the adjacent column centerline or to the beam midspan point. In this paper, e_h is utilized to define the bracing eccentricity in a BRBF for the ease of deriving the design equations for force demands on beams. Additionally, defining eccentricity horizontally aligns with the approach used for EBFs, though for EBFs, the clear eccentricity represents the actual range of the yield zone. In contrast, the centerline-to-centerline eccentricity is suggested for BRBFs because it is more practical for calculating force demands in the elastic design of BRBF beams. Furthermore, as shown in Figure 1(b)-top, the horizontal bracing eccentricities (denoted as e_{hL} and e_{hR} for the e_h to left and right of the beam midspan, respectively) in a chevron (inverted-V) braced frame can be unequal between the two sides of the beam midspan. However, this research focuses on the potentially common case where the bracing eccentricities are equal at both sides of the beam midspan (i.e., $e_{hL} = e_{hR}$).

This research investigates the design and performance of BRBFs with greater eccentricities than are currently permitted. BRBFs with eccentricities are not EBFs because they are designed for different intended plastic mechanisms as illustrated in Figure 2. In a BRBF with eccentricity, the braces are designed to yield and to serve as the main structural fuses, and the other members, including the columns and all regions of beams, are intended to remain elastic. The eccentricity is accounted for when designing the BRBF beam to ensure it remains elastic. By contrast, in an EBF, the beam is designed to yield at the link portion while other components remain essentially elastic. For the chevron BRBFs with eccentricity [Figure 2(a)] investigated in this study, each beam was assumed to be a pin-ended continuous member. For the single-diagonal BRBFs with eccentricity investigated in this study, each beam was assumed to be composed of two separate members (or segments): stub and beam [Figure 2(b)]. The stub is the member accommodating the eccentricity and is rigidly connected to the adjacent column, while the beam member is a pinned beam element placed between the stub and the column away from the stub. In this eccentric BRBF configuration, the stubs and the adjacent columns constitute an elastic half moment resisting frame (half-MRF), and the half-MRF columns would partially resist the story shears when the BRBF is subjected to lateral forces.

While conventional design practice neglects the lateral stiffness of the half-MRF and assumes the braces take total story shears for conservative brace sizing, this study incorporates the half-MRF stiffness into brace sizing to achieve a more economical design. Another design issue with the single-diagonal BRBFs with eccentricities is that the columns in the half-MRF may experience higher moment demands than the columns in concentric BRBFs. For simplicity, the half-MRF columns are treated as typical BRBF columns, with seismic moment demand neglected, as permitted by the AISC *Seismic Provisions* (2022a), in the case study designs presented in this paper. The effects of seismic

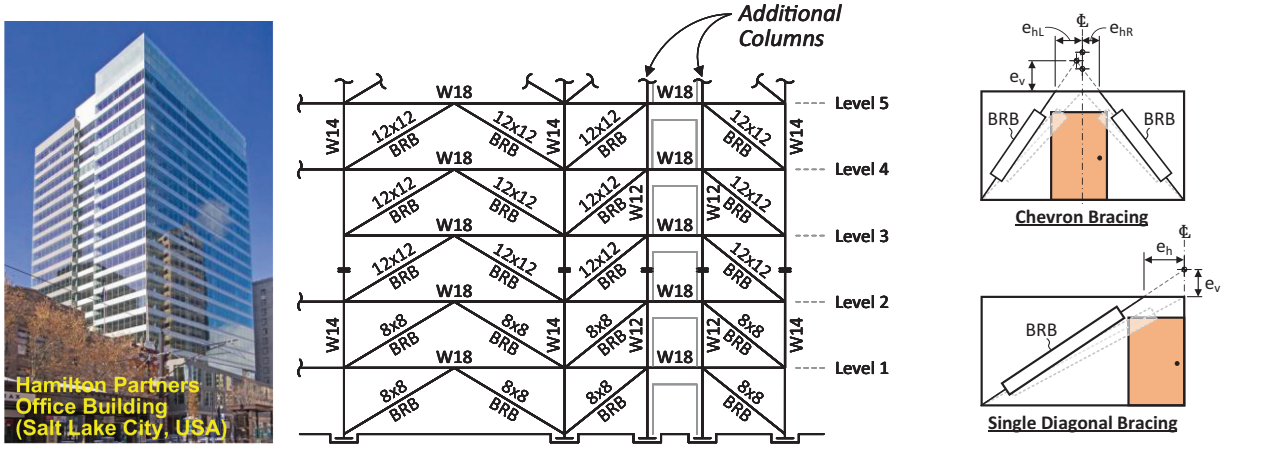

(a) Picture and elevation

(b) Bracing eccentricity definitions

Fig. 1. BRBF project where additional columns were added to address the architectural constraints.

moment demand on the design of the half-MRF columns will be discussed in the companion paper.

It is worth noting that, as shown in Figure 2, this study chooses the eccentric BRBFs with pin connections at the beam ends as the subjects to investigate because these configurations represent the least-stiff cases. In practice, these pin connections in the beams could be replaced by the moment connections, which could provide additional lateral resistance. In Figure 2(b), the nonalternating configuration is used for the single-diagonal BRBFs because this configuration can accommodate a corridor in the same location at each of the different floor levels. In addition, the nonalternating, single-diagonal bracing configuration represents a more challenging case for design of BRBF beams as the beams are subjected to higher axial forces as compared to the alternating single-diagonal BRBF. Thus, the feasibility of the nonalternating case proven by this study can be extended to the alternating case.

Prinz and Richards (2012) first proposed using BRBFs with eccentricities and investigated frames in the single-diagonal bracing configuration, comparing their design and performance with EBFs. Twelve BRBFs were designed with different story heights (three, six, and nine), two bay widths, and two strength levels. Response history analysis confirmed that frame yielding was confined to the braces. Maximum drifts were less than 2%, and residual drifts were less than 0.5% under design-level shaking. However, a comparison of frame weights indicated the BRBFs with eccentricities were 40% to 100% heavier than EBFs with comparable strength, largely due to a conservative design procedure for the BRBF columns. A subsequent economic analysis of the same frames by Vayda (2015) found that the savings in detailing and fabrication for those BRBFs with eccentricities was not sufficient to offset the higher material costs. It is noted that the previous studies assumed a conventional design approach, where braces in a BRBF are sized for total story shears. This research, however, accounts for the contribution of the half-MRF in single-diagonal BRBFs with eccentricities in resisting part of the story shear, leading to a refined evaluation of brace force demands and more economical design.

Other studies have investigated more economical BRBFs with eccentricities that had two-brace-per-bay (i.e., chevron-type) configurations. Lejano and Mas (2017) investigated BRBFs with a range of eccentricities (0.1 to 0.9 of the beam length) and a variety of brace configurations (one brace per bay, V, inverted V). The designs and pushover analyses indicated that eccentricities greater than 0.4 of the beam length required exceptionally large braces to meet drift limits. Shakib and Safi (2012) compared BRBFs with eccentricity and EBF performance from response history analysis (RHA) and identified cases (story height/ground shaking intensity) when each had the lower story drift. Hosseini and Amiri (2017) compared the collapse potential of buildings with either EBF or BRBF with eccentricity.

This study investigates the seismic design and performance of BRBFs with eccentricities and is presented in a two-part paper. This paper, constituting Part 1, first describes the design procedures for the eccentric BRBFs in chevron and single-diagonal configurations. Analysis methods for determining force demands in braces, beam, and columns are presented. Subsequently, the design considerations and results for nine case study buildings are described. The designs show the impact that eccentricities have on member sizing and overall frame weight. The accompanying paper, Part 2 (Li et al., 2026), presents the nonlinear analysis studies, including response history

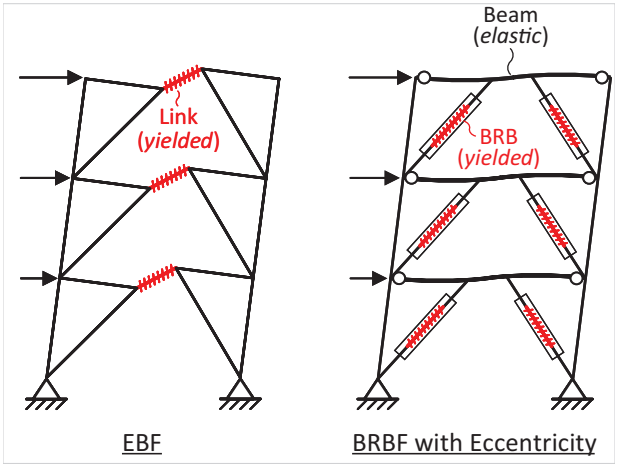

(a) Chevron bracing configuration

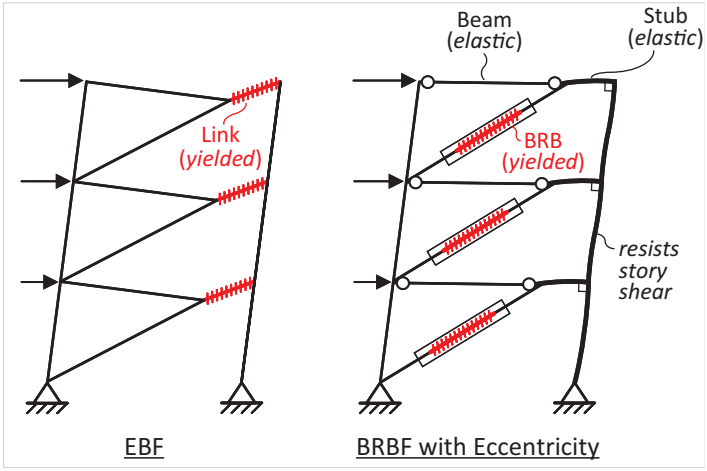

(b) Single-diagonal bracing configuration

Fig. 2. Different intended plastic mechanism for BRBFs with eccentricity as compared to EBFs.

analyses and pushover analysis, for evaluating the seismic performance of these nine case study designs and the design implications.

SEISMIC DESIGN OF ECCENTRIC BRBFS

Overview and Brace Design

The brace design procedures for BRBFs with eccentricity are the same as for concentric BRBFs. The braces are sized to remain elastic under the axial force demands resulting from the design seismic force effects, which can be determined from the equivalent lateral force (ELF) procedure or modal response spectrum analysis (MRSA) (ASCE, 2022). Additionally, the braces are checked to ensure they provide enough stiffness to satisfy drift requirements.

Figure 3 illustrates the effect of increasing brace eccentricity on elastic behavior of chevron BRBFs under lateral forces. Assuming the braces take the entire story shear in the BRBF, the brace axial force (P_{br}) increases with eccentricity because of the change in brace angle, leading to an increase in brace core area. Despite increasing brace core areas, the BRBF lateral stiffness, K_f, generally decreases with eccentricity due to the inefficiency of the braces in providing lateral stiffness resulting from the steeper angle and the larger beam flexural deflection. The trend of decreasing BRBF lateral stiffness with eccentricity implies that the brace design may be governed by drift when the eccentricity is large.

Figure 4 illustrates the effect of increasing brace eccentricity on single-diagonal BRBFs. It is noted that when the eccentricity exists, the half-MRF, composed of the stubs and the adjacent columns, resists partial story shear. As derived in Part 2 (Li et al., 2026), the fraction of story shear carried by the half-MRF column can be approximated by the ratio of the eccentricity to the BRBF span width, e/L, while the brace carries approximately $(1 - e/L)$ of the total story shear. Hence, as the eccentricity increases, the column shear, V_c, increases and the story shear taken by the braces, V_{br}, decreases, which tends to reduce the brace axial force, P_{br}. However, the steeper brace angle tends to increase P_{br}. Combined, the first effect is greater than the second, and P_{br} tends to decrease with eccentricity. Thus, the brace core area can be decreased with the brace eccentricity. Although the decreasing core area and steeper brace angle decrease the lateral stiffness provided by the brace when the eccentricity increases, the participation of the half-MRF increases with eccentricity. The analysis results in this study show that the net effect of these two actions tends to make the total frame lateral stiffness, K_f, slightly increase with the eccentricity for the single-diagonal eccentric BRBFs. It is worth noting that the effects of increasing eccentricity mentioned earlier are based on considering the contribution of the half-MRF in resisting story shear in the design of single-diagonal BRBFs, as this research explores the economy of this BRBF type. In contrast, neglecting the lateral stiffness of the half-MRF would result in a more conservative brace design, leading to an increase in brace core area with eccentricity (due to the steeper brace angle) in single-diagonal BRBFs.

Capacity Design: General

After the braces are sized using ELF or MRSA methods, the BRBF beams and columns are sized using capacity design concepts. This approach considers the maximum possible forces that could be generated in the braces and ensures that the beams and columns remain elastic under the force demands induced by these brace forces.

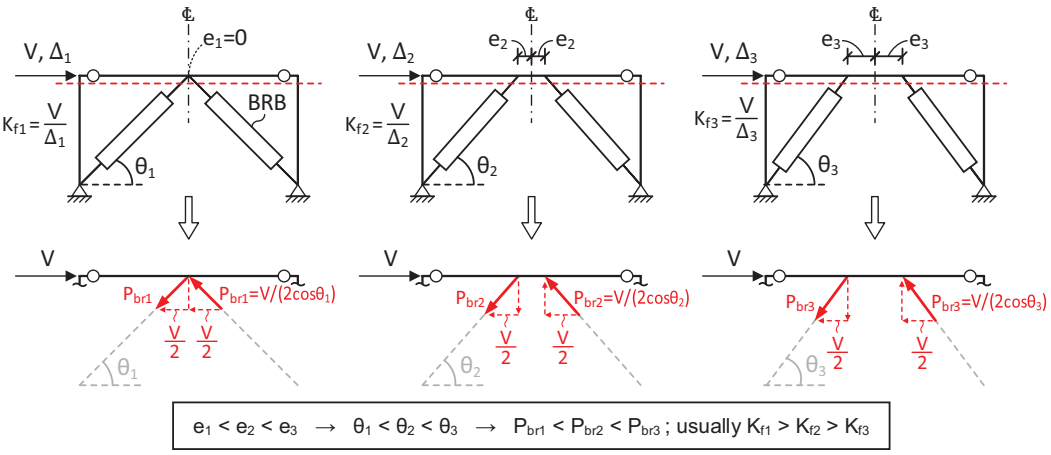

Fig. 3. Effects of increasing bracing eccentricity on elastic behavior of chevron BRBFs.

The maximum possible brace axial forces used in capacity design are estimated from the code-prescribed adjusted brace strengths (AISC, 2022a). The equations for the adjusted brace strengths in tension and compression, denoted as P_{uT} and P_{uC}, are:

$$P_{uT} = \omega F_{ysc} A_{sc} \tag{1}$$

$$P_{uC} = \omega \beta F_{ysc} A_{sc} \tag{2}$$

where ω is the strain-hardening adjustment factor and β is the compression strength adjustment factor (AISC, 2022a); A_{sc} is the area of steel core; and F_{ysc} is the actual yield stress, determined from a coupon test or estimated as $R_y F_y$, where R_y is the ratio of the expected yield stress to the specified minimum yield stress and F_y is the specified minimum yield stress.

The beam capacity design accounts for the effects induced by the adjusted brace strengths of the braces. In V and chevron (inverted-V) bracing configurations, unbalanced forces between the tensile and compressive braces affect the shear and flexural demands on the beams. For column capacity design, the cumulative effects of simultaneous yielding and development of adjusted strengths for all braces in a BRBF are considered.

Capacity Design of Beams

This section presents the determination of force demands for capacity design of beams in eccentric BRBFs. Design considerations for the chevron and single-diagonal bracing cases are discussed separately.

Chevron-Type Configurations

Figure 5 shows the determination of capacity-limited seismic effects, E_{cl}, in beams in chevron eccentric BRBFs (V configurations similar). As shown in Figure 5(b), each beam is divided into three regions for determining the force demands. Regions 1 and 3 refer to the exterior beam regions connected to columns, where Region 3 is the one attached to the column that experiences compression from the lateral forces (Figure 5). The interior portion is defined as Region 2. For clarity, Regions 1, 2, and 3 are abbreviated as R1, R2, and R3 in the subscripts of the corresponding symbols.

The chevron configuration in this paper represents BRBFs with beams that are pin connected at or near the columns. In such cases, as illustrated in Figure 5(c), the E_{cl} forces in each beam can be analyzed by using a simple beam model subjected to a pair of adjusted brace strengths, P_{uT} and P_{uC}, coming from the braces underneath the beam. The vertical components of brace forces induce the shear and moment demands in the beam [Figure 5(c)-left]. The equations for computing E_{cl} shear forces in Regions 1, 2, and 3 (designated as $V_{Ecl,R1}$, $V_{Ecl,R2}$, and $V_{Ecl,R3}$, respectively) are obtained:

$$V_{Ecl,R1} = \frac{(b+2e)P_{uT}\sin\theta - bP_{uC}\sin\theta}{2b+2e} \tag{3}$$

$$V_{Ecl,R2} = -\left(\frac{b}{2b+2e}\right)(P_{uT}\sin\theta + P_{uC}\sin\theta) \tag{4}$$

$$V_{Ecl,R3} = \frac{(b+2e)P_{uC}\sin\theta - bP_{uT}\sin\theta}{2b+2e} \tag{5}$$

where θ is the brace inclination angle measured from the horizontal, e is the horizontal eccentricity between the beam midspan and brace-to-beam intersection, and b is the span of exterior beam regions for the case where R1 and R3 are equal in length. In preliminary design, locations of

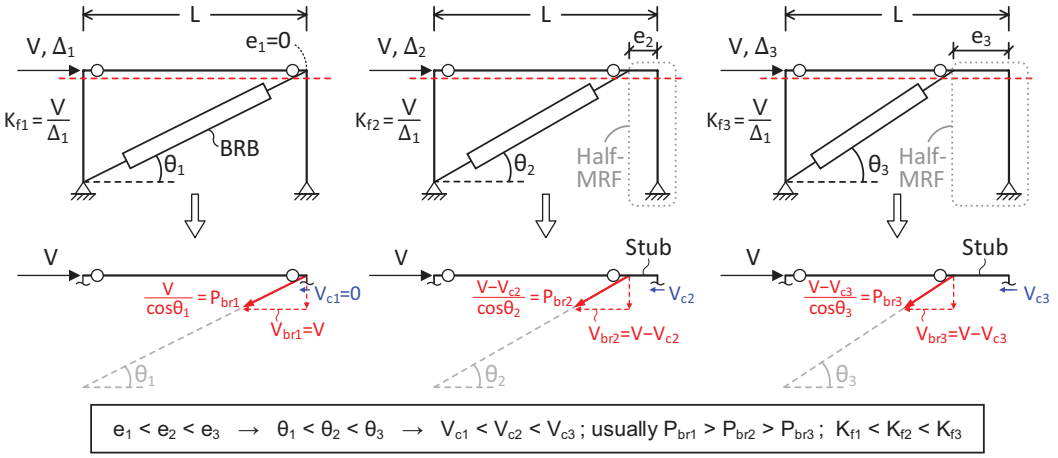

Fig. 4. Effects of increasing brace eccentricity on elastic behavior of single-diagonal BRBFs.

pin connections at the beam ends are assumed to be at the column centerline for simplicity. Note that the positive sign of a shear indicates that the shear causes clockwise rotation of beam elements. As demonstrated in the shear diagram in Figure 5(c)-left, a significant shear force is induced in the interior beam region and acts in the opposite direction to the relatively moderate shears developed in the exterior regions. Due to the imbalance of brace forces P_{uT} and P_{uC}, the shear forces in the two exterior regions are unbalanced as well, and the reactions are opposite directions from each other. Region 3 takes a higher shear than Region 1.

Figure 5(c)-left also presents the E_{cl} moment diagram in the beam. The maximum moments in the Regions 1 and 3 (designated as $M_{Ecl,R1}$ and $M_{Ecl,R3}$, respectively) can be calculated from:

$$M_{Ecl,R1} = V_{Ecl,R1} b = \frac{b(b+2e)P_{uT}\sin\theta - b^2 P_{uC}\sin\theta}{2b+2e} \quad (6)$$

$$M_{Ecl,R3} = -V_{Ecl,R3} b = -\left[\frac{b(b+2e)P_{uC}\sin\theta - b^2 P_{uT}\sin\theta}{2b+2e}\right] \quad (7)$$

As usual, the positive sign for moment indicates concavity upward. Note that the unbalanced shears between the Regions 1 and 3 cause the unbalanced moments between these two regions. Region 3 resists a higher flexural demand. Further, the moment demands $M_{Ecl,R1}$ and $M_{Ecl,R3}$ are also the end moments of the Region 2, and the large one, $M_{Ecl,R3}$, is taken as the governing moment demand for the Region 2.

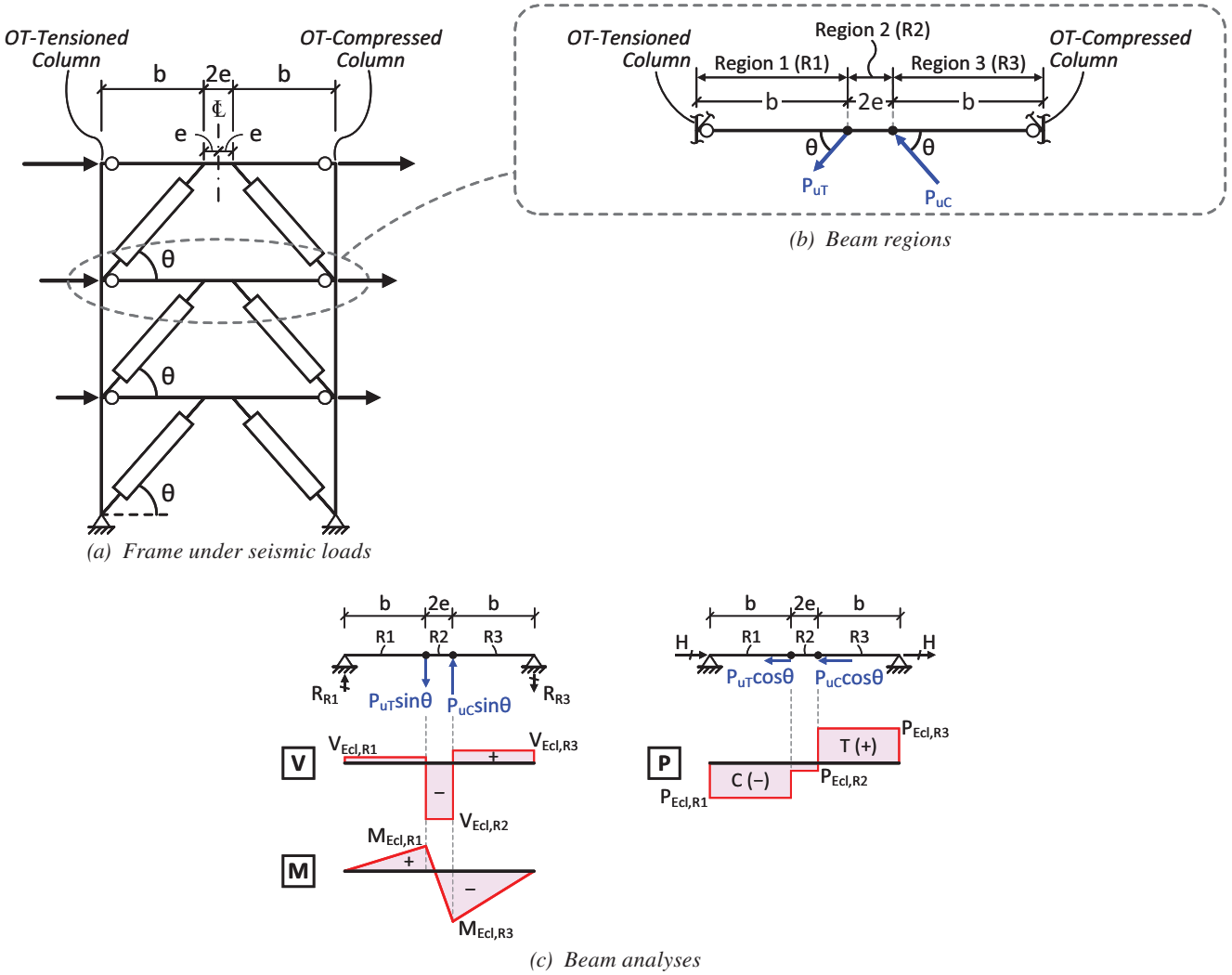

Fig. 5. Estimation of capacity-limited seismic demands in chevron eccentric BRBF beams.

These procedures capture the shear and moment in a centerline model of the beam. The local and global force issue in the concentric chevron braced frame presented in Fortney and Thornton (2017) may require additional consideration, but it is expected that local effects will be small compared to the centerline forces when the brace eccentricity exists. The adequacy of the current procedure for the case study designs can be seen in the FEM analysis presented in Part 2 (Li et al., 2026).

Figure 5(c)-right illustrates the determination of the E_{cl} axial forces. The horizontal components of the adjusted brace strengths, P_{uT} and P_{uC}, are applied on a simple beam model with horizontal reactions, representing the resultant horizontal external forces delivered to each end of the beam. The external forces include the collector force and the horizontal component of brace force coming from the upper story. In real applications, the ratio between the inertial forces delivered to two ends of the beam is dependent on the collector length and tributary seismic mass on each side of the beam. In this study, it is simply assumed that identical reactions, H, act at both ends of the beam model [Figure 5(c)-right], essentially representing the case where the tributary seismic mass to each side of the BRBF are identical. Thus, the E_{cl} axial forces in Regions 1, 2, and 3 (designated as $P_{Ecl,R1}$, $P_{Ecl,R2}$, and $P_{Ecl,R3}$, respectively) are estimated as:

$$P_{Ecl,R1} = -H = -\left(\frac{P_{uT}\cos\theta + P_{uC}\cos\theta}{2}\right) \tag{8}$$

$$P_{Ecl,R2} = H - P_{uC}\cos\theta = -\left(\frac{P_{uC}\cos\theta - P_{uT}\cos\theta}{2}\right) \tag{9}$$

$$P_{Ecl,R3} = H = \frac{P_{uT}\cos\theta + P_{uC}\cos\theta}{2} \tag{10}$$

As shown in the obtained axial force diagram [Figure 5(c)-right], the seismic effect would cause Regions 1 and 3 to resist significant compressive and tensile axial forces, respectively, while inducing relatively small compressive force in the Region 2.

As shown in Figure 6, the total force demands [Figure 6(a)] in the chevron eccentric BRBF beams come from the superposition of seismic [Figure 6(b)] and gravity [Figure 6(c)] effects. In general, the interior beam region (Region 2) is subjected to high shear and moment and moderate axial force, while the two exterior regions (Regions 1 and 3) are in significant combined axial and bending. This indicates that the design of a chevron beam may be governed by either combined axial and shear (i.e., *P-V* interaction) demands in the interior region, or combined axial and bending (i.e., *P-V* interaction) demands in the exterior regions. For the shear and moment demands, the gravity effect counteracts the seismic effect in Region 3, whereas

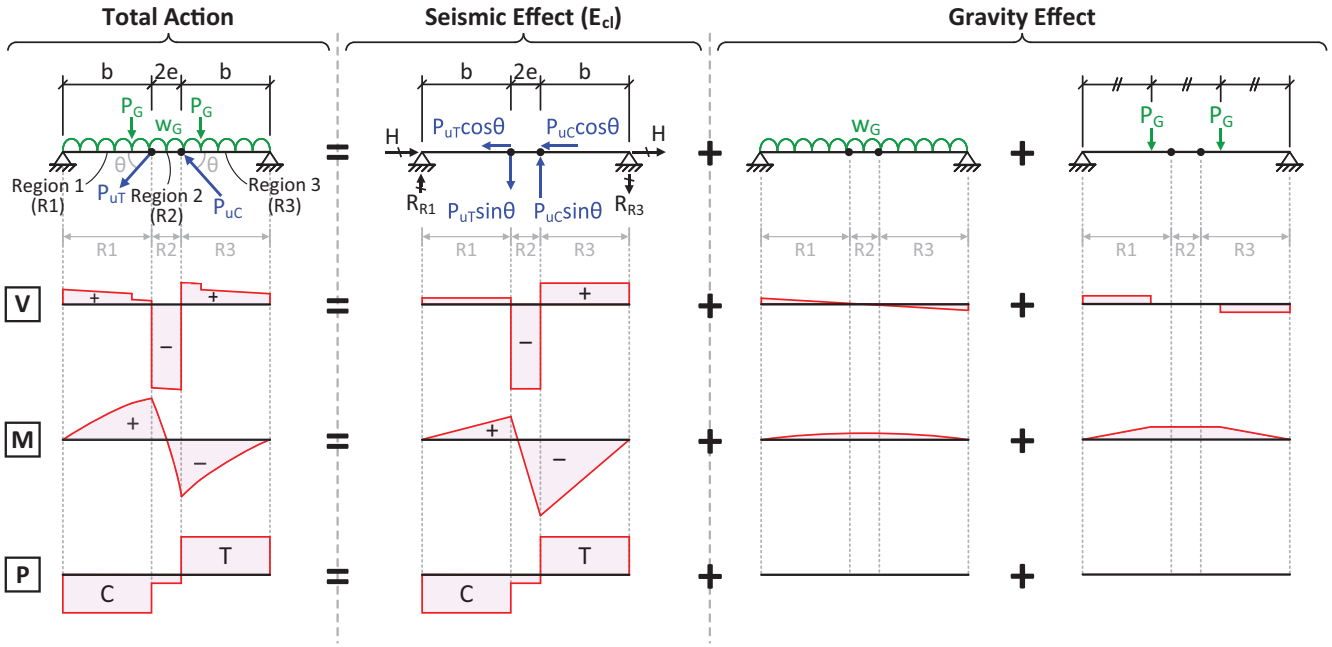

(a) Total from superposition *(b) Seismic effects* *(c) Gravity effects*

Fig. 6. Chevron eccentric BRBF beam design forces.

the two effects are additive in Region 1. As a result, the presence of gravity loads would make the seismic-induced unbalance in shear and moments between the two exterior regions less significant. Considering that seismic effects are usually much more intensive than gravity effects in typical buildings, it is expected that Region 3 generally takes higher total demands in shear and moment compared to Region 1. However, since Region 1 is subjected to compression while Region 3 is in tension, Region 1 has a lower axial capacity. It is hard to pre-judge which one of these two exterior regions represents the more critical case. As such design checks must be conducted for all three regions.

In accordance with strength design load combinations 6 and 7 from SEI/ASCE 7, Section 2.3 (ASCE, 2022), the governing total moment demand, M_u, which accounts for combined seismic and gravity effects and is used for the *P-M* interaction check for each beam region, will be the greater of the following two:

$$M_u = B_1\left[(1.2+0.2S_{DS})M_D + f_L M_L\right] + M_{Ecl} \tag{11}$$

$$M_u = B_1\left[(0.9-0.2S_{DS})M_D\right] + M_{Ecl} \tag{12}$$

where M_D and M_L are the moments due to dead load and live load, respectively. M_{Ecl} is the moment demand due to the E_{cl} effect. S_{DS} is the design spectral response acceleration parameter at short periods. The load factor for live load, f_L, defaults to 1.0 but is permitted to be reduced to 0.5 when the unreduced live load does not exceed 100 psf. B_1 is the multiplier factor, as stipulated in AISC *Specification* Appendix 8 (2022b), to account for the *P*-δ effect for the beam regions in compression (i.e., Regions 1 and 2). For Region 3, which is in tension, $B_1 = 1.0$. Similarly, the governing total shear demand, V_u, used for the *P-V* interaction check for each beam region will be the greater of the following two:

$$V_u = (1.2+0.2S_{DS})V_D + f_L V_L + V_{Ecl} \tag{13}$$

$$V_u = (0.9-0.2S_{DS})V_D + V_{Ecl} \tag{14}$$

Nonalternating Single-Diagonal Configuration

Due to the asymmetry of the braced frames in single-diagonal bracing configurations, the brace frame behavior varies with the direction of seismic forces. Two analysis cases must be considered separately in the capacity design of single-diagonal BRBFs regardless of concentric or eccentric frame. As shown in Figure 7(a), Analysis Case 1 is defined as the case where the seismic loading causes the braces to be in tension. Figure 8(a) shows Analysis Case 2, where the seismic forces cause the braces to be in compression. Figures 7(b) and 8(b) illustrate the brace forces considered for determining the E_{cl} effects on the beam in a typical floor for Analysis Cases 1 and 2, respectively. The characters *U* and *L* used in the symbols $P_{uT,U}$, $P_{uT,L}$, $P_{uC,U}$, and $P_{uC,L}$ represent the brace forces with adjusted strength (P_{uT} or P_{uC}) coming from the upper and lower stories of the beam, respectively. For the beam at the top level of a BRBF, there is no brace force ($P_{uT,U}$ or $P_{uC,U}$) coming from the upper story, and similarly at the lowest level of a BRBF (at the base plate), there is no brace force ($P_{uT,L}$ or $P_{uC,L}$) coming from the lower story.

Figures 7(c) and 8(c) illustrate the beam analyses and resulting beam actions for Analysis Cases 1 and 2, respectively. Note each BRBF beam is composed of two members: stub and beam. A beam model having one end simply supported and the other end fixed is used. An inner hinge is placed in the beam model to represent the pin connection between the beam and stub. In the preliminary design, the hinge can simply be set at the brace-to-beam intersection point. Likewise, the beam member length *b* can be taken as the distance measured from the column centerline to the brace-to-beam intersection point.

For Analysis Case 1 [Figure 7(c)-left], the vertical component of tensile brace force from the lower-story subjects the cantilever beam-like stub member to negative bending, while the beam member (beyond the stub) does not resist any shear and moment due to the seismic effect. The seismic shear and moment at the stub's fixed end, denoted as $V_{Ecl1,Stub}$ and $M_{Ecl1,Stub}$, respectively, can be estimated as:

$$V_{Ecl1,Stub} = -P_{uT,L}\sin\theta \tag{15}$$

$$M_{Ecl1,Stub} = -e\left(P_{uT,L}\sin\theta\right) \tag{16}$$

Note that the subscript *Ecl*1 represents the capacity-limited seismic effect, E_{cl}, in Analysis Case 1. As shown in Figure 7(c)-right, to analyze the seismic axial demand in the beams in single-diagonal BRBFs, the horizontal components of the braces forces coming from both upper and lower stories are considered. For simplicity, an identical reaction force, *H*, is assumed at both ends of the beam model to represent the case that the collector forces delivered to each side of the beam are identical. The E_{cl} axial forces induced in stub and beam (denoted as $P_{Ecl1,Stub}$ and $P_{Ecl1,Beam}$, respectively) can be estimated as:

$$P_{Ecl1,Stub} = \frac{(P_{uT,L}\cos\theta - P_{uT,U}\cos\theta)}{2} \tag{17}$$

$$P_{Ecl1,Beam} = -\frac{(P_{uT,L}\cos\theta + P_{uT,U}\cos\theta)}{2} \tag{18}$$

For Analysis Case 2 [Figure 8(c)], brace forces are compressive, subjecting the stub to positive bending and moderate compressive force, while significant tensile force is induced in the beam member. The equations for estimating the critical member forces in the beam are as follows:

$$V_{Ecl2,Stub} = P_{uC,L} \sin\theta \tag{19}$$

$$M_{Ecl2,Stub} = e(P_{uC,L} \sin\theta) \tag{20}$$

$$P_{Ecl2,Stub} = -\frac{(P_{uC,L} \cos\theta - P_{uC,U} \cos\theta)}{2} \tag{21}$$

$$P_{Ecl2,Beam} = \frac{(P_{uC,L} \cos\theta + P_{uC,U} \cos\theta)}{2} \tag{22}$$

where the subscript *Ecl*2 used in the symbols represents the E_{cl} effects in Analysis Case 2.

Figures 9 and 10 illustrate the superposition of the seismic and gravity effects on the beams in single-diagonal eccentric BRBFs for Analysis Cases 1 and 2, respectively. As shown in the diagrams of the total force demands [Figures 9(a) and 10(a)], in general, the stub is subjected to high shear and moment demands alongside moderate axial load, while the beam member resists significant axial load accompanied with relatively low flexural demand. For a complete design, both stub and beam need to be checked with *P-V* and *P-M* interaction demands developed in Analysis Cases 1 and 2. The general equations for computing the total moment demand (Eqs. 11 and 12) and total shear demands (Eqs. 13 and 14) are applied to both beam and stub members. Note that the beam member is in compression in Analysis Case 1 while resisting tensile force in Analysis Case 2. The flexural demand in the beam member, which is due to the gravity effect only, remains the same in both scenarios. Thus, the design of the beam member would be generally governed by the *P-M* interaction demands in Analysis Case 1.

On the other hand, it is hard to prejudge which analysis case would govern the design of stub. In Analysis Case 1,

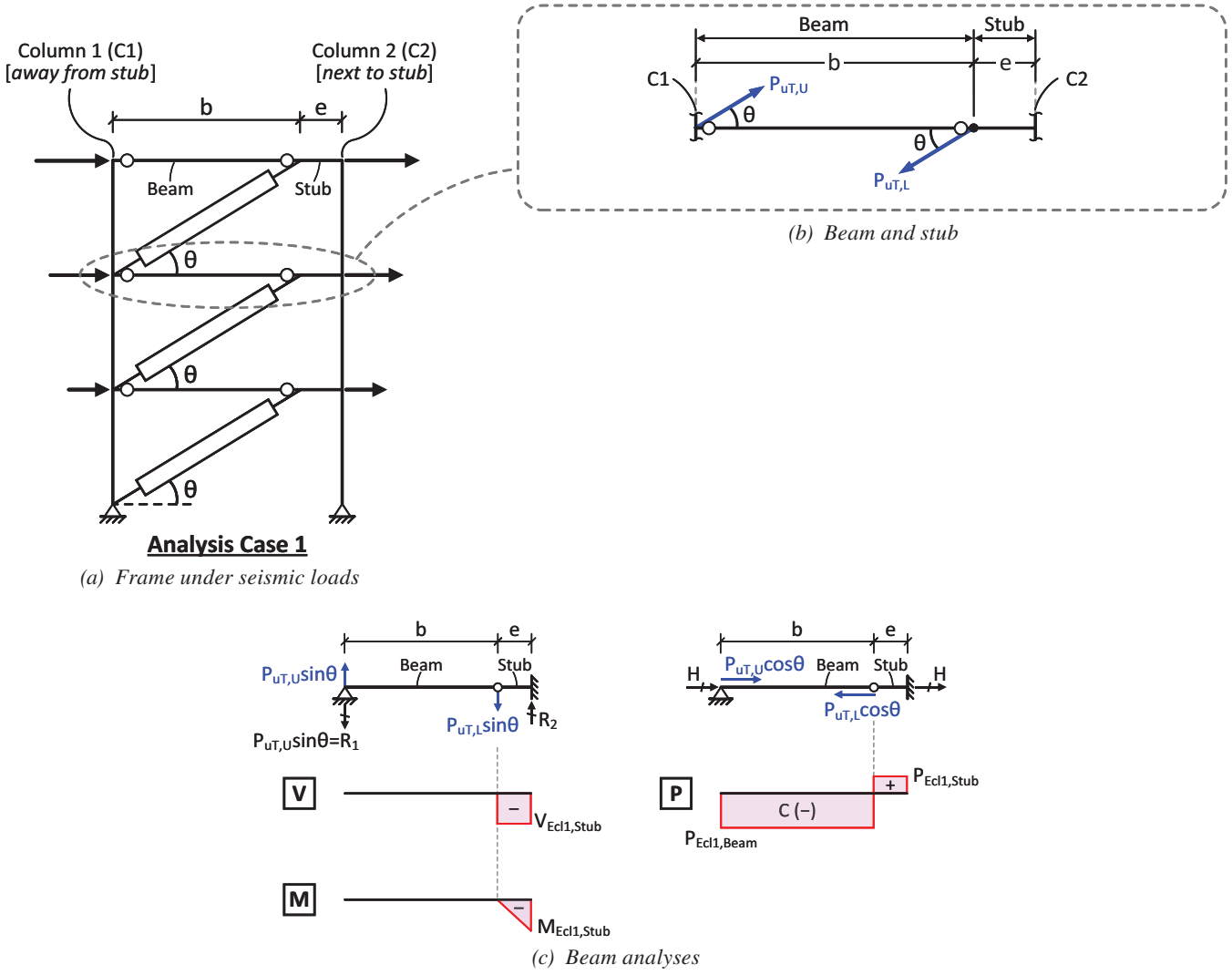

(a) *Frame under seismic loads*

(b) *Beam and stub*

(c) *Beam analyses*

Fig. 7. Estimation of capacity-limited seismic demands on beams in single-diagonal eccentric BRBFs in Analysis Case 1.

the seismic [Figure 9(b)] and gravity [Figure 9(c)] effects are additive for both shear and moment demands in the stub, whereas these two effects in Analysis Case 2 [Figures 10(b) and 10(c)] counteract with each other. Thus, the magnitudes of the total shear and moment demands induced in the stub in Analysis Case 1 [Figure 9(a)] would be higher than those developed in Analysis Case 2 [Figure 10(a)]. However, the stub is in tension in Analysis Case 1, but in compression in Analysis Case 2. Design checks for the stub must be conducted for both analysis cases.

Capacity Design of Columns

This section presents the determination of force demands for column capacity design in eccentric BRBFs. Design considerations for the chevron and single-diagonal bracing cases are discussed separately.

Chevron-Type Configurations

Figure 11 shows the determination of column axial forces due to the E_{cl} effect for chevron eccentric BRBFs. To estimate the maximum possible axial forces that can be developed in the columns, as shown in Figure 11(a), the plastic mechanism in which all the braces in a multistory braced frame simultaneously yield and develop their adjusted strengths (P_{uT} or P_{uC}) is considered. The resulting column axial forces can be obtained by taking the free-body diagrams [Figure 11(b)] for each side of columns in the braced frame with all the vertical forces, coming from the brace forces and beam end shears, applied on the columns. The sizing of the columns is governed by the axial demand in the overturning (OT)-compressed columns (i.e., the compressed columns under the OT action of the frame) because the seismic and gravity effects are additive. The general

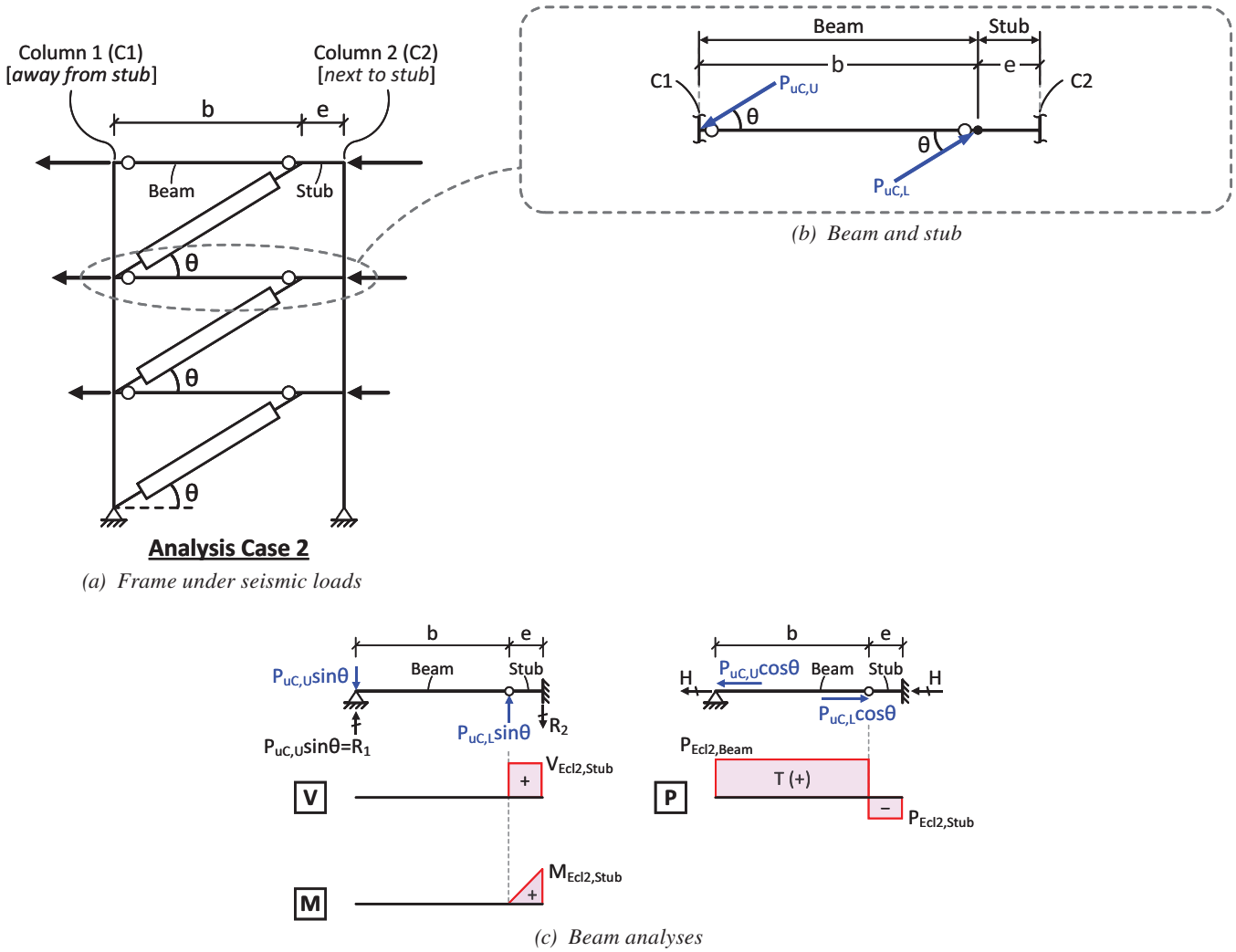

(a) *Frame under seismic loads*

(b) *Beam and stub*

(c) *Beam analyses*

Fig. 8. Estimation of capacity-limited seismic demands on beams in single-diagonal eccentric BRBFs in Analysis Case 2.

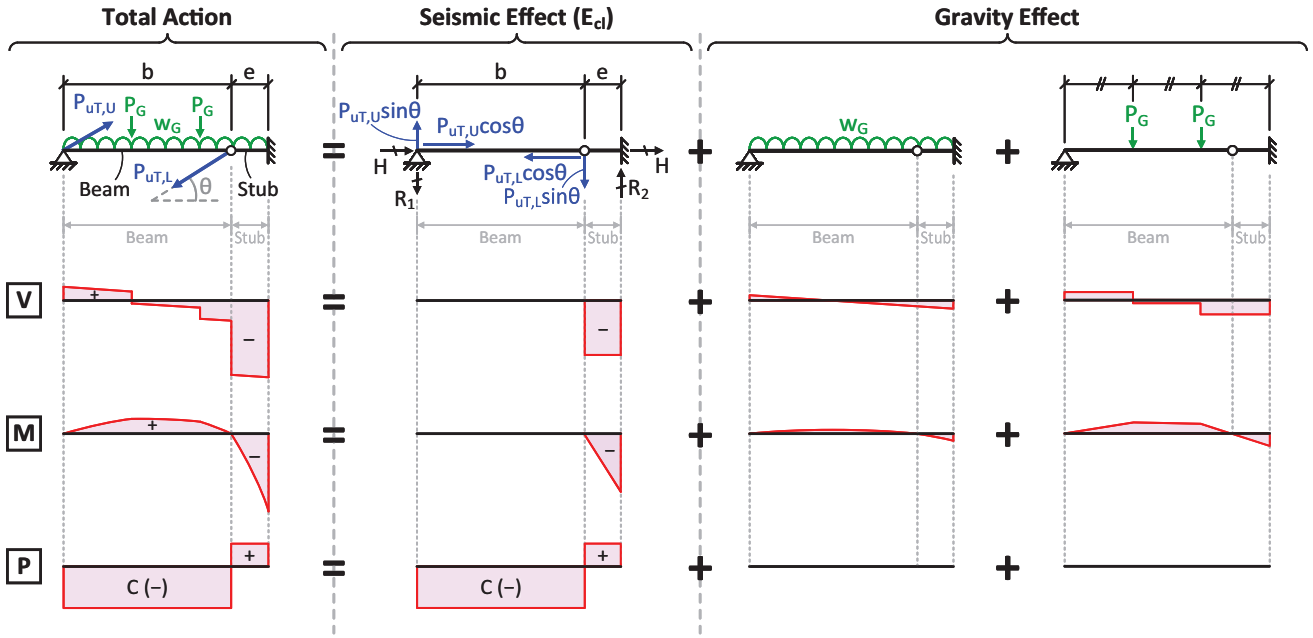

(a) Total from superposition (b) Seismic effects (c) Gravity effects

Fig. 9. Single-diagonal eccentric BRBF beam design forces in Analysis Case 1.

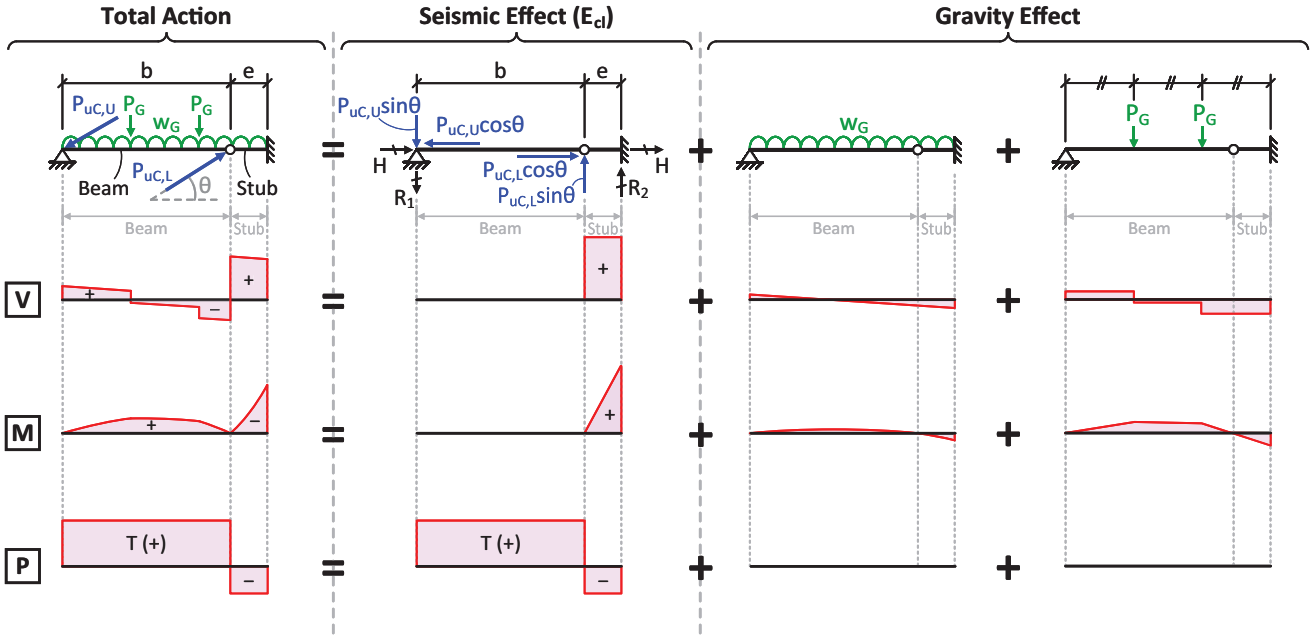

(a) Total from superposition (b) Seismic effects (c) Gravity effects

Fig. 10. Single-diagonal eccentric BRBF beam design forces in Analysis Case 2.

equation for computing the E_{cl} compressive force in the nth-story column, $P_{Ecl,C,n}$, of a N-story chevron eccentric BRBF is:

$$P_{Ecl,C,n} = \sum_{i=n+1}^{N} (P_{uC} \sin\theta)_i - \sum_{i=n}^{N} V_{Ecl,R3,i} \quad (23)$$

where $(P_{uC}\sin\theta)_i = P_{uC,i} \sin\theta_i$ estimates the vertical component of brace force from the ith story; $P_{uC,i}$ and θ_i are the compressive adjusted strength and inclination angle, respectively, for the ith-story braces; and $V_{Ecl,R3,i}$ is the shear in the beam Region 3 (R3) at the ith level, which is computed from Equation 5.

Finally, the total compressive axial force demand P_u, which accounts for the combined gravity and seismic effects is computed from:

$$P_u = (1.2 + 0.2S_{DS})P_D + f_L P_L + P_{Ecl} \quad (24)$$

where P_D and P_L are the axial force due to dead load and live load, respectively.

Nonalternating Single-Diagonal Configuration

Due to the asymmetry of single-diagonal BRBFs, regardless of whether the braces are concentrically or eccentrically oriented, the maximum seismic demands in the two sides of columns are different. In addition, two analysis cases must be considered in column design as shown in Figures 12(a) and 13(a). For discussion purposes, as shown in Figure 12(a), Column 1 is away from the stub, whereas Column 2 is near the stub (connected to it).

For column design, Figure 12(a) shows the considered plastic mechanism for Analysis Case 1, in which all the braces are assumed to yield and develop their tensile adjusted strength, P_{uT}. In this case, C1 members are OT-tensioned (i.e., tensioned under the overturning action of the frame), while C2 members are OT-compressed. By contrast, Figure 13(a) shows the case under Analysis Case 2 loading, where all the braces are assumed to reach the compressive adjusted strength, P_{uC}, and Columns 1 and 2 are OT-compressed and OT-tensioned, respectively. Figures 12(b) and 13(b) illustrate the analyses of the E_{cl} axial forces in the columns for Analysis Cases 1 and 2, respectively. Note that the member sizing of each side of columns is governed by the analysis case where that side of column is OT-compressed because the seismic and gravity effects are additive in producing compressive column forces.

The design of Column 1 is governed by Analysis Case 2 [Figure 13(b)], and the general equation for the E_{cl} compressive force in the nth-story C1 member, $P_{Ecl2,C1,n}$, of a N-story single-diagonal BRBF is:

$$P_{Ecl2,C1,n} = \sum_{i=n+1}^{N} (P_{uC} \sin\theta)_i \quad (25)$$

On the other hand, the design of Column 2 is governed by Analysis Case 1 [Figure 12(b)], and the general equation for the E_{cl} compressive force in the nth-story C2 member, $P_{Ecl1,C2,n}$ is:

$$P_{Ecl1,C2,n} = \sum_{i=n}^{N} \left|V_{Ecl1,Stub,i}\right| = \sum_{i=n}^{N} (P_{uT} \sin\theta)_i \quad (26)$$

where $V_{Ecl1,Stub,i}$ is the shear in the stub at the ith level under Analysis Case 1. Its magnitude (absolute value) equals to the vertical component of brace force in the ith story, $(P_{uT}\sin\theta)_i = P_{uT,i}\sin\theta_i$ where $P_{uT,i}$ is the tensile adjusted strength of ith-story braces.

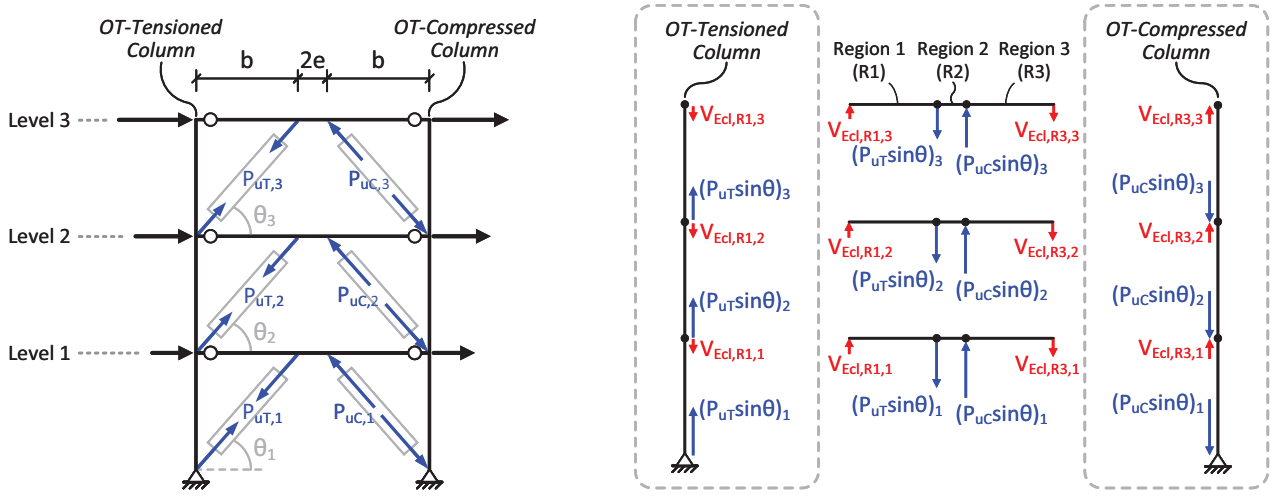

(a) *Frame under seismic loads* (b) *Force diagrams for analysis*

Fig. 11. Estimation of capacity-limited seismic column axial forces in chevron eccentric BRBFs.

By comparing the governing force diagram for determining seismic axial forces in C1 [Figure 13(b)-left] and that for C2 [Figure 12(b)-left], it can be found that, in any story, the C2 member resists one more vertical brace force above that story than the C1 member. This is reflected in the equation for $P_{Ecl1,C2,n}$ (Equation 26) which has a summation starting from the nth story, while the equation for $P_{Ecl2,C1,n}$ (Equation 25) is a summation starting from the $(n + 1)$th story. As a result, the C2 members resist higher seismic axial demand than C1 members. Hence, the two sides of columns in a nonalternating, single-diagonal BRBF may be sized separately to pursue an economical design. Finally, the total compressive axial force, P_u, for sizing the columns is determined per Equation 24, considering the combined gravity and seismic effects.

Furthermore, as shown in Figures 12(b) and 13(b), the stubs would deliver bending moments to the adjacent C2 members because the stubs are moment connected to the C2 members in a single-diagonal BRBF. This moment demand can be significant, especially with large eccentricity. Although the AISC *Seismic Provisions* (2016a) permits neglecting seismic-induced moments in conventional BRBF column design, it is unclear if this relaxation is proper for the single-diagonal BRBFs with eccentricities. For simplicity, the C2 members in the design cases presented later in this Part 1 paper were sized based on axial force demand

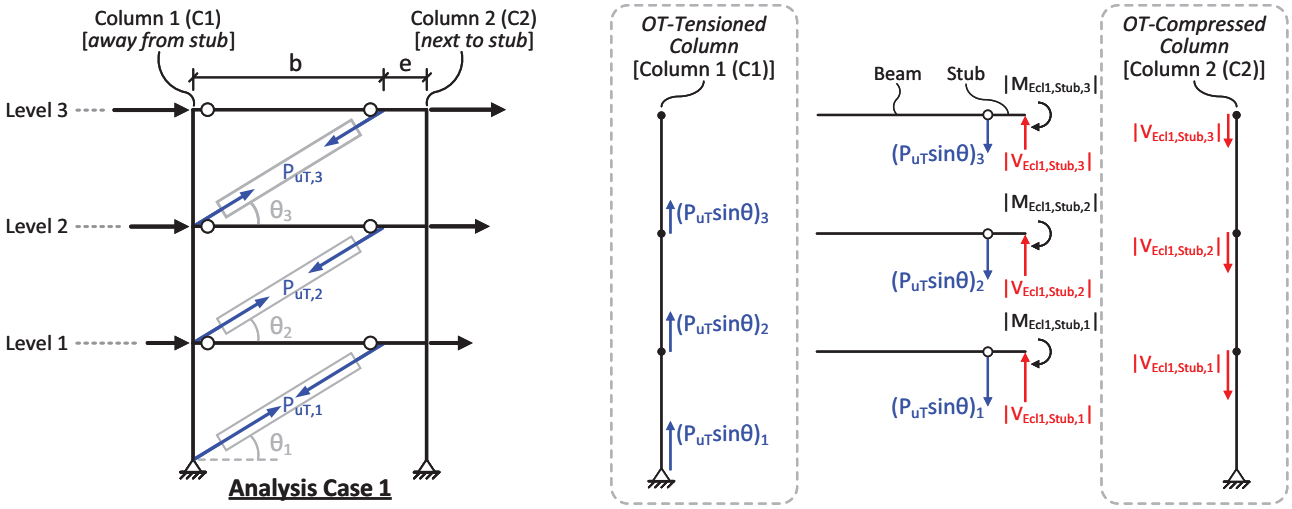

(a) *Frame under seismic loads* (b) *Force diagrams for analysis*

Fig. 12. Estimation of capacity-limited seismic column axial forces in single-diagonal eccentric BRBFs in Analysis Case 1.

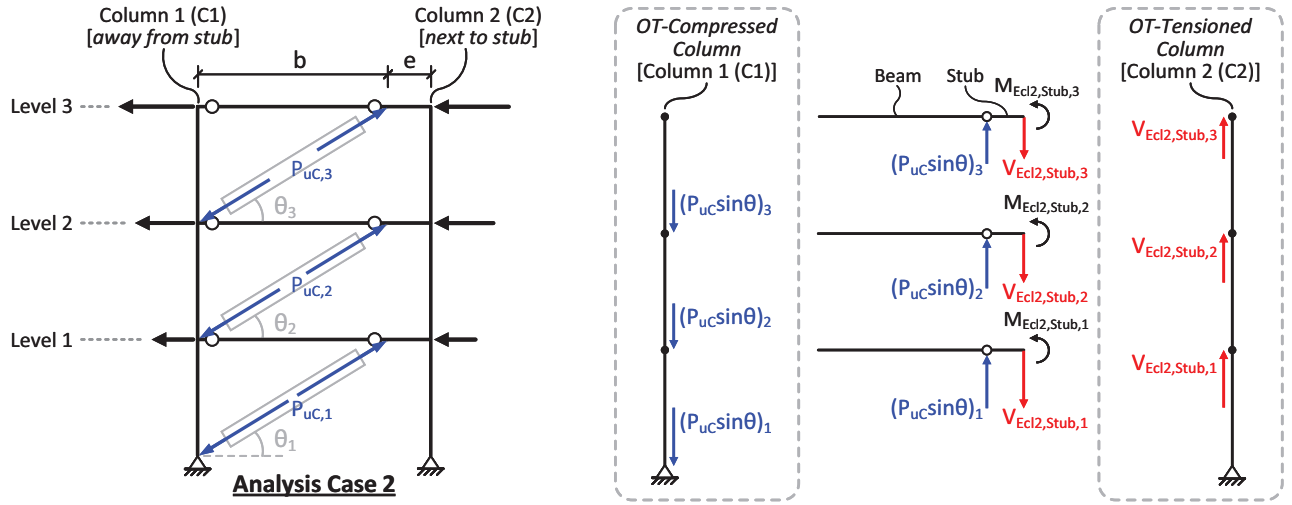

(a) *Frame under seismic loads* (b) *Force diagrams for analysis*

Fig. 13. Estimation of capacity-limited seismic column axial forces in single-diagonal eccentric BRBFs in Analysis Case 2.

only, without considering seismic moment demands and with sufficiency verified by the analytical study presented in Part 2 (Li et al., 2026). Further discussion on the performance of BRBFs with C2 members sized with and without consideration of seismic moment demand is also presented in Part 2.

CASE STUDY DESIGNS

Example Buildings Description

Nine BRBF designs representing two building heights (12- and 3-story), two bracing configurations (chevron and single-diagonal), and various eccentricities were developed to investigate the impact of eccentricity on BRBF weight and performance. The buildings were adapted from NIST GCR 10-917-8 (2010). Figures 14(a) and 14(b) show the floor plans for the 12- and 3-story buildings, respectively. The single-bay perimeter BRBF in the longitudinal direction of each building was used for the study, and Figure 15 shows the frame elevations of the nine designs. The designs comply with the 2016 editions of SEI/ASCE 7 (2016), the AISC *Seismic Provisions* (2016a), and the AISC *Specification* (2016b), which were in effect during this study. The buildings were designed for a site with seismic design spectral parameters S_{DS} = 1.0g and S_{D1} = 0.6g and using an importance factor I_e = 1.0 and a deflection amplification factor C_d = 5. The redundancy factor ρ = 1.0 was used, as permitted by SEI/ASCE 7-16 based on the floor plans considered, to avoid oversizing. The buildings, per the NIST report, had a roof dead load of 67 psf, floor dead load of 85 psf, roof live load of 20 psf, and floor live load of 50 psf. The curtain wall weight on the building perimeter was 15 psf.

Based on the number of stories and bracing configurations, as shown in Figure 15, the design cases were divided into four groups: 12S-CH, 12S-SD, 3S-CH, and 3S-SD. The prefixes 12S and 3S mean 12-story and 3-story, respectively, while the suffixes CH and SD represent the chevron and single-diagonal bracing configurations in the BRBFs. In each group, there is one design case with a concentric configuration (Case C) and another design case with braces oriented at an eccentricity, e, equal to 2 times the nominal beam depth (Case E2d). For all design cases, the nominal beam depth (d_b = 21 in.) of W21 beams was used to determine the eccentricity. The E2d cases in each group represent BRBFs with a brace eccentricity that exceeds the code-permitted upper limit (AISC, 2016a). Moreover, in Group 12S-CH, an additional case E1d with e equal to 1 times nominal beam depth was developed. For discussion purposes, each design case is named as its group name added with a suffix representing the eccentricity situation. For example, Design 12S-CH-C represents 12-story chevron BRBFs with concentric braces, while Design 3S-SD-E2d means 3-story single-diagonal BRBFs with e of 2 times beam depth.

Design Considerations and Results

Brace Design

The overall frame design results are summarized in Table 1. For brace design, three-dimensional frame models representing the example buildings with various design cases of BRBFs were developed in the structural analysis software ETABS (CSI, 2019). Each ETABS model was analyzed for both equivalent lateral force (ELF) and the modal response spectrum analysis (MRSA) to estimate the brace design

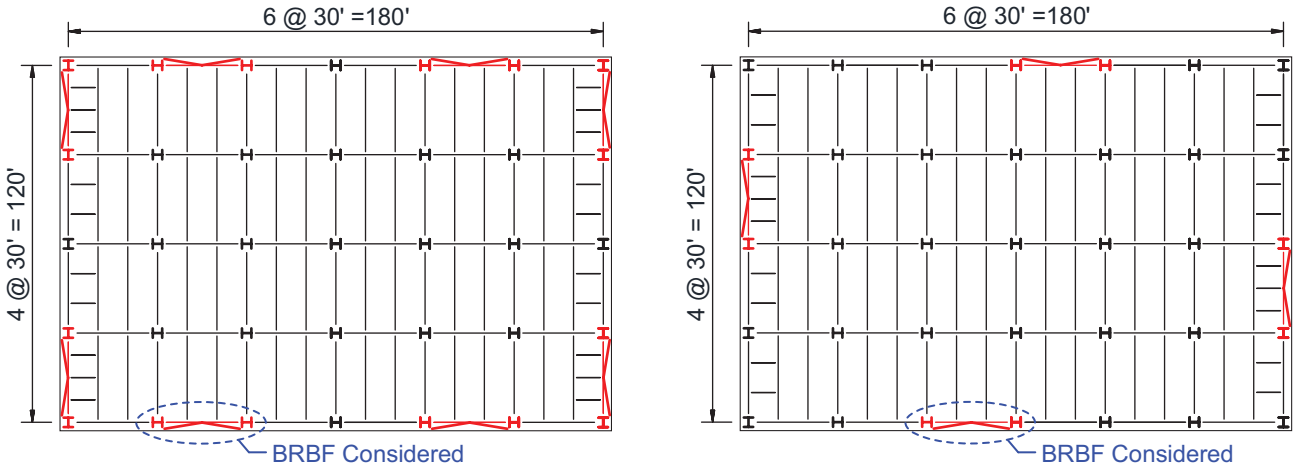

(a) 12-story design cases *(b) 3-story design cases*

Fig. 14. Floor plans for case study designs.

forces and story drifts. For most of the design cases considered in this study, the MRSA led to a more economical brace design than the ELF method did. Thus, the brace sizes determined from the MRSA are employed for all the design cases with an attempt to pursue the most economical code-permitted BRBF design.

The brace core areas, A_{sc}, rounded up to the nearest 0.5 in.^{2} precision, were sized based on the minimum yield stress of steel core, $F_{ysc,\min}$, of 38 ksi and a strength reduction factor $\phi = 0.9$. Tables 2 and 3 summarize the brace design results alongside the axial demand-to-capacity ratios (DCRs). The DCR for axial force is given by $DCR_P = P_u/(\phi A_{sc} F_{ysc,\min})$. These values are based on the brace force demand, P_u, estimated from the MRSA. The table also presents the design earthquake (DE) story-drift ratios (SDRs), SDR_{DE}, which were determined by amplifying the story drift ratios obtained from MRSA by a factor of (C_d/I_e). As shown in both Tables 2 and 3, all the DCR_P values are less than 1 and most of them are higher than 0.85, indicating an economical design of the braces. All the

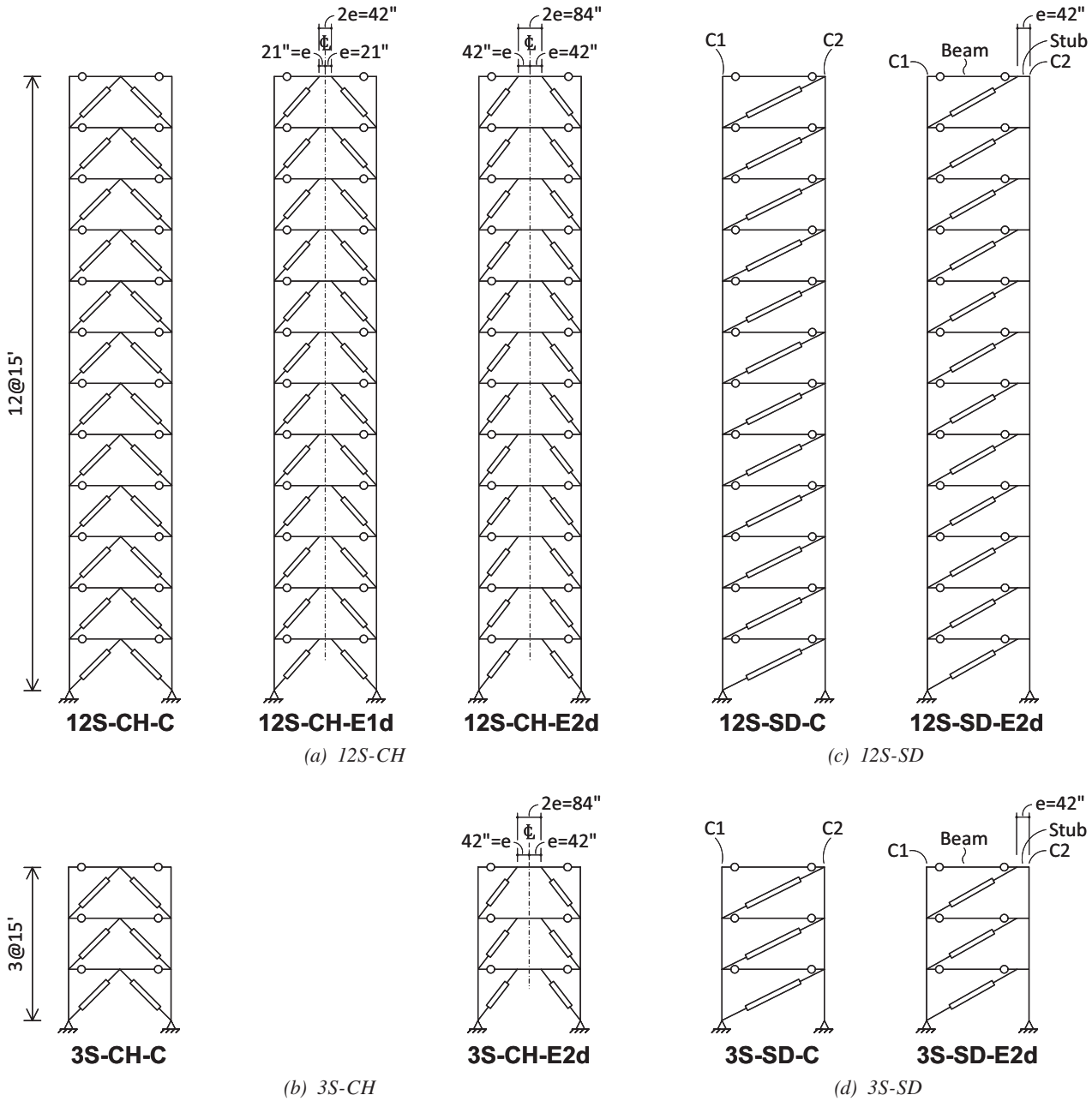

(a) 12S-CH

(c) 12S-SD

(b) 3S-CH

(d) 3S-SD

Fig. 15. Elevations for BRBF designs.

Table 1. Member Sizes for 3- and 12-Story Frames

Member	3-Story (3S) BRBF Design Cases				Member	12-Story (12S) Design Cases				
	CH-C	CH-E2d	SD-C	SD-E2d		CH-C	CH-E1d	CH-E2d	SD-C	SD-E2d
BRB3	3.0	3.5	4.5	3.5	BRB12	1.5	1.5	2.0	2.5	2.0
BRB2	5.0	6.0	8.0	7.0	BRB11	2.5	2.5	3.0	4.0	3.5
BRB1	6.0	7.0	10.0	9.0	BRB10	2.5	3.0	3.5	4.5	4.0
Bm3	W21×44	W21×68	W21×44	W21×44	BRB9	3.0	3.5	4.0	5.0	4.5
Bm1-Bm2	W21×57	W21×132	W21×83	W21×68	BRB8	3.0	3.5	4.0	5.5	5.0
Stub3	—*	—*	—*	W21×55	BRB7	3.5	4.0	4.5	6.0	5.5
Stub1-Stub2	—*	—*	—*	W21×111	BRB6	3.5	4.0	4.5	6.5	6.0
RC1-RC3†	W14×68	W14×74	W12×79	W14×109	BRB5	4.0	4.5	5.0	7.0	6.5
LC1-LC3†	—‡	—‡	W14×68	W14×61	BRB4	4.5	4.5	5.0	7.5	7.0
					BRB3	5.0	5.0	5.5	8.0	7.5
					BRB2	5.5	5.5	6.0	8.5	8.0
					BRB1	5.5	6.0	6.5	9.0	8.5
					Bm9-Bm12	W21×44	W21×62	W21×83	W21×55	W21×55
					Bm5-Bm8	W21×44	W21×68	W21×101	W21×68	W21×62
					Bm1-Bm4	W21×50	W21×83	W21×122	W21×73	W21×68
					Stub9-Stub12	—*	—*	—*	—*	W21×68
					Stub5-Stub8	—*	—*	—*	—*	W21×93
					Stub1-Stub4	—*	—*	—*	—*	W21×111
					RC11-RC12†	W14×43	W14×38	W14×34	W14×43	W14×48
					RC9-RC10†	W14×68	W14×68	W14×68	W14×82	W14×82
					RC7-RC8†	W14×109	W14×109	W14×109	W14×109	W14×120
					RC5-RC6†	W14×132	W14×132	W14×145	W14×145	W14×159
					RC3-RC4†	W14×176	W14×176	W14×193	W14×193	W14×211
					RC1-RC2†	W14×233	W14×233	W14×233	W14×257	W14×257
					LC1-LC12†	—‡	—‡	—‡	—§	W14×38
					LC9-LC10†	—‡	—‡	—‡	—§	W14×68
					LC7-LC8†	—‡	—‡	—‡	—§	W14×109
					LC5-LC6†	—‡	—‡	—‡	—§	W14×145
					LC3-LC4†	—‡	—‡	—‡	—§	W14×193
					LC1-LC2†	—‡	—‡	—‡	—§	W14×257

* Stubs are not used

† In single-diagonal BRBFs, the left column (LC) and right column (RC) represent Column 1 (C1) and Column 2 (C2), respectively.

‡ The same shape is used for RC and LC as the force demands in both sides of columns are identical in chevron BRBFs.

§ The demands in LC (C1) and RC (C2) are different, but the same shape is used for both sides as the demand difference is not large.

SDR_{DE} ratios are lower than the code-allowable limit of 2%, and most of them are less than 2% by a considerable margin, reflecting the fact that the brace design is governed by strength for majority of the braces in these design cases.

From the variations in A_{sc} and SDR_{DE} values among the design cases in each chevron BRBF Group [Groups 12S-CH (Table 2) or 3S-CH (Table 3)], it can be found that, in the chevron BRBFs, both brace sizes and story drifts increase with the eccentricity. As the eccentricity increases, the brace inclination angle gets steeper, which makes the braces less efficient in providing the lateral stiffness and resistance to the frame. It is noted that the design of the braces in the top three stories of Design 12S-CH-E2d is governed by story-drift check rather than strength design.

Table 2. BRB Axial DCRs (DCR_P) and Design Story-Drift Ratios (SDR_{DE}) for 12-Story BRBFs

Story	Group 12S-CH (12-Story Chevron BRBFs)								
	12S-CH-C			12S-CH-E1d			12S-CH-E2d		
	BRB		SDR_{DE}	BRB		SDR_{DE}	BRB		SDR_{DE}
	A_{sc} (in.^{2})	DCR_P	(%)	A_{sc} (in.^{2})	DCR_P	(%)	A_{sc} (in.^{2})	DCR_P	(%)
12	1.5	0.84	1.53	1.5	0.92	1.64	2.0*	0.75	1.67
11	2.5	0.83	1.63	2.5	0.89	1.78	3.0*	0.81	1.85
10	2.5	0.98	1.73	3.0	0.89	1.81	3.5*	0.84	1.93
9	3.0	0.91	1.62	3.5	0.86	1.74	4.0	0.83	1.88
8	3.0	0.95	1.58	3.5	0.91	1.70	4.0	0.91	1.82
7	3.5	0.91	1.44	4.0	0.89	1.56	4.5	0.89	1.74
6	3.5	0.95	1.35	4.0	0.94	1.48	4.5	0.94	1.70
5	4.0	0.94	1.17	4.5	0.92	1.36	5.0	0.92	1.58
4	4.5	0.91	1.04	4.5	0.98	1.25	5.0	0.99	1.46
3	5.0	0.90	0.90	5.0	0.98	1.11	5.5	0.98	1.33
2	5.5	0.91	0.77	5.5	0.96	0.99	6.0	0.97	1.22
1	5.5	0.97	0.71	6.0	0.96	0.87	6.5	0.97	1.12

Story	Group 12S-SD (12-Story Single-Diagonal BRBFs)					
	12S-SD-C			12S-SD-E2d		
	BRB		SDR_{DE}	BRB		SDR_{DE}
	A_{sc} (in.^{2})	DCR_P	(%)	A_{sc} (in.^{2})	DCR_P	(%)
12	2.5	0.82	1.85	2.0	0.85	1.84
11	4.0	0.83	1.87	3.5	0.86	1.89
10	4.5	0.88	1.92	4.0	0.88	1.85
9	5.0	0.87	1.87	4.5	0.87	1.80
8	5.5	0.86	1.77	5.0	0.85	1.68
7	6.0	0.85	1.64	5.5	0.84	1.56
6	6.5	0.85	1.52	6.0	0.83	1.42
5	7.0	0.85	1.39	6.5	0.83	1.30
4	7.5	0.87	1.26	7.0	0.84	1.17
3	8.0	0.90	1.14	7.5	0.86	1.06
2	8.5	0.93	1.03	8.0	0.89	0.94
1	9.0	0.93	0.98	8.5	0.95	0.94

* Sizing of BRBs is governed by story drift check: $SDR_{DE} \leq 2\%$

On the other hand, the tabulated A_{sc} and SDR_{DE} values in the single-diagonal BRBF groups [i.e., Groups 12S-SD (Table 2) and 3S-SD (Table 3)] show that both brace sizes and story drifts generally get reduced when the eccentricity is introduced in the single-diagonal BRBFs. This is attributed to the fact that the moment connections between the stubs and Column 2 (C2) members make the C2 members resist moments as well as shears under the seismic loading. Hence, in the single-diagonal eccentric BRBFs, the C2 members participate in providing the lateral-force-resisting stiffness and strength, leading to less force demands in the braces. Further, the design cases in this study show that, for the single-diagonal BRBFs, the BRBF with eccentricity tend to have higher lateral stiffness than the concentric BRBF.

Table 3. BRB Axial DCRs (DCR_P) and Design Story-Drift Ratios (SDR_{DE}) for 3-Story BRBFs												
Story	Group 3S-CH (3-Story Chevron BRBFs)						Group 3S-SD (3-Story Single-Diagonal BRBFs)					
	3S-CH-C			3S-CH-E2d			3S-SD-C			3S-SD-E2d		
	BRB		SDR_{DE}	BRB		SDR_{DE}	BRB		SDR_{DE}	BRB		SDR_{DE}
	A_{sc} (in.^{2})	DCR_P	(%)	A_{sc} (in.^{2})	DCR_P	(%)	A_{sc} (in.^{2})	DCR_P	(%)	A_{sc} (in.^{2})	DCR_P	(%)
3	3.0	0.89	0.92	3.5	0.88	1.06	4.5	0.92	1.07	3.5	0.95	1.02
2	5.0	0.93	0.88	6.0	0.94	1.00	8.0	0.92	1.00	7.0	0.93	0.92
1	6.0	0.98	0.77	7.0	0.97	0.97	10.0	0.92	0.94	9.0	0.97	1.02

Table 4. BRB Properties for 12-Story Chevron BRBFs																		
Story	12S-CH-C						12S-CH-E1d						12S-CH-E2d					
	A_{sc} (in.^{2})	L_{ysc} (in.)	ε_{BRB} (in./in.)	KF	ω	ωβ	A_{sc} (in.^{2})	L_{ysc} (in.)	ε_{BRB} (in./in.)	KF	ω	ωβ	A_{sc} (in.^{2})	L_{ysc} (in.)	ε_{BRB} (in./in.)	KF	ω	ωβ
12	1.5	130	0.0197	1.58	1.37	1.59	1.5	119	0.0202	1.61	1.38	1.60	2.0	148	0.0150	1.38	1.29	1.44
11	2.5	171	0.0150	1.33	1.29	1.44	2.5	159	0.0151	1.35	1.30	1.46	3.0	146	0.0151	1.36	1.30	1.46
10	2.5	171	0.0150	1.33	1.29	1.44	3.0	157	0.0152	1.35	1.30	1.46	3.5	144	0.0153	1.37	1.30	1.46
9	3.0	170	0.0151	1.33	1.30	1.46	3.5	156	0.0154	1.35	1.30	1.47	4.0	137	0.0162	1.44	1.32	1.49
8	3.0	170	0.0151	1.33	1.30	1.46	3.5	156	0.0154	1.35	1.30	1.47	4.0	137	0.0162	1.44	1.32	1.49
7	3.5	168	0.0152	1.34	1.30	1.46	4.0	148	0.0162	1.42	1.32	1.49	4.5	138	0.0160	1.41	1.31	1.48
6	3.5	168	0.0152	1.34	1.30	1.46	4.0	148	0.0162	1.42	1.32	1.49	4.5	138	0.0160	1.41	1.31	1.48
5	4.0	161	0.0159	1.40	1.31	1.48	4.5	150	0.0160	1.38	1.31	1.48	5.0	137	0.0161	1.42	1.31	1.48
4	4.5	163	0.0157	1.37	1.31	1.48	4.5	150	0.0160	1.39	1.31	1.48	5.0	137	0.0161	1.42	1.31	1.48
3	5.0	162	0.0157	1.37	1.31	1.48	5.0	149	0.0161	1.40	1.31	1.48	5.5	134	0.0165	1.46	1.32	1.49
2	5.5	159	0.0160	1.40	1.31	1.48	5.5	146	0.0163	1.43	1.32	1.49	6.0	129	0.0171	1.49	1.33	1.52
1	5.5	163	0.0157	1.38	1.31	1.48	6.0	143	0.0167	1.45	1.33	1.50	6.5	128	0.0172	1.50	1.33	1.52

Table 5. BRB Properties for 12-Story Single-Diagonal BRBFs												
Story	12S-SD-C						12S-SD-E2d					
	A_{sc} (in.^{2})	L_{ysc} (in.)	ε_{BRB} (in./in.)	KF	ω	ωβ	A_{sc} (in.^{2})	L_{ysc} (in.)	ε_{BRB} (in./in.)	KF	ω	ωβ
12	2.5	291	0.0111	1.28	1.23	1.35	2.0	260	0.0121	1.30	1.23	1.35
11	4.0	281	0.0115	1.32	1.23	1.35	3.5	257	0.0122	1.29	1.24	1.36
10	4.5	282	0.0114	1.29	1.23	1.35	4.0	250	0.0126	1.34	1.25	1.39
9	5.0	282	0.0114	1.30	1.23	1.35	4.5	251	0.0125	1.31	1.24	1.38
8	5.5	279	0.0116	1.32	1.23	1.35	5.0	250	0.0125	1.32	1.24	1.38
7	6.0	274	0.0118	1.34	1.23	1.35	5.5	247	0.0127	1.34	1.25	1.39
6	6.5	273	0.0118	1.34	1.23	1.35	6.0	243	0.0129	1.36	1.25	1.39
5	7.0	271	0.0119	1.34	1.23	1.35	6.5	242	0.0130	1.36	1.25	1.39
4	7.5	270	0.0119	1.34	1.23	1.35	7.0	240	0.0131	1.36	1.26	1.40
3	8.0	263	0.0123	1.37	1.24	1.36	7.5	239	0.0131	1.36	1.26	1.40
2	8.5	262	0.0123	1.37	1.24	1.36	8.0	232	0.0135	1.39	1.27	1.41
1	9.0	283	0.0114	1.29	1.23	1.35	8.5	249	0.0126	1.31	1.25	1.39

Table 6. BRB Properties for 3-Story Chevron BRBFs												
Story	3S-CH-C						3S-CH-E2d					
	A_{sc} (in.^{2})	L_{ysc} (in.)	ε_{BRB} (in./in.)	KF	ω	ωβ	A_{sc} (in.^{2})	L_{ysc} (in.)	ε_{BRB} (in./in.)	KF	ω	ωβ
3	3.0	169	0.0151	1.34	1.30	1.46	3.5	144	0.0153	1.37	1.30	1.46
2	5.0	161	0.0159	1.38	1.31	1.48	6.0	131	0.0169	1.48	1.33	1.52
1	6.0	159	0.0160	1.40	1.31	1.48	7.0	125	0.0177	1.50	1.34	1.53

Table 7. BRB Properties for 3-Story Single-Diagonal BRBFs												
Story	3S-SD-C						3S-SD-E2d					
	A_{sc} (in.^{2})	L_{ysc} (in.)	ε_{BRB} (in./in.)	KF	ω	ωβ	A_{sc} (in.^{2})	L_{ysc} (in.)	ε_{BRB} (in./in.)	KF	ω	ωβ
3	4.5	282	0.0114	1.30	1.23	1.35	3.5	258	0.0121	1.29	1.24	1.36
2	8.0	262	0.0123	1.37	1.24	1.36	7.0	241	0.0130	1.35	1.25	1.39
1	10.0	279	0.0116	1.31	1.23	1.35	9.0	250	0.0125	1.31	1.24	1.38

Capacity Design

The BRB design parameters, including the stiffness modification factor (KF) and strength adjustment factors, ω and β, are listed in Tables 4 through 7. These tabulated ω and β values are based on the tabulated core strain, ε_{BRB}, which is corresponding to an assumed 2% controlling story drift, the minimum allowed by the AISC *Seismic Provisions* (2016a) for calculating the expected BRB deformations. The BRBF beams and columns were assumed to be ASTM A992 (2022) steel W-shape members and sized for the capacity design considering the adjusted brace strengths in tension and compression, P_{uT} and P_{uC}. These strengths were computed using Equations 1 and 2, with the maximum yield stress, $F_{ysc,\max}$ = 46 ksi as an estimate of the actual yield stress of steel core, F_{ysc}, and the values of ω and β factors tabulated in Tables 4 through 7. Detailed descriptions of capacity designs for beams and columns follow.

Beam Design

Beam sizing in this study is based on two main criteria: capacity design and sectional compactness satisfying moderately ductile requirements, with the former governing all the cases. As shown in Figures 6, 9, and 10, the capacity design of BRBF beams considers the force demands from the superposition of gravity and capacity-limited seismic effects. For BRBFs with eccentricities, the beam at each floor is divided into multiple regions or members by the brace-to-beam intersection points, such as the three beam regions in the chevron bracing case and the stub and beam members in the single-diagonal bracing case. Each beam region or member must be checked to remain essentially elastic for both *P-M* and *P-V* interaction demands.

The DCR for the *P-M* interaction, DCR_{PM}, is calculated in accordance with AISC *Specification* Chapter H (2016b) as follows:

$$DCR_{PM} = \begin{cases} \left|\frac{P_u}{\phi P_n}\right| + \frac{8}{9}\left|\frac{M_u}{\phi_b M_n}\right|, \ for \left|\frac{P_u}{\phi P_n}\right| \geq 0.2 \\ \frac{1}{2}\left|\frac{P_u}{\phi P_n}\right| + \left|\frac{M_u}{\phi_b M_n}\right|, \ for \left|\frac{P_u}{\phi P_n}\right| < 0.2 \end{cases} \quad (28)$$

where the design axial strength, ϕP_n, is taken as the tensile yielding strength, $\phi_t P_y$, if the axial demand, P_u, is in tension, while the compressive strength $\phi_c P_n$ is used when P_u is compressive. Also, $\phi_b M_n$ is the design flexural strength. Note that for the BRBF beams, the compressive strength, $\phi_c P_n$, was determined considering several possible buckling modes, including strong-axis flexural buckling, torsional buckling, and constrained-axis torsional buckling (Timoshenko and Gere, 1961).

To quantify the DCR for the *P-V* interaction in the BRBF beams, DCR_{PV}, the formula for determining the shear strength of the shear-yielding links in the EBF stipulated in the AISC *Seismic Provisions* is adopted herein. DCR_{PV} is computed from:

$$DCR_{PV} = \frac{V_u}{\phi_v V_p^*} \quad (29)$$

where ϕ_v = 0.9 and V_p^* is the reduced plastic shear strength of W-shape member considering the presence of axial force demand P_u. The equation for V_p^* is as follows:

Table 8. Beam Design DCRs for 12-Story BRBFs									
Level	Group 12S-CH (12-Story Chevron BRBFs)								
	12S-CH-C			12S-CH-E1d			12S-CH-E2d		
	Beam			Beam			Beam		
	Shape	DCR		Shape	DCR		Shape	DCR	
		P-M	*Chev**		*P-M*	*P-V*		*P-M*	*P-V*
12	W21×44	0.51	0.33	W21×62	0.46	0.32	W21×83	0.56	0.28
11		0.85	0.51		0.73	0.49		0.83	0.43
10		0.85	0.51		0.82	0.59		0.91	0.50
9		0.85	0.62		0.87	0.69		0.99	0.58
8	W21×44	0.85	0.62	W21×68	0.78	0.65	W21×101	0.76	0.59
7		0.85	0.72		0.85	0.75		0.82	0.66
6		0.85	0.72		0.85	0.75		0.82	0.66
5		0.85	0.76		0.90	0.84		0.88	0.73
4	W21×50	0.74	0.78	W21×83	0.73	0.70	W21×122	0.72	0.61
3		0.74	0.87		0.78	0.78		0.78	0.68
2		0.80	0.96		0.83	0.86		0.87	0.75
1		0.80	0.95		0.88	0.95		0.96	0.81
Level	Group 12S-SD (12-Story Single-Diagonal BRBFs)								
	12S-SD-C			12S-SD-E2d					
	Beam			Beam			Stub		
	Shape	DCR		Shape	DCR		Shape	DCR	
		P-M	*P-V*		*P-M*	*P-V*		*P-M*	*P-V*
12	W21×55	0.43	0.09	W21×55	0.37	0.10	W21×68	0.47	0.33
11		0.82	0.13		0.69	0.15		0.76	0.56
10		0.94	0.14		0.80	0.15		0.84	0.62
9		0.99	0.14		0.85	0.15		0.91	0.68
8	W21×68	0.80	0.12	W21×62	0.77	0.14	W21×93	0.72	0.55
7		0.84	0.12		0.82	0.14		0.79	0.60
6		0.88	0.12		0.87	0.14		0.85	0.65
5		0.92	0.12		0.91	0.14		0.91	0.69
4	W21×73	0.88	0.12	W21×68	0.85	0.13	W21×111	0.77	0.78
3		0.92	0.12		0.90	0.13		0.82	0.83
2		0.96	0.12		0.94	0.14		0.87	0.89
1		1.00	0.12		0.98	0.14		0.91	0.92
* Design for chevron effect (Sabelli and Arber, 2017)									

$$V_p^* = \begin{cases} 0.6F_yA_{lw} & , for \left|\frac{P_u}{P_y}\right| \le 0.15 \\ 0.6F_yA_{lw}\sqrt{1-(P_u/P_y)^2} & , for \left|\frac{P_u}{P_y}\right| > 0.15 \end{cases} \quad (30)$$

where $A_{lw} = (d - 2t_f)t_w$ estimates the shear area of beam web considering the clear distance between the flanges and $P_y = F_yA_g$ is the nominal axial yielding strength of the gross beam section.

Tables 8 and 9 summarize the beam design results, including the selected W-shapes and the calculated DCRs (DCR_{PM} and DCR_{PV}) for all design cases. For the 12-story design cases (Table 8), identical beam sections were

Table 9. Beam Design DCRs for 3-Story BRBFs															
Level	Group 3S-CH (3-Story Chevron BRBFs)						Group 3S-SD (3-Story Single-Diagonal BRBFs)								
	3S-CH-C			3S-CH-E2d			3S-SD-C			3S-SD-E2d					
	Beam			Beam			Beam			Beam			Stub		
	Shape	DCR		Shape	DCR		Shape	DCR		Shape	DCR		Shape	DCR	
		P-M	*Chev**		*P-M*	*P-V*		*P-M*	*P-V*		*P-M*	*P-V*		*P-M*	*P-V*
3	W21×44	0.57	0.62	W21×68	0.99	0.59	W21×44	0.81	0.10	W21×44	0.65	0.11	W21×55	0.94	0.60
2	W21×57	0.63	0.73	W21×132	0.80	0.69	W21×83	0.71	0.10	W21×68	0.73	0.13	W21×111	0.79	0.78
1	W21×57	0.75	0.83	W21×132	0.97	0.81	W21×83	0.89	0.10	W21×68	0.95	0.14	W21×111	0.96	0.96
* Design for chevron effect (Sabelli and Arber, 2017)															

selected for every four floors. For 3-story cases (Table 9), different beam sections were used between the roof level and the other two floors. For the beams in chevron eccentric BRBFs, the governing (i.e., maximum) DCR_{PV} values occur in the interior segment, while the governing DCR_{PM} values come from the exterior segments. For the chevron BRBFs with eccentricity at one beam depth (CH-E1d cases), DCR_{PV} is higher than DCR_{PM} only in the bottom two stories of 12S-CH-E1d and in the first story of 3S-CH-E1d, whereas DCR_{PM} is greater than DCR_{PV} in all remaining stories of the two frames. When the eccentricity increases to twice beam depth (CH-E2d cases), DCR_{PM} is higher than DCR_{PV} over the entire building height in both 12S-CH-E2d and 3S-CH-E2d. It seems to suggest that, in multistory eccentrically chevron BRBFs, the design of the beams at intermediate through upper floors tend to be governed by the *P-M* interaction, whereas the beam design may be governed the *P-V* interaction at lower floors, where the brace forces acting on the beams are higher. Further, as the eccentricity increases, the beam design would lean more toward being governed by the *P-M* interaction.

For the concentrically chevron BRBFs (12S-CH-C and 3S-CH-C), the shear strength check for the beams was based on the design method proposed by Sabelli and Arber (2017) that considers the chevron effect, inducing the localized force demands in a beam within the in-span gusset plate region. The associated DCR, DCR_{Chev}, is defined as the ratio of the minimum required gusset plate length to the actual gusset plate length provided. A value of DCR_{Chev} less than 1.0 means that the original section of a beam is strong enough to handle the local force demand with no need for strengthening the beam web with doubler plates. For Case 12S-CH-C (see Table 8), the beam design is governed by the chevron effect, as evidenced by the fact $DCR_{Chev} > DCR_{PM}$, in the bottom four levels, while the design of remaining beams is governed by *P-M* interaction. In 3S-CH-C (Table 9), the chevron effect governs the design for all the beams. Moreover, by comparing the beam sizes among the design cases in each chevron BRBF group [Groups 12S-CH (Table 8) or 3S-CH (Table 9)], it is apparent that the beam sizes are increased with the bracing eccentricity in the chevron BRBFs.

For both concentrical and eccentric single-diagonal BRBFs, it is apparent from Tables 8 and 9 that DCR_{PM} values are much higher than DCR_{PV} values for the beam members, indicating that the design of these pinned-end beam members is governed by the *P-M* interaction, where the moment demand is due to the gravity effects only. By comparing the concentric and eccentric cases, it can be seen that the sizes of the pinned beam members could be slightly reduced as the bracing eccentricity is introduced to single-diagonal BRBFs. This is primarily due to the shorter beam lengths and smaller horizontal brace forces (due to the smaller braces and steeper brace angle) in the eccentric bracing configuration. In the single-diagonal BRBFs with eccentricity [12S-SD-E2d (Table 8) and 3S-SD-E2d (Table 9)], the sizes of the stubs are notably larger than the pinned beams because of the high seismic shear and moment demands in the stubs. The stub design is governed by *P-V* interaction for the bottom floors in 12S-SD-E2d, while *P-M* interaction governs the design for the stubs at the remaining floors. Although the design of all the stubs in 3S-SD-E2d is governed by *P-M* interaction, the DCR values for the *P-V* interaction are also very high for stubs at the bottom two floors. These seem to suggest that the stub design in the lower floors have a higher chance to be governed by the *P-V* interaction.

Column Design

The column sizing is based on capacity design and compactness requirements for moderately ductile members. As permitted by the AISC *Seismic Provisions* (2016a), the capacity design of BRBF columns for the all design cases presented in this Part 1 paper considered the axial force demand (P_u) only, where P_u was calculated by superimposing gravity effects with capacity-limited seismic effects (as illustrated in Figures 11–13), assuming all braces simultaneously develop their adjusted strength in compression or

Table 10. Column Compressive Axial DCR (DCR_P) for 12-Story BRBFs

Story	12S-CH-C		12S-CH-E1d		12S-CH-E2d		12S-SD-C				12S-SD-E2d			
	Column		Column		Column		Column 1 (C1)		Column 2 (C2)		Column 1 (C1)		Column 2 (C2)	
	Shape	DCR_P	Shape	DCR_P	Shape	DCR_P	Shape	DCR_P	Shape	DCR_P	Shape	DCR_P	Shape	DCR_P
12	W14×43	0.16	W14×38	0.20	W14×34	0.14	W14×43	0.18	W14×43	0.39	W14×38	0.26	W14×48	0.33
11	W14×43	0.66	W14×38	0.92	W14×34	0.97	W14×43	0.67	W14×43	0.99	W14×38	0.97	W14××48	0.86
10	W14×68	0.62	W14×68	0.57	W14×68	0.56	W14×82	0.52	W14×82	0.65	W14×68	0.59	W14×82	0.65
9	W14×68	0.92	W14×68	0.89	W14×68	0.89	W14×82	0.79	W14×82	0.92	W14×68	0.92	W14×82	0.93
8	W14×109*	0.63	W14×109*	0.63	W14×109*	0.64	W14×109*	0.65	W14×109	0.73	W14×109*	0.63	W14×120	0.67
7	W14×109*	0.80	W14×109*	0.81	W14×109*	0.82	W14×109*	0.84	W14×109	0.92	W14×109*	0.82	W14×120	0.84
6	W14×132	0.82	W14×132	0.83	W14×145	0.75	W14××145	0.76	W14×145	0.82	W14×145	0.75	W14×159	0.76
5	W14×132	0.97	W14×132	1.00	W14×145	0.90	W14×145	0.92	W14×145	0.97	W14×145	0.91	W14×159	0.91
4	W14×176	0.84	W14×176	0.86	W14×193	0.80	W14×193	0.81	W14×193	0.85	W14×193	0.80	W14×211	0.79
3	W14×176	0.98	W14×176	0.99	W14×193	0.91	W14×193	0.94	W14×193	0.97	W14×193	0.93	W14×211	0.91
2	W14×233	0.85	W14×233	0.85	W14×233	0.86	W14×257	0.80	W14×257	0.82	W14×257	0.80	W14×257	0.85
1	W14×233	0.97	W14×233	0.96	W14×233	0.97	W14×257	0.91	W14×257	0.93	W14×257	0.91	W14×257	0.96

* Column design is governed by sectional compactness requirement of moderately ductile members

Table 11. Column Compressive Axial DCR (DCR_P) for 3-Story BRBFs

Story	3S-CH-C		3S-CH-E2d		3S-SD-C				3S-SD-E2d			
	Column		Column		Column 1 (C1)		Column 2 (C2)		Column 1 (C1)		Column 2 (C2)	
	Shape	DCR_P	Shape	DCR_P	Shape	DCR_P	Shape	DCR_P	Shape	DCR_P	Shape	DCR_P
12	W14×68	0.07	W14×74	0.06	W14×68	0.08	W12×79	0.20	W14×61	0.09	W14×109*	0.13
11	W14×68	0.40	W14×74	0.42	W14×68	0.41	W12×79	0.55	W14×61	0.42	W14×109*	0.35
10	W14×68	0.90	W14×74	0.99	W14×68	0.90	W12×79	0.95	W14×61	0.96	W14×109*	0.62

* Column design is governed by sectional compactness requirement of moderately ductile members

tension. Moderately ductile member requirements, rather than highly ductile ones, were applied to the columns in the case study BRBFs to achieve a more efficient design and enable clearer observation of eccentricity effects on column sizes. This approach followed design requirements outlined in the 2016 AISC *Seismic Provisions* (2016a), which required columns to only be moderately ductile. Tables 10 and 11 summarize the column design results alongside the values of axial DCRs, $DCR_P = P_u/(\phi_c P_n)$, where $\phi_c P_n$ is the design compressive strength. W14 sections were chosen to be the default size for all columns. For the 12-story cases, identical column sizes were selected for every two stories. For the 3-story cases, the same column sizes were used for all three stories. The asterisk (*) in these two tables marks the columns that were sized based on the compactness requirement instead of capacity design.

In the chevron BRBF cases, it appears that column sizes increase with eccentricity in a "slow" manner. In comparing 12S-CH-C and 12S-CH-E1d (Table 10), all the columns except for the top two stories are the same. Comparing 12S-CH-E1d and -E2d, the column sizes are heavier only in some levels (the 3rd to 6th stories) of 12S-CH-E2d. Also, as shown in Table 11, the column size in 3S-CH-E2d is slightly heavier than that in 3S-CH-C. It has been shown in Tables 2, 3, 8, and 9 that a notable increase in both brace and beam sizes with the bracing eccentricity is observed in all levels of chevron BRBFs. By contrast, the rate of increase in column sizes with the bracing eccentricity is much slower. This is attributed to the fact that the beam-end shears and the vertical brace forces delivered to the columns are acting in the opposite direction [Equation 11(b)] in the chevron BRBFs. Although the column axial force demands are generally increased with the bracing eccentricity because of

the increased vertical brace force, the increased beam end shears essentially offset the increase in the column axial force demand with the eccentricity.

For single-diagonal BRBF cases, the two sides of columns (i.e., C1 and C2 members, to which the bottom and top ends of braces are adjacent, respectively) in each frame were designed separately. In any story, the C2 member is designed for higher capacity-limited axial forces than the C1 member in the same story because the C2 member resists the vertical forces from one more brace than the C1 member does. The discrepancy of axial demand between two sides of column is notable for low-rise BRBFs but may become insignificant for high-rise BRBFs, especially on the columns in the lower stories. Take, for example, the concentric design cases: The design of 3S-SD-C (Table 11) ended up with different column sizes between C1 and C2 members, while the same column sizes were selected for the two sides of 12S-SD-C (Table 10). It can be found that in 12S-SD-C, the DCR_P values of C1 members are smaller than those of C2 members over the entire building height, and discrepancy in DCR_P between the two sides of columns is diminishing as it goes from top to bottom of the building. The low DCR_P values for the C1 members in the top part (9th to 12th stories) of 12S-SD-C indicates a potential for using lighter columns. However, no commercially available lighter sections can be selected for these columns.

For the single-diagonal eccentric BRBF design cases, the discrepancy in the axial force demand between C1 and C2 members becomes more significant than that in the concentric design cases because the moment connections used between the stubs and C2 members is much stiffer than the pin connections between the beam and C1 members, causing C2 members to carry more gravity loads than C1 members. Therefore, for both 12S-SD-E2d (Table 10) and 3SD-SD-E2d (Table 11), except for the bottom two stories of 12-SD-E2d, the C2 members are heavier than C1 members over the building height.

Moreover, by comparing the column sizes between the concentric (-C) and eccentric (-E2d) cases in each single-diagonal BRBF group [Groups 12S-SD (Table 10) or 3S-SD (Table 11)], it can be seen that eccentricity can make C1 members lighter while C2 members get heavier. This would be mainly attributed to the fact that uneven gravity loads are distributed to the C1 and C2 members in the eccentric cases. Another factor varying the column axial demands with the eccentricity is the change of the vertical component of brace forces delivered to the columns, which is related to the changes in size and inclination angle for the braces. However, this factor is shown to be insignificant from the design cases in this study. Although the brace sizes as well as the brace adjusted strengths become smaller when the eccentricity increases, the steeper brace angle would lead to greater vertical components of the brace forces. These two effects are counteractive, making the resulting vertical components of brace forces delivered to the columns similar, regardless of eccentricity.

Weight Comparison

Tables 12 and 13 respectively, present the steel weights for the 12-story and 3-story case study designs. For the group of chevron BRBF design cases, the brace steel weights (including casing but excluding the infill grout) were similar among the three 12-story design cases (12S-CH-C, 12S-CH-E1d, and 12S-CH-E2d). Likewise, the brace steel weights of the two 3-story chevron cases (3S-CH-C and 3S-CH-E2d) were close. These results indicate that the increase in core area with eccentricity was offset by the shorter brace lengths and casing weight. Furthermore, in each chevron group (Groups 12S-CH or 3S-CH), the column weights were similar between the cases, reflecting that the column sizes slowly increase with the eccentricity for chevron BRBFs. However, for both Groups 12S-CH and 3S-CH, the beams were substantially heavier for the BRBFs with eccentricities. Case 12S-CH-E2d is more than double the beam weight as compared to the concentric case (12S-CH-C). Similarly, the beam weight in Case 3S-CH-E2d is about twice that in 3S-CH-C. Overall, it is apparent that the total steel weight increases with the eccentricity for the chevron BRBFs. For Group 12S-CH, Case 12S-CH-E1d was 1.10 times heavier than the concentric Case 12S-CH-C, and 12S-CH-E2d was 1.27 times heavier. For Group 3S-CH, Case 3S-CH-E2d was 1.32 times heavier than the concentric Case 3S-CH-C.

For the single-diagonal BRBF design cases, the brace steel weight in the frames with eccentricities were notably less than their benchmark concentric frames. The brace steel weight in eccentric Case 12S-SD-E2d was about 18% lighter than that in the concentric Case 12S-SD-C. Likewise, the brace steel weight in 3S-SD-E2d was about 24% lighter than that in 3S-SD-C. This is attributed to the fact that C2 members in the eccentric BRBF take partial story shears so that the braces in the eccentric case carry less story shears than those in the concentric case, resulting in the decrease in the steel core area in the eccentric BRBFs. In addition, the brace length was shortened in the eccentric case because of the steeper brace angle. The reduction in brace length and core area results in the notable decrease in the brace steel weight with the eccentricity in the single-diagonal BRBFs. For the column weight, the eccentric Case 12S-SD-E2d was slightly higher than the concentric Case 12S-SD-C. Similarly, for Group 3S-SD, the column weight in Case 3S-SD-E2d was moderately heavier than that in 3S-SD-C. These suggest that, as the eccentricity is introduced into a single-diagonal BRBF, the weight increase in C2 members would be somewhat offset by the weight decrease in the C1 members, resulting in a slight

Table 12. Steel Weights for 12-Story Case Study Designs							
Group	Design	BRB (kips)	Column (kips)	Beam (kips)	Frame (kips)	Frame + BRB (kips)	Increase (%)
12S-CH	12S-CH-C	16.7	45.7	16.6	62.2	78.9	—
	12S-CH-E1d	16.2	45.4	25.6	70.9	87.2	+10.4%
	12S-CH-E2d	16.4	46.9	36.7	83.6	100	+26.8%
12S-SD	12S-SD-C	21.2	49.7	23.5	73.3	94.5	—
	12S-SD-E2d	17.4	50.6	23.4	74.0	91.4	–3.27%
	12S-SD-E2d*	19.3	56.0	24.9	80.9	100	+5.99%

Table 13. Steel Weights for 3-Story Case Study Designs							
Group	Design	BRB (kips)	Column (kips)	Beam (kips)	Frame (kips)	Frame + BRB (kips)	Increase (%)
3S-CH	3S-CH-C	4.83	6.12	4.74	10.9	15.7	—
	3S-CH-E2d	4.74	6.66	9.36	16.0	20.8	+32.3%
3S-SD	3S-SD-C	6.22	6.62	6.30	12.9	19.1	—
	3S-SD-E2d	4.74	7.65	5.74	13.4	18.1	–5.24%
	3S-SD-E2d*	5.32	8.46	6.11	14.6	19.9	+3.91%

increase in the total column weight. For the beam weight, Case 12S-SD-E2d was slightly less than Case 12S-SD-C. Similarly, for Group 3S-SD, the beam weight in 3S-SD-E2d was moderately lighter than that in 3S-SD-C. Compared to the beam sections employed in the concentric frame, lighter sections were used for the beam members (which occupy a large portion of the span width) in the eccentric frame, despite heavier sections required for the short stub members. This results in slightly lighter beam weight in the eccentric frame. Overall, the total weight of Case 12S-SD-E2d was about 3% lighter than 12S-SD-C, while 3S-SD-E2d was about 5% lighter than 3S-SD-C.

Alternative designs were generated neglecting the effects of the half-SMF in resisting story shear. Using this conservative assumption, larger brace sizes were required, and heavier beams and columns were needed to match the capacity of the larger braces. The steel weights for the "re-design" results (denoted as 12S-SD-E2d* and 3S-SD-E2d*) are listed in Tables 12 and 13. The total weight of Case 12S-SD-E2d* was 6% higher than Case 12S-SD-C, while 3S-SD-E2d* was 4% higher than 3S-SD-C. This indicates that neglecting the half-MRF action when designing single-diagonal BRBF with eccentricity would lead to somewhat increased total steel weight

The weight economy for single-diagonal frames in these case study designs is much better than what has been reported in previous studies on BRBFs with eccentricity because of differences in the design approach. In the single-diagonal frames reported by Prinz and Richards (2012), and others that have followed their approach, the stub and beam were selected to be the same size, the columns were designed for the seismic moments, and the beneficial effects of the half-MRF were neglected. Part 2 of this paper (Li et al., 2026) demonstrates that these design assumptions from past studies are overly conservative.

Beam Weight Parameter Study

An additional parameter study was conducted to investigate the beam weight increase when the beam depth is not fixed, as it was for the case-study designs. Allowing the beam depth to increase may result in a more economical beam design. Seven eccentricities (including zero) were investigated in combination with four reference brace areas and two frame configurations (single-diagonal, chevron). The reference brace area established the story shear strength for the concentric case that was matched for all eccentric cases. Beam weights were normalized by the beam weight with zero eccentricity, other things being equal.

Figure 16 shows results from the parameter study. The vertical axis shows total beam weights normalized by the weight of the concentric case. As with the case study designs (Tables 12 and 13), the beam weights increased with eccentricity for the chevron frames. However, for chevron frames with an eccentricity of 48 in., the beam weight increase was less than 2 times, since the beam depth was allowed to vary (Figure 16). For single-diagonal frames, the beam weight

slightly decreased for eccentricities up to around 72 in. (Figure 16). However, the parameter study showed that for eccentricities greater than 72 in. with single-diagonal frames, beam weight increases (Figure 16).

CONCLUSIONS

This paper discussed the formulation of design equations for BRBFs with eccentricity. The analysis methods for determining the shear, axial force, and bending moment demands for capacity design of beams and columns were presented. Then, nine BRBF designs representing two building heights (3 and 12 stories), two bracing configurations (chevron and single-diagonal), and various eccentricities were shown to demonstrate the impact of eccentricity on BRBF member sizing and weights.

The study supports the following conclusions:

- For BRBFs with chevron configuration, brace steel weights (steel cores, lugs, and outer casings) were similar regardless of eccentricity. The heavier brace cores for the chevron BRBF with eccentricity were offset by the reduced brace lengths.
- For BRBFs with a chevron configuration, the beam weight increases significantly with eccentricity, while the column weight increases more slowly. This slower increase in column weight is due to the offset effect of the beam-end shears, which increase with eccentricity but partially counteract the rise in vertical brace forces transmitted to the columns due to eccentricity.
- For chevron BRBFs, the 12-story design cases with eccentricities were 1.10 to 1.27 times heavier than the concentric case for eccentricities of 1 to 2 times the beam depth. The 3-story design case with eccentricity of 2 times the beam depth was 1.32 times heavier than the concentric frame. The difference in weight was almost entirely due to heavier beams in the chevron BRBF with eccentricity.
- For nonalternating, single-diagonal BRBFs with eccentricities, the columns with the stubs help resist the story shear, leading to decreasing story shear resisted by the braces. Thus, both the required brace sizes and brace length decreased for an eccentricity of 2 times the beam depth, resulting in lower brace weight.
- For nonalternating, single-diagonal BRBFs with eccentricities of 2 times the beam depth, the beam weight slightly decreased with the brace eccentricity, while the column weight slightly increased with the eccentricity. The total steel weights of single-diagonal cases with eccentricity of 2 times the beam depth were less than the concentric cases by about 3% to 5%.
- For nonalternating, single-diagonal BRBFs with eccentricities, designed by sizing the braces for the entire story shears (neglecting moment frame action), the total frame weights for cases with eccentricity of 2 times the beam depth were greater than the concentric cases by about 4% to 6%.

REFERENCES

AISC (1990), *Seismic Provisions for Structural Steel Buildings,* American Institute of Steel Construction, Chicago, Ill.

AISC (2016a), *Seismic Provisions for Structural Steel Buildings*, ANSI/AISC 341-16, American Institute of Steel Construction Chicago, Ill.

AISC (2016b), *Specification for Structural Steel Buildings*, ANSI/AISC 360-16, American Institute of Steel Construction, Chicago, Ill.

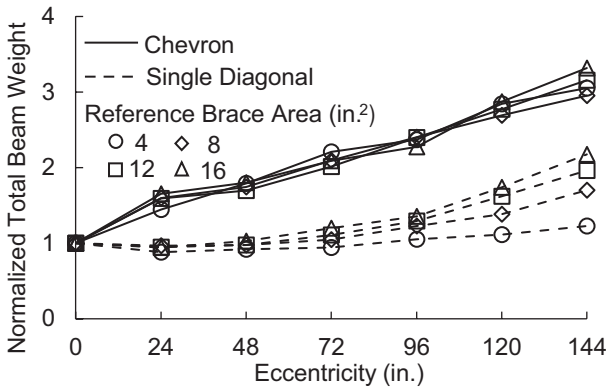

Fig. 16. Normalized beam weights for various eccentricities when beam depth is increased to use the most efficient shapes.

AISC (2022a), *Seismic Provisions for Structural Steel Buildings*, ANSI/AISC 341-22, American Institute of Steel Construction, Chicago, Ill.

AISC (2022b), *Specification for Structural Steel Buildings*, ANSI/AISC 360-22, American Institute of Steel Construction, Chicago, Ill.

ASCE (1993), *Minimum Design Loads for Buildings and Other Structures*, ASCE 7-93, American Society of Civil Engineers, New York, N.Y.

ASCE (2016), *Minimum Design Loads and Associated Criteria for Buildings Structures*, ASCE/SEI-7-16, American Society of Civil Engineers, Reston, Va.

ASCE (2022), *Minimum Design Loads and Associated Criteria for Buildings and Other Structures*, ASCE/SEI-7-22, American Society of Civil Engineers, Reston, Va.

ASTM (2022), *Standard Specification for Structural Steel Shapes*, ASTM A992/A992M, ASTM International, West Conshohocken, Pa.

CSI (2019), *CSI Analysis Reference Manual for SAP2000, ETABS, SAFE and CSiBridge*, Computers & Structures, Inc., Berkeley, Calif.

Engelhardt, M.D. and Popov, E.P. (1992), "Experimental Performance of Long Links in Eccentrically Braced Frames," *Journal of Structural Engineering*, Vol. 118, No. 11, pp. 3,067–3,088.

Fortney, P.J. and Thornton, W.A. (2017), "The Chevron Effect and the Analysis of Chevron Beams—A Paradigm Shift," *Engineering Journal*, Vol. 54, No. 4, pp. 263–296.

Hines, E. and Jacob, C. (2010), "Eccentric Braced Frame System Performance," Structures Congress, Orlando, Fla.

Hjelmstad, K.D. and Popov, E.P. (1983), "Cyclic Behavior and Design of Link Beams," *Journal of Structural Engineering*, Vol. 109, No. 10, pp. 2,387–2,403.

Hosseini, S.M. and Amiri, G.G. (2017), "Successive Collapse Potential of Eccentric Braced Frames in Comparison with Buckling-Restrained Braces in Eccentric Configurations," *International Journal of Steel Structures*, Vol. 17, No. 2, pp. 481–489.

Kasai, K. and Popov, E.P. (1986), "Cyclic Web Buckling Control for Shear Link Beams," *Journal of Structural Engineering*, Vol. 112, No. 3, pp. 505–523.

Lejano, B.A. and Mas, M.J.S. (2017), "Numerical Study on the Effect of Structural Parameters on the Behavior of BRBF-E," The Third International Conference on Civil Engineering Research (ICCER), Surabaya, Indonesia.

Li, C.-H., Richards, P.W., and Saxey, B.W. (2026), "Seismic Design and Performance of Buckling Restrained Brace Frames with Eccentric Brace Configurations Part 2: Analysis Studies and Design Implications," *Engineering Journal*, AISC, Vol. 63, No. 1, pp. 75–108.

Malley, J.O. and Popov, E.P. (1984), "Shear Links in Eccentrically Braced Frames," *Journal of Structural Engineering*, Vol. 110, No. 9, pp. 2,275–2,295.

NIST (2010), *Evaluation of the FEMA P-695 Methodology for Quantification of Building Seismic Performance Factors* (GCR 10–917–8), National Institute of Standards and Technology, Gaithersburgh, Md.

Prinz, G.S. and Richards, P.W. (2012), "Seismic Performance of Buckling-Restrained Braced Frames with Eccentric Configurations," *Journal of Structural Engineering*, Vol. 138, No. 3, pp. 345–353.

Roeder, C.W. and Popov, E.P. (1978), "Eccentrically Braced Steel Frames for Earthquakes," *Journal of Structural Engineering*, Vol. 104, No. 3, pp. 391–412.

Sabelli, R. and Arber, L. (2017), "Design of Chevron Gusset Plates," S*EAOC Convention Proceedings*, San Diego, Calif.

Shakib, H. and Safi, R. (2012), "Behavior Evaluation of the Eccentric Buckling-Restrained Braced Frame under the Near-Fault Ground Motions," 15th World Conference on Earthquake Engineering, Lisbon, Portugal.

Timoshenko, S.P. and Gere, J.M. (1961), *Theory of Elastic Stability,* 2nd Ed., McGraw-Hill Book Company, New York, N.Y.

Vayda, P.T. (2015), *Comparative Analysis of Buckling-Restrained Braced Frames in Eccentric Configurations (BRBF-Es) and Eccentrically Braced Frames (EBFs),* University of Arkansas, Fayetteville, Ark.

Seismic Design and Performance of Buckling Restrained Braced Frames with Eccentric Brace Configurations Part 2: Analysis Studies and Design Implications

CHAO-HSIEN LI, PAUL W. RICHARDS, and BRANDT W. SAXEY

ABSTRACT

This is the second of two companion papers discussing the seismic design and performance of buckling-restrained braced frames (BRBFs) with braces oriented in eccentric configurations. The companion paper (Li et al., 2026) introduces the proposed design procedures for the BRBFs with eccentricities and presents the elastic design results of nine case study buildings representing two building heights (12- and 3-story), two bracing configurations (chevron and single-diagonal), and various eccentricities. This paper first presents nonlinear response history analysis (NLRHA) results for the nine design case study buildings subjected to 16 ground motions scaled to the design basis earthquake (DBE) and maximum considered earthquake (MCE) levels. The analytical results demonstrate that BRBFs with eccentricities equal to twice the beam depth—double the current code limit of one beam depth—perform satisfactorily under seismic loading, provided they are properly capacity designed to account for brace eccentricities. The paper explores the relationship between brace eccentricity and key response parameters. The NLRHA results also validate the accuracy of the proposed analysis methods in estimating beam force demands in capacity design. Subsequently, nonlinear pushover analysis results for specific stories in selected chevron design cases are presented, with a focus on the effects of connection geometry, specifically combined and split gusset configurations, on local stress state in the beam region, analyzed through detailed finite element modeling. Lastly, the NLRHA results suggest that intentionally introducing brace eccentricities in single-diagonal BRBFs could potentially lead to more economical designs with enhanced seismic performance (e.g., reduced residual story drifts) as compared to concentric frames. Accordingly, design implications for single-diagonal eccentric BRBFs are explored, particularly concerning column capacity design with moment demands and the approximate story drift distribution for preliminary brace sizing.

Keywords: buckling restrained braced frames, eccentric bracing, eccentric braced frames.

INTRODUCTION

Buckling-restrained braced frames (BRBFs) are primarily used in concentric configurations as the AISC *Seismic Provisions* (2022a) limit eccentricities in BRBFs to less than a beam depth. However, architectural needs, like doorways or corridors, may require eccentric bracing. If the eccentricity exceeds a beam depth, additional columns can be added to meet the requirements of the AISC *Seismic Provisions*, but these added columns affect the cost and architecture. Several previous analytical studies (Hosseini and Amiri, 2017; Lejano and Mas, 2017; Prinz and Richards, 2012; Shakib and Safi, 2012; Vayda, 2015) demonstrated the feasibility of BRBFs in eccentric configurations without adding columns, although this can result in reduced cost effectiveness in cases of large eccentricities.

Recent research also highlights that BRBFs with eccentricities, besides offering architectural benefits, may help control residual drifts during seismic events. Gholami et al. (2021) investigated BRBFs with eccentricities as a means for controlling residual drift but only found them particularly effective when used in parallel with post-tensioned frames. Hariri and Christopoulos (2024) investigated BRBFs that are configured to induce beam bending and found they were able to limit residual drifts to 0.5% or less.

This study investigates the seismic design and performance of BRBFs with eccentricities and is presented in two companion papers. Part 1 (Li et al., 2026) presents design procedures and analysis methods for capacity design of the beams and columns in BRBFs with eccentricities and then presents design results for nine case study BRBFs (see Figure 1) with eccentric or concentric bracing configurations. This paper, Part 2, presents the analytical studies for evaluating the seismic performance of these case study designs.

Figure 1 shows BRBF designs for nine archetypes adapted from NIST GCR 10-917-8 (2010). The archetypes featured two heights (12- and 3-story), two bracing configurations

Chao-Hsien Li, Senior Research Engineer, CoreBrace, LLC, West Jordan, Utah. Email: chaohsien.li@corebrace.com

Paul W. Richards, Associate Professor, Brigham Young University, Provo, Utah. Email: paul.richards@byu.edu (corresponding)

Brandt W. Saxey, Technical Director, CoreBrace, LLC, West Jordan, Utah. Email: brandt.saxey@corebrace.com

Paper No. 2024–19R

(chevron and single-diagonal), and various eccentricities. In Figure 1, the BRBF design cases are grouped into four categories: 12S-CH, 12S-SD, 3S-CH, and 3S-SD. The prefixes 12S and 3S denote the 12-story and 3-story heights, respectively, while the suffixes CH and SD refer to the chevron and single-diagonal bracing configurations in the BRBFs. Each group includes two cases: one concentric (C) and one eccentric (E2d), with the eccentricity of twice the nominal beam depth (21 in.) of W21 beams. Group 12S-CH, also has an additional case (E1d) with an eccentricity equal to the beam depth. The E2d cases exceed the AISC *Seismic Provisions* limit (2022a), while the E1d case meets the code's maximum eccentricity allowance. Design cases are named using the group name and eccentricity condition (see Figure 1).

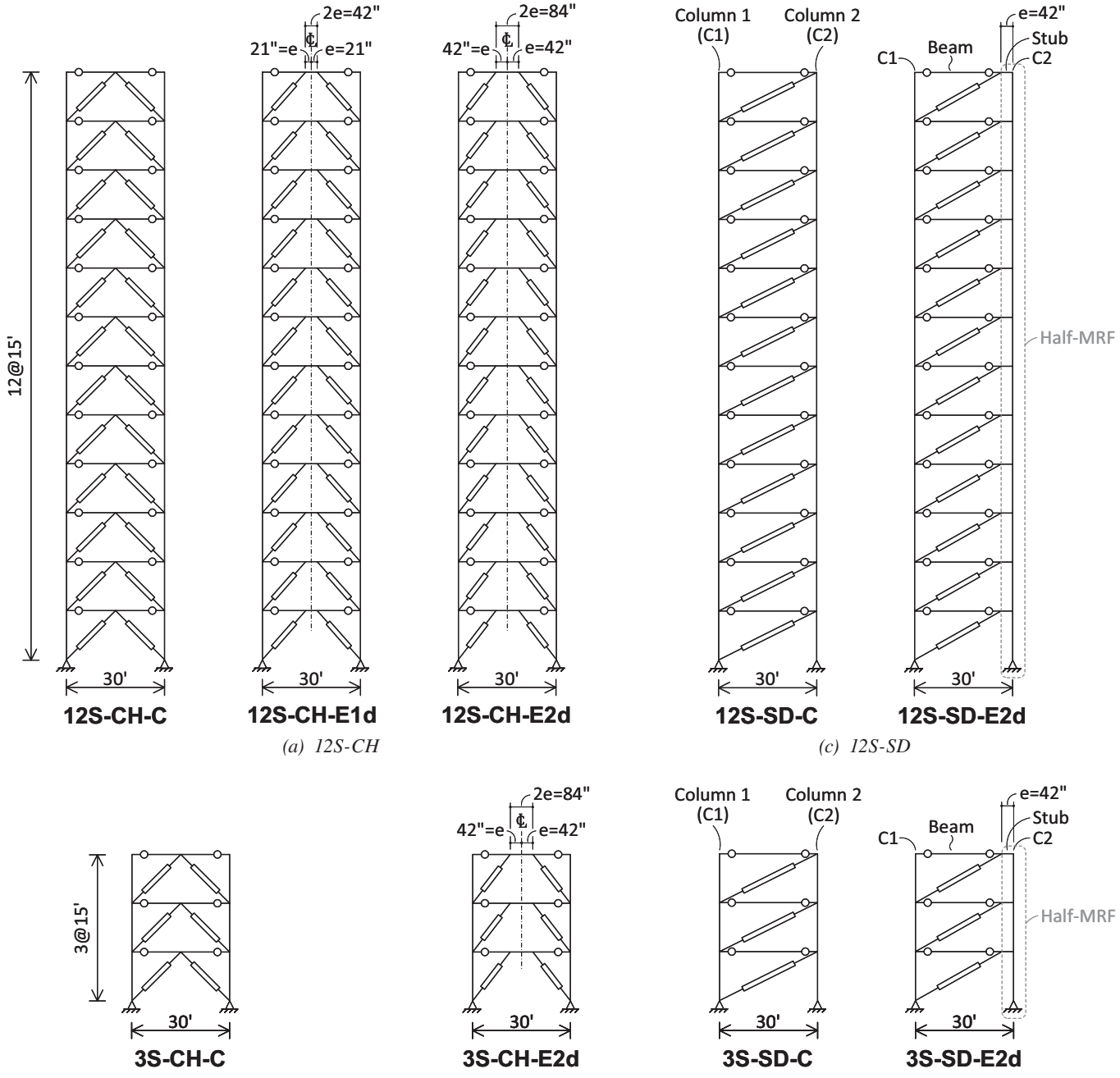

Fig. 1. Frame elevations for BRBF case designs.

This Part 2 paper first presents a nonlinear response history analysis (NLRHA) of the seismic performance for the nine design cases. It then discusses nonlinear pushover analysis results for specific stories, focusing on the effects of connection geometry through detailed finite element modeling. Lastly, design implications for single-diagonal eccentric BRBFs are explored.

RESPONSE HISTORY ANALYSIS STUDY

Overview

Nonlinear response history analysis (NLRHA) was used to investigate the response of the case study buildings and validate the proposed design procedure. A suite of 16 historical ground motion records were selected and scaled to design basis earthquake (DBE) and maximum considered earthquake (MCE) levels, which were used as the input motions for NLRHA. The mean structural responses (such as peak story drifts, peak brace core strains, etc.) averaged from the 16 ground motions are reported in this section.

Modeling

OpenSees (Mazzoni et al., 2006) was used to create nonlinear models for the BRBFs in this study. Individual BRBFs were modeled and tied to a fishbone system (Lignos et al., 2013) to represent the gravity framing, including lateral stiffness of the gravity beam-to-column connections [Figure 2(a)]. Gravity loads and seismic masses were applied to the fishbone system. For the BRBF portion of the models (BRBF-C and BRBF-E), beam-to-column intersections were modeled as rigid joints (representing gusset plates), and pins were introduced in the beam outside the connections (representing bolted connections) [Figure 2(a)]. Offset elements were used to model the stiffened regions inside of panel zones and locations of corner gussets. Offsets regions were assigned 10 times the elastic flexural properties of the members framing into centerline nodes. Base connections were modeled as pinned.

BRBF beams and columns were modeled with elastic beam-column elements, and the member forces in these elements were evaluated using NLRHA to confirm that forces did not exceed elastic limits. BRBF beams were pinned outside of the gusset region [Figure 2(a)]. Resistance provided by simple gravity connections [within the fishbone frame shown in Figure 2(a)] was modeled using nonlinear hinges representing lumped properties of gravity shear tab connections in the part of gravity system tributary to the BRBFs. These gravity connections were modeled using the Pinching4 material (Lowes et al., 2003) with parameters calculated according to ATC-114/NIST guidelines (Liu and Astaneh-Asl, 2000, 2004; NIST, 2017).

Buckling restrained braces (BRBs) were modeled as corotational truss elements (using workpoint-to-workpoint length, L_{WP}) with a hysteretic behavior defined by a Menegatto-Pinto steel material (SteelMPF) with isotropic strain hardening. Initial stiffness of the BRBs was defined by the effective stiffness factor, KF [see Tables 4–7 in Part 1 (Li et al., 2026)] using the bay geometry and L_{WP}. Cyclic properties of BRBs were calibrated to match the ultimate strength for both tension (P_{uT}) and compression (P_{uC}) at the expected deformation at a 2% story drift, aligning with the experimental brace response per the AISC *Seismic Provisions* (2022a) loading protocol. BRBs were modeled and calibrated using an expected core yield strength, $P_{ysc,exp}$, of 42 ksi. An illustration of a calibrated BRB material and backbone targets is shown in Figure 2(b).

Models included second-order effects both locally on the braced frame and through the leaning column as part of the fishbone gravity framing model. Inherent viscous damping was included as 2% Rayleigh damping at the first- and third-mode periods. Mass proportional damping was applied to all nodes, but stiffness proportional damping was only assigned to linear elastic elements.

Modal Results

Tables 1 and 2 summarize the OpenSees (Mazzoni et al., 2006) modal analysis results for the 12-story and 3-story design cases, respectively. The structural periods for the first three modes and the associated cumulative modal mass participation ratios, Γ_{cum}, are reported. From the period variations between the design cases in Group 12S-CH or 3S-CH, it can be seen that the structural period increases with the eccentricity, indicating the decreasing frame lateral stiffness with the eccentricity for the chevron BRBFs since all the design cases in the same groups carry identical seismic masses. By contrast, for the single-diagonal BRBFs (Groups 12S-SD or 3S-SD), the analysis results show a trend that the structural period decreases (i.e., the frame lateral stiffness increases) with the eccentricity. The half-moment resisting frame (half-MRF), formed by the stubs and the adjacent columns [i.e., Column 2 (C2) members] as shown in Figures 1(c) and 1(d) (see also Figure 17), in the single-diagonal eccentric frames provides extra lateral stiffness to the system despite the decreasing stiffness provided by the braces as the eccentricity increases. The contribution from the half-MRF leads to an increasing total lateral stiffness with the eccentricity for the single-diagonal BRBFs.

Ground Motions Selection and Scaling

Sixteen ground motion records selected from the FEMA P-695 far-field set (ATC, 2009) were used for NLRHA in this study (see Appendix). The target spectral shape for

scaling ground motions was the design spectrum prescribed by SEI/ASCE 7, *Minimum Design Loads and Associated Criteria for Buildings and Other Structures* (ASCE, 2022), with S_{DS} = 1.0g and S_{D1} = 0.6g, which is consistent with that employed for the three design cases in this study. As shown in Figure 3, the suite of selected ground motions was scaled such that the average of the 5% damped spectra does not fall below 90% of the target response spectrum over the code-prescribed period range (ASCE, 2022). The averaged 1st-mode and 3rd-mode periods (denoted as $T_{1,avg}$ and $T_{3,avg}$, respectively) of the OpenSees models (Mazzoni et al., 2006) in 12-story or 3-story design case groups were used to determine the period range. The upper bound of the period range was set at $2T_{1,avg}$, while the lower bound was set at the lessor between $0.2T_1$,avg and $T_{3,avg}$ to ensure the period range includes at least the number of modes necessary to achieve 90% mass participation. Each ground motion was scaled to both design basis earthquake (DBE) and maximum considered earthquake (MCE) levels. While NLRHA was conducted for both levels, the results presented in this paper focus on the MCE-level responses, obtained from the peak structural responses averaged across the suite of MCE ground motions.

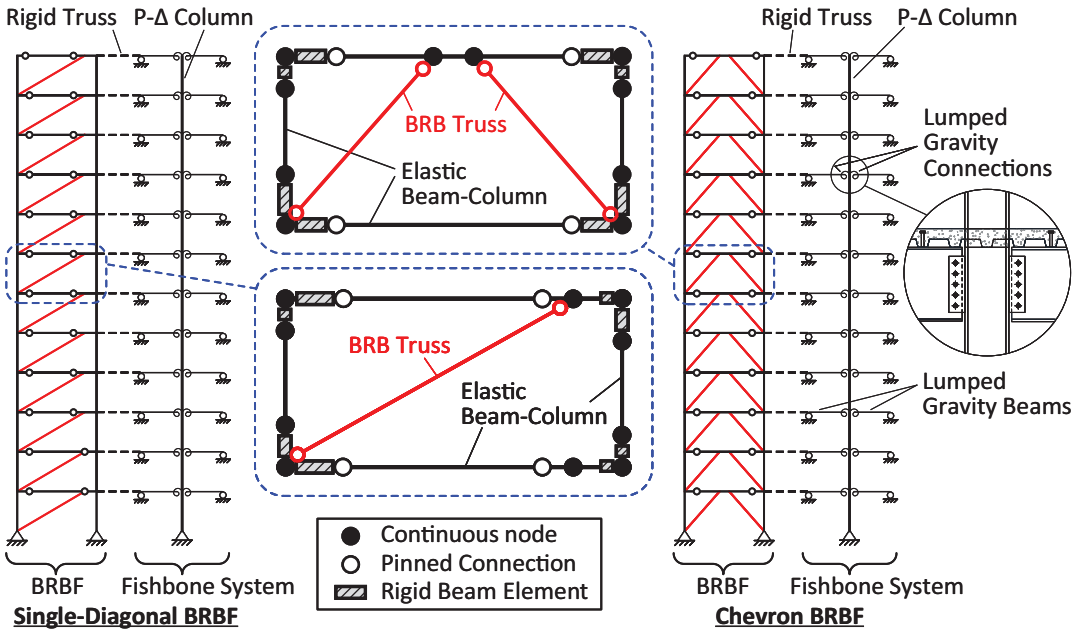

(a) Elements and constraints

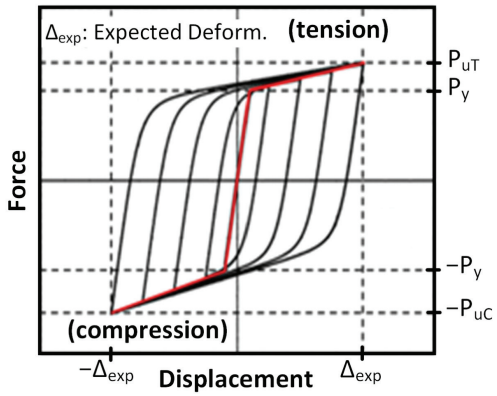

(b) Example of BRB modeling and calibration

Fig. 2. OpenSees modeling methods.

Table 1. Modal Analysis Results for 12-Story BRBF Design Cases										
Mode	Group 12S-CH						Group 12S-SD			
	12S-CH-C		12S-CH-E1d		12S-CH-E2d		12S-SD-C		12S-SD-E2d	
	Period (s)	Γ_{cum}	Period (s)	Γ_{cum}	Period (s)	Γ_{cum}	Period (s)	Γ_{cum}	Period (s)	Γ_{cum}
1	2.920	71.3%	2.972	72.5%	3.081	73.8%	3.228	73.6%	3.043	72.9%
2	0.975	89.4%	1.015	89.5%	1.075	89.7%	1.086	89.8%	1.015	89.8%
3	0.546	94.4%	0.567	94.3%	0.610	94.5%	0.610	94.3%	0.569	94.4%

Table 2. Modal Analysis Results for 3-Story BRBF Design Cases								
Mode	Group 3S-CH				Group 3S-SD			
	3S-CH-C		3S-CH-E2d		3S-SD-C		3S-SD-E2d	
	Period (s)	Γ_{cum}	Period (s)	Γ_{cum}	Period (s)	Γ_{cum}	Period (s)	Γ_{cum}
1	0.793	86.3%	0.895	86.9%	0.918	85.9%	0.896	87.4%
2	0.308	97.7%	0.352	97.9%	0.340	97.5%	0.340	98.3%
3	0.183	99.9%	0.192	100.0%	0.193	99.8%	0.202	99.8%

Analysis Results

Story-Drift Response

Story-drift results from the NLRHA analyses are summarized in Figures 4, 5, and 6. For DBE loading, the peak interstory drift ratios were similar among the cases in each group [see Figures 4(a), 4(b), 4(c), and 4(d) for Groups 12S-CH, 3S-CH, 12S-SD and 3S-SD, respectively], with values less than 0.02 rad, consistent with the design intent. For chevron BRBFs under MCE loading [see Figures 5(a) and 5(b) for Groups 12S-CH and 3S-CH, respectively], the story-drift response generally increases with the eccentricity in the lower stories, where the largest story drifts along the building height took place. However, the interstory drift of some intermediate stories in the 12-story eccentric frames (Cases 12S-CH-E1d and 12S-CH-E2d) were less than those in the eccentric frame (12S-CH-C), as shown in Figure 5(a).

On the other hand, for single-diagonal BRBFs, the peak story-drift response generally decreases with brace eccentricity. For 12-story design cases [Figure 5(c)], the MCE-level

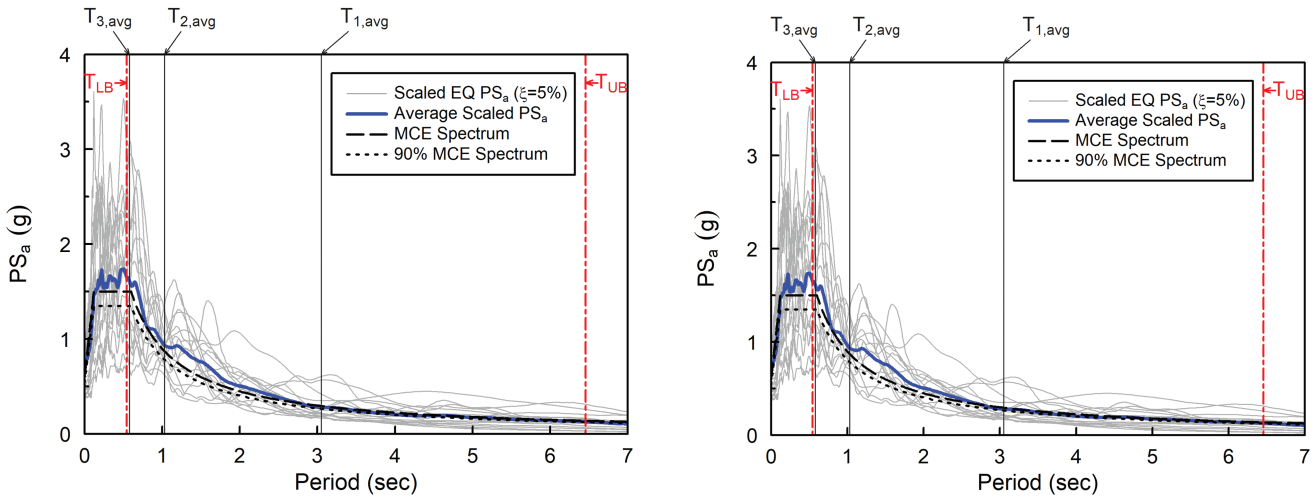

(a) For 12-story BRBF models *(b) For 3-story BRBF models*

Fig. 3. Pseudo-acceleration spectra of MCE-scaled input ground motions used for analyses.

story-drift response in the eccentric Case 12S-SD-E2d was noticeably less than that in the concentric case 12S-SD-C for the lower half of the frame. For 3-story design cases [Figure 5(d)], the MCE-level story drifts in 3S-SD-E2d were also smaller than those in 3S-SD-C, although to a smaller degree. The reduced drifts in the single-diagonal eccentric BRBFs could be attributed to the fact that the half-MRF [see Figures 1(c) and 1(d)] serves as an elastic backup lateral system, providing stiffness after the braces yield, leading to a reduction on the inelastic story drift of the frame.

It is noted that, in Figures 5(c) and 5(d), there are two additional curves, 12S-SD-E2d* and 3S-SD-E2d*, respectively representing alternative designs for Cases 12S-SD-E2d and 3S-SD-E2d in which an alternate method for column design is considered. In contrast to the proposed design for 12S-SD-E2d and 3S-SD-E2d, where Column 2 (C2) shears are considered, the alternative designs for 12S-SD-E2d* and 3S-SD-E2d* follow the practice of assuming the entire story shears are carried by the braces only. Hence, the conventional practice considered in the alternate design would lead to conservative design results. All the member sizes for the braces, beams, and columns in Cases 12S-SD-E2d* and 3S-SD-E2d* are larger than those in 12S-SD-E2d and 3S-SD-E2d, respectively. As reported in Part 1, the alternative designs are 4% to 6% heavier. As shown in Figures 5(c) and 5(d), the alternative design Cases 12S-SD-E2d* and 3S-SD-E2d* generally had smaller story-drift response than 12S-SD-E2d and 3S-SD-E2d.

Furthermore, Figure 5 shows that the MCE-level peak story drifts in all design cases for both chevron and single-diagonal configurations were less than the associated code-prescribed story-drift limits (0.04 and about 0.034 rad for the 3-story and 12-story design cases, respectively), determined in accordance with ASCE/SEI 7 and based on the full height of building. This confirms the feasibility and satisfactory seismic performance of the eccentric BRBFs.

Figure 6 shows the residual story drift response after the MCE loading. For Group 12S-CH design cases [Figure 6(a)], it is seen that the residual story drifts in the lower stories of the eccentric Cases 12S-CH-E1d and 12S-CH-E2d were noticeably higher than those in the concentric

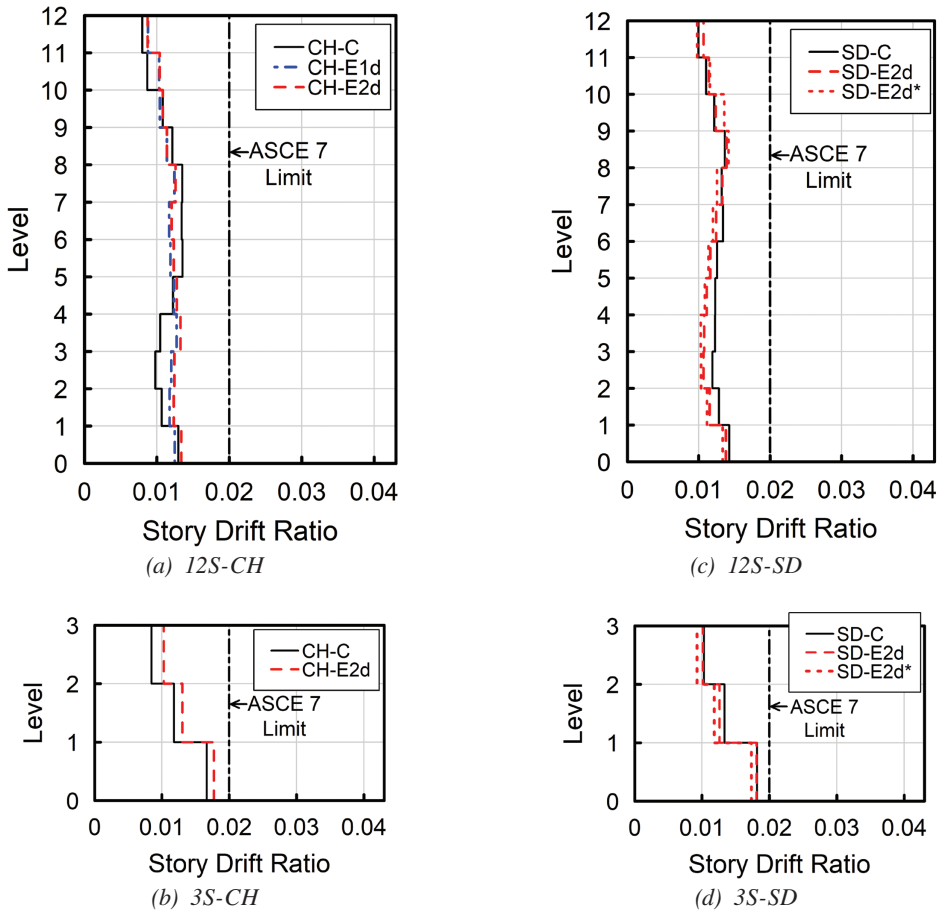

(a) 12S-CH *(c) 12S-SD*

(b) 3S-CH *(d) 3S-SD*

Fig. 4. DBE-level peak story drifts (mean of maximums).

Case 12S-CH-C. Also, the response in 12S-CH-E2d was generally higher than 12S-CH-E1d. For Group 3S-CH [Figure 6(b)], the residual story drifts in 3S-CH-E2d were slightly higher than those in 3S-CH-C, despite similar response in the first story for both cases. To summarize, analysis results show that for chevron BRBFs, the residual story drifts generally increase with brace eccentricity.

In contrast to the chevron BRBFs, the eccentric single-diagonal BRBFs had noticeably smaller residual response compared to the corresponding concentric frames. As shown in Figure 6(c), the residual story drifts in 12S-SD-E2d were significantly lower than those in 12S-SD-C for the lower stories of the building. For 3-story design cases [Figure 6(d)], all the residual story drifts along the entire building heights in 3S-SD-E2d were less than those in 3S-SD-C. Furthermore, as shown in both Figure 6(c) and Figure 6(d), the alternative design cases 12S-SD-E2d* and 3S-SD-E2d*, with the associated heavier frame members, had further reduced residual story drift response.

In summary, these analysis results suggest that using eccentric configurations for single-diagonal BRBFs would be an efficient way to reduce story drifts, especially residual drifts. It is noted that, based on the design procedure proposed in this study, the eccentric Cases 12S-SD-E2d and 3S-SD-E2d were even lighter than the corresponding concentric frames by about 3% and 5%, respectively (see Part 1 for details) while achieving a better control of the story-drift response. When the conventional, but conservative, design practice is used, the eccentric Cases 12S-SD-E2d* and 3S-SD-E2d* had further enhanced seismic performance in controlling the story drift with only a modest increase in weight [about 6% and 4%, respectively (see Part 1 for details)].

Brace Response

Plots of peak BRB core strains from the NLRHA analyses at MCE level are shown in Figure 7. The peak BRB strains are within the expected values corresponding to a story drift ratio of 0.02, as listed in Part 1 Tables 4 through 7 (Li et al., 2026), at all levels except for the bottom three stories in the 12-story cases [Figures 7(a) and 7(c)] and for the ground floor in the 3-story cases [Figures 7(b) and 7(d)]. The higher strains (2.44% maximum) at these bottom levels

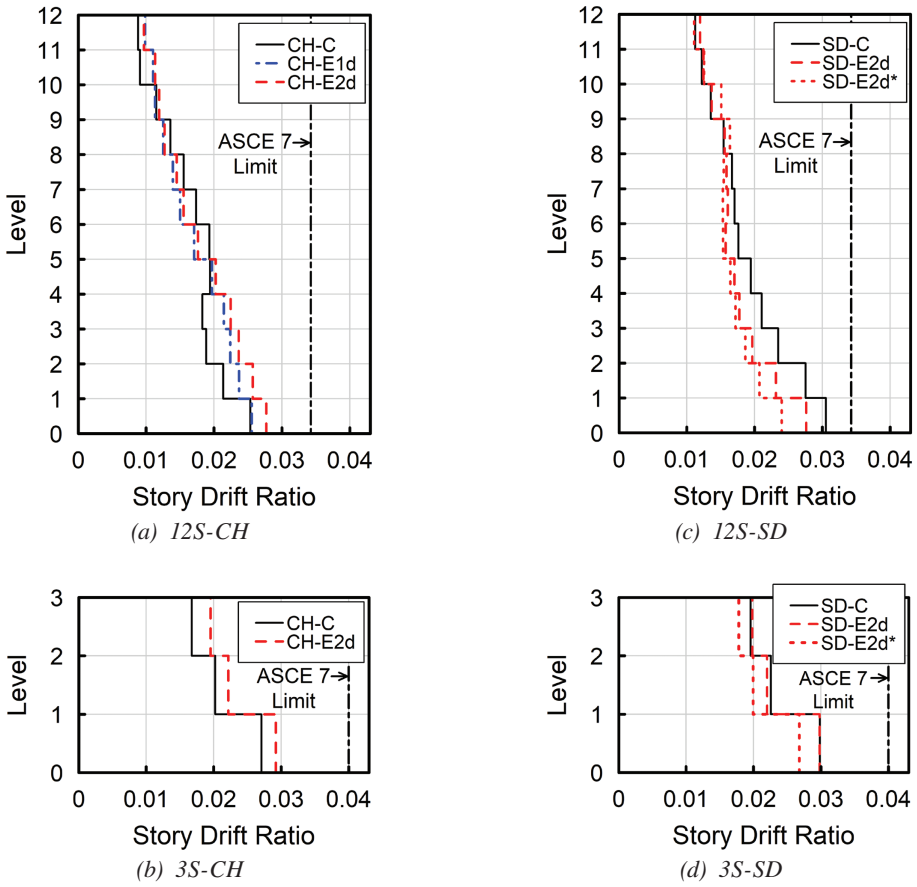

Fig. 5. MCE-level peak story drifts (mean of maximums).

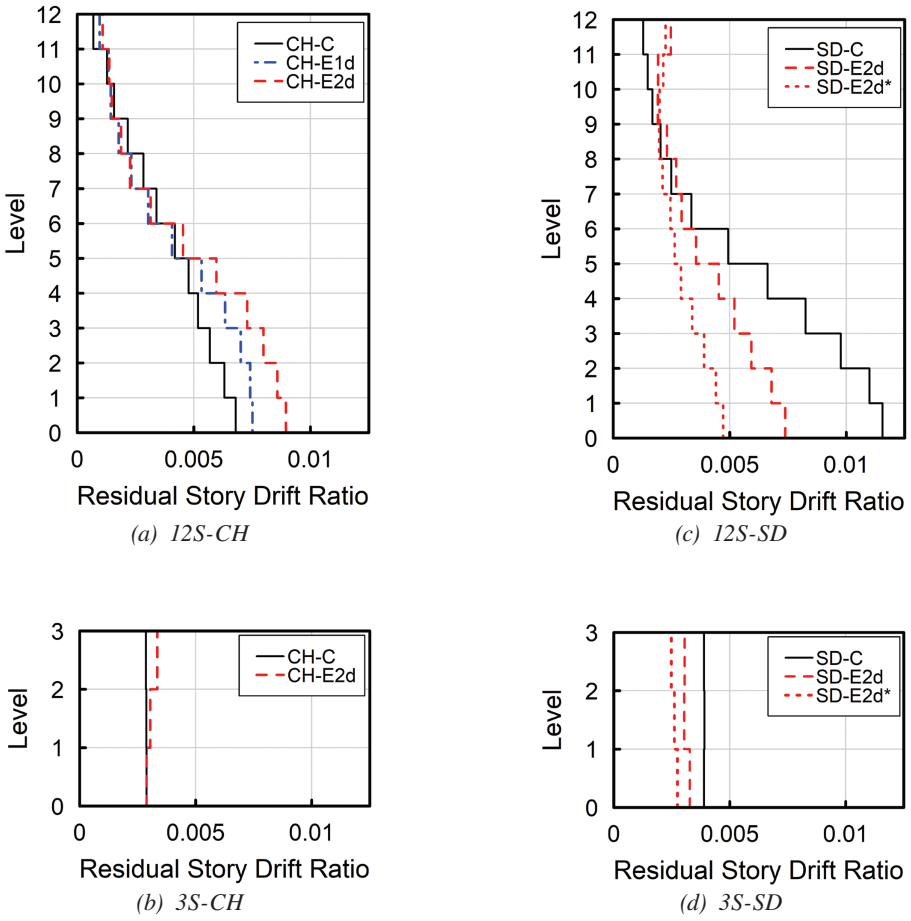

(a) 12S-CH *(c) 12S-SD*

(b) 3S-CH *(d) 3S-SD*

Fig. 6. MCE-level residual story drifts (mean of maximums).

remain, however, within the experimental BRB deformation capacities (which typically achieve at least 3% strain). For comparison between eccentric and concentric frames, there seems to be a trend that the eccentric frames generally develop BRB core strains somewhat higher than the concentric frames, at least for those braces experiencing the highest strains. For Groups 12S-SD, 3S-CH, and 3S-SD, the eccentric frames had almost all BRB strains higher than the corresponding concentric frames. For Group 12S-CH [Figure 7(a)], the two eccentric frames (12S-CH-E1d and 12S-CH-E2d) developed higher BRB core strains at the bottom four stories, where the largest overall BRB strains were seen, than in the concentric case (12S-CH-C) with smaller core strains at the upper stories.

BRB normalized ultimate force represents the ratio of the maximum compressive force, P_u, in a BRB from the NLRHA to its expected yield force, P_{ye}, which is the multiplication of yielding core area, A_{sc}, and the expected yield stress, $F_{ysc,\text{exp}}$. It is a measure of the overstrength, ωβ, seen in the BRB, where ω is the strain-hardening adjustment factor, and β is the compression strength adjustment factor. The plots of the analytical peak BRB normalized forces at MCE levels are provided in Figure 8. BRBs were modeled as having a $F_{ysc,\text{exp}}$ of 42 ksi, and as such, this normalized force is only a measure of the strain hardening and compression overstrength that develops and does not include any material overstrength that would exist when a material yield stress range ($F_{ysc,\text{min}}$ to $F_{ysc,\text{max}}$) is allowed for. Because the brace overstrength is dependent on the core strain response, similar trends are observed between the BRB core strains and normalized ultimate forces. They include that the BRB normalized ultimate forces are within the expected overstrength ωβ values [see Tables 4 through 7 in Part 1 (Li et al., 2026)] except for the bottom three stories in the 12-story cases [Figures 8(a) and 8(c)] and for the ground floor in the 3-story cases [Figures 8(b) and 8(d)], where the observed overstrength in the first story exceeded the expected values by about 9.7% and 12.4% for 12-story and 3-story cases, respectively.

In addition, the eccentric BRBFs generally developed slightly higher brace overstrength than the corresponding concentric frames did. It should be noted that while the story drifts considerably exceeded 2% as seen in Figure 5 by as much as 50%, the resulting overstrength only

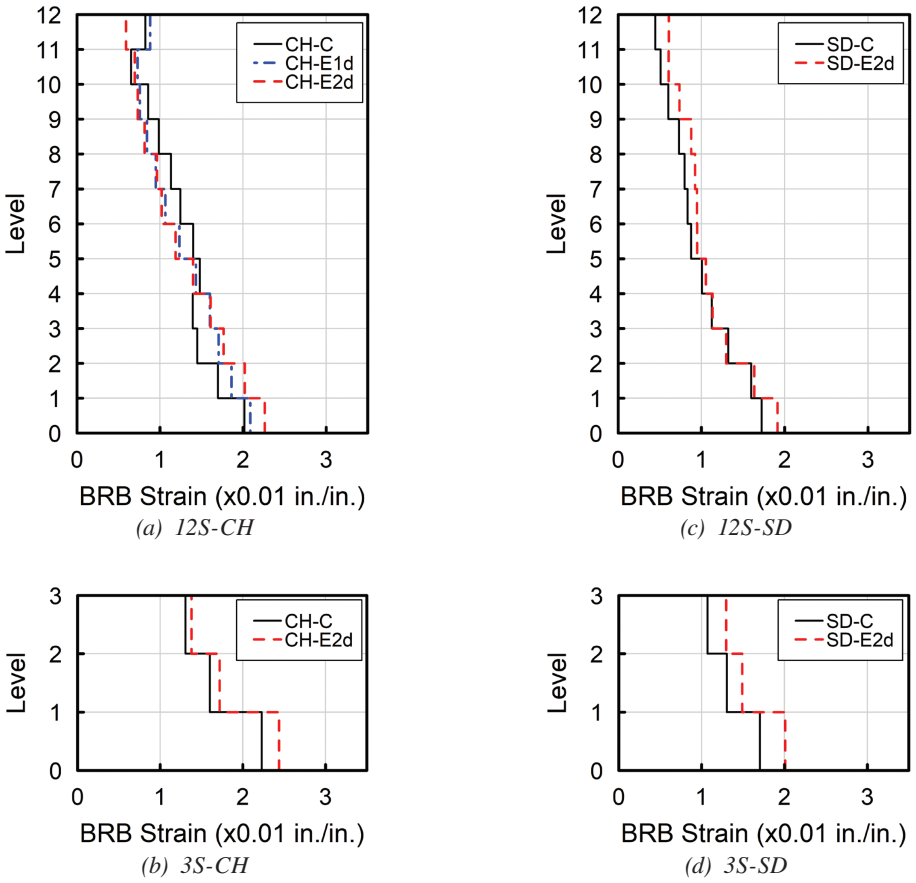

Fig. 7. MCE-level peak BRB strains (mean of maximums).

exceeded the values expected at 2% by a small amount. A similar statement about the resulting core strain is also true. These facts speak to the large total strain ranges experienced in AISC testing protocols relative to the generally lower total strain ranges seen in earthquake records even with higher absolute reference strains.

Beam Member Forces

To validate the beam capacity design methods proposed in Part 1 (Li et al., 2026) for BRBFs with eccentricities, selected beam member force diagrams from an NLRHA for 12-story design cases were plotted in Figures 9 and 10. These diagrams, showing beam member forces at a story-drift ratio of 0.02, are compared with the estimates from the proposed methods. Note that the 0.02 drift ratio was used to set brace overstrength factors (ω and β), which were used to estimate brace forces in the BRBF capacity design. The input motion for selected NLRHA is from the north-south component of the 1994 Northridge earthquake (Canyon Country–W Lost Cany), scaled to MCE level. The analysis with this ground motion was chosen because it produced peak drift ratios of about 0.02 in the lower three stories of all 12-story cases.

Figure 9 presents beam member force diagrams from the 12-story chevron BRBF design cases. The beams on the 2nd, 3rd, and 4th floors were selected for Cases 12S-CH-C, 12S-CH-E1d, and 12S-CH-E2d, respectively, because the braces beneath these beams are identical in size (A_{sc} = 5.5 in.^{2}). The consistent brace sizes were chosen to ensure comparable forces on the selected beams, clearly illustrating how beam forces are influenced by brace eccentricity without being affected by variations in brace force. The forces are shown at point in time when the story below each beam reached about 0.02 rad drift.

In each subfigure displaying the member forces, both the response from the NLRHA (represented by a solid line) and the estimated force diagrams, calculated using the proposed analysis methods, are shown. The estimates are depicted as dashed lines and labeled as Est. For discussion purposes, two sets of estimated member forces are presented in Figure 9: one due to seismic effects only, labeled Est. (E), and the other due to the combined seismic and gravity effects, labeled Est. (E+G). For the shear and moment diagrams,

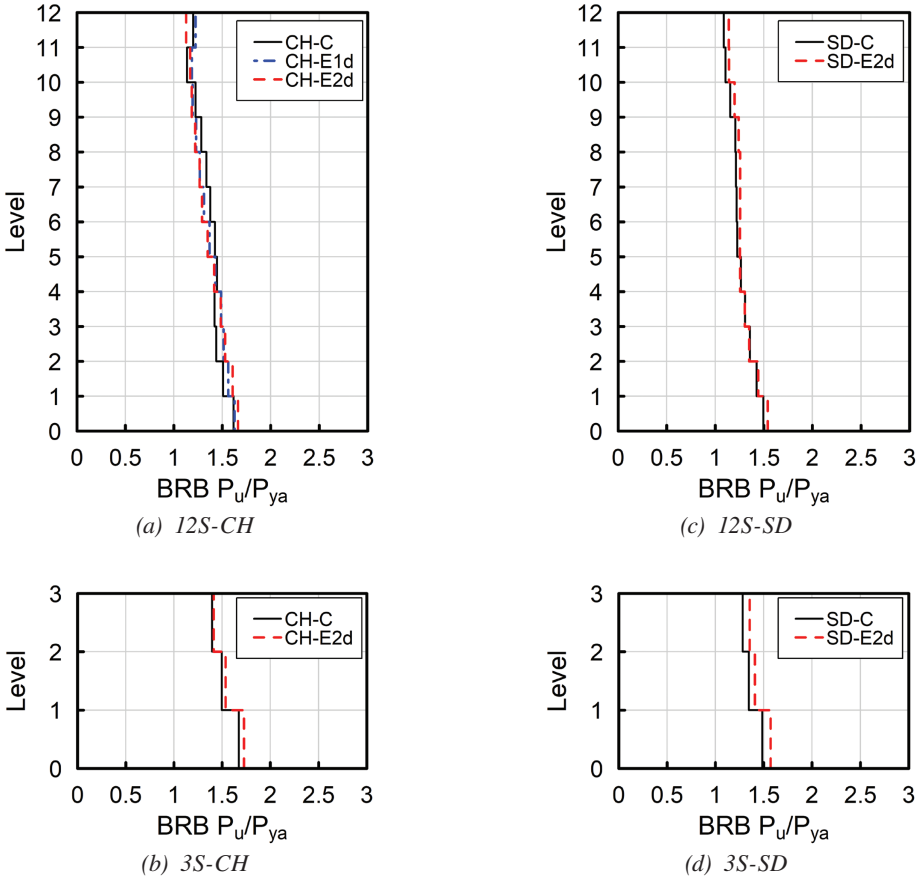

(a) 12S-CH *(c) 12S-SD*

(b) 3S-CH *(d) 3S-SD*

Fig. 8. MCE-level peak BRB normalized axial forces, P_u/P_{ye} (mean of maximums).

the estimated response Est. (E+G) is compared with the NLRHA response because both represent forces induced by combined seismic and gravity effects. The comparison between Est. (E+G) and Est. (E) demonstrates how gravity affects the member forces. In the axial force diagrams, only Est. (E) is presented for comparison with the NLRHA response, since the axial forces are due to the seismic effect alone. Notably, across all three design cases (Figure 9), the strong agreement between the Est. (E+G) and NLRHA responses in the shear and moment diagrams, along with the fair match between Est. (E) and the NLRHA axial force diagrams, validates the proposed analysis methods for estimating beam force demands in the capacity design of chevron BRBFs.

For concentric Case 12S-CH-C [Figure 9(a)], the Est. (E+G) and NLRHA curves in the shear and moment diagrams show low shear and moment demands in the concentric chevron BRBF beams. In the moment diagram, the Est. (E) curve reveals a certain amount of negative bending moment induced by the seismic effect, which arises from the net upward brace force due to the imbalance between the two brace forces beneath the beam. Meanwhile, the low magnitude of the Est. (E+G) response suggests that gravity effect helps counteract the seismic-induced moment.

For Cases 12S-CH-E1d [Figure 9(b)] and 12S-CH-E2d [Figure 9(c)], significant shear and moment demands are induced in the beams due to brace eccentricity. Comparing the shear diagrams between these two eccentric frames reveals a trend: As brace eccentricity increases, the shear demand in the interior region slightly decreases, while there is a moderate increase in shear demands in the exterior regions. This shift highlights the impact of increasing eccentricity on the distribution of shear forces along the beam.

The comparison of moment diagrams between the two eccentric design cases [Figures 9(b) versus 9(c)] reveals

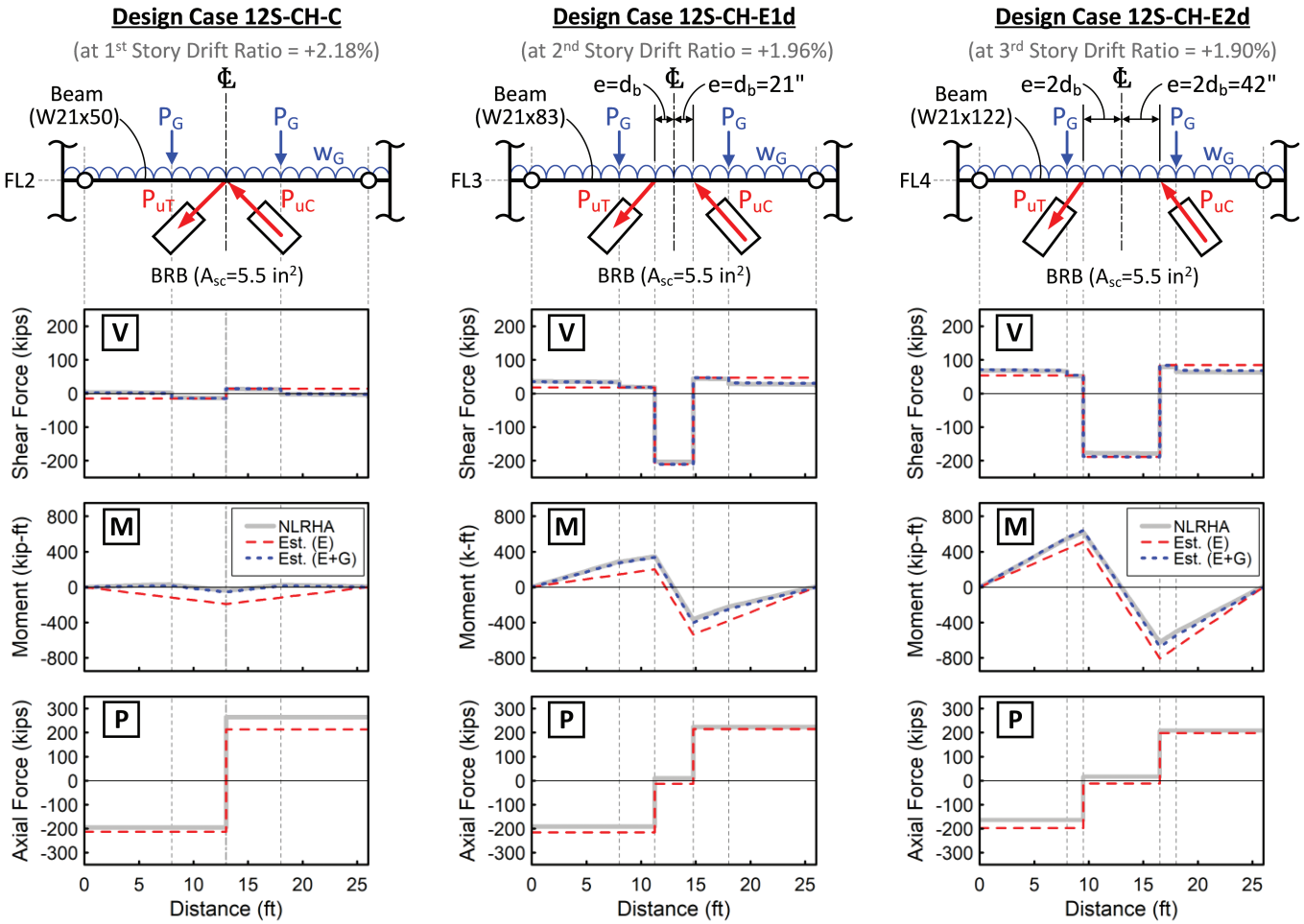

(a) 12S-CH-C, floor 2 *(b) 12S-CH-E1d, floor 3* *(c) 12S-CH-E2d, floor 4*

Fig. 9. Member forces in selected beams from a NLRHA.

a clear trend: The beam moment demand increases with brace eccentricity. Noticeable discrepancies between the Est. (E+G) and Est. (E) moment diagrams are seen in both eccentric frames. The seismic-induced moment diagram [Est. (E)] shows a notable imbalance in the magnitude of moment demands between the two exterior beam regions, stemming from the imbalance between the brace forces. In contrast, this imbalance is insignificant in the total action diagram [Est. (E+G)], indicating that the gravity effect tends to offset the discrepancies in moment demand between the two exterior regions.

In the beam axial force diagrams (Figure 9-bottom), comparing the three cases shows a similarity in the magnitude of the peak axial forces. It can be observed that the axial force magnitude slightly decreases with increasing eccentricity, primarily due to the steeper brace angle, which results in a reduced horizontal component of the brace forces.

In summary, for chevron BRBF beams with eccentricities [Figures 9(b) and 9(c)], the interior beam region experiences higher shear forces and relatively lower axial forces, while the exterior beam regions are subject to significant *P-M* interaction demands. When the brace eccentricity is small, the shear design of the interior region may dominate beam sizing. However, as eccentricity increases, the beam sizing is likely to be governed by the *P-M* interaction in the exterior regions.

Figure 10 shows selected beam force diagrams from the 12-story single-diagonal BRBF design cases. Beams on the 4th and 3rd floors were selected for Cases 12S-SD-C and 12S-SD-E2d, respectively, as braces beneath both beams are identical in size (A_{sc} = 8.0 in.^{2}). The forces are shown at point in time when the story below each beam reached about 0.02 rad drift. The NLRHA responses are plotted alongside the estimated force diagrams calculated using the proposed analysis methods. Curves labeled Est. (E), Est. (G), and Est. (E+G) represent the estimated force diagrams for the seismic effect only, gravity effect only, and combination of two effects, respectively. Overall, Figure 10 demonstrates good agreement between the NLRHA and estimated responses across all force diagrams, validating the accuracy of the proposed analysis methods in estimating beam force demands for the capacity design of single-diagonal BRBFs.

As described in Part 1 (Li et al., 2026), the asymmetry of the frame geometry requires two analysis cases for the capacity design of single-diagonal BRBFs. Analysis Case 1 refers to the scenario where seismic loading causes tension in the braces, while Analysis Case 2 involves seismic loading causing compression in the braces. For the concentric Case 12S-SD-C [Figure 10(a)], only the beam actions at positive story drift (braces in tension) are shown since Analysis Case 1 governs the beam capacity design in the concentric frame, as further explained in the following paragraph. In contrast, for the eccentric Case 12S-SD-E2d, beam actions at both positive [Figure 10(b)] and negative [Figure 10(c)] drifts—corresponding to Analysis Cases 1 and 2, respectively—are presented to account for both design scenarios.

In the concentric Case 12S-SD-C [Figure 10(a)], the beam shear and moment demands are primarily due to the gravity effect, as shown by the close alignment of the NLRHA and Est. (G) force diagrams. Thus, these demands remain unchanged regardless of the frame drift direction. For beam axial force [Figure 10(a)-bottom], the compressive force occurs when the braces above and below the beams are in tension, corresponding to Analysis Case 1 for capacity design. Note that the ultimate compressive force in the beam is driven by the maximum possible tensile brace forces, estimated by the tensile adjusted brace strength, P_{uT}, while the ultimate tensile beam force corresponds to the compressive adjusted brace strength, P_{uC}. Since P_{uC} is about 10% higher than P_{uT} (i.e., $\beta = 1.1$) for the braces used for this design case, the magnitude of the ultimate tensile force is expected to exceed the compressive force by around 10%. However, the compressive beam force scenario (Analysis Case 1) is considered to govern the beam design, as a beam's compressive strength is typically lower than its tensile strength by more than 10%.

For the eccentric Case 12S-SD-E2d [Figures 10(b) and 10(c)], each level's BRBF beam consists of two members: the stub and the beam. The shear and moment diagrams indicate that the stub, acting as a cantilever beam, carries significant shear and moment, while the beam member experiences relatively low magnitudes of both demands. Notably, in the shear and moment diagrams within beam member range, the approximately zero magnitude of the Est. (E) curves and the close alignment of the NLRHA and Est. (E+G) responses indicate the two demands in the beam are primarily due to the gravity effect.

In addition, the peak values of shear and moment demands [Figures 10(b) and 10(c)] on the beam member in the eccentric frame are slightly lower than those in the concentric frame [Figure 10(a)], likely due to the shorter length of the beam member in the eccentric frame. This suggests that potentially lighter beam members could be used in the eccentric frame.

For the axial actions in the beam member, it carries high magnitudes of compressive force [Figure 10(b)-bottom] when the adjacent brace is in tension (Analysis Case 1) and axial tension [Figure 10(c)-bottom] when the brace is in compression (Analysis Case 2). Thus, Analysis Case 1 governs the beam member design, as it has a lower capacity in compression.

Regarding the stub, the shear and moment diagrams corresponding to positive drift (braces in tension) [Figure 10(b)] show higher magnitudes for the NLRHA and Est.

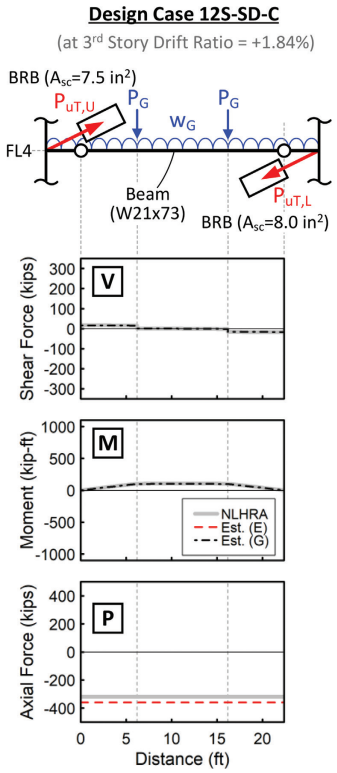

(a) 12S-SD-C, floor 4 at positive drift

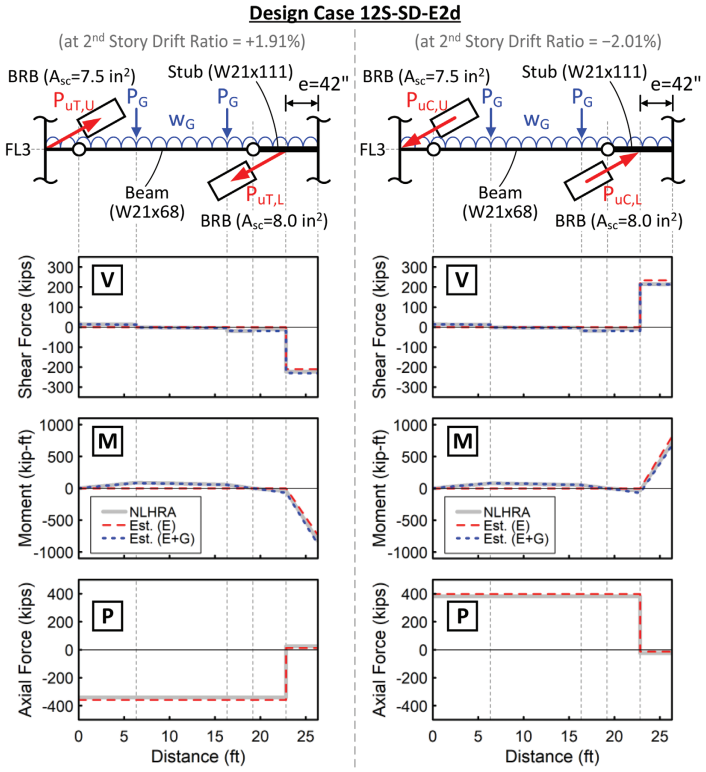

(b) 12S-SD-E2d, floor 3 at positive drift

(c) 12S-SD-E2d, floor 3 at negative drift

Fig. 10. Member forces in selected beams from a NLRHA.

(E+G) responses compared to the Est. (E) response, indicating that the seismic and gravity effects are additive in Analysis Case 1. Conversely, when the adjacent brace is in compression [Figure 10(c)], the magnitudes of NLRHA and Est. (E+G) responses for shear and moment in the stub are lower than those of the Est. (E) response, suggesting that the gravity effect counteracts the seismic effect in Analysis Case 2.

Although the seismic effect is the primary source of the shear and moment demands in the stub, and the magnitudes of seismic-induced demands [Est. (E) response] are expected to be higher in Analysis Case 2 (braces in compression) due to $P_{uC} > P_{uT}$, the total shear and moment demands under the combined seismic and gravity effects in Analysis Case 1—where the two effects are additive—may be higher than the total demands in Analysis Case 2, evidenced by the selected beam responses shown in Figures 10(b) and 10(c). On the other hand, when the adjacent brace has a high β value (i.e., high compression overstrength), the stub may experience higher total shear and moment demands in the Analysis Case 2.

For the axial actions in the stub, it experiences low magnitudes of axial tension [Figure 10(b)-bottom] when the adjacent brace is in tension (Analysis Case 1) and compression [Figure 10(c)-bottom] when the brace is in compression (Analysis Case 2). Although Analysis Case 2 is more critical for the stub's axial action due to being in compression and having a lower capacity, there remains a possibility that the high shear and moment demand in Analysis Case 1 could govern the design. In summary, both Analysis Cases 1 and 2 must be considered for the capacity design of subs.

Column Axial Response

Figure 11 shows the compressive axial demand-to-capacity ratios (DCRs), $P_u/(\phi P_n)$, for the BRBF columns obtained from the NLRHA. Here, P_u is the mean peak compressive forces, averaged from 16 ground motions, for the columns in each story, and ϕP_n is the design compressive strength calculated in accordance with the AISC *Specification for Structural Steel Buildings* (2022b). For the chevron BRBFs, where identical member sizes are used for both sides of columns due to the symmetry of the structure, P_u is taken as

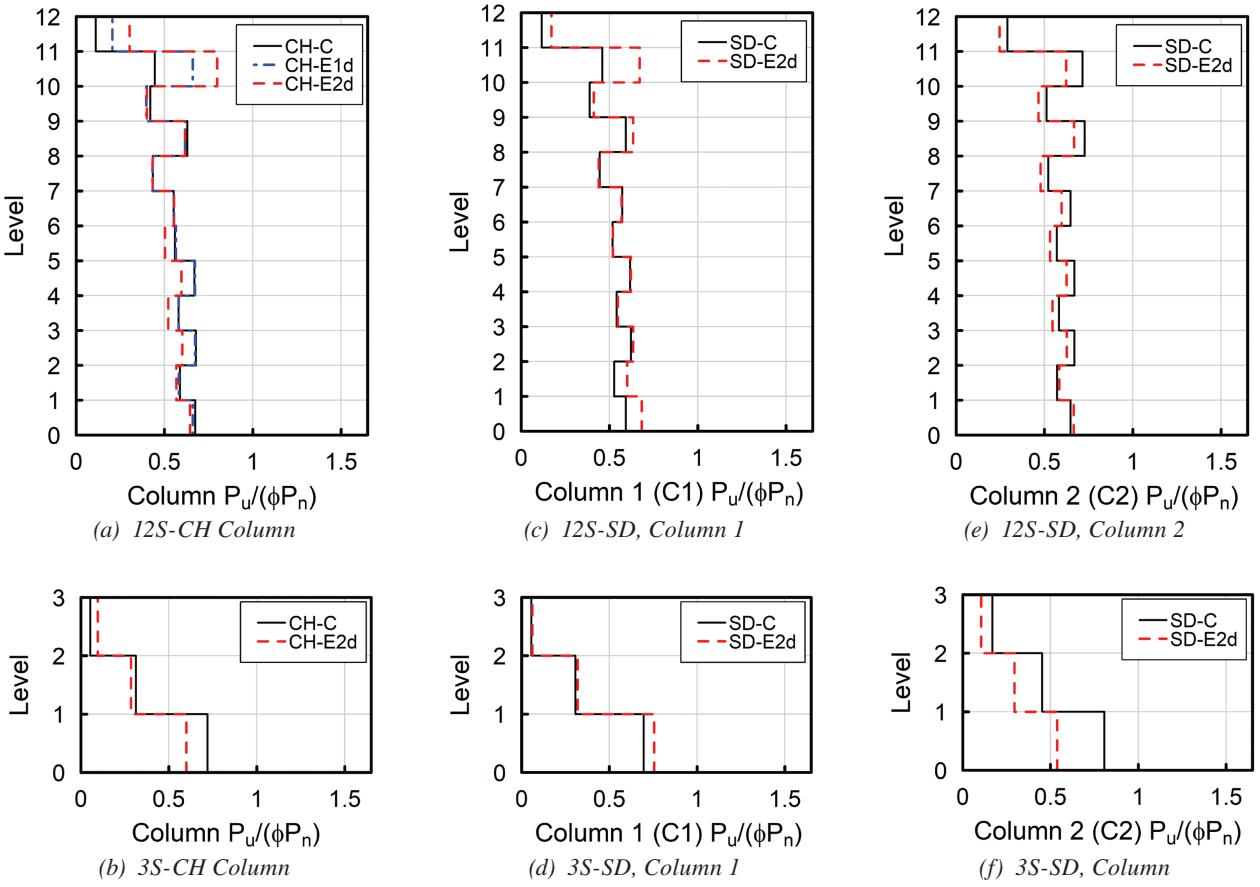

(a) 12S-CH Column *(c) 12S-SD, Column 1* *(e) 12S-SD, Column 2*

(b) 3S-CH Column *(d) 3S-SD, Column 1* *(f) 3S-SD, Column*

Fig. 11. MCE-level compressive DCRs, $P_u/(\phi P_n)$ (mean of maximums).

the larger of peak responses between the two columns in the same story. In contrast, for the single-diagonal BRBFs, where the structure is asymmetric, the columns on each side are designed separately. As illustrated in Figures 1(c) and 1(d), the Column 1 (C1) members refers to the side of the columns adjacent to the brace bottom ends (away from the stubs in eccentric frames), while Column 2 (C2) members refers to the columns adjacent to the brace top ends (next to the stubs in eccentric frames). For these single-diagonal frames, the compressive DCRs for C1 and C2 members were determined separately and are presented individually in Figure 11.

Overall, Figure 11 shows that the column compressive DCR distributions along the building height are similar between the concentric and eccentric BRBFs for all groups, except for Column 2 in Group 3S-SD [Figure 11(f)], where the DCRs of C2 members in Case 3S-SD-E2d were notably smaller than those in 3S-SD-C throughout the building height. This is due to the C2 member size in 3S-SD-E2d being increased to meet the compactness requirements for moderately ductile members, resulting in oversized columns for capacity design. This is reflected in the low DCR values (e.g., 0.62 for the first-story C2 member) in capacity design check as shown in Table 11 of Part 1 (Li et al., 2026). For the 12-story design cases [Figures 11(a), 11(c), and 11(e)], most of the column compressive DCRs from NLRHA ranged between 0.5 to 0.7. For the 3-story frames [Figures 11(b), 11(d), and 11(f)], the largest NLRHA column DCRs, occurring in the first story in each frame, reached about 0.6 to 0.8. It is worth noting that most first-story columns were sized based on the demand from capacity design, with no oversizing for conservatism, as indicated by the capacity design DCR values for exceeding 0.95 [see Tables 10 and 11 of Part 1 (Li et al., 2026)]. As a result, the column design strength ϕP_n closely matches the estimated demand in capacity design, making the NLRHA column DCRs in the first story reflect the ratio of peak dynamic response to the expected axial demand. Thus, the first-story column DCRs in Figure 11 can serve as an index for evaluating the conservatism of the capacity design. The DCR values being notably lower than 1.0 suggest that the assumed plastic mechanism used in capacity design—where all braces in a BRBF develop the adjusted brace strengths (P_{uT} or P_{uC})—is somewhat conservative for estimating the column axial demand, also indicating a low likelihood of simultaneous yielding (to reach the adjustment braces strength) of all braces in a BRBF during the earthquakes.

DETAILED FINITE ELEMENT ANALYSIS

To complement the response history analysis, additional simulations were performed to investigate the stress state in BRBF beams when braces reach design deformations. Pushover analyses were performed on individual frame models where the geometry of the beam and gussets in the connection region were considered explicitly. The ANSYS software (ANSYS, 2022) was used for these analyses.

Frame Geometries

Figure 12 illustrates three frames that were investigated: BRBF-CH-C, BRBF-CH-E1d, and BRBF-CH-E2d. The beam, column, and brace sizes for the frames, came from the first-story designs of the 12-story chevron case study frames: 12S-CH-C, 12S-CH-E1d, and 12S-CH-E2d, respectively. [See Table 1 of Part 1 (Li et al., 2026) for the member sizes.] The three frames have comparable design strength, but different brace and beam sizes based on the proposed design procedures for BRBF with eccentricity (see Section 2 of Part 1).

Modeling Techniques

Three types of elements were used in the models to represent the various components efficiently. The gusset and beam (in the connection region) were modeled with solid hexahedral elements (SOLID186), with a 1 in. mesh size. The gusset-to-beam welds were not modeled explicitly. Outside the gusset region, the beam was represented with elastic beam elements (BEAM188), as were the columns. The BRBs were represented with nonlinear springs

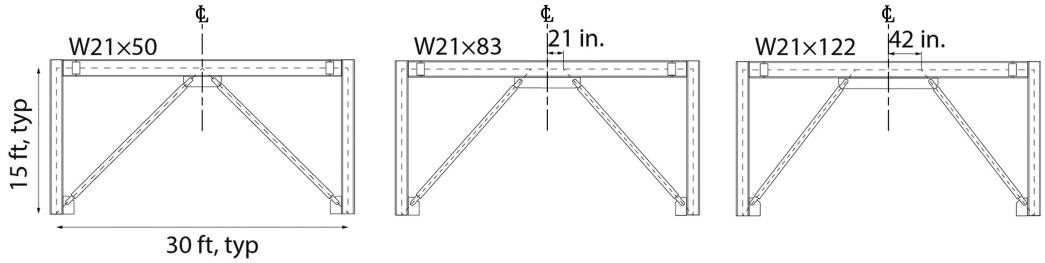

(a) BRBF-CH-C *(b) BRBF-CH-E1d* *(c) BRBF-CH-E2d*

Fig. 12. Frame geometries investigated with detailed finite element analysis.

(COMBIN39) with the elastic stiffness, yield strength, and the post-yield properties summarized in Table 4 of Part 1 (Li et al., 2026).

The boundary conditions and loading in the model were for a displacement-controlled pushover analysis (Figure 13). The column bottom nodes were pinned. Fully restrained connections were assumed at the beam-to-column connection, reflecting gusset plates that would be present from the story above (not modeled). Brace connections were modeled as pinned at each end. The frame was constrained against any out-of-plane displacements. For the lateral loading, in-plane horizontal displacements were imposed at the nodes at the top of the columns. The displacements were ramped up to 3.6 in., corresponding to 2% story drift.

The materials in the finite element (FE) model, for the beams, columns, and gussets, simulated nominal steel properties (Grade 50 material). The elastic modulus was 29,000 ksi, Poisson's ratio was 0.3, yield stress was 50 ksi, and the post-yield modulus was 150 ksi (the material would reach the nominal tensile strength of 65 ksi at 0.1 strain). The material models, with nominal strengths, were appropriate for checking the presence of undesirable yielding/deformations in the beams and gussets.

Validation

As a check on the reasonableness of the models, the results from the pushover analyses were compared with pushover results from centerline models, with the same modeling techniques as used for the NLRHA (discussed earlier). Brace force-deformation plots were checked to confirm that the braces were represented as shown in Figure 2(b).

Figure 14(a) shows the pushover curves for the solid-element models (solid), and the reference centerline models (dashed). For all three geometries, the solid-element model, where the connection geometry was explicitly represented, had essentially the same pushover curve as the centerline model. The frames with eccentricity had less elastic stiffness than the concentric frame, as was previously discussed, but all the frames had similar lateral strength and post-yield stiffness (governed by the braces).

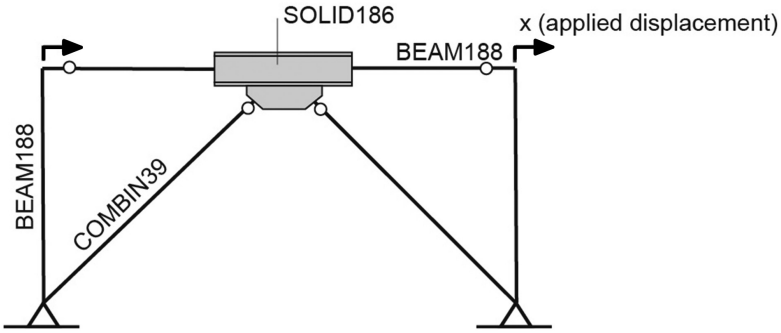

Fig. 13. Element types and boundary conditions for the FE analysis.

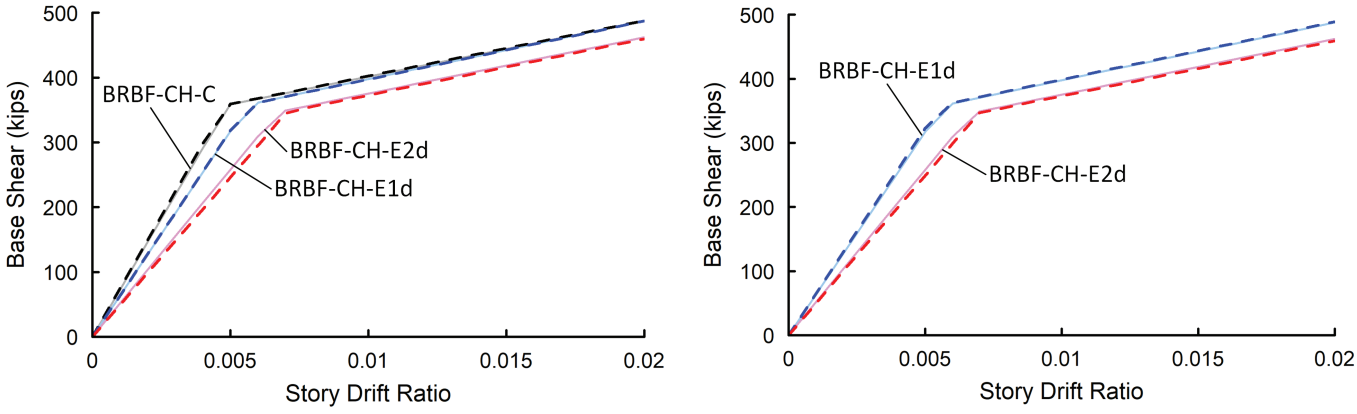

(a) Single gusset models (solid line) and centerline models (dashed line)

(b) Single gusset models (solid line) and split gusset models (dashed line)

Fig. 14. Pushover curves from the detailed FE analysis.

Results

Figure 15 shows the displaced geometry and the equivalent (von Mises) stress in the connection region for the frames at 2% story drift. From Figure 15, beam deformations are essentially imperceptible at that drift. Figure 15(a) shows the case for BRBF-CH-C with a W21×50 beam. The colored contours show that the equivalent (von Mises) stress reached 39.0 ksi in the center of the beam web, caused by beam shears from the chevron effect (Sabelli and Arber, 2017), which was considered in design. Figure 15(b) shows BRBF-CH-E1d (W21×83 beam), where the equivalent (von Mises) stress reached 35.3 ksi in the center of the beam web, caused by beam shears from the eccentricity (which were considered in the design). The design procedure for the beam conservatively neglected any shear carried by the gusset plate. The model confirmed that the design methods discussed in the second section of Part 1 (Li et al., 2026) are conservative for preventing the beam from reaching a shear yielding limit state, even when the braces are at their design deformation. Figure 15(c) shows BRBF-CH-E2d (W21×122 beam), where the web stresses reflect beam shears and moments caused by the eccentricity. Here, the equivalent (von Mises) stress was even further below 50 ksi, at 29.6 ksi in the center of the beam web, confirming the reasonableness of the design approach. Considering all three together,

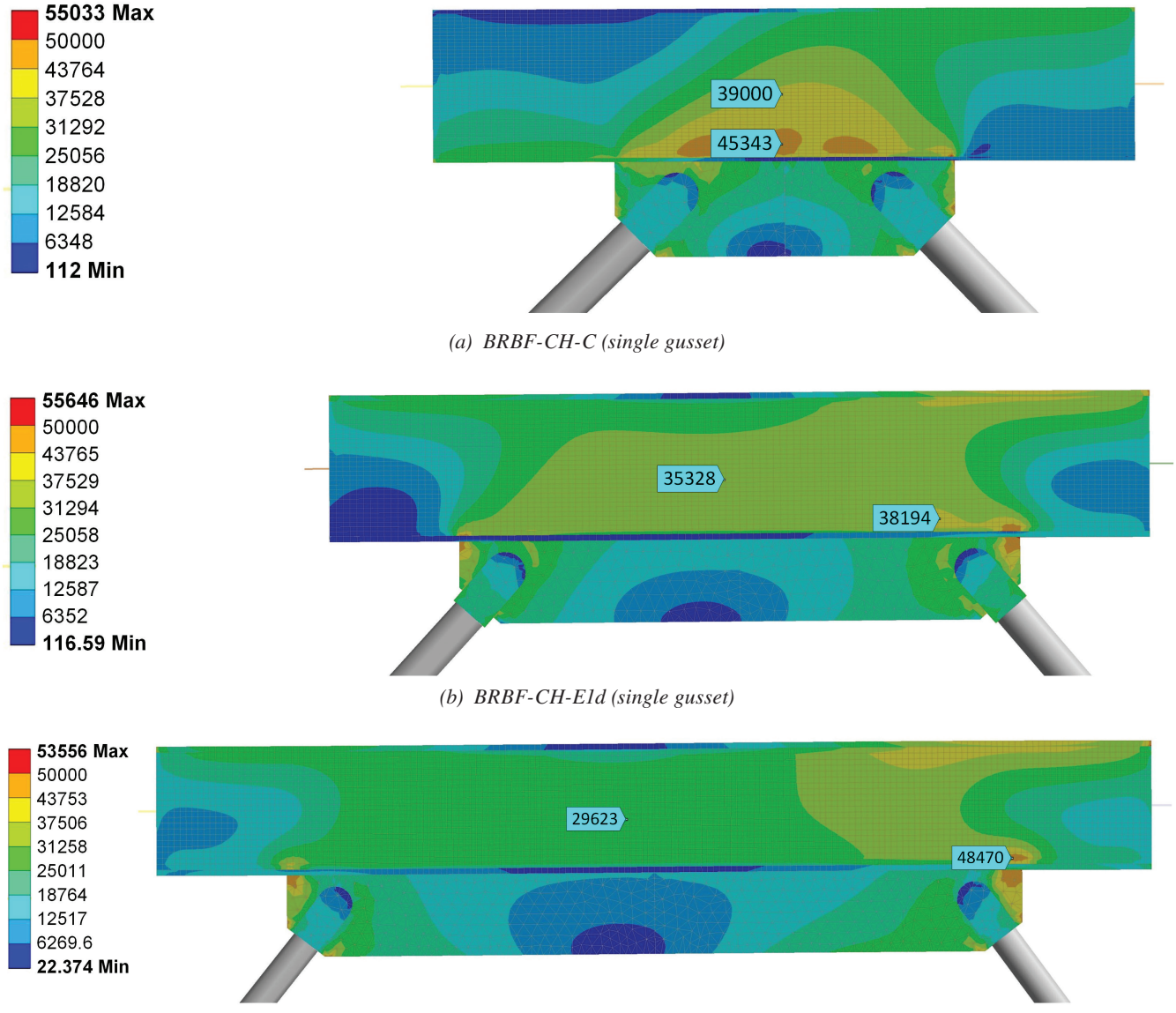

(a) BRBF-CH-C (single gusset)

(b) BRBF-CH-E1d (single gusset)

(c) BRBF-CH-E2d (single gusset)

Fig. 15. Equivalent (von Mises) stress contours (unit: psi) in the gusset connection regions at 2% story drift in single gusset models.

BRBF-CH-E1d and BRBF-CH-E2d had lower shear stress in the beam web than BRBF-CH-C, and the source of the beam web shear stress was different (the chevron effect for BRBF-CH-C, and connection eccentricity for BRBF-CH-E1d and BRBF-CH-E2d).

Figures 16 and 14(b) shows results for variants of the models that have split gusset plates. From Figure 16, the split gusset plate results in higher beam web stresses, but a limit state has not been reached. The two cases in Figure 16 appear to be on the verge of requiring stiffeners to address web local yielding in the beam at the end of the gusset. From Figure 14(b), the pushover curves are essentially the same for the combined (i.e., single) and split gusset configuration. For the BRBF-CH-E1d frame, the combined gusset model exhibits slightly less elastic lateral stiffness compared to the split gusset model, which was unexpected and is likely due to the increased flexural deformations in the beams outside the combined gusset. However, for the BRBF-CH-E2d frame, the combined gusset slightly enhances the frame's elastic lateral stiffness compared to the split gusset.

Moreover, the stress ratios of the equivalent stress in the beam web (within the eccentricity range) divided by the yield stress of 50 ksi, as obtained from the split-gusset models (Figure 16), are approximately 0.88 and 0.74 for BRB-CH-E1d and BRB-CH-E2d, respectively. For comparison, an adjusted DCR for PV interaction, denoted as $DCR_{PV,adj}$, is introduced. This value is obtained by multiplying the estimated DCR_{PV} of chevron beam design [listed in Table 8 in Part 1 (Li et al., 2026)] by ϕ_v to remove the conservatism inherent in the ϕ_v factor. The calculated $DCR_{PV,adj}$ values for the first-story beams in Design Cases 12S-CH-E1d and 12S-CH-E2d are about 0.86 and 0.73, respectively, both of which are close to the beam web stress ratios developed in the corresponding FE model. It should be noted that the estimated DCR_{PV} was based on the simplified beam model using concentrated brace forces without considering the local chevron effect (Fortney and Thornton, 2017) from the chevron gusset connection geometry. The strong agreement between $DCR_{PV,adj}$ values and stress ratios from FE models reflecting the localized effect indicates that the chevron effect is small relative to the shears and moments caused by the eccentricity.

DESIGN IMPLICATIONS ON SINGLE-DIAGONAL BRBF WITH ECCENTRICITY

Design of Half-Moment Frame Column

General

When a single-diagonal BRBF with eccentricity is subjected to lateral forces, as illustrated in Figure 17, the stubs transfer bending moments to the adjacent Column 2 (C2) members due to the moment connections between the stubs

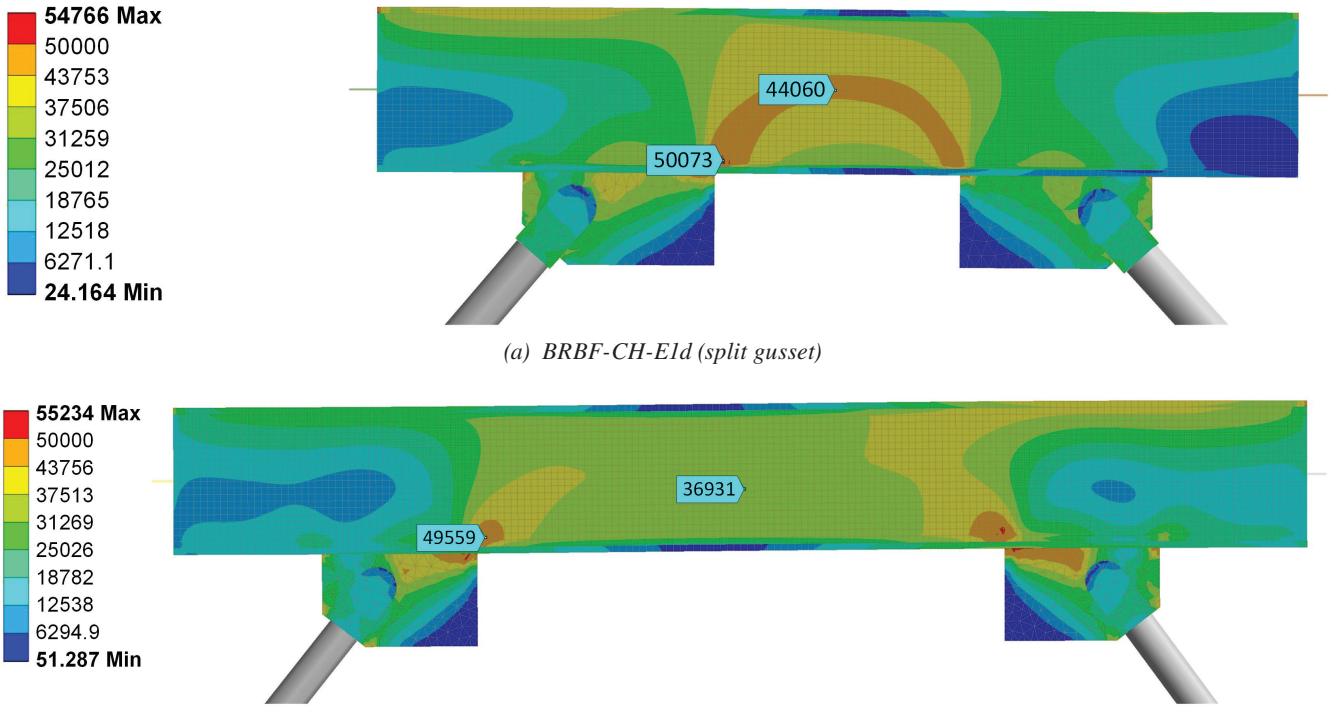

(a) BRBF-CH-E1d (split gusset)

(b) BRBF-CH-E2d (split gusset)

Fig. 16. Equivalent (von Mises) stress contours (unit: psi) in the gusset connection regions at 2% story drift in split gusset models.

and C2 members that make up the half-moment frames. This moment demand can become significant, especially in cases where the eccentricity is large. Although the AISC *Seismic Provisions* (2022a) permit the neglecting of seismic-induced moment demands in the design of conventional BRBF columns, it is unclear whether this provision is suitable for single-diagonal eccentric BRBFs. Therefore, this sub-study examines the impact of including moment demands in the design of C2 members through a series of NLRHA analyses, which will be discussed in this section.

Estimation of Moment Demand in Column

This study proposes a method, illustrated in Figure 17, to estimate seismic moment demands in the C2 members. Recall that two analysis cases must be considered separately for capacity design of single-diagonal BRBFs. Analysis Cases 1 and 2 refer to the scenarios where seismic loading causes the braces in tension and compression, respectively. Figures 12 and 13 of Part 1 (Li et al., 2026) present the axial force analyses in column capacity design for these respective analysis cases. It is hypothesized that the governing moment demand in C2 members would occur in Analysis Case 1, rather than Analysis Case 2, for two reasons:

1. Axial load interaction: In Analysis Case 1, as shown in Figure 12 of Part 1, C2 members are subjected to overturning (OT) compression, and simultaneous moment demands should be considered for the combined axial-flexure (*P-M*) interaction design. This makes Analysis Case 1 more critical as the interaction between axial compression and bending moments intensifies the demand on C2 members.
2. Combination of seismic and gravity effects: In Analysis Case 1, as shown in Figure 9 of Part 1, seismic and gravity effects on the bending actions in the stubs are additive. In contrast, these two effects counteract each other in Analysis Case 2, as depicted in Figure 10 of Part 1. Consequently, both the stubs and the adjacent C2 members are expected to resist higher moment demands in Analysis Case 1 compared to Analysis Case 2 under typical conditions. An exception to this could occur if the brace exhibits high compression overstrength, indicated by a high β value, which could lead to higher moment demands in the stub and C2 members in Analysis Case 2. Despite this, Analysis Case 1 would still govern the design because C2 members experience OT tension in Analysis Case 2, which is less critical than OT compression in Analysis Case 1.

The proposed distribution of seismic moments at stub-to-column intersections is illustrated in Figure 17-right. This approach estimates the capacity-limited seismic load effects, E_{cl}, on C2 member end moments. First, the maximum moment at the stub is determined in Analysis Case 1, where each stub is subjected to the tensile adjusted strength, P_{uT}, from the adjacent brace. The seismic moment at the ith level stub's end, $M_{Ecl1,Stub,i}$ (where the subscript $Ecl1$ refers to E_{cl} effect in Analysis Case 1), is given by:

$$M_{Ecl1,Stub,i} = e(P_{uT,i}\sin\theta_i) \tag{1}$$

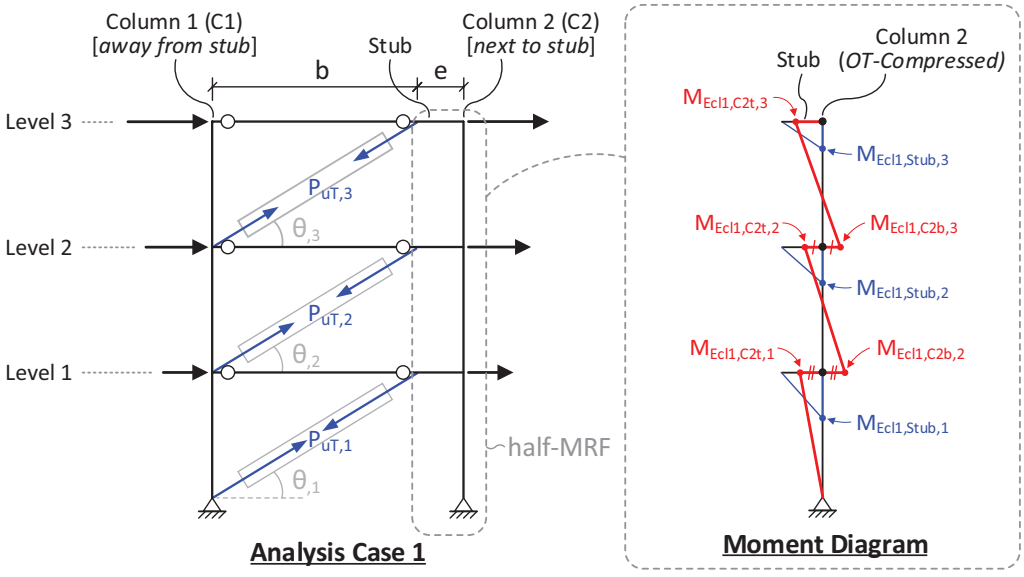

Fig. 17. Estimation of capacity-limited seismic load effects on moment demands in Column 2 (C2) members in a single-diagonal eccentric BRBF.

Here, $P_{uT,i}$ is the tensile adjusted strength, and θ_i is the inclination angle of the ith story brace.

For typical floors, the seismic moment at the stub end calculated from Equation 1 is assumed to be equally distributed between the adjacent C2 members above and below the stub:

$$M_{Ecl1,C2b,i+1} = M_{Ecl1,C2t,i} = \frac{M_{Ecl1,Stub,i}}{2} \tag{2}$$

At the roof (Nth level), the entire stub-end moment is transferred to the adjacent C2 member's top end:

$$M_{Ecl1,C2t,N} = M_{Ecl1,Stub,N} \tag{3}$$

Finally, the total moment demand at the ends of C2 member, $M_{u,C2}$ for beam-column design is determined by combining gravity and seismic load effects:

$$M_{u,C2} = B_1\left[(1.2+0.2S_{DS})M_{D,C2} + f_L M_{L,C2}\right] + M_{Ecl1,C2} \tag{4}$$

where $M_{D,C2}$ and $M_{L,C2}$ are the moments due to dead and live loads, respectively; f_L is the load factor for live load; $M_{Ecl1,C2}$ is the capacity-limited seismic moment estimated from Equations 2 or 3; S_{DS} is the design spectral response acceleration parameter at short periods (ASCE, 2022); and B_1 is the multiplier factor from AISC *Specification* Appendix 8 (AISC, 2022b), accounting for the P-δ effect.

It is important to acknowledge that the assumption of equal moment distribution between the columns may underestimate the peak dynamic moment at one of the columns at the stub-to-column intersection during seismic events. The actual distribution of moments may be influenced by the relative flexural stiffness of the two adjacent columns and higher-mode effects of the building. Consequently, the distribution may not be perfectly symmetrical, especially when stiffness variations or higher-mode effects are significant. Nonetheless, the assumption of even moment distribution offers a practical simplification for design purposes. Additionally, as shown in Figure 11, the capacity design method often overestimates the actual peak axial force in the columns during earthquakes, indicating some tolerance for underestimating moment demand in combined axial and flexural design. A series of NLRHA were conducted, and the results of these analyses will be presented later to provide further insight into the adequacy of the proposed column moment demand estimations.

Candidate Design Methods and Additional Design Cases

To investigate the effect of including moment demand for design of C2 members, three candidate design methods were utilized in this study for sizing and resizing the C2 members in Design Cases 12S-SD-E2d and 3S-SD-E2d. The three design methods are described as follows:

1. Design Method N (axial-only design): The designation N refers to normal and axial-only design, where the C2 members in the single-diagonal eccentric BRBFs are treated as the normal BRBF columns. The seismic moment is neglected, as permitted by the AISC *Seismic Provisions* (2022a), provided the capacity-limited seismic effect is considered for sizing the BRBF columns. Further, in the design cases considered in this study, the gravity moment demands in the C2 members are minimal and considered negligible. Therefore, for Design Method N, the C2 members are designed based solely on axial force demand, excluding moment demand from the design process. The demand-to-capacity ratio (DCR) for axial force, DCR_P, is calculated as:

$$DCR_P = \frac{P_u}{\phi_c P_n} \tag{5}$$

where P_u is the axial force due to combined gravity and capacity-limited seismic effects [as determined in Part 1, Equations 24 and 26 (Li et al., 2026)], and $\phi_c P_n$ is the design compressive strength.

2. Design Method M (strong column–weak beam design): The label M stands for moment-resisting frame (MRF) column design. This method acknowledges that the stubs and C2 members in a single-diagonal eccentric BRBF function together as a half-MRF [Figures 1(c) and 1(d)] and thus treats the C2 members as MRF columns. The strong column–weak beam (SCWB) design approach, which is typically used for the special moment frame (SMF) columns, is adapted for sizing the C2 members. The associated DCR, DCR_{SCWB}, for each stub-to-column intersection is calculated as:

$$DCR_{SCWB} = \frac{M_{u,Stub}}{\sum M^*_{pc}} = \frac{M_{u,Stub}}{\sum\left[Z_{xc}\left(F_{yc} - \frac{P_u}{A_{gc}}\right)\right]} \tag{6}$$

The term $M_{u,Stub}$ is the total stub-end moment demand projected to column centerlines, incorporating both gravity effect and capacity-limited seismic effect from the adjacent brace's adjusted strength. This differs from the conventional SCWB equation for SMF, which uses the sum of beam plastic moment projections to the column centerline, as shown in ΣM^*_{be} in the AISC *Seismic Provisions* (2022a), reflecting the different performance objectives between the half-MRF and SMF.

It is also noted that the stubs and moment connections between the stubs and C2 members are designed to remain elastic, with force demands capped by the adjacent braces' capacity. Therefore, the stub-to-column connections do not require strict seismic detailing typical of SMFs, such as WUF-W welds. Additionally, these

welds can be made in the shop, with quality achieved without seismic detailing. The equation for determining $M_{u,Stub}$ is as follows:

$$M_{u,Stub} = (1.2 + 0.2S_{DS})M_{D,Stub} + f_L M_{L,Stub} + M_{Ecl1,Stub} \quad (7)$$

where $M_{D,Stub}$ and $M_{L,Stub}$ are the moments due to dead and live loads, respectively, and $M_{Ecl1,Stub}$ is the capacity-limited seismic moment, estimated from Equation 1. The term ΣM^*_{pc} in Equation 6 is the sum of the nominal flexural strengths of the columns above and below the stub-to-column intersection, projected to the beam centerline, with a reduction for the total axial demand, P_u, including seismic capacity-limited effect in C2 members, as determined in Part 1, Equations 24 and 26 (Li et al., 2026). The symbols F_{yc}, A_{gc}, and Z_{xc} in Equation 6 denote the nominal yield strength, gross area, and plastic modulus, respectively, for the C2 member. Notably, in contrast to the SCWB equation for SMF, the column capacity term ΣM^*_{pc} is intentionally placed in the denominator term of Equation 6 to ensure that a value of $DCR_{SCWB} \leq 1.0$ indicates compliance of SCWB requirements. This arrangement facilitates discussions concerning two other candidate design methods.

3. Design Method X (*P-M* interaction design): The notation X signifies the extra conservatism in the *P-M* interaction design check for C2 members, with an attempt to maintain their elasticity under the capacity-limited seismic effect for both axial and flexural demands. In this design method, the associated DCR, DCR_{PM}, is calculated using the *P-M* interaction equation in AISC *Specification* Chapter H (2022b) as follows:

$$DCR_{PM} = \begin{cases} \left|\frac{P_u}{\phi P_n}\right| + \frac{8}{9}\left|\frac{M_u}{\phi_b M_n}\right|, \ for \left|\frac{P_u}{\phi P_n}\right| \geq 0.2 \\ \frac{1}{2}\left|\frac{P_u}{\phi P_n}\right| + \left|\frac{M_u}{\phi_b M_n}\right|, \ for \left|\frac{P_u}{\phi P_n}\right| < 0.2 \end{cases} \quad (8)$$

where P_u [Part 1, Equations 24 and 26 (Li et al., 2026)] and M_u (Equation 4) represent total axial and flexural demands, respectively, including the capacity-limited seismic effect. In Equation 8, the design axial strength ϕP_n is taken as the compressive strength $\phi_c P_n$, and $\phi_b M_n$ is the design flexural strength.

It is worth noting the comparison of the design intentions of the three methods (N, M, and X). First, Design Method N follows the general rule from the AISC *Seismic Provisions* (2022a) for designing columns in the seismic force resisting system (SFRS), where the SFRS columns are designed based solely on axial force demand (i.e., Design Method N), provided the capacity-limited seismic effect is included in the axial force calculation. This approach aims to prevent global column failure but does not guarantee the columns from yielding under the combined axial and moment demands. The rationale is that in the SFRS, bending moments tend to peak at the column ends, often resulting in reversed curvature in the columns, which minimizes the impact of bending moments on column buckling. With this relaxation in ignoring moment demand, Design Method N serves as the "baseline" for C2 member design.

Second, Design Method M adopts the strong column–weak beam (SCWB) design concept, which is specific to SMF systems, to address the potential issue of the significant moments in the MRF columns. This approach aims to ensure that columns are strong enough to avoid concentrating inelastic action in a single story, though it offers no assurance that individual columns will remain elastic. Notably, the SCWB method evaluates the reduced moment capacity due to axial force using the sectional yield criterion, without considering column buckling, making it less stringent in estimating the moment strength than the typical *P-M* interaction check for beam-column design. In summary, the SCWB-based Design Method M represents the code-specified additional design criterion for SMF columns, typically subjected to significant moments. In SMF column design, the SCWB method often surpasses the axial-only approach, which is the baseline design for general SFRS columns, and governs the final design, particularly in moment-critical scenarios.

Lastly, Design Method X incorporates the proposed estimation of column moment demand into *P-M* interaction check for conducting beam-column design of C2 members. This method aims to maintain elasticity of C2 members under combined axial and flexural forces, including capacity-limited seismic effects. It is stricter than the AISC *Seismic Provisions* (2022a) requirements for columns in any SFRS system and typically results in a heavier design than the other two methods. Thus, Design Method X embodies extra conservatism beyond regulatory standards. Despite this conservatism, its effectiveness in preventing the yielding of individual columns is evaluated through the NLRHA studies presented later.

Note that the C2 members in both single-diagonal eccentric cases, 12S-SD-E2d and 3S-SD-E2d, presented earlier were effectively sized using Design Method N. In addition to the two original cases, the C2 members in these two designs were redesigned using Design Methods M and X, while keeping the sizes of the other members (braces, beams, and C1 members) the same. This resulted in three additional design cases, bringing the total to five design cases of single-diagonal eccentric BRBFs, which will be discussed later. Tables 3 and 4 summarize the design results of the C2 members, including member sizes and associated DCRs for the three design methods across the five design

Table 3. Design DCRs for Column 2 (C2) in Two Designs of 12-Story Single-Diagonal Eccentric BRBFs								
	12S-SD-E2d-N/M (= Original 12S-SD-E2d)				12S-SD-E2d-X			
Story	C2 Shape	DCR_P	DCR_{SCWB}	DCR_{PM}	C2 Shape	DCR_P	DCR_{SCWB}	DCR_{PM}
12	W14×48	0.33	0.96	1.13	W14×68	0.18	0.62	0.70
11	W14×48	0.86	0.95	1.62	W14×68	0.47	0.58	0.98
10	W14×82	0.65	0.92	1.11	W14×109	0.39	0.55	0.73
9	W14×82	0.93	0.91	1.43	W14×109	0.56	0.53	0.93
8	W14×120	0.67	0.87	1.03	W14×145	0.54	0.55	0.84
7	W14×120	0.84	0.86	1.23	W14×145	0.68	0.57	1.00
6	W14×159	0.76	0.86	1.07	W14×193	0.62	0.55	0.87
5	W14×159	0.91	0.88	1.24	W14×193	0.74	0.54	1.01
4	W14×211	0.79	0.82	1.05	W14×257	0.65	0.49	0.86
3	W14×211	0.91	0.78	1.19	W14×257	0.75	0.46	0.97
2	W14×257	0.85	0.79	1.08	W14×311	0.70	0.46	0.89
1	W14×257	0.96	0.80	1.19	W14×311	0.79	0.45	0.97

Table 4. Design DCRs for Column 2 (C2) in Three Designs of 3-Story Single-Diagonal Eccentric BRBFs												
	3S-SD-E2d-N				3S-SD-E2d-M (= Original 3S-SD-E2d)				3S-SD-E2d-X			
Story	C2 Shape	DCR_P	DCR_{SCWB}	DCR_{PM}	C2 Shape	DCR_P	DCR_{SCWB}	DCR_{PM}	C2 Shape	DCR_P	DCR_{SCWB}	DCR_{PM}
3	W14×82	0.21	0.82	0.56	W14×109	0.13	0.57	0.64	W14×132	0.10	0.46	0.52
2	W14×82	0.58	0.91	1.42	W14×109	0.35	0.61	0.96	W14×132	0.29	0.48	0.79
1	W14×82	1.03	1.69	1.87	W14×109	0.62	0.98	1.23	W14×132	0.51	0.73	1.01

Table 5. Steel Weights for Design Cases							
Group	Design Case	BRB (kips)	Column (kips)	Beam (kips)	Frame (kips)	Frame + BRB (kips)	Increase (%)
12S-SD	12S-SD-E2d-N/M†	17.39	50.61	23.42	74.03	91.42	—
	12S-SD-E2d-X	17.39	56.79	23.42	80.21	97.60	+6.76%
3S-SD	3S-SD-E2d-N	4.74	6.44	5.74	12.17	16.92	—
	3S-SD-E2d-M‡	4.74	7.65	5.74	13.39	18.13	+7.18%
	3S-SD-E2d-X	4.74	8.69	5.74	14.42	19.17	+13.30%

† Original Case 12S-SD-E2d
‡ Original Case 3S-SD-E2d

cases. Table 5 presents the steel weights for these design cases.

For 12-story frames (Table 3), the original Case 12S-SD-E2d is renamed 12S-SD-E2d-N/M, with the postfix N/M indicating that the results are derived from both Design Methods N and M. For most stories, both DCR_P and DCR_{SCWB} range from 0.8 to 1.0. Notably, for this 12-story frame, the SCWB design does not require heavier C2 members as compared to the baseline design. Case 12S-SD-E2d-X represents the results from Design Method X, as evidenced by all DCR_{PM} essentially not greater than 1.0, along with all DCR_{PM} and DCR_{SCWB} values notably lower than 1.0. As shown in Table 5, Design Method X (Case 12S-SD-E2d-X), aiming to ensure the elasticity of

individual columns, requires approximately a 7% increase in the total steel weight of the entire frame compared to the other two design methods.

For 3-story frames (Table 3), the original Case 3S-SD-E2d is renamed 3S-SD-E2d-M, with the postfix M indicating that it represents Design Method M. It should be noted that the size of C2 members (W14×109) in this design case was originally determined by the compactness requirements for moderately ductile members. This choice unintentionally results in a DCR_{SCWB} value slightly less than 1.0 for the first story, serving as a good representative for Method M. However, this design also indicates an overdesign for Design Method N, as evidenced by DCR_P values notably less than 1.0. Hence, an additional Case 3S-SD-E2d-N was developed to represent Method N, with the DCR_P (1.03) being slightly higher than 1.0 for the C2 member in first story, while the DCR_{SCWB} and DCR_{PM} values notably exceed 1.0 in the same story. Furthermore, another case, 3S-SD-E2d-X, was developed to represent Design Method X, as evidenced by its DCR_{PM} value (1.01) barely exceeding 1.0, accompanied with relatively low DCR_P and DCR_{SCWB} values for the first story. From Table 5, it can be observed that for these 3-story frames, the SCWB-based Design Method M (3S-SD-E2d-M) requires an increase of about 7% in the total steel weight as compared to the baseline Design Method N (3S-SD-E2d-N). In contrast, achieving Design Method X (3S-SD-E2d-X) requires an increase of approximately 13% in total steel weight.

Analytical Study Results

A series of NLRHA studies were conducted to evaluate the seismic performance of the five design cases representing different design methods for C2 members. For each design case, two OpenSees models (Mazzoni et al., 2006) were developed using the modeling setup illustrated in Figure 2(a). One model uses fiber beam column elements for the BRBF column elements to simulate the nonlinear response under *P-M* interaction, while the other employs elastic beam column elements for the BRBF columns to represent a pseudo case with perfectly elastic column behavior. The models are named after their respective design cases, with a postfix fib or ela to represent the use of fiber or elastic beam column elements.

Figures 18 through 20 show the MCE-level NLRHA results for these models subjected to the same two suites of 16 ground motions used for analyses on 12-story and 3-story models discussed in Section 2. These figures display the mean structural responses, including peak story drifts and peak *P-M* interaction demands on C2 members, averaged across 16 ground motions. To quantify the *P-M* interaction at each end of C2 members, two parameters were employed: the conventional DCR for *P-M* interaction (DCR_{PM}), as defined in Equation 8, and the yield ratio (YR), which evaluates the sectional yielding at the column ends. The YR is calculated as:

$$\text{YR} = \left|\frac{P_u}{P_{ye}}\right| + \left|\frac{M_u}{M_{pe}}\right| \tag{9}$$

where the axial demand, P_u, and flexural demand, M_u, are obtained from the NLRHA. The expected sectional yield axial force, P_{ye}, and the expected plastic moment, M_{pe}, are calculated as:

$$P_{ye} = R_y F_{yc} A_{gc} \tag{10}$$

$$M_{pe} = R_y F_{yc} Z_{xc} \tag{11}$$

where the factor R_y = 1.10 accounts for the material overstrength. A value of YR exceeding 1.0 indicates the sectional yielding of the column end.

The value of DCR_{PM} is determined using Equation 8 with the demands P_u and M_u obtained from the NLRHA. As C2 members experience alternating tension and compression during the NLRHA, the design axial strength ϕP_n in Equation 8 is taken as the tensile yielding strength $\phi_t P_y$ if the axial demand P_u is in tension, while the compressive strength $\phi_c P_n$ is used when P_u is compressive. Since DCR_{PM} accounts for buckling strength in compressive axial forces and incorporates the strength reduction factors (ϕ-factors) for both axial and moment capacities, its values are always greater than the YR values, which reflect sectional yielding based on the expected yield strength.

Figure 18 compares the NLRHA results between Cases 12S-SD-E2d-N/M and 12S-SD-E2d-X. For all responses shown, the overlapping results between the fib (with fiber columns) and ela (with elastic columns) models for both cases indicate no significant column yielding in either frame. As illustrated in Figure 18(a), both design cases perform well, with their story drifts remaining below the code-prescribed limit (ASCE, 2022). The story drifts of Case 12S-SD-E2d-X were slightly smaller than those of 12S-SD-E2d-N/M in several stories, specifically in the bottom two and upper five stories. This indicates that using heavier C2 members, as determined from the stricter Design Method X, does not notably enhance the performance of this 12-story eccentric BRBF compared to the frame designed with the other two methods.

Figure 18(b) shows that all the mean peak DCR_{PM} values at the ends of the C2 members in Case 12S-SD-E2d-X are less than 1.0, indicating that the objective of Design Method X is achieved. In contrast, DCR_{PM} values exceed 1.0 in only few stories (the 9th and 11th stories) in Case 12S-SD-E2d-N/M. Figure 18(b) gives the results of forces taken from the NLRHA and analyzed using Equation 8. It should be noted that a value of DCR_{PM} slightly above 1.0 from MCE-level NLRHA does not necessarily indicate column yielding and should not be directly interpreted as

failure. This is because the AISC *Seismic Provisions* generally allow the neglect of seismic moment demands (permitting some sectional yielding under *P-M* interaction) and supports an axial-only design approach for SFRS columns, which helps prevent global instability due to column buckling. The justification for applying the same principle to the C2 members in the 12-story cases is discussed below.

First, the conservative assumption of simultaneous yielding for all braces in a BRBF in column capacity design leads to an overestimate in the dynamic column axial force, as evidenced by the axial-only NLRHA DCR_P values being notably less than 1.0, as shown in Figure 11(e). These low DCR_P values indicate that the C2 members are far from column buckling.

Second, the moderate exceedance of DCR_{PM} in 12S-SD-E2d-N/M need not be of concern, as evidenced by the fact that all mean peak yield ratios are notably less than 1.0 as shown in Figure 18(c), indicating no yielding of any C2 members in 12S-SD-E2d-N/M. In addition, the peak yield ratios (denoted as Max. Response) from the 16 ground motions for the C2 members in 12S-SD-E2d-N/M are also plotted in Figure 18(c). Even these extreme column responses had yield ratios lower than 1.0. This suggests that relying solely on Design Methods N (axial-only design) or M (SCWB design) for this 12-story eccentric BRBF can effectively prevent sectional yielding under *P-M* interaction in the C2 members.

Lastly, the overestimation in axial forces in column capacity is particularly significant for high-rise buildings, which explains why the C2 members in 12-story BRBF considered, despite being designed for axial force only, do not fully consume all their capacity for axial action and retain sufficient strength to accommodate the concurrent moment demands.

Figure 19 compares the NLRHA results between Cases 3S-SD-E2d-N and 3S-SD-E2d-X. Figure 19(a) shows that all story drifts in both frames remain below the code limit (ASCE, 2022), indicating satisfactory global performance for both cases. For Case 3S-SD-E2d-X, the overlapping results between the fib and ela models for all responses indicate no notable column yielding. In this design case, the mean peak DCR_{PM} mildly exceeds 1.0 only at the top end of the first-story C2 member [Figure 19(b)] while remaining below 1.0 for the other C2 members. This suggests that, although the conventional *P-M* interaction check (Design Method X) is used for sizing C2 members, and the dynamic axial demands are generally overestimated for these members [Figure 11(f)], the proposed estimation method—assuming an even distribution of moments between column ends at a stub-to-column intersection—may underestimate the moment demands at certain ends of C2 members in a low-rise BRBF, leading to the observed exceedance of DCR_{PM} [Figure 19(b)]. Nonetheless, Figure 19(c) shows that in Case 3S-SD-E2d-X, the mean peak yield ratios are less than 1.0 for all C2 members, indicating that employing Design Method X is likely effective in preventing sectional yielding in C2 members for low-rise BRBFs.

In Case 3S-SD-E2d-N, there are clear deviations between the fib and ela models for the responses of DCR_{PM} [Figure 19(b)] and yield ratio [Figure 19(c)] for C2 members in the lower two stories. Additionally, the mean peak yield ratios exceed 1.0 for these C2 members. These findings indicate that considerable yielding occurs at the top end of the first-story column and at both ends of the

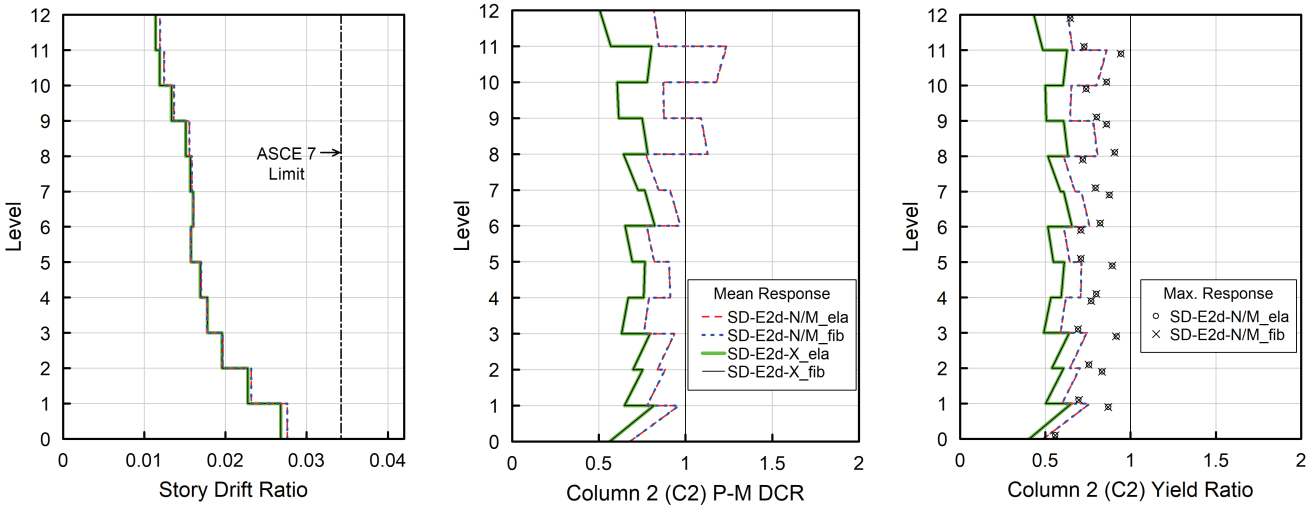

(a) Story-drift ratio

(b) P-M interaction DCR of Column 2 (C2) members

(c) Yield ratio of C2 members

Fig. 18. Comparison of NLRHA results between Design Cases 12S-SD-E2d-N/M and 12S-SD-E2d-X.

second-story column, suggesting that relying solely on the axial-only design (Design Method N) could lead to yielding of the C2 members in low-rise BRBFs. However, this sectional nonlinearity may not be of a concern, as the AISC *Seismic Provisions* (2022a) do not prohibit yielding at the SFRS column ends. Moreover, for the story drifts of Case 3S-SD-E2d-N [see Figure 19(a)], the responses from the fib and ela model are close to each other, exhibiting only minor deviations. This suggests that, despite some yielding developing in the C2 members (in the fib model), the global response of the BRBF remains very similar to that of the elastic case (in the ela model). Moreover, the story drifts of Case 3S-SD-E2d-N are only mildly greater than those of the conservatively designed Case 3S-SD-E2d-X in the bottom two stories. These indicate that employing the baseline axial-only design would not significantly reduce the global seismic performance of low-rise BRBFs, despite the potential local yielding in some C2 members.

Figure 20 shows the NLRHA results of Case 3S-SD-E2d-M in comparison to 3S-SD-E2d-X. For the story-drift response [Figure 20(a)], Case 3S-SD-E2d-M barely exceeds 3S-SD-E2d-X in the first story, accompanied with almost overlapping results between the two frames in the upper two stories. This suggests that using the SCWB-based Design Method M for C2 members can achieve a global seismic performance very close to that of the conservative Design Method X for low-rise BRBFs.

For Case 3S-SD-E2d-M, there are sight deviations between the fib and ela models for the responses of DCR_{PM} [Figure 20(b)] and the yield ratio [Figure 20(c)] of C2 members at the top of first story. In addition, the mean peak yield ratio slightly exceeded 1.0, indicating minor yielding, at the top of a first-story C2 member. It should be noted that while the SCWB design for the C2 members (3S-SD-E2d-M) requires merely about a 7% increase in total steel weight compared to the frame (3S-SD-E2d-N) determined from the axial-only design for C2 members, the yielding of C2 members in 3S-SD-E2d-M [Figure 20(c)] is significantly less than that of 3S-SD-E2d-N [Figure 19(c)]. This suggests that, for the low-rise BRBFs, employing SCWB design for the C2 members could be an efficient way to minimize the column yielding.

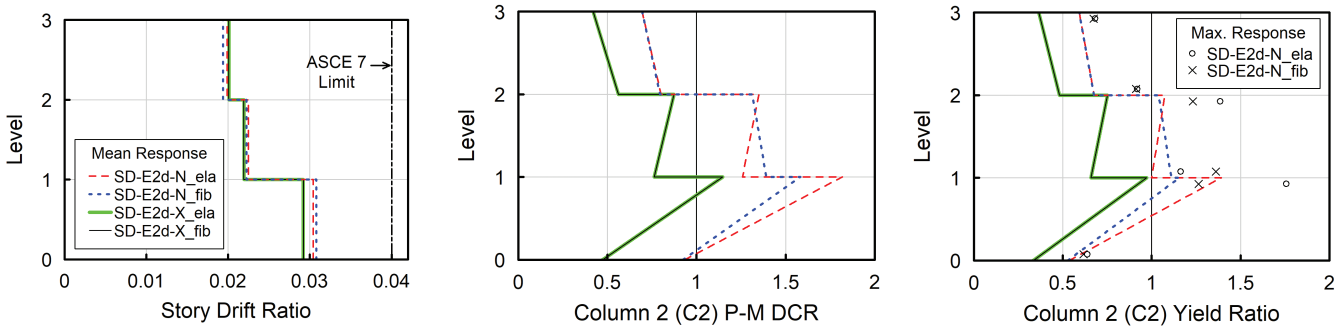

(a) Story-drift ratio *(b) P-M interaction DCR of Column 2 (C2) members* *(c) Yield ratio of C2 members*

Fig. 19. Comparison of NLRHA results between Design Cases 3S-SD-E2d-N and 3S-SD-E2d-X.

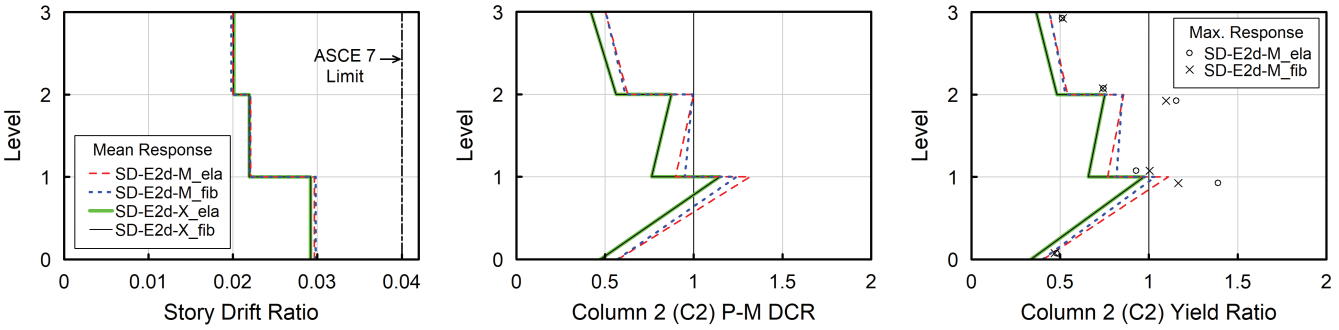

(a) Story-drift ratio *(b) P-M interaction DCR of Column 2 (C2) members* *(c) Yield ratio of C2 members*

Fig. 20. Comparison of NLRHA results between Design Cases 3S-SD-E2d-M and 3S-SD-E2d-X.

Approximate Story Shear Distribution

This section provides the estimation of the percentage of story shear resisted by the C2 members in a single-diagonal eccentric BRBF. This information can be applied to the efficient preliminary design of this type of BRBF by accounting for the contribution of C2 members to the story shear resistance. As shown in Figure 21-left, the total story shear, V_{Total}, in a typical story is the sum of the story shear components (denoted as V_{br}, V_{C1}, and V_{C2}) resisted by the braces, C1 member, and C2 member, respectively. Since the beam members are assumed to be pin connected to the C1 members, the shear in the C1 member is negligible (i.e., $V_{C1} = 0$). Thus, the total story shear can be approximated as the sum of the shears in the brace and C2 member, expressed as:

$$V_{Total} = V_{br} + V_{C1} + V_{C2} \cong V_{br} + V_{C2} \tag{12}$$

Furthermore, Figure 21-right illustrates the assumed moment diagrams for the stub and C2 member in the typical story. Because the stub behaves like a cantilever beam subjected to the vertical component of the brace axial force, P_{br}, the magnitude of bending moment at the stub end, M_{Stub}, is calculated as:

$$M_{Stub} = (P_{br} \sin\theta)e \tag{13}$$

where θ and e are the brace inclination angle and brace eccentricity, respectively.

To approximate the moment diagram in the C2 member, two assumptions are made: (1) The stub-end moment, M_{Stub}, is evenly distributed to the ends of C2 members above and below the stub-to-column joint, and (2) similar to typical SMF columns, the C2 member is assumed to bend in double curvature with an inflection point at the mid-height of the column, resulting in a linear moment diagram with equal but opposite moments at the two ends. These assumptions yield the following relationship:

$$M_{C2t} \cong M_{C2b} \cong \frac{1}{2} M_{Stub} \tag{14}$$

where M_{C2t} and M_{C2b} are the magnitudes of moments at the top and bottom ends of the C2 member, respectively. Furthermore, the shear in the C2 member, V_{C2}, can be estimated as the slope of the moment diagram, given as:

$$V_{C2} = \frac{M_{C2t} + M_{C2b}}{H} \cong \frac{2\left(\frac{1}{2} M_{Stub}\right)}{H} = \frac{M_{Stub}}{H} = \frac{(P_{br} \sin\theta)e}{H} \tag{15}$$

where H is the story height. Substituting P_{br} with $V_{br}/\cos\theta$ into Equation 15 yields:

$$V_{C2} \cong \frac{\left(\frac{V_{br}}{\cos\theta} \sin\theta\right)e}{H} = \frac{(V_{br} \tan\theta)e}{H} \tag{16}$$

Furthermore, substituting tan θ with H/b, where b is the span width tributary to the brace (calculated as the total span width L minus the brace eccentricity e, i.e., $b = L - e$), into Equation 16 gives:

$$V_{C2} \cong \frac{\left(V_{br} \frac{H}{b}\right)e}{H} = \left(\frac{e}{b}\right)V_{br} \Rightarrow \frac{V_{C2}}{V_{br}} \cong \frac{e}{b} \tag{17}$$

Thus, the ratio of story shear resisted by the C2 member to that resisted by the brace can be approximated as the ratio of the tributary span widths for each part. Finally, substituting Equation 17 into Equation 12, the following relationships can be established:

$$\frac{V_{br}}{V_{Total}} \cong \frac{b}{L} \tag{18}$$

$$\frac{V_{C2}}{V_{Total}} \cong \frac{e}{L} \tag{19}$$

These equations provide a simplified method for estimating the contributions of the brace and C2 member to the total story shear in a single-diagonal eccentric BRBF. The percentage of story shear resisted by the brace or C2

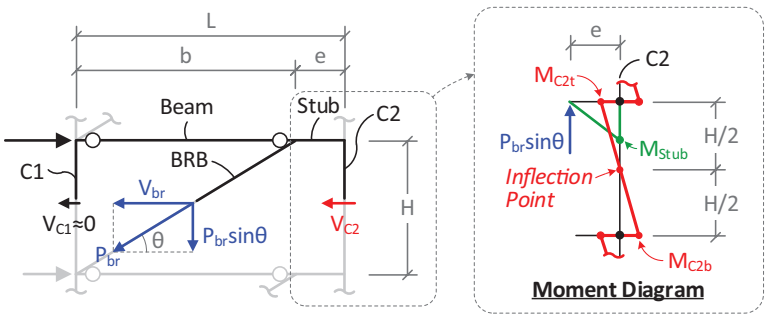

Fig. 21. Approximate analysis of story shear distribution in a typical story of a single-diagonal eccentric BRBF.

member can be approximated as the ratio or their tributary span widths to the total span width.

To validate the proposed approximation for the story shear components, V_{br} and V_{C2}, the analytical results of Design Case 12S-SD-E2d are evaluated for two levels of seismic loading. The first level is the equivalent lateral force (ELF) (ASCE, 2022), which reflects the structure's response near its elastic upper limit, while the second level corresponds to MCE, representing the peak structural response with nonlinearity during extreme seismic events. Note that, although modal response spectrum analysis (MRSA) was used for brace sizing in the case study designs, it was not applied herein to investigate story shear components at the elastic level. This is because MRSA combines modal responses using methods that inherently lose the original signs of member forces, potentially disrupting the equilibrium of internal forces among members. As a result, MRSA results are unsuitable for accurately assessing the distribution of story shear among members. Figure 22(a) shows the ELF-level story shear responses (V_{Total}, V_{br}, and V_{C2}), derived from the elastic model in ETABS (CSI, 2019) subjected to the ELF procedure. Figure 22(b) displays the MCE-level story shears, obtained from the mean peak responses of the NLRHA using the OpenSees nonlinear model (Mazzoni et al., 2006) subjected to 16 ground motions, as detailed earlier.

Figures 22(c) and 22(d) present the analysis results on the vertical distributions of the V_{br}/V_{Total} and V_{C2}/V_{Total} ratios, respectively. In each figure, the results at both the ELF and MCE levels are plotted and compared with the proposed approximation (Equations 18 or 19), denoted as Approx. The approximation reasonably matches the ELF and MCE analytical responses for all stories except for the top and bottom stories. The deviation in these two stories occurs because the assumed pattern for the moment diagram in C2 member (Figure 21-right), which applies to typical stories, may not be applicable for these atypical cases. Notably, for typical stories, the approximation predicts both V_{br}/V_{Total} and V_{C2}/V_{Total} very well at the ELF level, confirming that it offers simple and reliable measure for preliminary brace sizing while considering the contribution of C2 members to story shear resistance.

CONCLUSIONS

This paper presents the NLRHA results on the nine design cases of BRBFs with eccentricities, representing two building heights (3 and 12 stories), two bracing configurations (chevron and single-diagonal), and various eccentricities, all subjected to 16 ground motions scaled to the DBE and MCE levels. The effects of brace eccentricity on the BRBF seismic performance are also explored. Subsequently, detailed finite element modeling was performed to investigate the effects of connection geometry on beam stresses for chevron eccentric BRBFs. Lastly, the implications for the efficient design of single-diagonal eccentric BRBFs are examined, focusing on issues such as column capacity design considering moment demands and approximate story shear distribution for preliminary brace sizing.

The study supports the following conclusions:

- The NLRHA results demonstrate that the proposed design procedure [Part 1 (Li et al., 2026)] results in BRBFs with eccentricities that perform well during the DBE- and MCE-level earthquakes with story drifts staying lower than the code-prescribed limit. The results confirm the satisfactory seismic performance of BRBFs having eccentricities equal to twice the beam depth, (exceeding

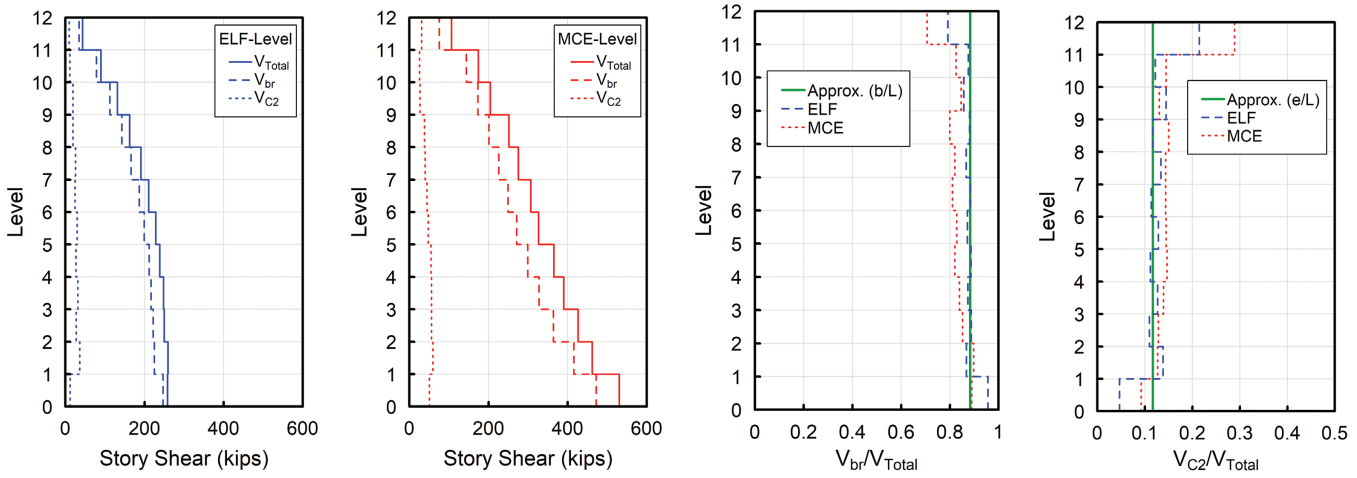

(a) ELF *(b) MCE levels and distributions* *(c) V_{br}/V_{Total}* *(d) V_{C2}/V_{Total}*

Fig. 22. Analysis results on distributions of story shear components for Case 12S-SD-E2d.

the current code limit of one beam depth), provided they are properly capacity-designed to keep the beams and columns essentially elastic (with minor column yielding allowed, provided buckling is prevented), while confining the majority of inelasticity to the BRBs. Additionally, the analytical results validate the accuracy of the proposed methods in estimating force demands for the capacity design of BRBF beams with brace eccentricity.

- In chevron BRBFs, there is a general trend of slightly increasing peak and residual drifts with eccentricity, particularly in the lower stories of the building. In contrast, single-diagonal BRBFs exhibit significantly lower peak and residual drifts in eccentric configurations compared to concentric frames, with a particularly notable reduction in residual drifts. This improvement is primarily due to the half-MRF formed by the stubs and adjacent columns, which serves as an elastic backup lateral system for single-diagonal eccentric BRBFs. This study demonstrates that by accounting for the columns' contribution to resisting story shear, single-diagonal eccentric BRBFs can be designed to be more economical than the single-diagonal concentric BRBFs, while also offering superior seismic performance. The design cases considered in this study indicate a potential reduction of approximately 3% to 5% in steel weight.
- The results of pushover analyses on detailed finite element models confirm that the proposed capacity design method on chevron BRBF beams with eccentricity, despite not accounting for the local stress distribution, would not lead to local stress concentration issues in the beam region near the brace-to-beam intersection. Additionally, the analysis demonstrates that the combined gusset configuration used for chevron BRBF beams results in lower beam web stress compared to the split gusset configuration.
- NLRHA results at the MCE level reveal that for high-rise BRBFs, the code-minimum axial-only design is sufficient to maintain C2 member elasticity due to overestimated axial demands. In low-rise BRBFs, the axial-only design may result in minor C2 member yielding without significantly affecting performance. The adapted strong column–weak beam (SCWB) design efficiently minimizes C2 member yielding in low-rise BRBFs with only a moderate increase in steel weight, while the code-beyond *P-M* interaction method achieves stringent design goal of eliminating the C2 member yielding but requires substantial additional steel.
- This study proposes an approximation of the story shear contribution for single-diagonal eccentric BRBFs, enabling hand calculations of force demand for preliminary brace sizing while accounting for the C2 members' contribution to resisting story shear. The effectiveness of this approximation is confirmed by the analysis data.

REFERENCES

AISC (2022a), *Seismic Provisions for Structural Steel Buildings*, ANSI/AISC 341-22, American Institute of Steel Construction, Chicago, Ill.

AISC (2022b), *Specification for Structural Steel Buildings*, ANSI/AISC 360-22, American Institute of Steel Construction, Chicago, Ill.

ANSYS (2022), *Ansys Mechanical Release 22.1 Help System*, ANSYS, Inc., Canonsburg, Pa.

ASCE (2022), *Minimum Design Loads and Associated Criteria for Buildings and Other Structures*, ASCE/SEI-7-22, American Society of Civil Engineers, Reston, Va.

ATC (2009), *Quantification of Building Seismic Performance Factors,* FEMA P695, Federal Emergency Management Agency, Washington D.C.

CSI (2019), *CSI Analysis Reference Manual for SAP2000, ETABS, SAFE and CSiBridge,* Computers and Structures, Inc., Berkeley, Calif.

Fortney, P.J. and Thornton, W.A. (2017), "The Chevron Effect and the Analysis of Chevron Beams—A Paradigm Shift," *Engineering Journal*, Vol. 54, No. 4, pp. 263–296.

Gholami, M., Zare, E., Gorji Azandariani, M., and Moradifard, R. (2021), "Seismic Behavior of Dual Buckling-Restrained Steel Braced Frame with Eccentric Configuration and Post-Tensioned Frame System," *Soil Dynamics and Earthquake Engineering*, Vol. 151, No. 2021, pp. 106977.

Hariri, B. and Christopoulos, C. (2024), "Numerical Hybrid Simulation Assessment of E-BRBF and E-FBF Systems for Mitigating P-Delta Effects and Enhancing Post-Earthquake Performance," *Earthquake Engineering & Structural Dynamics*, Vol. 53, No. 12, pp. 3754–3774.

Hosseini, S.M. and Amiri, G.G. (2017), "Successive Collapse Potential of Eccentric Braced Frames in Comparison with Buckling-Restrained Braces in Eccentric Configurations," *International Journal of Steel Structures*, Vol. 17, No. 2, pp. 481–489.

Lejano, B.A. and Mas, M.J.S. (2017), "Numerical Study on the Effect of Structural Parameters on the Behavior of BRBF-E," The Third International Conference on Civil Engineering Research (ICCER), Surabaya, Indonesia.

Li, C.-H., Richards, P.W., Saxey, B.W., and Richards, H.L. (2026), "Seismic Design and Performance of Buckling Restrained Brace Frames with Eccentric Brace Configurations Part 1: Design Procedures and Case Studies," *Engineering Journal*, AISC, Vol. 63, No. 1, pp. 49–74.

Lignos, D.G., Putman, C., and Krawinkler, H. (2013), "Seismic Assessment of Steel Moment Frames Using Simplified Nonlinear Models," in *Computational Methods in Applied Sciences* (Vol. 2, pp. 91–109), Springer Nature.

Liu, J. and Astaneh-Asl, A. (2000), "Cyclic Testing of Simple Connections Including Effects of Slab," *Journal of Structural Engineering*, Vol. 126, No. 1, pp. 32–39.

Liu, J. and Astaneh-Asl, A. (2004), "Moment–Rotation Parameters for Composite Shear Tab Connections," *Journal of Structural Engineering*, Vol. 130, No. 9, pp. 1371–1380.

Lowes, L.N., Mitra, N., and Altoonash, A. (2003), *A Beam-Column Joint Model for Simulating the Earthquake Response of Reinforced Concrete Frames*, Pacific Earthquake Engineering Research Center, Berkeley, Calif.

Mazzoni, S., McKenna, F., Scott, M., and Fenves, G. (2006), *OpenSees Command Language Manual,* Pacific Earthquake Engineering Research Center, Berkeley, Calif. http://opensees.berkeley.edu/wiki/index.php/Command_Manual

NIST (2010), *Evaluation of the FEMA P-695 Methodology for Quantification of Building Seismic Performance Factors*, GCR 10-917-8, National Institute of Standards and Technology, Gaithersburgh, Md.

NIST (2017), *Recommended Modeling Parameters and Acceptance Criteria for Nonlinear Analysis in Support of Seismic Evaluation*, GCR 17-917-45, National Institute of Standards and Technology, Gaithersburg, Md.

PEER. (2006), *PEER NGA Database*, Pacific Earthquake Engineering Center, Berkeley, Calif.

Prinz, G.S. and Richards, P.W. (2012), "Seismic Performance of Buckling-Restrained Braced Frames with Eccentric Configurations," *Journal of Structural Engineering*, Vol. 138, No. 3, pp. 345–353.

Sabelli, R. and Arber, L. (2017), "Design of Chevron Gusset Plates," *SEAOC Convention Proceedings*, San Diego, Calif.

Shakib, H. and Safi, R. (2012), "Behavior Evaluation of the Eccentric Buckling-Restrained Braced Frame under the Near-Fault Ground Motions," 15th World Conference on Earthquake Engineering, Lisbon, Portugal.

Vayda, P.T. (2015), *Comparative Analysis of Buckling-Restrained Braced Frames in Eccentric Configurations (BRBF-Es) and Eccentrically Braced Frames (EBFs)*, University of Arkansas, Fayetteville, Ark.

See Appendix on next page

APPENDIX

Ground motion records for the response history analysis were taken from the PEER NGA database (PEER, 2006). Tables A.1 and A.2 summarize the records and scaling factors used for the analyses of the 12- and 3-story frames, respectively.

Table A.1. Gound Motions for 12-Story Models

Ground Motion Number	Earthquake	Station	PEER-NGA Record Information		DBE Scale Factor	MCE Scale Factor
			Record Sequence Number	File Name (Horizontal Record)		
1	1994 Northridge	Canyon Country—W Lost Cany	960	NORTHR/LOS000	1.4511	2.1767
2	1994 Northridge	Canyon Country—W Lost Cany	960	NORTHR/LOS270	1.4525	2.1787
3	1999 Hector Mine	Hector	1787	HECTOR/HEC000	2.3605	3.5407
4	1999 Hector Mine	Hector	1787	HECTOR/HEC090	1.6594	2.4891
5	1979 Imperial Valley	Delta	169	IMPVALL/H-DLT262	2.5082	3.7623
6	1979 Imperial Valley	Delta	169	IMPVALL/H-DLT352	1.9454	2.9180
7	1995 Kobe (Japan)	Shin-Osaka	1116	KOBE/SHI000	1.9341	2.9012
8	1995 Kobe (Japan)	Shin-Osaka	1116	KOBE/SHI090	2.6483	3.9725
9	1999 Kocaeli (Turkey)	Duzce	1158	KOCAELI/DZC180	1.0021	1.5031
10	1999 Kocaeli (Turkey)	Duzce	1158	KOCAELI/DZC270	1.1035	1.6552
11	1992 Landers	Yermo Fire Station	900	LANDERS/YER270	1.0399	1.5598
12	1992 Landers	Yermo Fire Station	900	LANDERS/YER360	1.8081	2.7122
13	1987 Superstition Hills	El Centro Imp. Co. Cent	721	SUPERST/B-ICC000	1.8399	2.7598
14	1987 Superstition Hills	El Centro Imp. Co. Cent	721	SUPERST/B-ICC090	2.1067	3.1600
15	1999 Chi Chi (Taiwan)	CHY101	1244	CHICHI/CHY101-E	0.9894	1.4841
16	1999 Chi Chi (Taiwan)	CHY101	1244	CHICHI/CHY101-N	0.7959	1.1938

Table A.2. Gound Motions for 3-Story Models						
Ground Motion Number	Earthquake	Station	PEER-NGA Record Info.		DBE Scale Factor	MCE Scale Factor
			Record Sequence Number	File Name (Horizontal Record)		
1	1994 Northridge	Beverly Hills—14145 Mulhol	953	NORTHR/MUL009	1.0662	1.5994
2	1994 Northridge	Beverly Hills—14145 Mulhol	953	NORTHR/MUL279	0.8999	1.3499
3	1994 Northridge	Canyon Country—W Lost Cany	960	NORTHR/LOS000	1.4809	2.2214
4	1994 Northridge	Canyon Country—W Lost Cany	960	NORTHR/LOS270	1.0129	1.5194
5	1999 Düzce (Turkey)	Bolu	1602	DUZCE/BOL000	0.7725	1.1587
6	1999 Düzce (Turkey)	Bolu	1602	DUZCE/BOL090	0.8931	1.3396
7	1999 Hector Mine	Hector	1787	HECTOR/HEC000	1.9542	2.9313
8	1999 Hector Mine	Hector	1787	HECTOR/HEC090	1.4777	2.2166
9	1995 Kobe (Japan)	Shin-Osaka	1116	KOBE/SHI000	1.6243	2.4364
10	1995 Kobe (Japan)	Shin-Osaka	1116	KOBE/SHI090	2.0485	3.0728
11	1992 Landers	Yermo Fire Station	900	LANDERS/YER270	1.4278	2.1417
12	1992 Landers	Yermo Fire Station	900	LANDERS/YER360	1.5792	2.3688
13	1999 Chi Chi (Taiwan)	CHY101	1244	CHICHI/CHY101-E	1.2059	1.8089
14	1999 Chi Chi (Taiwan)	CHY101	1244	CHICHI/CHY101-N	0.9942	1.4913
15	1999 Chi Chi (Taiwan)	TCU045	1485	CHICHI/TCU045-E	1.4831	2.2246
16	1999 Chi Chi (Taiwan)	TCU045	1485	CHICHI/TCU045-N	1.4307	2.1460

ERRATA

Generalized Elastic Lateral-Torsional Buckling of Steel Beams

ROBERT S. GLAUZ and BENJAMIN W. SCHAFER

Vol. 62, No. 1, 2025

On page 29, change the '+' to '–' before the last term:

$$EI_{\dot{x}}\dot{v}^{iv} + P\dot{v}'' - P(\dot{x}_o - e_{\dot{x}})\phi'' = 0 \tag{2}$$

On page 33, revise Equations 41 and 42 to change the $\beta_{\dot{y}}$ to $\beta_{\dot{x}}$:

$$L^2 = \frac{C_b\pi^2 EI_{\dot{y}}}{M_{cr}}\left[C_s\frac{\beta_{\dot{x}}}{2} + \frac{C_bGJ}{2M_{cr}} + \sqrt{\left(C_s\frac{\beta_{\dot{x}}}{2} + \frac{C_bGJ}{2M_{cr}}\right)^2 + \frac{C_w}{I_{\dot{y}}}}\right] \tag{41}$$

$$L_r^2 = \frac{C_b\pi^2 EI_{\dot{y}}}{M_r}\left[C_s\frac{\beta_{\dot{x}}}{2} + \frac{C_bGJ}{2M_r} + \sqrt{\left(C_s\frac{\beta_{\dot{x}}}{2} + \frac{C_bGJ}{2M_r}\right)^2 + \frac{C_w}{I_{\dot{y}}}}\right] \tag{42}$$

Guide for Authors

Scope *Engineering Journal* is dedicated to the improvement and advancement of steel construction. Its pages are open to all who wish to report on new developments or techniques in steel design, research, the design and/or construction of new projects, steel fabrication methods, or new products of significance to the uses of steel in construction. Only original papers should be submitted.

General Go to **aisc.org/ej** for complete submittal instructions.

All papers within the scope outlined above will be reviewed by engineers selected from among AISC, industry, design firms, and universities. The standard review process includes outside review by an average of three reviewers, who are experts in their respective technical area, and volunteers in the program. Published papers become the property of the American Institute of Steel Construction and are protected by appropriate copyrights. No typesetting proofs will be provided to authors.

Manuscripts Manuscripts must be provided in Microsoft Word format. Include a PDF with your submittal so we may verify fonts, equations, and figures. View our complete author guidelines at **aisc.org/ej**.

Archives Search at **aisc.org/ej**. Article downloads are free.

Smarter. Stronger. Steel.

American Institute of Steel Construction
130 E Randolph St, Ste 2000, Chicago, IL 60601
312.670.2400 | aisc.org/ej